# Electropermanent Magnetic Connectors and Actuators: Devices and Their Application in Programmable Matter

by

Ara Nerses Knaian

S.B. Massachusetts Institute of Technology (1999)
M. Eng. Massachusetts Institute of Technology (2000)
M.S. Massachusetts Institute of Technology (2008)

Submitted to the Department of
Electrical Engineering and Computer Science
in partial fulfillment of the requirements for the degree of
Doctor of Philosophy in Electrical Engineering and Computer Science
at the
MASSACHUSETTS INSTITUTE OF TECHNOLOGY
June 2010



Author .....
Department of
Electrical Engineering and Computer Science
May 21, 2010

Certified by .....
Daniela L. Rus
Professor
Thesis Supervisor

Certified by .....
Neil A. Gershenfeld
Professor
Thesis Supervisor

Accepted by .....
Terry P. Orlando
Chairman, Department Committee on Graduate Theses

# Electropermanent Magnetic Connectors and Actuators: Devices and Their Application in Programmable Matter

by

Ara Nerses Knaian

Submitted to the Department of
Electrical Engineering and Computer Science
on May 21, 2010, in partial fulfillment of the
requirements for the degree of
Doctor of Philosophy in Electrical Engineering and Computer Science

## Abstract

Programmable matter is a digital material having computation, sensing, and actuation capabilities as continuous properties active over its whole extent. To make programmable matter economical to fabricate, we want to use electromagnetic direct drive, rather than clockwork, to actuate the particles. Previous attempts to fabricate small scale (below one centimeter) robotic systems with electromagnetic direct-drive have typically run into problems with insufficient force or torque, excessive power consumption and heat generation (for magnetic-drive systems), or high-voltage requirements, humidity sensitivity, and air breakdown. (for electrostatic-drive systems) The electropermanent magnet is a solid-state device whose external magnetic flux can be stably switched on and off by a discrete electrical pulse. Electropermanent magnets can provide low-power connection and actuation for programmable matter and other small-scale robotic systems. The first chapter covers the electropermanent magnet, its physics, scaling, fabrication, and our experimental device performance data. The second introduces the idea of electropermanent actuators, covers their fundamental limits and scaling, and shows prototype devices and performance measurements. The third chapter describes the smart pebbles system, which consists of 12-mm cubes that can form shapes by stochastic self-assembly and self-disassembly. The fourth chapter describes the millibot, a continuous chain of programmable matter which forms shapes by folding.

Thesis Supervisor: Daniela L. Rus
Title: Professor

Thesis Supervisor: Neil A. Gershenfeld
Title: Professor

# Acknowledgments

Thanks to Neil Gershenfeld for nurturing my creativity, constantly pushing me to question the established ways of doing things, sparking what I'm sure will be a life-long fascination with machine tools, and for letting me be a part of what must be one of the most interesting laboratories and groups of people on Earth.

Thanks to Daniela Rus for introducing me to the larger robotics community, and for teaching me the value of data. For every graph in this thesis with actual gritty data points instead of smooth mathematical curves, I have Daniela to thank for her weekly encouragement to report the state of the world as it actually is, as well as how I would like for it to be.

Thanks to Markus Zahn and the late Jin Au Kong for teaching me Electromagnetism. They taught me how to do in twenty minutes on the board what used to take me two weeks with a computer model. After taking their classes, all the sudden my devices started actually working.

Thanks to Joseph Jacobson, Carol Livermore, Bill Butera, and Saul Griffith for getting me thinking about the problems in this thesis in the first place. Without them, this thesis would have been about some other topic entirely. Thanks to Terry Orlando, my academic advisor, for all his help.

Thanks to Kyle Gilpin, my collaborator on the Robot Pebbles system. Our rough division of labor starting out was that I handled magnetics and mechanics and he handled electronics and software. But this doesn't tell the whole story; in addition to inventing the algorithms, designing the circuits and writing the code, Kyle did all the hard development work to get the Pebbles fabricated and functioning, and I am thankful for the opportunity to work with someone so dedicated.

Thanks to Maxim Lobovsky, Asa Oines, Peter Schmidt-Nielsen, Forrest Green, David Darlrymple, Kenny Cheung, Jonathan Bachrach, Skylar Tibbets, and Amy Sun, my collaborators on the Millibot project. Max and Asa have designed several parts of the motor and Millibot, as well as logged a sizable number of hours in the lab helping me to build these systems. Amy, always ready with her camera, took many

of the photos shown in this thesis. Thanks to my other lab-mates in PHM, DRL, and the Harvard Microrobotics lab for all their help – whether it was helping me work something out on the whiteboard, teaching me how to use a machine, pointing out an article I should read, or just being around to dream about the possibilities of technology.

Thanks to Robert Wood and Peter Whitney for introducing me to what it is possible to build with tweezers, a microscope, and a laser, and for their gracious hospitality.

Thanks to Joe Murphy, Sherry Lassiter, Nicole Degnan, and Kathy Bates, for doing a spectacular job keeping all of the supplies and equipment I needed to do this work flowing into the lab, and for making the Center for Bits and Atoms and the Distributed Robotics Lab the well-oiled machines that they are. Thanks to John DiFrancesco, Tom Lutz, and Ron Wiken for their help in the machine shop. Thank you to DARPA for funding this work, to program managers Mitch Zakin and Gill Pratt, and to the taxpayers of the United States of America.

Thanks to Harry Keller, David Newburg, Mr. Martins, Mr. Wells, and Dr. Duffy, high-school teachers and mentors who made a difference in my life.

My father taught me how to use a wood saw, how to build an amplifier, and how to solder. My mother taught me to look at the world as a scientist. Thank you to my parents for what you started.

I owe my wife Linda thanks on many levels. She is a mechanical engineer and introduced me to many of the vendors and products mentioned in the text. Throughout the time we have known each other, she has worked tirelessly to get me out of the lab and off on some fun adventure, and I thank her for that. From our dinner conversation over the last couple years she is intimately familiar with electropermanent magnetic connectors and actuators, both the devices *and* their application to programmable matter. Right now she is in the other room proofreading this manuscript.

Finally, thanks my son Aaron, who is 13 months old. Watching and helping him grow up brings to my life the greatest joy of all.

# Contents

# List of Figures

# List of Tables

# Chapter 1

# Introduction

This thesis introduces a new type of actuator and connector to the field of robotics. The electropermanent magnet is a device that can have its external magnetic field switched on and off by an electrical pulse, and retains its magnetic state with zero power. We show that electropermanent magnets are strong, low-power devices at small scales, because their switching energy scales with volume, while their holding force scales with area.

Using these devices, we construct two new modular robotic systems, both of which have the smallest modules of any of their type in the published literature. In our Robot Pebbles system, electropermanent magnets provide all of the module-to-module forces needed for shape reconfiguration, as well as providing a channel for module-to-module communication and power transfer. This eliminates the need for any off-the-shelf mechanical components, enabling a 12 mm module size.

We introduce a new type of electric motor, the electropermanent stepper, which scales well to small dimensions and maintains its efficiency down to zero speed, allowing operation without gearing. We use this motor to build the Millibot, a chain-type modular robot capable of shape change and locomotion, with a 12 mm module pitch.

This work is part of the larger academic enterprise to construct programmable matter, a universal material with the ability to change its shape and other properties on command. Programmable matter could be synthesized using a batch photolithographic process, motivating our study of connection mechanisms and actuators that

are simple to construct and scale well to small dimensions. The enterprise to create programmable matter can be seen as a project to digitize the process of fabrication [31], building on the work of those who digitized computation and communication.

## 1.1 The Quest for a Universal Machine

In 1833, Charles Babbage invented the analytical engine, a universal mechanical machine for evaluating arbitrary mathematical expressions. The machine was to be controlled by punched cards, powered by a steam engine, and to represent numbers by the positions of geared wheels. Babbage, who once wrote a paper entitled "Table of Relative Frequency of the Causes of Breaking of Plate Glass Windows" was fascinated with data and statistics, and was taken with the idea of a machine to perform arbitrary computations automatically. With the help of the British government, he launched a massive effort to build a prototype. Sadly, due to the machine's enormous complexity, as well as interpersonal disputes and funding difficulties, the machine was never finished. But during the same period, and just a few miles away, the ground was already being laid for those who would follow Babbage in his quest; Michael Faraday was hard at work discovering the laws of electricity and magnetism.

Just over a century later in 1941, Konrad Zuse would construct the Z3, a punch-card controlled digital computer, realizing Babbage's vision of a universal computing machine. The Z3 used electromechanical relays rather than clockwork, greatly simplifying its design and construction. Still, the Z3 weighted 1000 kg, consumed 4 kW power, had a clock rate of 5.3 Hz, and just 64 words of memory.

So it was not until the invention of the integrated circuit by Jack Kilby and Robert Noyce in the late 1950's, and the microprocessor by Ted Hoff in the 1960's, that the computing revolution really took off. The integrated circuit allowed in-place fabrication of all of the components and electrical connections for a computer in parallel, by photolithography. Now the complexity of a feasible design was no longer limited by the need for painstaking hand assembly; only by the achievable resolution of photographic patterning.

Over the past fifty years, the semiconductor industry has worked tirelessly to improve the resolution of photolithography following Moore's law, [64] [63] which states that the number of transistors that can be placed in a given area doubles every two years. Because of this, today one can buy a billion-transistor computing machine for less than the cost of the desk that holds it up off of the floor.

## 1.2 Programmable Matter

There are other types of universal machines. Even before Babbage, Jacquard constructed a punch-card controlled loom, able to weave fabric with any conceivable pattern.

Programmable matter is universal material, long discussed in science fiction under various names [62], which would be able to change its shape and other physical properties, such as stiffness and color, on command. There are many potential approaches for synthesizing programmable matter, such as synthetic biology [25], molecular nanotechnology [20], quantum dots [4], and metamaterials. [81]

The approach considered in this thesis is electromechanical: the construction of miniature electronic modules, able to process information, communicate, transfer power, and exert mechanical force on each other through magnetic fields. Once the modules were too small to easily see, and if there were enough of them, we might start to think of them as a material. The module size does not have to micron-scale: the pixel size of the Apple II monitor was 1 mm; in this thesis we show experimental results with modules that are just 10 times larger than that. The applications for programmable matter are many and varied, but would depend on the range of properties that could be expressed, the resolution, and the cost. An expensive, weak material might find application as a tactile three-dimensional display [37], a programmable tip for an endoscope, or a highly adaptive mobile robot. [56] Applications for a cheap, strong material are almost unlimited; one example is a universal aircraft mechanic's tool, able to transform from a wrench to a screwdriver to a walkie-talkie at the push of a button, or Albert Hibbs' swallowable robotic surgeon. [26] Of course, just as the

builders of early computers could not have imagined Facebook or Twitter, we cannot imagine exactly what uses people will eventually find for programmable matter—but then that is the point of making it universal in the first place.

## 1.3 Solid-State Programmable Matter

A self-reconfigurable modular robot is a machine, made of a large number of repeated modules, that is able to change its shape. Since the construction of the first modular robot by Fukada in 1988, [29] over 20 systems have been constructed by research groups around the world.

A self-reconfigurable modular robot is a form of programmable matter. But most modular robots have been hand-assembled from off-the-shelf electric motors and mechanical components. This has made construction of the modules expensive and time-consuming, and kept the minimum size of the modules at about 40 mm.

We might try to build miniaturized programmable matter using miniaturized versions of macroscopic mechanical components: essentially, using miniaturized clockwork. But this may be a difficult path to programmable matter. In a 1992 paper, Slocum [83] points out that while macromechancial machines have been manufactured with part-per-million relative tolerances for over a century, micromechanical machines have much lower relative precision, and resemble the maromachines of the early 1700's in their complexity and accuracy. A 1 mm machine produced with 100 nm tolerance has a relative tolerance of just one part in 10,000.

But what if we could design out the internal moving parts and build programmable matter out of electronics only? The modules could exert forces on each other through the force between current-carrying wires, or the force between plates with a potential difference. The overall system could still move; but it would be made of solid-state, non-mechanical parts.

This approach is taken by White and Lipson with their Stochastic system [95], by Kirby and Goldstein with the Catoms [54], and by An with the EM-Cubes. [5]

In these systems, heat from $I^2R$ losses in the electromagnets has been a major

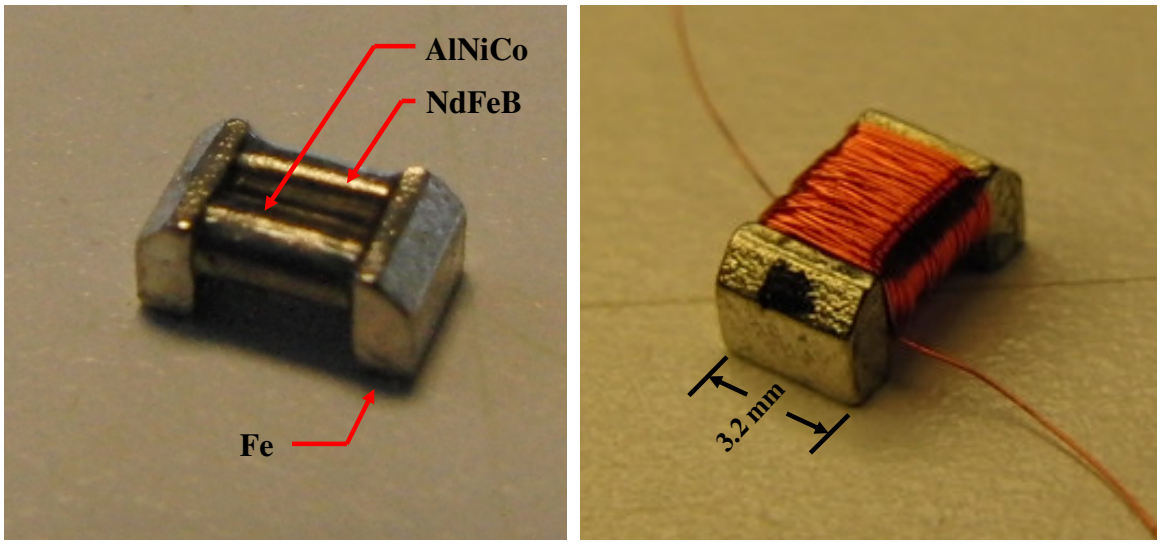


Figure 1-1: Miniature electropermanent magnet. This magnet is made from cylindrical rods of hard NIB, semi-hard Alnico, iron pole pieces, and a copper wire coil. The magnet can hold 4.4 N, which is over 2000 times its own weight, switches with a 5 mJ electrical pulse, and holds its state with zero power.

limit on performance, manifesting itself either as destructive temperature rise, high power requirements, or low force capability. In this thesis, we will show how to solve the problem of excessive $I^2R$ losses in programmable matter or other miniaturized robotic systems, by using pulse-driven electropermanent magnets.

## 1.4 The Electropermanent Magnet

This thesis will show that switching the magnetization of a semi-hard ferromagnetic material with discrete electrical pulses enables high-force, low-power actuation at small scales—allowing electronic circuits to exert forces on one another for shape change or locomotion.

An electropermanent magnet is a solid-state device whose external magnetic field can be modulated by an electrical pulse. No electrical power is required to maintain the field, only to do mechanical work or to change the device's state. The electropermanent magnets described in this thesis contains two magnetic materials, one magnetically hard (NIB) and one semi-hard, (Alnico), capped at both ends with a

magnetically soft material (Iron) and wrapped with a coil. A current pulse of one polarity magnetizes the materials together, increasing the external flow of magnetic flux. A current pulse of the opposite polarity reverses the magnetization of the semi-hard material, while leaving the hard material unchanged. This diverts some or all of the flux to circulate inside the device, reducing the external magnetic flux.

## 1.5 Properties of Electropermanent Magnets

One of the most exciting properties of the electropermanent magnet is that it is scalable. The energy required to switch an electropermanent magnet scales with its volume, while the force it can exert scales with its area. Objects made from programmable matter with modules scaled down or up in size would have the same mechanical properties and require the same amount of energy for magnet switching.

The instantaneous power draw during the switching pulse for an electropermanent magnet is higher than for the equivalent electromagnet, by about a factor of 10. But the switching time is short, only $100\mu s$ for the magnets used in the Pebbles. Electropermanent magnets result in an energy savings so long as they are switched infrequently enough—in the case of the Pebbles, less than every two milliseconds. At smaller length scales, this break-even time goes down further.

The curve of force versus distance is similar to that of a permanent magnet made from the semi-hard material. Practically, this means that for contacting or very close magnets, the holding force is as large as that of rare-earth magnets, but decays more rapidly at long distances. (See Section 3.5.2)

Electropermanent magnets are capable of greater holding pressure than electrostatic plates in air, use lower drive voltages, and are less sensitive to humidity. (See Section 3.3.1)

Under tensile loading, our electropermanent magnets have a holding pressure of 230 kPa, measured over their whole frontal area. This is similar to or better than the maximum rated tensile loading of mechanical modular robotic connectors based on pins and hooks, although our connector's strength in rotation and shear are lower.

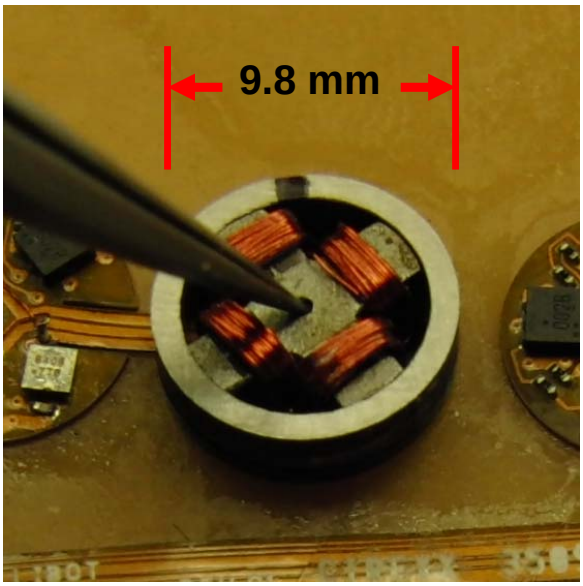


Figure 1-2: Electropermanent Stepper Motor. This new motor works by remagnetizing a semi-hard permanent magnet, which then does work over an arbitrary period of time. It holds with the zero power, and maintains efficiency to asymptotically zero speed. This allows the continuous (but slow) lifting of weight with an arbitrarily small power source. Additionally, its large torque of 1.1 N-mm allows its use without a gearbox.

(See Chapter 7) The maximum theoretical magnetic force density (at 2 T) for a magnetic system is 3 MPa; compare this to the 0.6 MPa maximum force density for electrostatics in air (see Section 3.3.1), the 12 MPa yield strength of polypropylene, or the 1 GPa yield strength of steel. Purely magnetic bonding is not as strong as the covalent bonds of materials. But our magnetic connectors are strong enough for programmable matter. With our Pebbles system, the magnetic connectors are strong enough in principle to support the weight of nearly a meter of modules.

## 1.6 Properties of Electropermanent Actuators

Using the electropermanent magnet principle enables the construction of motors and actuators capable of operation at constant efficiency at arbitrarily low speeds. The magnet is switched by a discrete pulse containing a fixed amount of energy, and then can do a fixed amount of work, but over an arbitrarily long period of time. This is

in contrast to ordinary electric motors, which because of $I^2R$ heating in the windings have an efficiency that goes asymptotically to zero as the speed is reduced.

The electropermanent actuator is a one-bit memory, allowing the controller to send the device a command calling for force, and then to open the circuit while the force is exerted, preventing excessive $I^2R$ dissipation at low speed.

Electropermanent motors can provide useful torque for robotic applications without additional gearing. The electropermanent wobble motor we present in this thesis, which has a diameter of 10 mm and a mass of 1 gram, can provide 1.1 N-mm of torque, enough to lift a 23 gram weight suspended from a string wrapped around its outer diameter.

The linear actuator characterized in this thesis achieves an efficiency of 8%, and the rotary motor 1%. These figures are very favorable when compared to similarly sized electromagnetic and piezoelectric motors operating in the low-speed limit. See Chapter 7 for a detailed comparison.

## 1.7 The Robot Pebbles

Our Robot Pebbles system, shown in Figure 1-3, has the smallest modules of any working modular robotic system in the published literature. The small size of the modules is enabled by the use of our electropermanent magnets for all aspects of inter-module connection: mechanical bonding, power transfer, and communication. The system is capable of self-assembling itself into a square lattice, then self-disassembling itself into arbitrary user-defined shapes. It is all-electronic: the modules contain no moving parts.

Each Pebble can, in principle, hold up the weight of 82 other modules; this is higher than for macroscopic systems based on mechanically-switched permanent magnets, and a similar figure to that of macroscopic systems based on mechanical latching. (See Chapter 7) The primary reason is surface-area-to-volume scaling; the mass of a node scales with volume, but the holding force of the connectors scale with area.

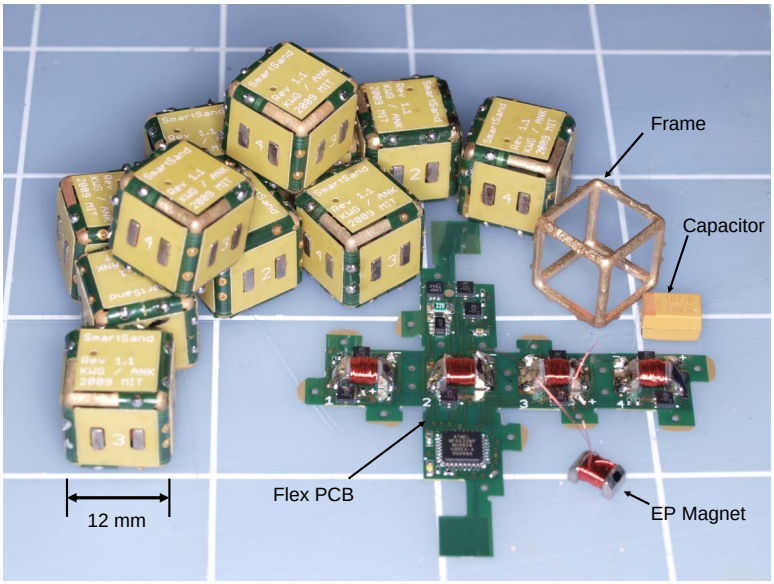


Figure 1-3: The Robot Pebbles are fully printed-circuit integrated, solid-state programmable matter. All of the components, including the four electropermanent magnet connectors and the frame are soldered to a flexible printed circuit board. The electropermanent magnet connectors provide mechanical connection, electrical power transfer, and inductive communication between modules.

## 1.8 The Millibot

The Millibot is programmable matter inspired by the folding of proteins. It is a continuous flexible circuit with periodically placed electropermanent stepper motors, capable of folding itself into shapes. Each module is a single, solid-state device, with no moving parts. We have succeeded in constructing a two-node Millibot, and verified that one node can lift the other. From experimental measurements of the torque of the motors and weight of the Millibot modules, we expect that each joint of the Millibot will be able to lift three of its neighbors in a cantilever. This is a similar figure to macroscopic modular robotic systems employing 100:1 gearboxes. (See Chapter 7) The favorable surface-area-to-volume scaling of the electropermanent magnet allows us to build solid-state robotic systems at 1 cm scale with similar performance to larger systems requiring moving parts.

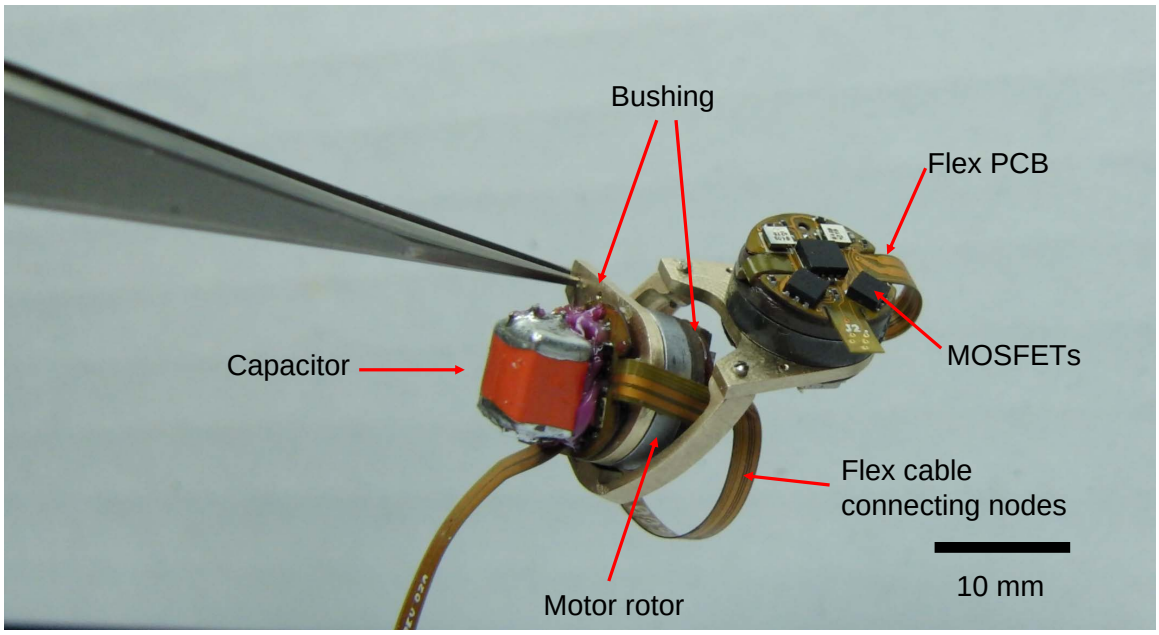


Figure 1-4: A two-module Millibot, showing the major components.

## 1.9 How to Fabricate Smart Sand

The Robot Pebbles and the Millibot are both PCB-integrated systems, constructed with nearly the smallest available off-the-shelf electronic components, integrated with flexible printed circuits and hot-air reflow soldering. We feel that we are close to the limit with this approach to miniaturization—our current nodes are 12 mm across—with better component selection and increased packing cleverness, perhaps we could get them down to 8 mm or 6 mm—but not much smaller.

To get to the next level of miniaturization, 1 mm modules, we propose to use multi-layer, multi-metal electrodeposition. We would deposit copper, iron, cobalt-platinum (an electroplatable permanent magnet alloy), and silicon dioxide in a series of hundreds of photo-patterned 5 $\mu m$ thick layers. Part-way through the process, we would insert a bare-die custom CMOS ASIC containing the circuitry, and an off-the-shelf ceramic capacitor for the energy storage. (See Appendix A) Then the electrodeposition process would continue, encapsulating these components. Finally, we would singulate the wafer into a container, producing a pile of "Smart Sand"—monolithic blocks of metal, air, and glass with the ability to compute, communicate,

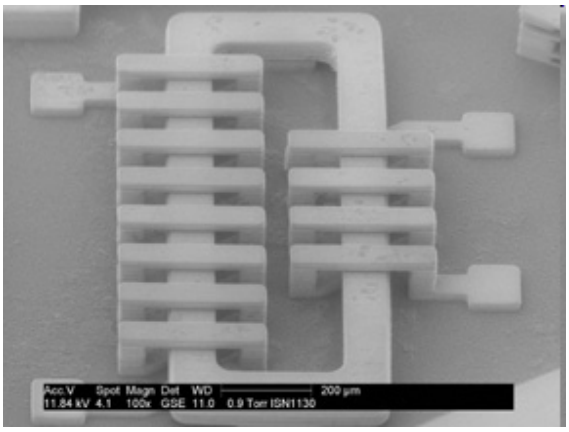


Figure 1-5: A transformer fabricated using EFAB. (MEMgen Corp.)

change shape, and exert forces on each other for shape change and locomotion.

The basis for our proposed fabrication process is EFAB, developed by Cohen at the USC Information Sciences Institute and commercialized for a limited set of materials by Microfabrica Inc. (Van Nuys, CA) The EFAB process allows metal micro-devices with thousands of layers to be built using a single photographic mask, by repetitive electroplating into molds, in a process called "Instant Masking." [17] A set of molds, one for each layer, are fabricated using photolithography. The molds are arrayed next to each other on a single plate, so only one mask and one set of photolithography steps is required, even for a device with hundreds of layers.

The device is built on a conductive substrate. The substrate is immersed in an electroplating bath, and the portion of the mold for the first metal layer is pressed against it. This leaves only the area where metal is to be deposited exposed to the electroplating solution. Current is applied and metal is electroplated. A second filler metal is plated, then the surface is planarized by mechanical lapping. The mold is stepped to the next position and the process continues for the next layer, until all of the layers are fabricated. The filler metal is then dissolved, revealing the completed devices. Figure 1-5 shows a sub-millimeter transformer fabricated using the EFAB process.

In standard EFAB, there is only one mask impression per layer. But, to get the multiple metals needed for magnetic devices, we propose to add a step where the

substrate is transferred to another electroplating bath and a second metal is plated according to a second set of molds.

On each layer, we would electroplate copper for the coils, iron for the soft magnetic material, and cobalt-platinum [12] for the hard magnetic material. The semi-hard material could be formed by thin layers of hard material interleaved with thick layers of soft material. Once all the metals were deposited for a given layer, we would add a layer of silicon dioxide to fill space with dielectric, planarize by lapping, then proceed to the next layer.

## 1.10 Contributions

The primary contribution of this thesis is the identification of the electropermanent magnet as a scalable, strong, low-power means of actuation and connection for programmable matter and other microrobotic systems. In particular, I did the following work:

- Developed a magnetic circuit model for the electropermanent magnet, suitable for device design and analysis. Verified this model experimentally and with finite-element analysis.

- Worked out the scaling relationships for the electropermanent magnet, showing that the device is scalable to small dimensions because the switching energy is proportional to volume but the force is proportional to surface area.

- Computed the break-even voltage for electropermanent magnets as compared to electrostatic plates. Showed that electropermanent magnets are stronger than air-breakdown-limited electrostatic plates at any size scale.

- Computed the break-even time for electropermanent magnets versus electromagnets. Showed that electropermanent magnets use less energy then electromagnets so long as the holding time is long enough, and that this is just a few milliseconds at 1 cm scale.

- Constructed 6 mm electropermanent magnets and characterized their performance.
- Showed how to use electropermanent magnets to achieve inter-module latching, power transfer, and communication in a modular robotic system
- Collaborated on the design and construction of a the new modular robotic system, the Robot Pebbles, which has the smallest modules of any system in the published literature. Demonstrated self-assembly into a lattice and self-disassembly of user-defined shapes. Constructed 15 working modules.
- Introduced the idea of using the electropermanent magnet principle in motors, to improve efficiency at low speed and at small dimensions.
- Mapped out the electropermanent actuation thermodynamic power cycle, and showed how energy flows through electropermanent actuators through a model of their electrical and mechanical dynamics.
- Invented a new type of motor, the electropermanent stepper motor. Constructed a working prototype of the motor, characterized its performance, and presented formulas for design.
- Showed that the prototype electropermanent stepper motor is more efficient than commercial 10mm diameter electromagnetic motors at speeds below 1000 RPM.
- Proved that the maximum efficiency of an electropermanent actuator is 20%.
- Designed a new chain-style modular robotic system, the Millibot, with the smallest axis-to-axis distance of any system in the published literature. Constructed two working modules.

# Chapter 2

# Related Work

This thesis builds on work in miniaturization, mesoscale and microscale actuation, autonomous microsystems, modular robotics, and electromagnetic devices using magnetic hysteresis. In the following sections, we present a survey of related work in each of these areas.

## 2.1 Miniaturization

At the annual meeting of the American Physical Society in 1959, Richard Feynman gave a talk called "There's Plenty of Room at the Bottom," a transcript of which was later reprinted in [26] and is widely available online. In this talk, he calls attention to the then-theoretical possibility of manipulating matter on a very small scale. He points out, for example, that if the entire 24 volumes of the Encyclopedia Britannica were to be engraved onto the head of a pin, the halftoning dots of the images would still be 32 atoms across. He offers several suggestions for how to do this, from fabrication by photolithography and evaporation (which is how integrated circuits are actually made today) to using a mechanical pantograph to build tiny hands, using those tiny hands to build tiny machine tools, and then using those tiny machine tools to build even tinier hands. He warns that the endeavor of miniaturization will not be straightforward, because different physical phenomena scale differently with size. He suggests several applications for micro-technology: from miniature computers to swal-

lowable surgical robots. In the domain of microelectronics, today we have achieved something close to Feynman's vision, with billion-transistor computing machines in our homes and square-centimeter FLASH memory cards in our pockets capable of storing the contents of thousands of printed volumes.

### 2.1.1 Integrated Circuits

Integrated circuits are typically fabricated on single-crystal silicon wafers. The semiconductor fabrication process is a repeated series of photolithography and pattern transfer operations. The wafer is coated with photoresist; that photoresist is exposed to light through a mask, defining the pattern; the photoresist is developed, removing it from the desired areas of the wafer; the desired material is added or etched away through the holes in the photoresist; finally, the photoresist is chemically stripped, leaving only the desired material in the desired pattern. This process is repeated, layer by layer, to build up the desired structure. The fabrication process for a CMOS integrated circuit starts with ion implantation to define the N and P type areas that will become transistors, continues with chemical vapor deposition of oxide and polysilicon to define the transistor gates, sputtering of aluminum to define the wiring, and finally singulation into individual chips with a diamond circular saw.

There are many different types of integrated circuits, using many different processes and materials, and to actually fabricate an integrated circuit is much more complicated than it would seem from the simplified overview above. For a more detailed introduction to integrated circuit design and fabrication, see *Microelectronics: An Integrated Approach* by Howe and Sodini. [42]

### 2.1.2 MEMS

The acronym *MEMS* stands for Micro Electro-Mechanical Systems. However, in common usage, any mechanical system with features measured in micrometers can be called MEMS, whether electromechanical or not.

MEMS devices are typically produced using processes derived from integrated

circuit fabrication. The first MEMS device was a pressure sensor featuring a piezoresistive silicon strain gauge, which began commercial development in 1958 and was brought to market by National Semiconductor in 1974. [93]

Since then, a huge number of MEMS devices have been built in the laboratory, and many have become successful commercial products. [82] These include accelerometers, rate gyroscopes, ink jet print heads, thin-film magnetic disk heads, reflective displays, projection displays, RF components, optical switches and microfluidic lab-on-a-chip systems such as DNA microarrays.

One reason for the adoption of MEMS devices is simply because they are small: they can fit in small spaces, use little material, and are lightweight. Another is that they can be inexpensive to manufacture, because they are made using batch fabrication, so executing the process once yields thousands of saleable devices.

From a systems perspective, MEMS devices are interesting because they enable large numbers of identical devices to be deployed and integrated at low cost as a single system. A famous example is Texas Instruments Digital Micromirror Device, [79] which uses an array of millions of tilting mirrors to form an image.

From a scientific perspective, MEMS devices allow interaction with the world on a smaller scale than macrodevices. As an example, Manalis has used MEMS cantilevers to weigh biomolecules and cells. [9]

Physical phenomena take on different relative importance at the microscale than the macroscale, sometimes enabling improved device performance of MEMS devices over their large-scale counterparts. At the microscale, fluids tend to exhibit laminar, rather than turbulent flow, enabling the orderly manipulation of fluids and droplets in microfluidic systems and ink-jet print heads. [76] Time scales tend to be faster at the microscale, so MEMS relays switch faster than their macroscale counterparts.

However, the picture is not all rosy. For many types of MEMS components, especially power components such as engines, motors, and batteries, physical scaling phenomena make things harder, not easier. Power MEMS [45] is an exciting and active area of academic research, and one to which this thesis attempts to make a contribution.

The techniques for MEMS fabrication can be divided into four categories: wet bulk micromachining, surface micromachining, micromolding, and traditional machining.

In wet bulk micromachining, a single-crystal silicon wafer is shaped by etching with potassium hydroxide. Because the anisotropic crystal structure of silicon leads to different etch rates in different directions, a surprising variety of angled shapes can be made using this technique.

In surface micromachining, structures are built up on the surface of a wafer by repeated combination of thin-film deposition, photolithography, and etching. Sacrificial materials allow the release of moving parts such as gears and cantilevers, fabricated in place to avoid the need for assembly. Thin films of materials with conductive, insulating, magnetic, piezoelectric, and many other properties can be deposited.

The micromolding processes include LIGA, EFAB, and soft lithography. In the LIGA process, X-ray radiation is used to produce molds for electroplating, allowing the fabrication of high aspect-ratio metal parts. The EFAB process allows three-dimensional free-form fabrication of metal microdevices, made from thousands of stacked two-dimensional layers. The basic EFAB process step is to mate a mold with the device, electroplate the structural material, remove the mold, electroplate a sacrificial material into the remaining space, and then planarized in preparation for the next layer. With the soft lithography process, structures are built up from PDMS and other flexible polymers using photoresist molds.

Finally, MEMS devices can be made using traditional machining and assembled using the GSWT[1] method. Even the most ordinary numerically controlled machining center can achieve 3 $\mu m$ positioning resolution, and 50 $\mu m$ diameter end mills are readily available. Small parts can be fixtured using glue, ice, or wax. On the one hand, these devices can take advantage of the full range of engineering materials; on the other hand, they are time-consuming and expensive to produce.

Two excellent books about MEMS design and fabrication are *Fundamentals of Microfabrication* by Madou [61] and *Microsystem Design* by Senturia. [82]

[1]Graduate Student with Tweezers—thanks to a salesman from Microfabrica, Inc. for teaching me this lovely acronym.

## 2.2 Electrical Actuators

An electrical actuator is a device that causes mechanical movement under the control of an electrical signal. A motor is an actuator that allows for continuous movement over a large range. Michael Faraday constructed the first electrical motor in 1821, a current-carrying wire, able to rotate around a permanent magnet in a mercury-filled dish.

There are wide variety of different types and configurations of electrical actuators in service today, ranging in size from the hundred-megawatt electromagnetic synchronous machines used to pump water at the Grand Coulee Dam down to the picowatt electrostatic torsion beams used to deflect light in digital micromirror projectors. [79] There is no single "best" type of electrical actuator—the best for a given application depends on a variety of design considerations. These include requirements on power, speed, torque, size, durability, mechanical configuration, precision, voltage, current, driving complexity, and cost. [102] [7]

Physical scaling laws make different physical phenomena relatively more important at different length scales. This changes the characteristics of different types of actuator as they are implemented at smaller sizes. There are also practical differences of fabrication technology and economics at different scales. Assembly of parts made from different materials is easy for macroscopic systems, but is not a readily available microfabrication process step. Material cost is significant for a large motor, but insignificant for a microscopic one.

In this section we will focus on mesoscale and microscale actuators, which we define as those below 15 mm in all dimensions. To narrow the scope further, we will discuss actuators where the input energy is electrical and the output energy is mechanical. For a more complete survey, including actuators using chemical, fluid, magnetostrictive, magnetothermal, magnetofludic, electrofluidic, and optical operating principles, see *Actuators* by Janocha [46] and *Microactuators* by Tabib-Azar [87].

### 2.2.1 Electrostatic

Electrostatic actuators use the force of attraction between opposite electrical charges or the repulsion of like charges. In everyday life, we observe electrostatic forces brought on by the mechanical movement of charge on dielectrics. By rubbing our stockings on the carpet, we can make our hair stand on end or make Styrofoam peanuts stick to each other. The author is not aware of a practical actuation device making use of this phenomenon of tribocharging. Electrostatic actuators are typically based on the variable capacitance principle; capacitor plates with an applied potential difference pull together or pull in conducting or dielectric materials.

Electrostatic actuators can be made with nothing but conductors and insulators, and can exert static force with zero power dissipation. However, large forces require large electric fields. $\epsilon_0$ is the permittivity of free space. The force F between two capacitor plates in air, with a voltage V, separation d, and area A is

$$F = \frac{\epsilon_0 A V^2}{2d^2} \tag{2.1}$$

For air gaps greater than a millimeter, where the breakdown field of air is 3 MV/m, [89] the maximum electrostatic pressure, calculated with the above formula, is 40 Pa. Larger forces are achievable in vacuum or in dielectric materials. For a micrometer gap, the breakdown voltage of air is higher, and this figure rises to almost 600 kPa. (See Section 3.3.1.)

Fields for real electrostatic actuators may be computed using Maxwell's Equations, either on paper or with finite-element software such as COMSOL Multiphysics. Force computation may be accomplished using the energy method, the Lorentz force law, or the Maxwell stress tensor. *Electromechanical Dynamics* by Woodson and Melcher [96] is a helpful reference for modeling, even if using software to solve the equations.

Macroscale electrostatic motors with liquid dielectric can achieve the same gravimetric power densities as magnetic motors. Niino, Higuchi, and Egawa's DEMED[2] motors [68] [97] are made from plastic films with embedded 200$\mu$m pitch three-phase

[2]Dual Excitation Multiphase Electrostatic Drive

electrodes. The sheets operate immersed in dielectric fluid (3M Flourinert) to allow operation at up to 1400 Vrms. The authors built a 50-layer stack; it has a mass of 3.6 kg and a propulsive force of 300 N.

In MEMS devices, electrostatic actuators are commonly combined with flexural bearings. Common building blocks are the electrostatic cantilever, [82], electrostatic comb drive, and the electrostatic torsion beam. [79] The mechanical coupling of an electrostatic actuator with the elasticity of a flexure leads to the pull-in instability. Below the pull-in voltage, the system is stable—small increases in voltage lead to small decreases in plate spacing. Above the pull-in voltage, the system becomes unstable and the plates violently slam together, often becoming permanently attached through stiction. [82]

In another type of electrostatic actuator, the electrostatic induction motor, the stator is a series of voltage-driven electrodes, and the rotor is a poorly-conducting disc. A travelling potential wave on the stator surface induces and pulls along charges on the rotor. Freschette, Nagle, Ghodssi, Umans, Schmidt, and Lang constructed an electrostatic induction micromotor by deep-reactive ion etching and wafer bonding. The motor was designed to power a compressor in a micro gas-turbine, and supported by an aerostatic bearing. [28] The rotor diameter was 4.2 mm. The motor achieved a torque of 0.3 $\mu$N-m and a rotational speed of 15,000 RPM when driven with 100 V at 1.8 MHz.

### 2.2.2 Electrothermal

Electrothermal actuators can achieve greater deflections and greater forces than electrostatic or magnetic actuators, and permit looser tolerances and simplified drive; although they are slower, less efficient, and require static power to maintain force.

#### Thermal Expansion Actuators

Most materials expand when heated, with great force although with small displacement. For example, a copper bar will lengthen by 0.17% when heated to 100 °C. A

bimetallic strip is made by bonding two materials with different thermal expansion coefficients; it bends when heated, and the bending displacement is much greater than the linear expansion of either material alone.

Comtois and Bright constructed a lateral thermal actuator, composed of two cantilevers connected at the free end, with a polysilicon heater on one side.[18] The $200\mu m$ long device achieved a $16\mu m$ deflection when operated at 3V with 3.5mA current.

#### Shape Memory Alloy

Shape memory alloys undergo a reversible phase transition from martensite to austenite upon heating. With some limitations, they can remember one shape at the low temperature and another at the high temperature, and switch between them repeatedly.

Shape memory alloys are capable of impressive stress and strain, but, like other thermal actuators, have low efficiency and are slow-acting. The most common shape memory alloy is Nitinol, a Nickel-Titanium alloy developed at the Naval Ordinance Laboratory (NOL) in 1962.

Nitinol wire becomes 3.5% longer, acting with 100 MPa pressure, upon heating above 100 °C. It then returns to its original length upon cooling below 45 °C. For example, a 1 m long, 0.4 mm diameter wire pulls with an impressive 16N force, but requires 15 seconds of heating at 5 W to stretch 3.5 mm. [46] This corresponds to an energy efficiency of about 0.07%.

### 2.2.3 Electrostrictive

#### Piezoelectric Actuators

Lead Zirconium Titanate (PZT) is a piezoelectric material, meaning that it displays an inherent coupling between mechanical strain and electrical potential. Applying a potential results in a strain, and applying a strain results in a potential. In addition, PZT is a ferroelectric material, displaying a hysteresis curve between its electric

displacement and electric field and exhibiting a remnant polarization.

A slab of PZT (of any thickness) expands by 580 pm/V; for example, applying a voltage of 100 V results in an expansion of 58 nm. Expansion pressure can be over 100 MPa. Single piezoelectric sheets are typically used for making very fine adjustments to optical setups, or as acoustic transducers.

Increased displacement can be obtained using a stack of thin sheets of piezo material. For example, Piezo Systems of Woburn,MA sells a 5 mm x 5 mm x 18mm stack, with a weight of 4.5 grams, a maximum deflection of 14.5 $\mu$m, a response time of 50 $\mu$s, and a force of 840 N.

Driving a piezoelectric actuator stores energy in its electrical capacitance and its mechanical strain field. If driven with a resonant circuit, so the stored energy can be recovered, piezoelectric actuators can have impressively high efficiency, 50%-80%. [78] Piezoelectric actuators do not require static power to maintain force and displacement, a major advantage over thermal and most magnetic actuators.

However, if driven with a non-resonant circuit, especially if operated at light loading compared to their capacity, piezoelectric actuators can have arbitrarily low efficiency, because the energy stored when deforming the crystal will be dissipated as heat when the driving voltage is removed.

### Ultrasonic Motors

Ultrasonic motors use repeated small displacements of piezoelectric actuators to achieve a large net displacement. Compared to typical magnetic motors, which operate most efficiently at low torque and high speed, ultrasonic motors can efficiently produce high torque at low speeds. In many applications, they can be run without gearing. [91] Ultrasonic motors hold position with the power off.

Ultrasonic motors are a mature commercial product. They are used to actuate the focus ring in SLR cameras, drive automatic window blinds, and turn the hands of watches, among many other applications. [80]

The first ultrasonic motor, invented by H.V. Barth of IBM in 1973, simply used a piezoelectric actuator to repeatedly push on a wheel off-axis, spinning it around.

Modern ultrasonic motors use a travelling wave design. Sinusoidal electrical potential applied to the piezoelectric stator ring sets up a travelling flexural wave on its surface. The rotor ring, which is pushed against it by a spring, is rotated by friction, riding the tips of the wave.

The energy conversion efficiency of ultrasonic motors can be as high as 87% [80] with a single-point contact design. However, since the torque is proportional to contact surface area, multi-point contact designs lead to higher torque, but to lower efficiency, typically around 40-60%. Ultrasonic motors tend to have maximum efficiency at about half the no-load speed, with the efficiency tending toward zero at stall and at no load. Sashida [80] and Ueha [91] cover the physics, characteristics, applications, and fabrication of ultrasonic motors in detail.

The smallest ultrasonic motors (below 10 mm in size) do not appear to have the energy conversion efficiency of their larger cousins, as the following survey will illustrate.

The Squiggle motor (New Scale Technologies, Victor, NY) drives a leadscrew using a piezoelectric nut. Oscillating voltage is used to induce a deformation wave through the nut that drives it along the screw. The smallest model is 2.8 mm x 2.8 mm x 6 mm. It can exert 490 mN force at stall, and runs at 10 mm/sec with a 150 mN load. Under these conditions it draws 340 mW, an efficiency of 0.4%.

Physik Instruments (Auburn, MA) produces a linear ultrasonic motor measuring 9mm x 5.7mm x 2.2mm. It has a peak driving force of 50 mN and a maximum velocity of 80 mm/sec. Under these conditions it draws 500 mW, an efficiency of 0.8%.

The Seiko watch company developed a miniature rotary ultrasonic motor for use as a vibrating alarm in a watch. It measures 10 mm (diameter) by 4.5 mm, has a starting torque of 0.1 mN-m and a no-load speed of 6000 RPM, and requires 60 mA at 3V, for an efficiency of 0.06%. [91]

Flynn [27] constructed a rotary ultrasonic motor measuring 8mm diameter by 2 mm high. It achieved a torque of 10 mN-m and a no-load speed of 870 RPM.

### 2.2.4 Magnetic

At macro-scale, electromagnetic motors are the dominant means of electromechanical energy conversion. At the largest scale, synchronous machines and induction machines [1] are used, due to their very high efficiency.

Ahn [3] constructed a micromachined planar variable reluctance magnetic motor, with a diameter of 500 $\mu m$ . Application of of a sequence of pulses at 500 mA resulted in rotation; the torque was 3.3 nN-m.

Dario [19] and his colleagues won the 1998 IEEE microbot maze competition with a mobile robot using two electromagnetic wobble motors for drive wheels. The robot fit inside a cubic centimeter; the wobble motors were slightly larger that those presented here, 10 mm in diameter and 2.5 mm thick. They had a maximum torque of 0.16 N-mm and no load speed of 200 RPM. Heat dissipation limited the coil current to 140 mA, for an $I^2R$ power dissipation of 82 mW.

Kafader and Schuzle, researchers for the Maxom Motor AG of Switzerland, conducted a study of the dimensional scaling of DC motors. [48] They found that $I^2R$ resistive losses are the dominant loss mechanism in small motors, and that the ability to dissipate heat, generally proportional to motor area, determines the maximum continuous torque rating, which is proportional to volume.

If we want to have a large number of small motors do the work of a single large motor, then we need the mechanical power output proportional to volume. For a DC motor, we can get this with a constant rotational speed—but with $I^2R$ losses proportional to area. This means that the large number of small motors will have higher losses—be less efficient—than the large motor. We can get around this problem by increasing the rotational speed as the size goes down, allowing us to decrease the torque and keep the losses proportional to volume instead. However, with increased rotational speed, bearing losses increase, and eventually become dominant.

## 2.3 Connection Mechanisms

### 2.3.1 Covalent: Mechanical Latching

Many modular robot connectors are based on mechanical latching. The use of interlocking hooks or pins spanning the two modules allows control of a large, ultimately covalent bonding force, using a much smaller actuation force.

Khoshnevis, Will and Shen developed the CAST (Compliant-And-Self-Tightening) connector. [52] A stainless steel pin on one module is inserted into a slot on the other module, then secured with an electromagnetically actuated mechanical latch. The connector is 25 mm square, weighs 50 grams, and holds 10 kg, a net holding pressure of 160 kPa.

Nilsson developed the Dragon connector, [69] which is a genderless, latching, two-cone, two-funnel structure, actuated by shape-memory alloy. It has a diameter of 75 mm, a mass of 170 g, and supports 70 kg. This is a net holding pressure of 155 kPa.

It should be noted that the strength of these connectors is well below that of the yield strength of plastics or metals. This is because they rely on latching members with a much smaller cross-section than the connector itself, and because the failure mode of the connector is not tensile breaking of the material, but slipping out, bending, or buckling.

### 2.3.2 Magnetic

Electromagnets have been used as a modular robot connector by White and Lipson with their Stochastic system [95], by Kirby and Goldstein with the Catoms [54], and by An with the EM-Cubes. [5] These systems have been groundbreaking in their achievement of robotic behavior without moving parts. But in these systems, heat from $I^2R$ losses in the electromagnets has been a major limit on performance, manifesting iteself either as destructive temperature rise, high power requirements, or low force capability.

Mechanically switched permanent magnets actuated by shape memory alloys were

used on the M-TRAN modular robot. [57] Mechanically switched permanent magnets actuated by gearmotors were used on the MICHE system. [35].

### 2.3.3 Electrostatic

Electrostatic forces can be used to hold modules together, by placing capacitor plates on the faces of each module. Electrostatic actuation and latching is covered in more detail in Sections 3.3.1 and 2.2.1.

Karagozler and his colleagues on the Claytronics project have constructed several electrostatic connectors for modular robotics. [49] They found that the use of shear forces, to prevent peeling, and the use of flexible electrodes were essential to maximize performance. Their latch holds with a pressure of 6 kPa when driven with 500 V, and consumes zero static power while holding.

### 2.3.4 Van der Waals

Geckos have the amazing ability to climb smooth vertical surfaces. Their feet have 500,000 individual setae, hairs which provide adhesion to surfaces via van der Waals forces. The force is strong in shear but not in tension, allowing the Gecko to easily pull its foot up off a surface, even though it is strongly adhered. [6]

Kim has constructed a robot that runs up hard walls, using Gecko-inspired sheets of polymer fibers. [53] Murphy has fabricated synthetic anisotropic Gecko-inspired adhesive materials, with an shear adhesive force of 200 kPa in one direction but just 20 kPa in the opposite direction. [67]

Northern fabricated a material for programmable adhesion by van der Waals forces, by microfabricating an array of Nickel paddles. A permanent magnet can pull the paddles up off the surface, reducing the magnitude of the adhesion force. Northern measured an on-state adhesion of 14 Pa. [70]

Gecko-inspired adhesives are strong in shear while magnets are strong in tension. Together, they might be used to build a connector with strength in both directions.

## 2.4 Autonomous Microsystems

Most integrated circuits or MEMS devices are placed in an IC package before they leave the factory, and soldered to a circuit board in a box before they reach the consumer. Autonomous microsystems are the exception; they are millimeter-scale systems meant to accomplish tasks on their own.

### 2.4.1 Smart Dust

In this Smart Dust project, Pister, Warneke, and colleagues constructed solar-powered integrated circuits capable of acting as sensors and communications transceivers. [94] Their systems fit into just a few cubic millimeters. Because the devices were too small to contain RF antennas, they used optical communications. One of the lessons from the Smart Dust project was the small amount of power available to autonomous microsystems.

### 2.4.2 Paintable Computing

In the Paintable Computing project, Butera envisioned construction of a display by mixing autonomous microsystems containing LED's with paint, then coating them onto a surface with a brush. [10] Butera and I worked together to build a 1000-node macroscale testbed, and use it to run his distributed postscript rendering algorithm to display the letter "A." [55]

## 2.5 Modular Robotics

A self-reconfigurable modular robot [98] is a robot, composed of a set of modules, that can change its shape by changing the connectivity of the modules. A self-reconfigurable modular robot might move like a snake through a narrow tunnel, then reconfigurable into a legged shape for travel over ground.

Modular robots can be divided into three general classes: Lattice Architectures, Chain/Tree Architectures, and Mobile Architectures. [98] In systems with a lattice

architecture, modules move between positions on a regular grid. In chain/tree architectures, a set of connected modules use actuated joints to change configuration. In mobile architectures, modules move from position to position with the help of the environment, for example with rolling wheels. In this thesis, we present two new modular robot systems using electropermanent actuation: The Pebbles are a lattice architecture system and the Millibot is a chain architecture system.

Many modular robots systems have been constructed over the past twenty years. Rather than attempt an exhaustive survey, [98] in the following sections we will describe in some detail a selection of systems that we feel are most relevant to our work.

### 2.5.1 Polybot

Polybot, developed by Yim, Duff, and Roufas in the late 1990's at Xerox PARC, [100] [99] is a tree-type self-reconfigurable robot with two types of modules, called the segment and node. The segment, shown in Figure 2-1, is a rotary joint with two square connection faces. The node is a cube with six connection faces. Through combinations of nodes and segments, one can build a variety of different structures. The segments are about 50 mm across and are actuated by geared servo motors. Each module contains a microcontroller. Communication is via a CAN bus connecting all modules. Power is external; the modules transfer power and communicate via custom-made hermaphroditic electrical connectors on the faces. Latching between connection faces is done by placing grooved pins in chamfered holes then rotating a plate with an SMA actuator to secure the grooved pins.

Polybot demonstrates locomotion versatility through reconfiguration. Using the same modules, it can roll like a wheel, slither like a snake, walk like a spider, and even ride a tricycle.

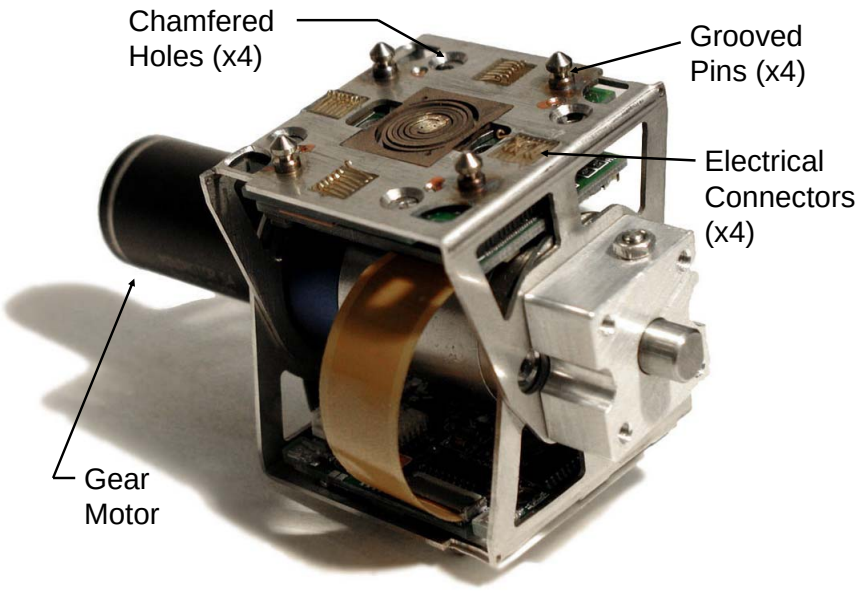


Figure 2-1: Polybot G2 segment module. The segment has a rotary joint and two square connection faces. Polybot also uses node modules, which are cubes with six connection faces. (Yim [101])

### 2.5.2 M-TRAN

M-TRAN (Modular Transformer) is a modular robot developed by Murata, Yoshida, Kamimura, Kurokawa, Tomita, and Kokaji at the National Institute for Advanced Industrial Science and Technology in Japan. [66] [57] Figure 2-3 shows an M-TRAN module, which consists of two semi-cylindrical boxes connected by a link. The two rotary joints are actuated by gearmotors. The module has six connecting faces, each with four-way rotation symmetry. The modules are held together using four permanent magnets on each connecting face; module release is achieved by pulling the magnets into the module using an SMA coil / spring linear actuator. Each node contains a microcontroller; nodes communicate serially; electrical connectivity for power distribution and communication is through conductive contacts on the connecting faces. The connecting faces are 66 mm square, and the motors have enough torque to lift two other nodes. Figure 2-4 shows three basic M-TRAN reconfiguration motifs. Figure 2-5 shows M-TRAN moving over ground through cluster flow, and Figure 2-6 shows M-TRAN reconfiguring into a quadruped and walking.

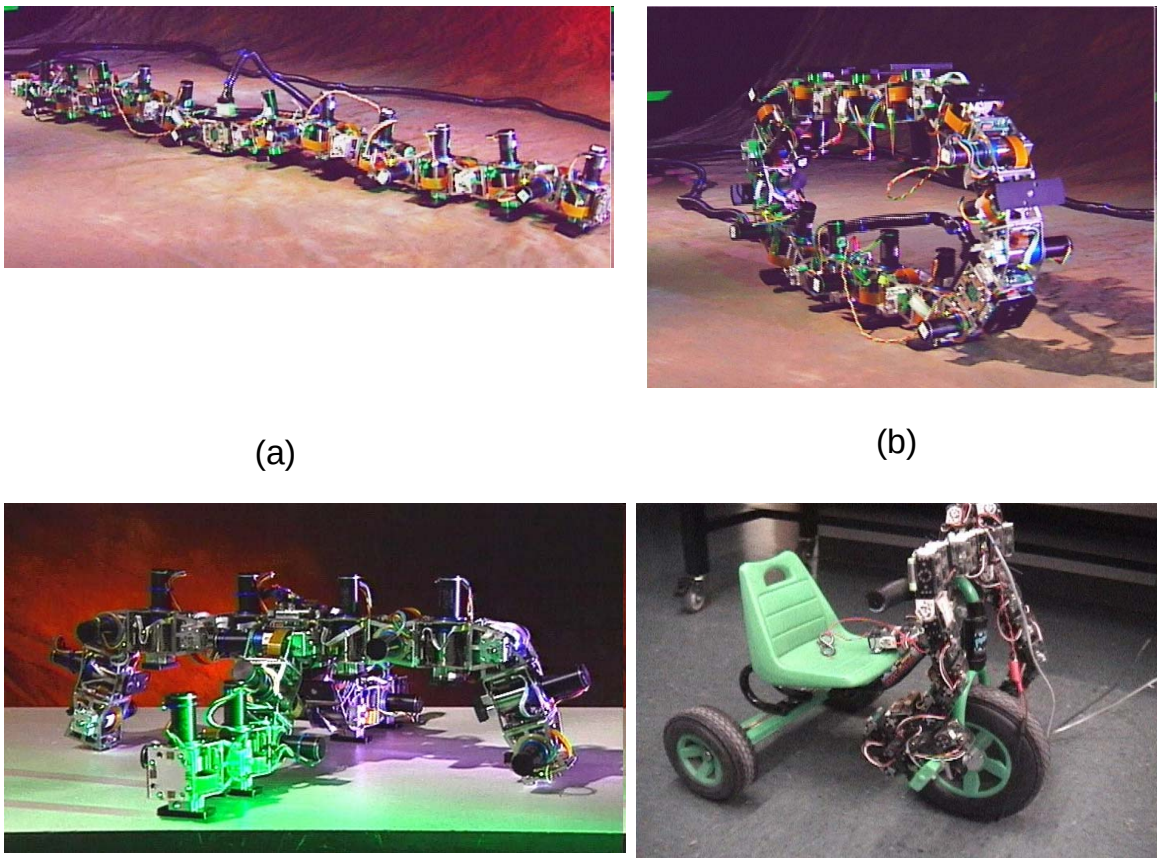


Figure 2-2: Polybot in action. Locomotion as a (a) snake, (b) rolling track, (c) spider, and (d) Polybot riding a tricycle. (Yim [101])

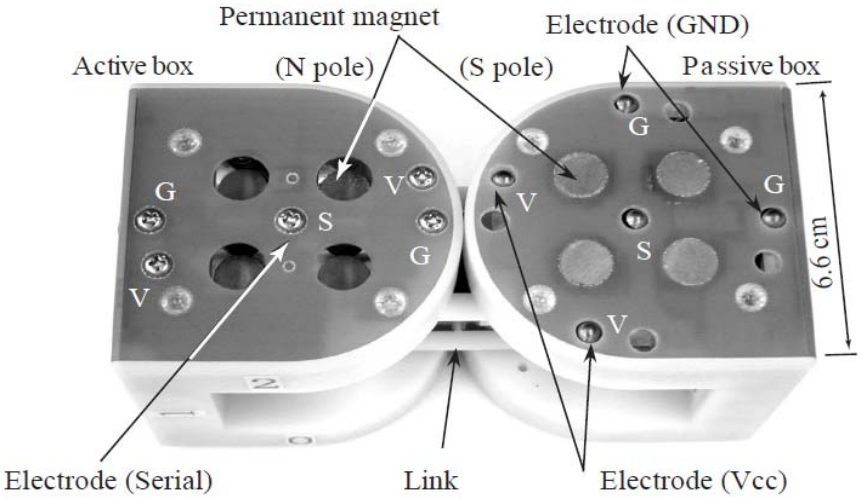


Figure 2-3: M-TRAN module. The two boxes are connected by a link and both rotary axes connecting the box to the link are motorized and independently controllable. The North-out permanent magnets on the left box can be retracted by an SMA actuator to allow disconnection. The South-out magnets on the right box are fixed. (Murata [66])

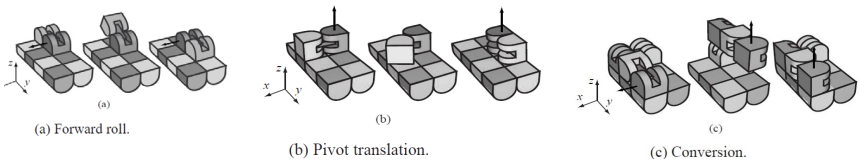


Figure 2-4: M-TRAN reconfiguration motifs. A single node can move in two dimensions either by the forward roll, allowing it to move in one direction or upwards (a) or pivot translation (b), allowing it to move anywhere in the plane but not upwards. With the aid of another node, it can switch between these two modes. (c) (Murata [66])

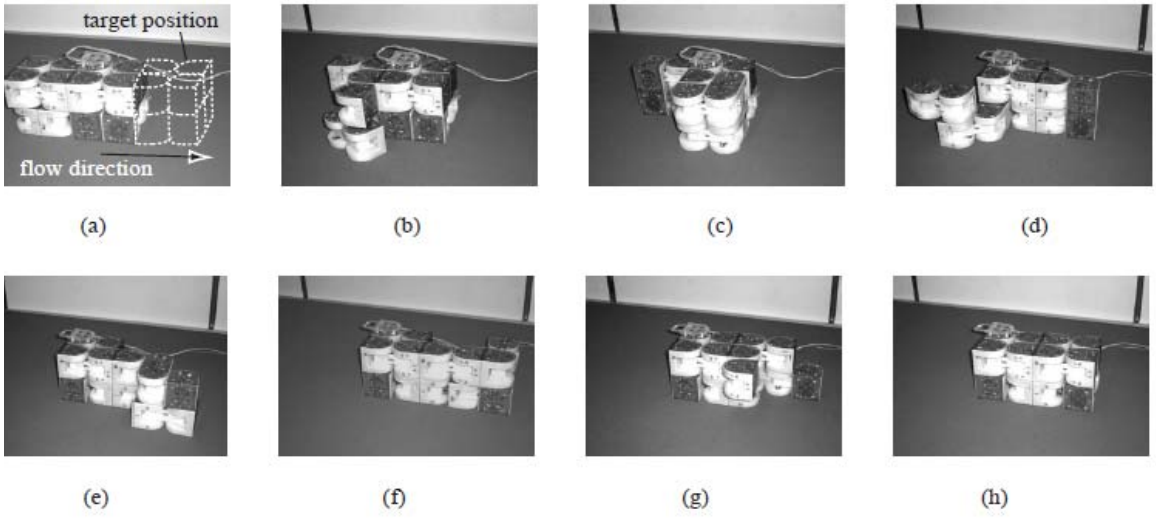


Figure 2-5: M-TRAN cluster flow experiment. A block of nodes can move along the floor as shown through self-reconfiguration. (Murata [66])

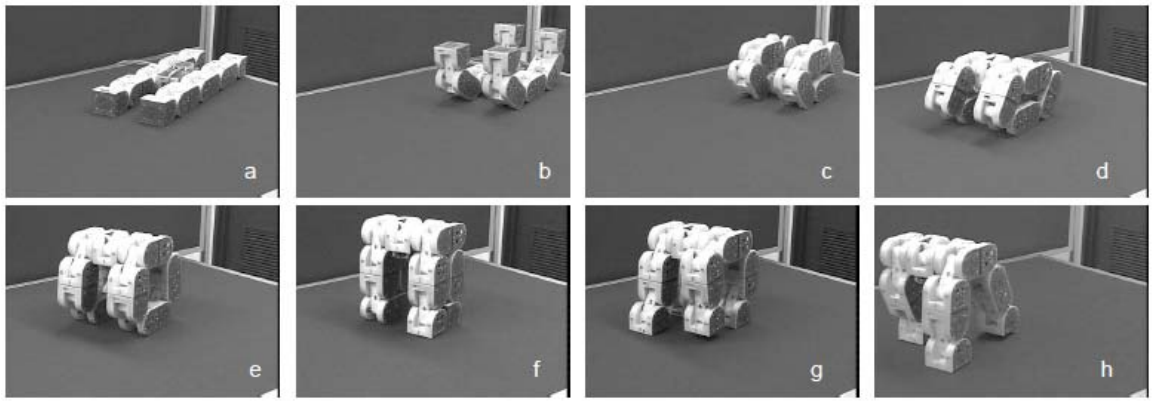


Figure 2-6: M-TRAN walking. The system first self-reconfigures from a planar configuration to a quadruped, then walks over ground. (Murata [66])

Figure 2-7: ATRON system, consisting of hemispheres connected by a rotary joint, and connected to each other by a right-angle bracket. The hemispheres are 110 mm in diameter. (Østergaard [71])

### 2.5.3 ATRON

The system most similar to the Millibot in the published literature is ATRON, a chain/lattice hybrid system developed by Østergaard, Kassow, Beck, and Lund at the University of Southern Denmark. [71] An ATRON module is two hemispheres connected by a rotary joint. ATRON modules are permanently connected to each other at 90 °, forming a chain that can reconfigure itself into three dimensional shapes. ATRON modules can fill space in a face-centered cubic lattice.

According to the ATRON Wiki, the modules are 110 mm in diameter, weigh 850 grams, and can lift the weight of two other modules against gravity. They use a geared DC motor for actuation and a slip ring for power transfer and communication. Most of the complexity of the modules comes from the cross-linking hook-type connectors, which are used to strengthen packed shapes.

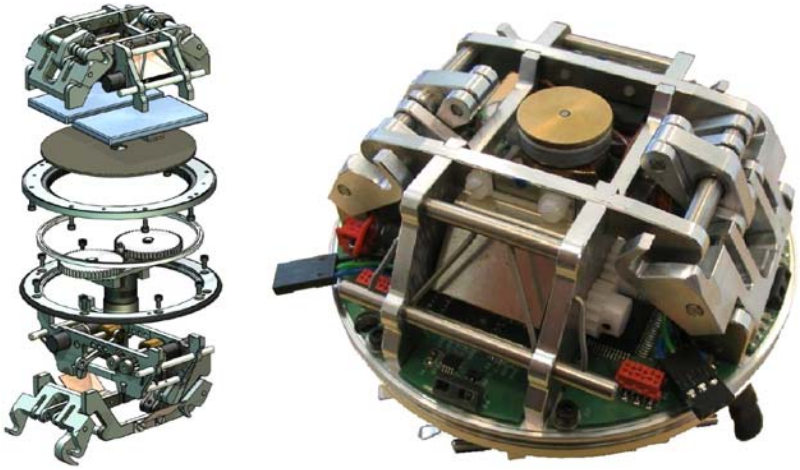

Figure 2-8: ATRON module mechanics. (Østergaard [71])

### 2.5.4 Catoms

The Claytronics project, a collaboration between Carnegie Mellon University and Intel Corporation, seeks to create ensembles of submillimeter robots, which will work together to form dynamic three-dimensional objects, for applications like telepresence and rapid prototyping. [37] They share our vision that nodes can be made infinitesimally inexpensive by microfabrication of large batches, and by using electric or magnetic field cooperative actuation to avoid moving parts or precision bearings inside the modules.

In their paper "A Modular Robotic System Using Magnetic Force Effectors," [54] Kirby, Aksak, Hoburg, Mowry, and Pillai describe the planar magnetic Catoms. These are cylindrical modules, 45 mm in diameter, each containing an array of radially-oriented electromagnets, plus computation and power-storage capabilities. The electromagnets were driven with 1.5A at 50V, and the authors report that this was "sufficient to cause thermal breakdown in our coils in a matter of seconds," necessitating drive at lower duty cycle. Nodes communicate with and localize their neighbors using a circular array of infrared LED's. Nodes transfer power inductively using the electromagnets, at 300mW, with 15% efficiency. Each node contains a carbon aerogel capacitor, which is charged inductively and then discharged during actuation.

Figure 2-9: The planar magnetic Catoms. The cylindrical modules are 45 mm in diameter. They use an array of electromagnets for cooperative actuation and inductive power transfer and communicate using an array of infrared LED's. (Kirby [54])

Karagozler, Goldstein, and Reid, in their paper "Stress-driven MEMS assembly + Electrostatic Forces = 1 mm Diameter Robot," describe their progress toward a 1 mm diameter planar electrostatic Catom. [50] They show a process for forming aluminum-on-silicon-dioxide hollow tubes using microfabrication. Electrode features are patterned onto the oxide, then the silicon wafer is etched away, and compressive stresses cause the once-rectangular chip to roll up into a tube. (Figure 2-10). The authors also show that it is possible to roll a conductive 1 mm tube along a row of linear electrodes using electrostatic forces. (Figure 2-12) In doing so, they show proof-of-concept for their plan to place a custom logic IC inside the tube to construct a 1 mm planar Catoms, which will roll over each other via electrostatic forces, using the mechanism shown in Figure 2-11.

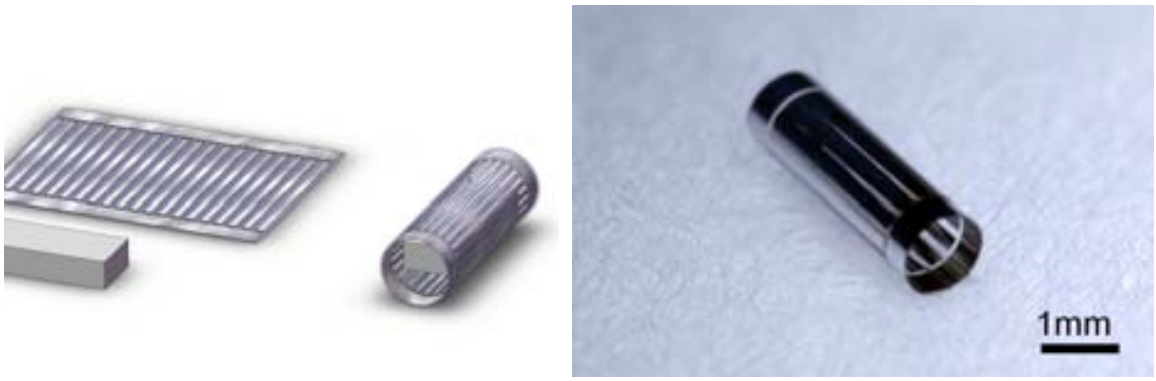


Figure 2-10: Microfabrication process for aluminum-on-silicon-dioxide tubes to be used for the electrode shells of electrostatic Catoms. (Karagozler [50])

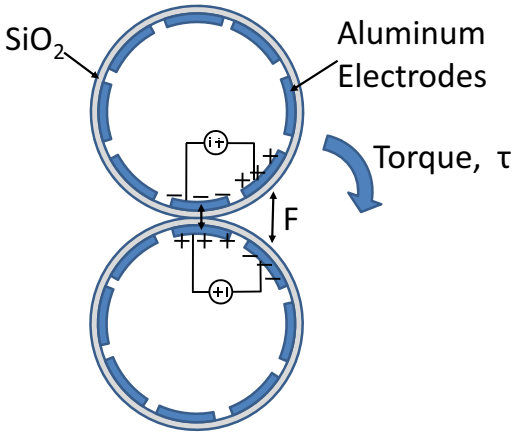


Figure 2-11: Electostatic Catom actuation: The force from the electric fields between the capacitor plates will move the Catoms. (Reprinted from "Stress-Driven MEMS Assembly + Electrostatic Forces = 1mm Diameter Robot." [50])

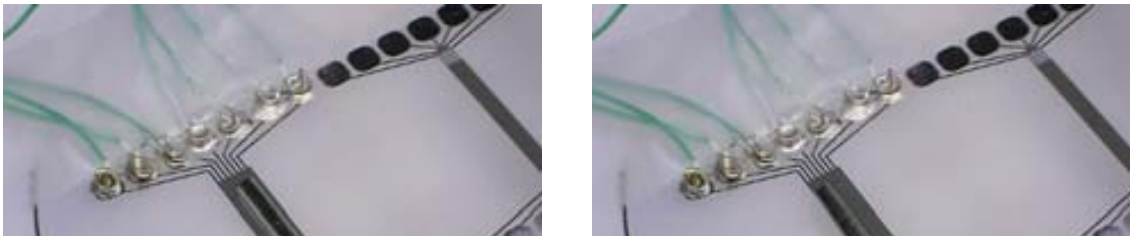

Figure 2-12: Demonstration of electrostatic actuation of a 1 mm aluminum tube, showing proof of concept for the Electrostatic Catoms. (Karagozler [50])

## 2.6 Programmed Self-Assembly

A major goal of the cellular robotics community over the past few years has been to simplify the module, to enable the construction of systems with larger numbers of modules at lower cost, and eventually to enable microfabrication.

One potentially very simple type of module is the zero-degree-of-freedom module, with no actuation capability, but merely the ability to bond to the desired module should it happen to come into contact due to stochastic environmental forces.

### 2.6.1 Penrose's Plywood Modules

The origin of the idea for stochastic program-driven self-assembly of machines can be traced back to L.S. Penrose and R. Penrose in 1957. [74] [73] The structure of DNA had recently been discovered by Watson, Crick, and Franklin in 1953, but the mechanism for replication was not yet understood. In their 1957 letter to Nature, "A self-reproducing analogue," Penrose and Penrose shows two simple interlocking plywood shapes, "A" and "B," which will not interlock, except in the presence of an existing "AB" or "BA" complex, which they will replicate upon external agitation.

L.S. Penrose's 1959 paper goes further. He describes his aim like this:

> "Suppose we have a sack or some other container full of units jostling one another as the sack is shaken and distorted in all manner of ways. In spite of this, the units remain detached from one another. Then we put into the sack a prearranged connected structure made from units exactly similar to the units already within the sack. ... Now we agitate the sack again in the same random and vigorous manner, with the seed structure jostling about among the neutral units. This time we find that replicas of the seed structure have been assembled from the formerly neutral or "lifeless" material." (L.S. Penrose, 1959 [73])

Penrose goes on to show diagrams of modules for self-replication of a one-dimensional binary string, to be shaken in a tray full of neutral modules. The modules were mechanical state machines, (as we would now call them) constructed from plywood

shapes with pin joints. Penrose built the modules and replicated strings with them manually, but evidently did not achieve fully autonomous replication. [38] Schematics of Penrose's modules are shown in Figure 2-13 and a photograph of him using them to replicate a string is shown in Figure 2-14.

### 2.6.2 Griffith's Electromechanical Assemblers

S. Griffith wrote a doctoral thesis in 2004 [38], and Griffith, Goldwater, and Jacobson published a paper in 2005, "Self-Replication from Random Parts," [39] where they demonstrate self-replication of a 5-bit string on an air-hockey table, achieving the goal of Penrose's system. Griffith originally built mechanical state machines from laser-cut acrylic, but like Penrose, found that the requirements on the speed, angle, and position of the collision needed to achieve mating were too severe for successful autonomous operation. Griffith then designed electromechanical tiles, shown in Figure 2-15, each containing a microcontroller, battery, and magnetically operated mechanical latches. The use of electronics for the state machine greatly eased the mechanical design, allowing for a larger basin of attraction. These tiles were able to self-replicate a string, shown in Figure 2-16, and were also used to produce checkerboards and other patterns using internal control. The tiles were 50 mm square and had a mass of 26 grams. Replication of the strings took about 20 minutes of agitation.

### 2.6.3 White's Magnetic Modules

In their paper, "Stochastic Self-Reconfigurable Cellular Robotics," White, Kopanski, and Lipson describe their magnetic modules for shape assembly. [95] They show two types of modules: a square module with electromagnets on the faces and a triangular module with swiveling permanent magnets, both shown in Figure 2-17. The modules contain no power source, simplifying fabrication, and receive power instead from neighboring modules by ohmic conduction through spring contacts on the faces. The units were 60 mm square. The electromagnet units were able to form a 3-unit chain in 960 seconds; the swiveling permanent magnet units in 14 seconds. (Figure 2-18

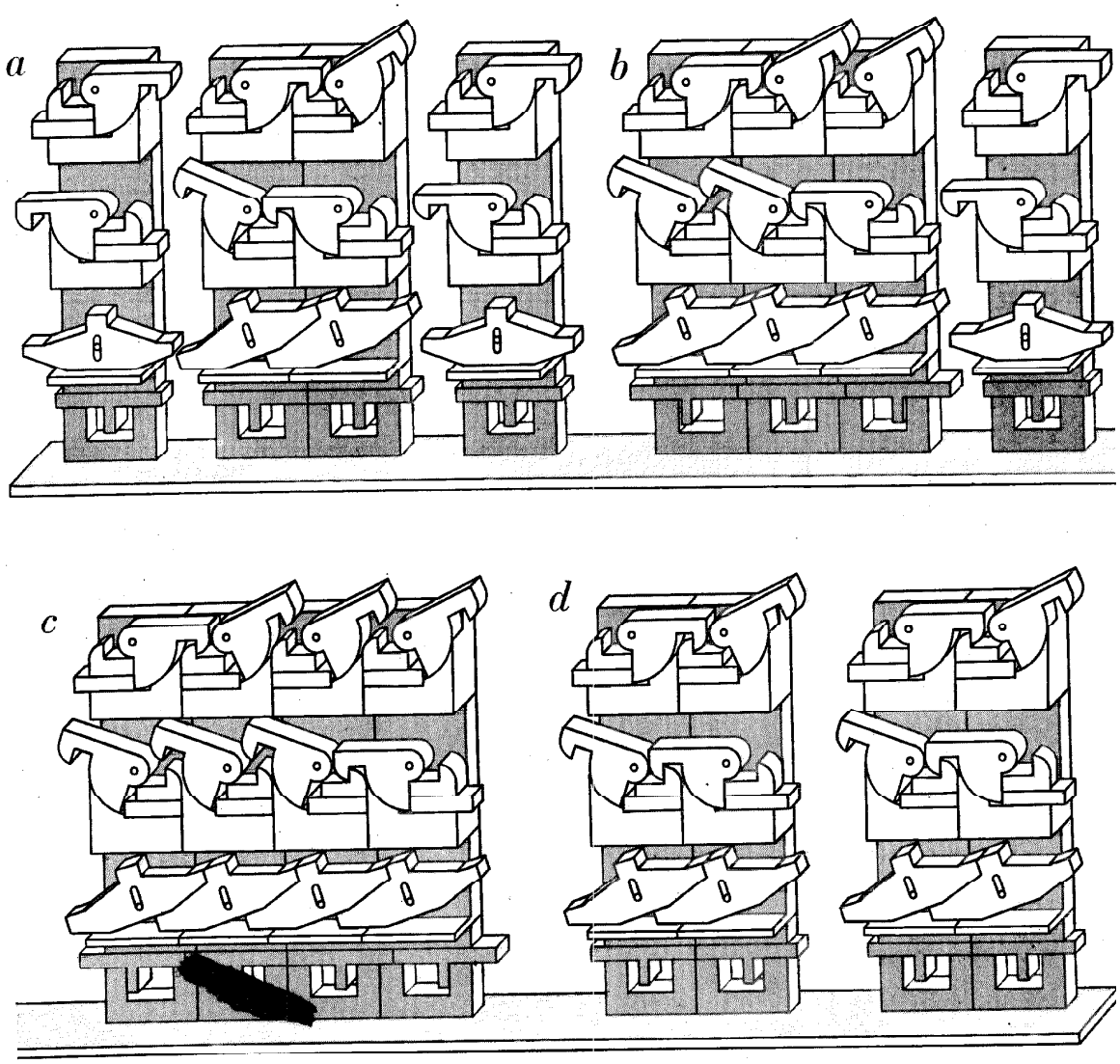


Figure 2-13: Penrose's self-reproducing machine. "The seed (at center in a) is linked by double hooks, incorporating the tilted cam-lever activating principal and is protected by the blocking device at its base. When the neutral unit at left joins the seed (b), it disengages one of the hooks holding the seed together and sets the blocking mechanism so that only one more neutral unit can be added. When the fourth unit joins the triple group (c), it disengages the second hook in the original seed, causing it to come apart in the middle and form two replicas of itself (d)." (Penrose [73])

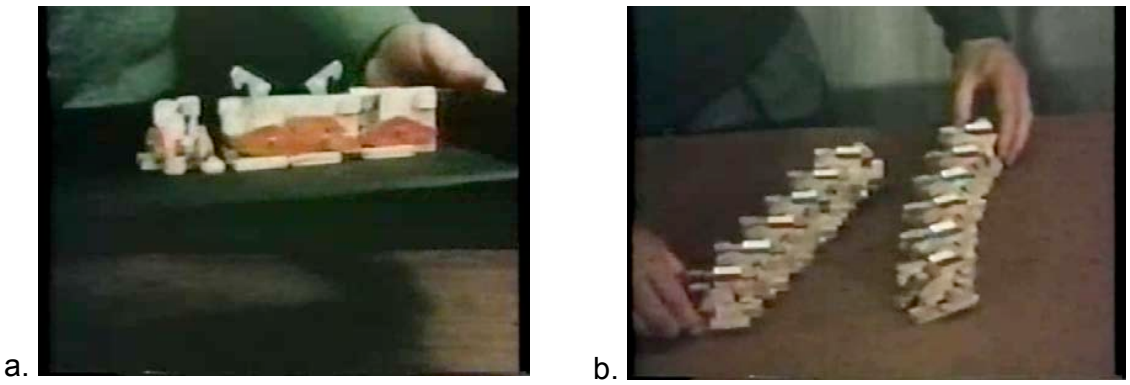


Figure 2-14: Penrose manually replicating a string using his plywood modules. (Griffith [38])

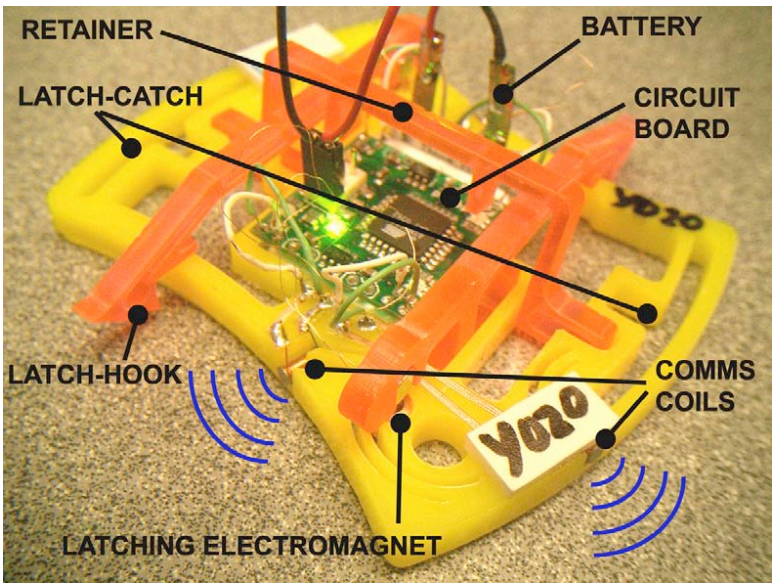


Figure 2-15: One of Griffith, Goldwater, and Jacobson's electromechanical assembler modules. (Griffith [38])

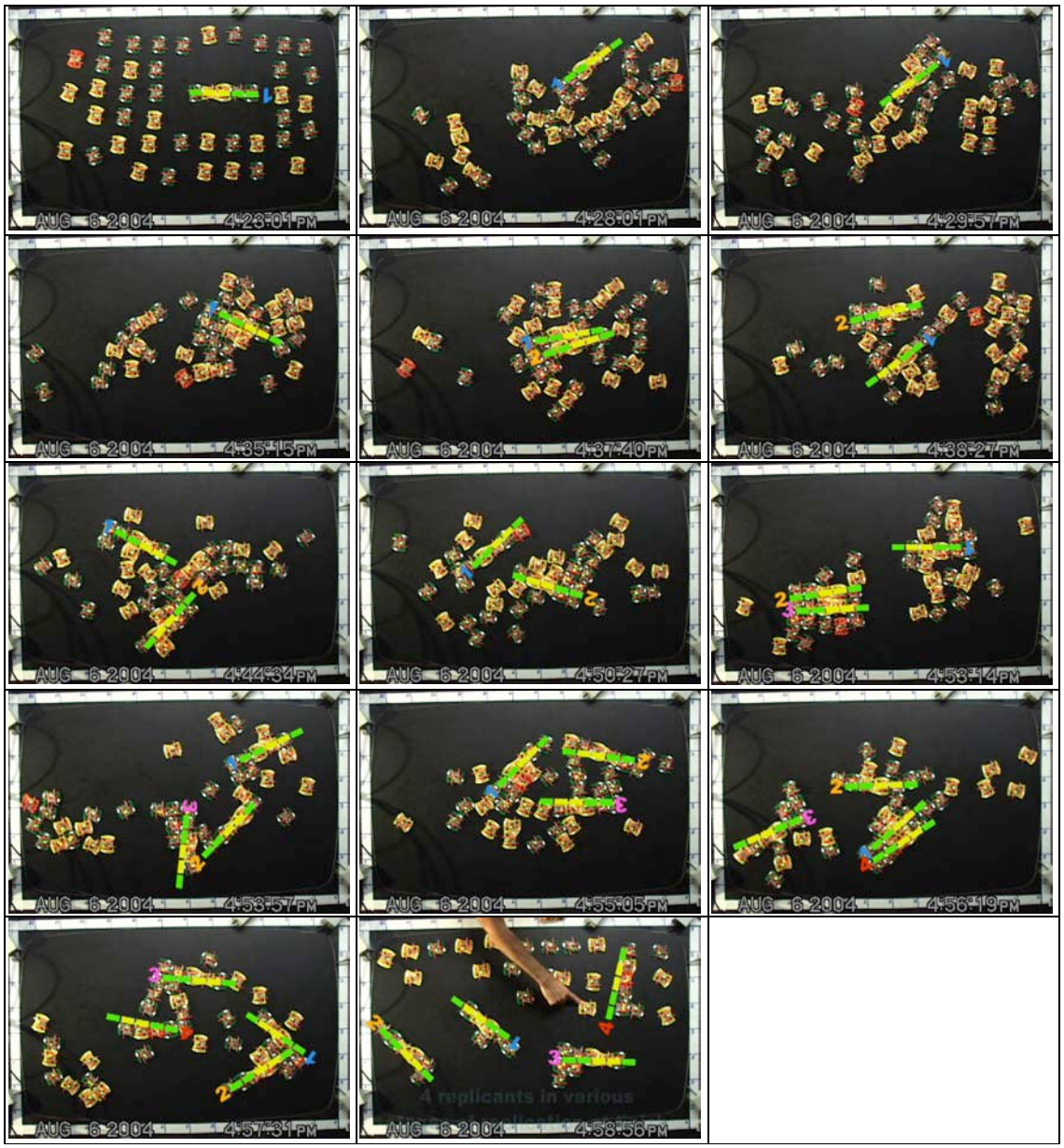


Figure 2-16: Griffith's electromechanical assemblers make three copies of a 5-bit string. The modules move stochastically on an air table, and can engage electromechanical latches to hold onto a neighboring module. A microcontroller on each module guides the replication, in communication with neighboring modules. (Griffith [38])

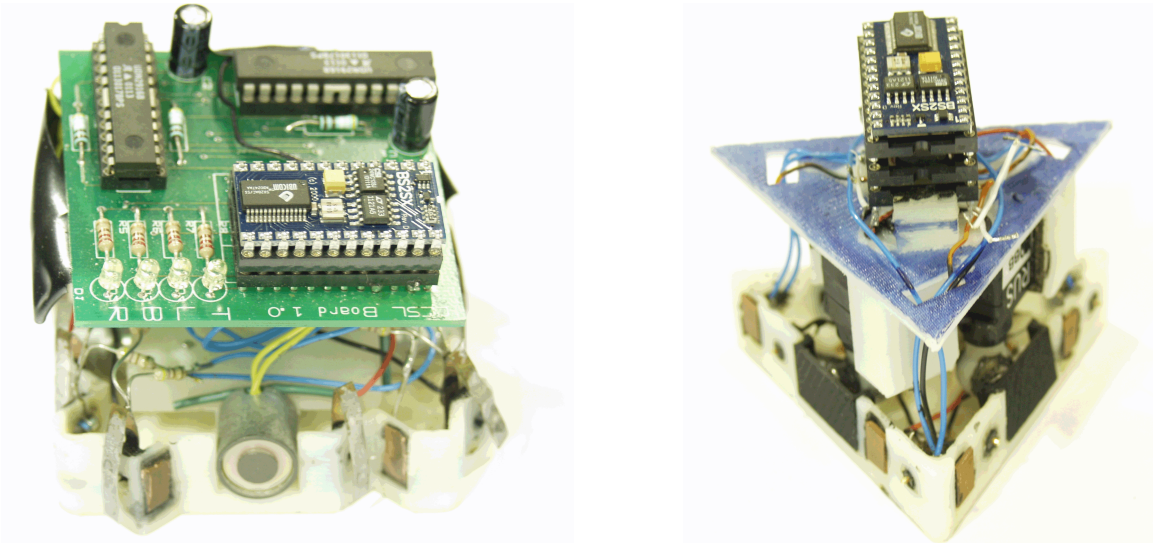

Figure 2-17: White, Kopanski, and Lipson's Magnetic Modules for Stochastic Self-Reconfiguration. (a) Square unit with electromagnets. (b) Triangular unit with swiveling permanent magnets. (White [95])

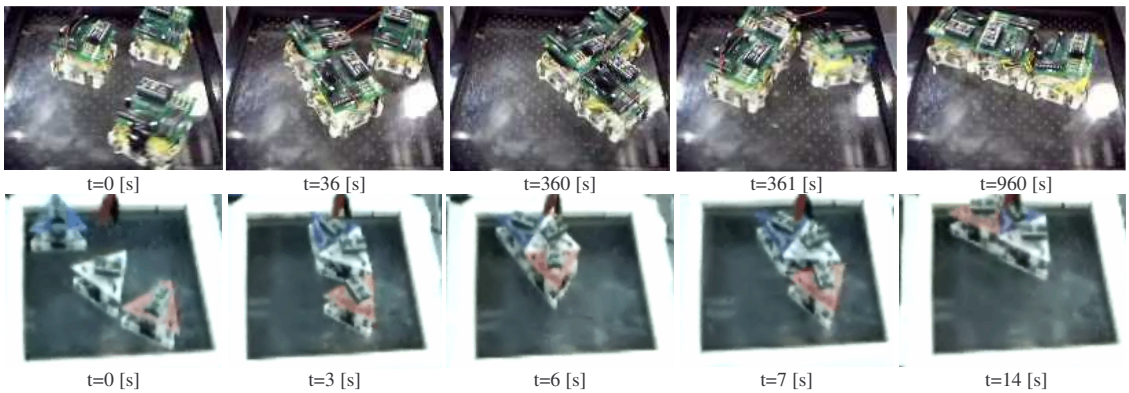


Figure 2-18: Stochastic self-reconfiguration of White, Kopanski, and Lipson's Magnetic Modules. The top row shows the square units assembling into a line. The bottom shows the triangular units. (White [95])

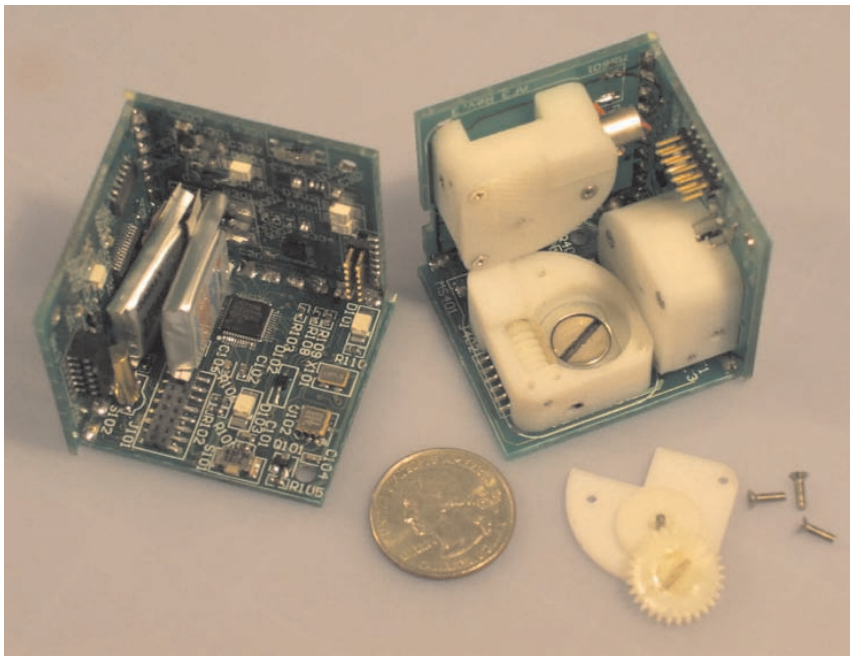

Figure 2-19: A disassembled MICHE module, showing the lithium polymer batteries, mechanically switched permanent magnets, and circuitry. (Gilpin [35])

### 2.6.4 MICHE

Gilpin, Kotay, Rus, and Vasilescu's MICHE system [34] [35] consists of cubes with mechanically switchable permanent magnets on each face to hold themselves together in a three-dimensional lattice. Each cube, shown in Figure 2-19, contains a microprocessor and a lithium-polymer battery, and neighboring cubes communicate by infared communication. The modules are 46 mm on a side and have a mass of 128 g. The mechanically switched permanent magnets can hold 2 kg.

The MICHE system form shapes by self-disassembly. The cubes start connected as a lattice. The user inputs the desired shape, and the magnets release the unused cubes, which fall away by gravity. The user is then left with the specified shape. (Figure 2-20)

The Robot Pebbles system described in this thesis is the successor to the MICHE system, and is the result of a collaboration between Gilpin, Rus, and myself.

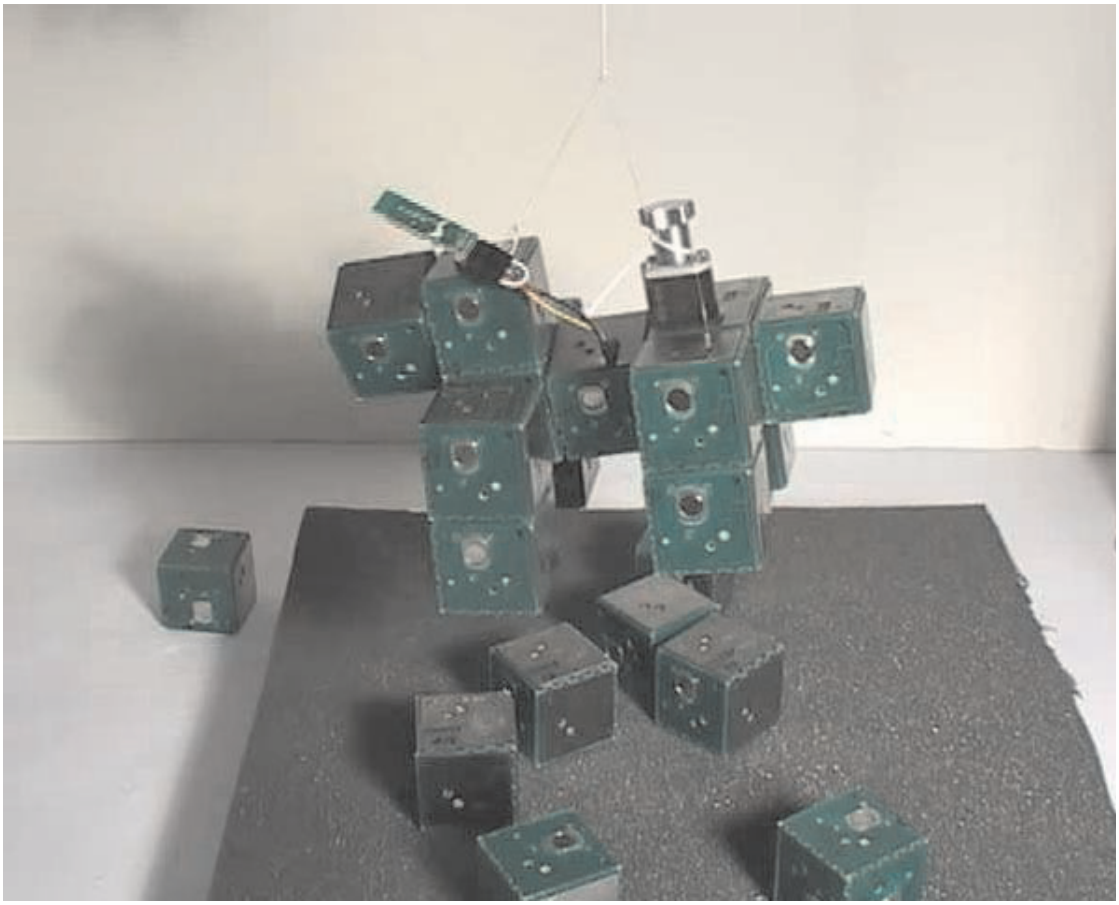

Figure 2-20: MICHE system forming a 15-module dog out of a 27-module block. The mechanically-switched permanent magnets release un-needed modules and they fall away. (Gilpin [35])

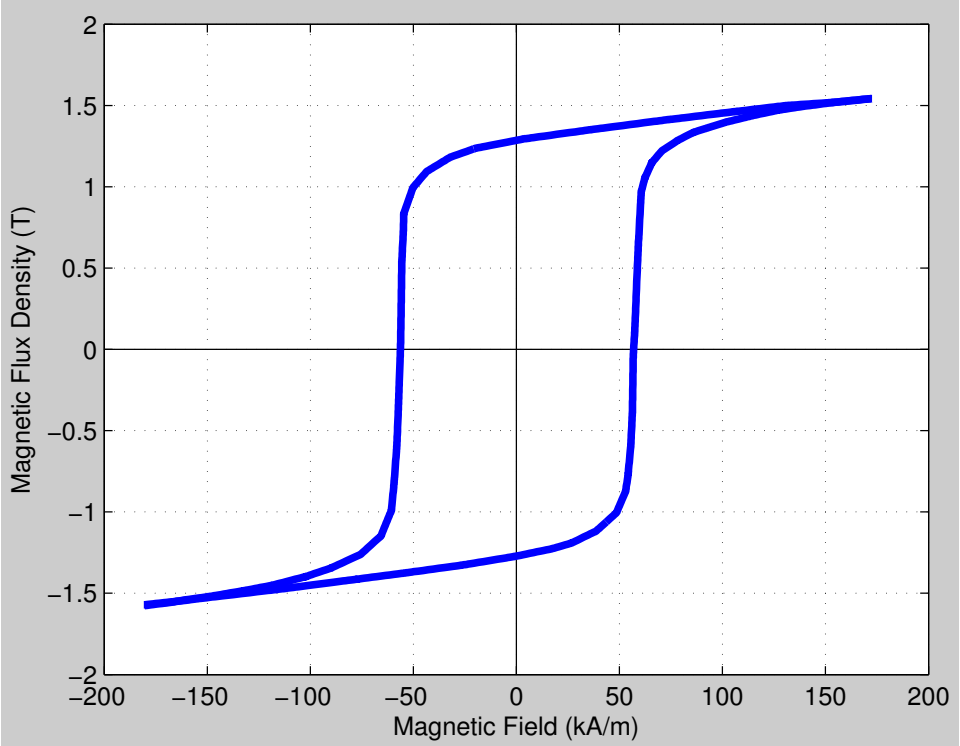


Figure 2-21: Hysteresis loop of Alnico 5. (Data from Campbell [11])

## 2.7 Magnetic Hysteresis

In a vacuum and in most materials, magnetic flux and magnetic field are proportional, related, at least approximately, by the relationship $B = \mu H$. However, in ferromagnetic materials, the phenomenon of magnetic hysteresis occurs. J.A. Ewing coined the term hysteresis in 1890, to describe his observation that the magnetic induction in a metal lagged the applied current. He theorized that the molecules of a ferromagnetic material acted as reversible permanent magnets. [22]

A plot of the outer hysteresis loop for Alnico 5 is shown in Figure 2-21. This plot was generated by cycling a sample of Alnico 5 between extreme values of magnetic field, and plotting the resultant magnetic flux versus the field. The flux follows the lower curve as the field is increased, and the upper curve as the field is reduced. The remnant flux density, when the field is zero, is about 1.28 T. The normal coercivity, which is the field when the flux is zero, is about 50 kA/m. The outer hysteresis loop is not a complete characterization of the material; if the field is reversed at lower

values, the material will follow minor hysteresis loops inside the outer loop.

The most important commercial applications of magnetic hysteresis have been in information storage and retrieval. The hard disk drives used in modern computers, as well as the older technologies of magnetic tape recording, magnetic wire recording, bubble memory, and core memory are all based on storing information in the hysteresis state of a magnetic material. [32]

The phenomenon of magnetic hysteresis also has uses in electromechanical systems. In the following sections, we will describe some related work in this area. An excellent additional reference for the interested reader is the Permanent Magnet Design and Application Handbook by Lester R. Moskowitz. [65]

### 2.7.1 Hysteresis Motors

A hysteresis motor [41] has a rotor made from a hard ferromagnetic material such as Alnico. Current applied on the stator windings applies a magnetic field to the stator that cycles its magnetization through all four quadrants of the hysteresis loop as the motor rotates. Because time is required to change the magnetization of the material, there is a continuous phase lag between the rotor field and stator flux, and this results in torque. Hysteresis motors are synchronous motors and run at a constant multiple of the AC line frequency. Because the rotor is a homogenous cylinder with no poles or other features, they are smooth-starting and quiet. These characteristics make hysteresis motors suitable for use in electric clocks and record players.

Like the electropermanent motor presented in this thesis, hysteresis motors produce torque through changes in the magnetization of a hard ferromagnetic material. Unlike the electropermanent motor, a hysteresis motor requires continuous current to exert torque, so its efficiency decreases toward zero at zero speed.

### 2.7.2 Ferreed Switches

In 1960, Feiner, Lovell, Lowry, and Ridinger of AT&T Bell Laboratories published a paper called "The Ferreed—A New Switching Device." [24] In their paper, they

describe a new type of reed relay, shown in Figure 2-22, in which a flexible metallic reed is placed in series with a ferrite core with a coil wrapped around it. Applying a positive current pulse to the coil magnetizes the ferrite and closes the relay. Applying a negative current pulse of precisely the correct magnitude and duration demagnetizes the ferrite opening the relay. There is no static power consumption. I believe this is the first historical example of an actuator using discrete pulse switching of a magnetic material.

The authors go on to describe a number of variations on the basic Ferreed design, including two-branch ferreeds with a parallel permanent magnet and series ferreeds with two permanent magnets in parallel.

The AT&T 1ESS telephone switch, introduced in 1965 was the first electronic, computerized telephone switching system. [51] The 1ESS switch used a Ferreed crosspoint matrix for switching voice calls. (Figure 2-23) In 1973, new systems began using the smaller Remreed switch, in which the magnetization of the reed itself was switched by an electrical pulse. [13]

In the design of an electronic telephone switch, the key advantage of the Ferred switch (over the mechanically latching relay) was that it could take its command from the central processor on the microsecond time scale of electronics, and autonomously complete the switching operation on the millisecond time scale of a mechanical relay. [13] This allowed the expensive stored-program computer in the switch to handle more calls in a given time.

The continuously improving lithography pitch of integrated circuit fabrication eventually made it economical to replace electromechanical crosspoint switches with semiconductor-based time-division-multiplexed digital switches, in which the whole switch operates at electronic speeds. But electropermanent magnetic switches may make a comeback in telecommunications; they have been investigated for use as optical switches. [47]

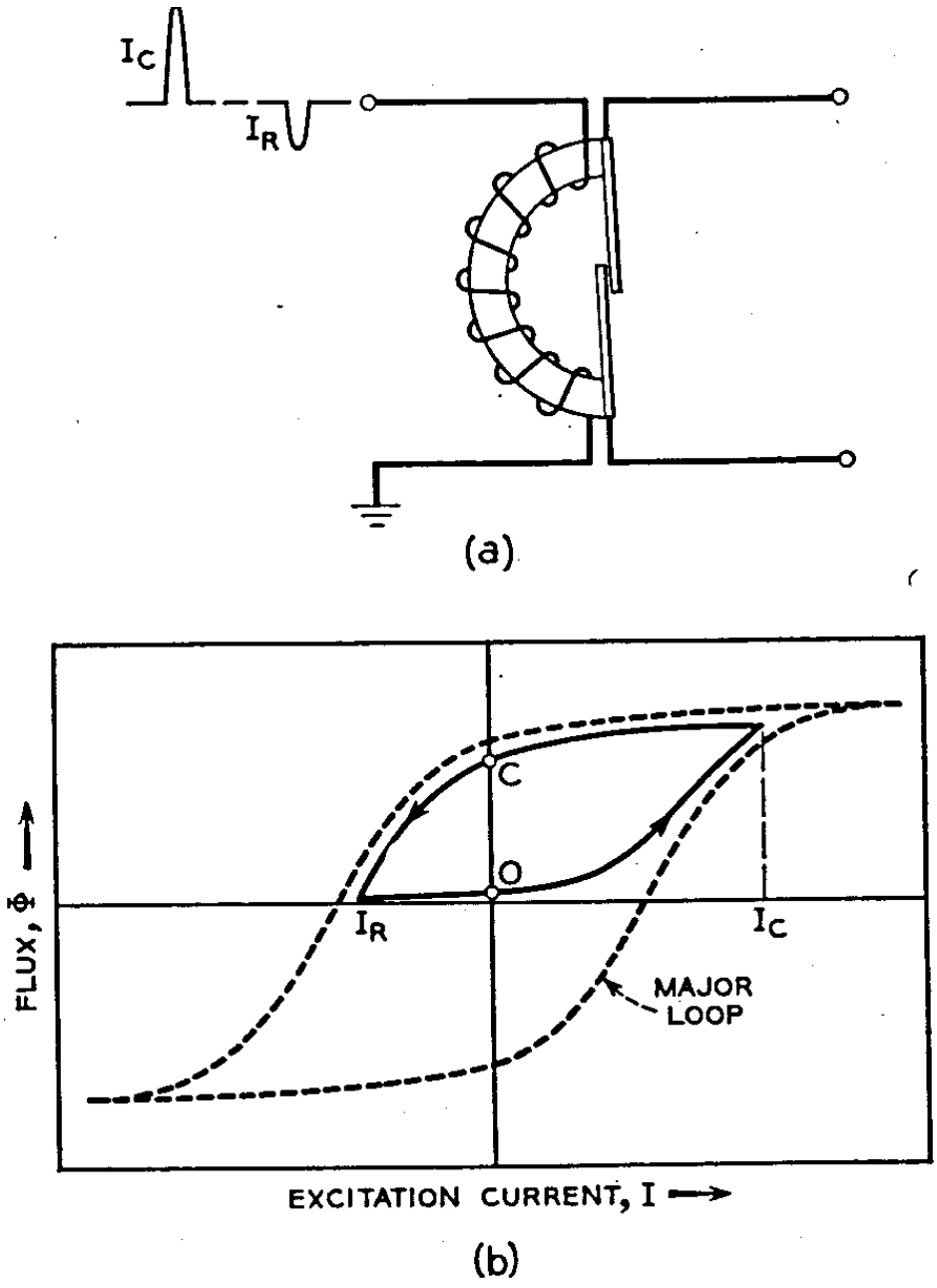


Figure 2-22: (a) The single-branch ferreed (b) its magnetization characteristic. (Feiner [24])

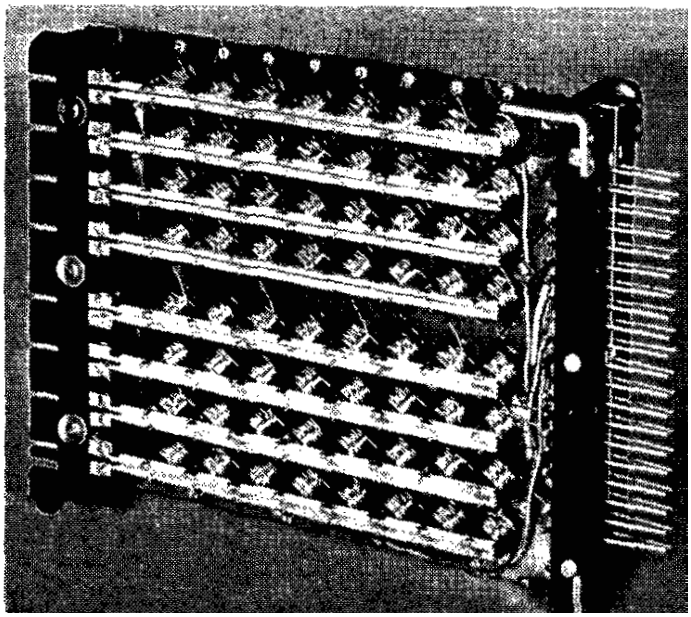

Figure 2-23: Ferreed switch containing 64 crosspoints, used to switch telephone calls by Bell System 1ESS Switch, the first electronic telephone switching system, which went into service in 1960. (Ketchledge [51])

### 2.7.3 Switchable Permanent Magnets

#### Mechanically-Switched Permanent Magnets

Although not technically a system that uses magnetic hysteresis, the mechanically switched permanent magnet provides useful background for the solid-state devices described in the next sections.

Arlo F. Israelton, chief engineer of the Eriez manufacturing company of Erie, Pennsylvania, patented a device called the "Turn-Off Permanent Magnet" in 1969. [43] As is shown in Figure 2-24, it contained two permanent magnets, sandwiched between two pole pieces. One of the permanent magnets was fixed but the other could be rotated using a crank. With both magnets aligned, the magnet was "on" and could be used for lifting heavy objects such as steel girders and plates. Rotating the crank could make the magnets face opposite directions, making the magnetic flux circulate inside the device only, and releasing the hold on the objects.

Israelton notes in his patent that "this circuit depends on the high coercive char-

acteristics of oriented ceramic material because when the movable magnet is returned to its original position there is a brief, but strong tendency to demagnetize the magnets. Ceramic magnets can resist this, but Alnico magnets could not." This provides some explanation for why this device did not appear on the scene earlier.

The turn-off magnet is a useful device both because it provides the operator with mechanical advantage and because it is bi-stable. A permanent magnet can lift a heavy weight, but typically only through a small distance. Using this device, the operator must supply the energy to lift the load by turning the crank. But the operator can supply this energy over a distance equal to half the circumference of the crank, which can be much longer than the lifting distance; so mechanical advantage is obtained and a much smaller force than the weight of the lifted object is required to turn the crank. Once the crank is turned, the object is held in place without additional work until the crank is turned again.

Mechanically-switchable permanent magnets are familiar to anyone who works with optics hardware; they are used to mount posts to an optics table. In this application they are useful because, with the magnet off, the post can be finely adjusted to have any position and orientation and then the magnet can be turned on to lock the post into position.

### Monostable Electropermanent Magnets

In 1972 Robert Edgar, Francois Martzloff, and Russell Tompkins, of the General Electric Corporation, patented two types of temporarily reversible permanent magnets and showed how they could be used to build electrical relays and impact print heads.

The first type, based on the "flux-cancellation" principle, is shown in Figure 2-25. It is constructed by wrapping a permanent magnet with a coil. With the coil switched off, the permanent magnet holds a load. Switching on the coil cancels the field from the permanent magnet, releasing the load. When the coil is switched off, the field returns.

In the patent, the inventors state that this configuration is uniquely enabled by

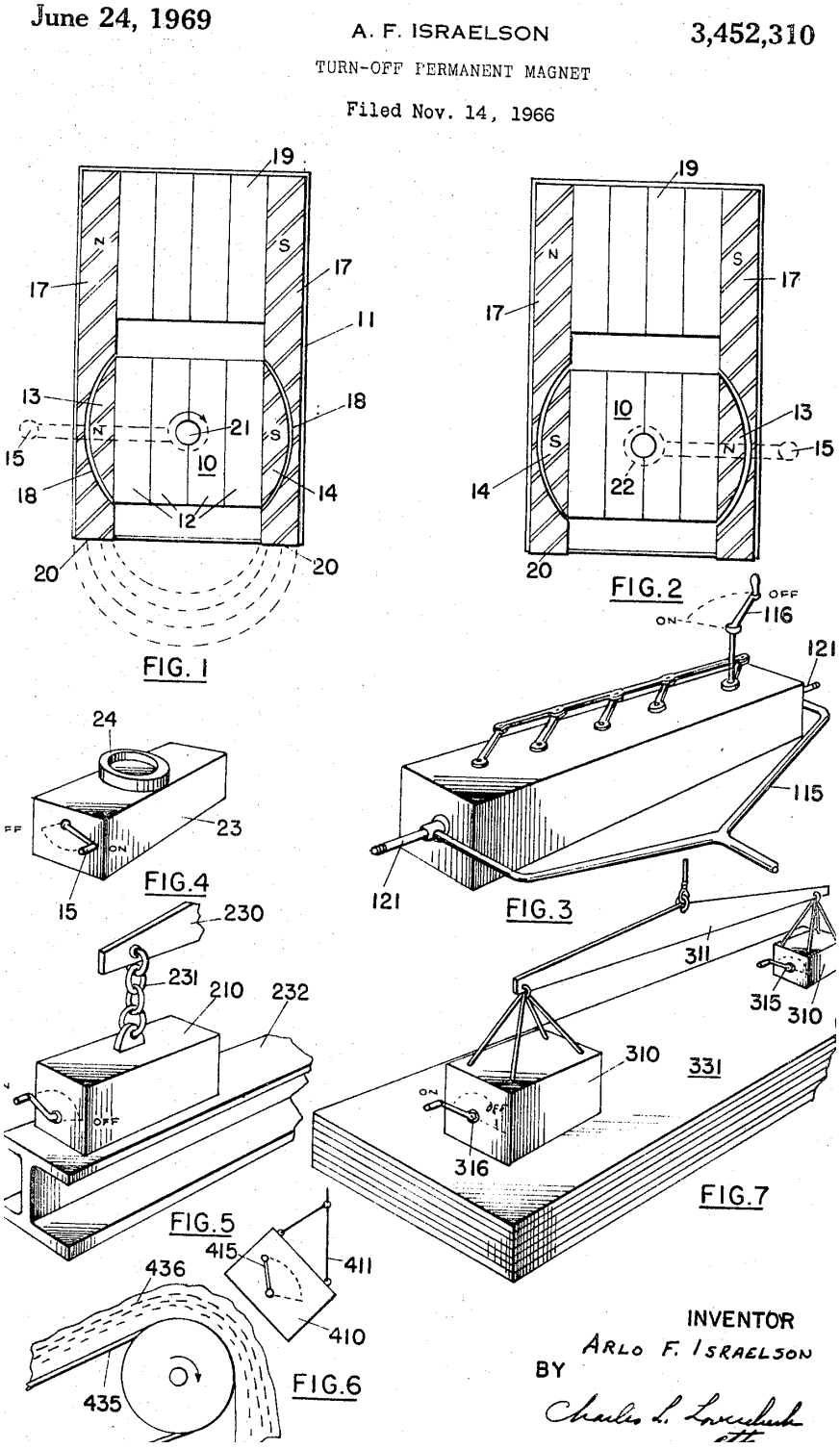


Figure 2-24: The mechanically switchable permanent magnet. Turning the crank switches the two permanent magnets between the aligned and anti-aligned positions, switching the holding force on and off. (Israelton [43])

the properties of the newly developed rare-earth Samarium Cobalt permanent magnet material. Shown in Figure 2-25 are the B/H curves for Samarium Cobalt magnets (introduced in 1967) and the older Alnico magnets. The holding force is zero at B = 0. From the figure, we can see that demagnetizing an Alnico magnet to B = 0 takes it out of its linear region, indicating that permanent demagnetization will occur and a reverse field would be required to remagnetize it. On the other hand, the Samarium Cobalt material has a linear demagnetization curve clear down to B = 0, so its demagnetization to B=0 is reversible, and after removal of the current, its original holding force will be restored.

The second type, based on a "flux-switching" principle, is shown in Figure 2-26. It is constructed by placing a permanent magnet and a coil in parallel between two ferromagnetic pole pieces. With the coil off, the permanent magnet exerts a holding force on a nearby object. When the coil is turned on, the flux from the permanent magnet is shunted through the coil, and the holding force switches off. When the coil is turned off, the holding force resumes. In this configuration, the field from the coil reinforces the magnetization of the permanent magnet, increasing its flux while switching off the holding force, and so there is no requirement for a permanent magnet that is reversible down to B = 0; any permanent magnet material could be used. However, the inventors note, this configuration has a larger volume.

It is possible to build a bistable latching relay by using a monostable electropermanent magnet and a spring. The magnet should be strong enough to resist the force of the spring in the closed position, with zero air gap, but not strong enough to pull the gap closed from the open position. Reinforcing the magnet with a momentary current pulse closes the switch. Cancelling the magnet with a momentary opposite current pulse opens the switch.

### Series Electropermanent Magnet

Philibert Maurice Braillon patented the "Magnetic Plate Comprising Permanent Magnets and Electropermanent Magnets" in 1978. [8] This device, shown in Figure 2-27 is designed for magnetic work-holding in machine tools.

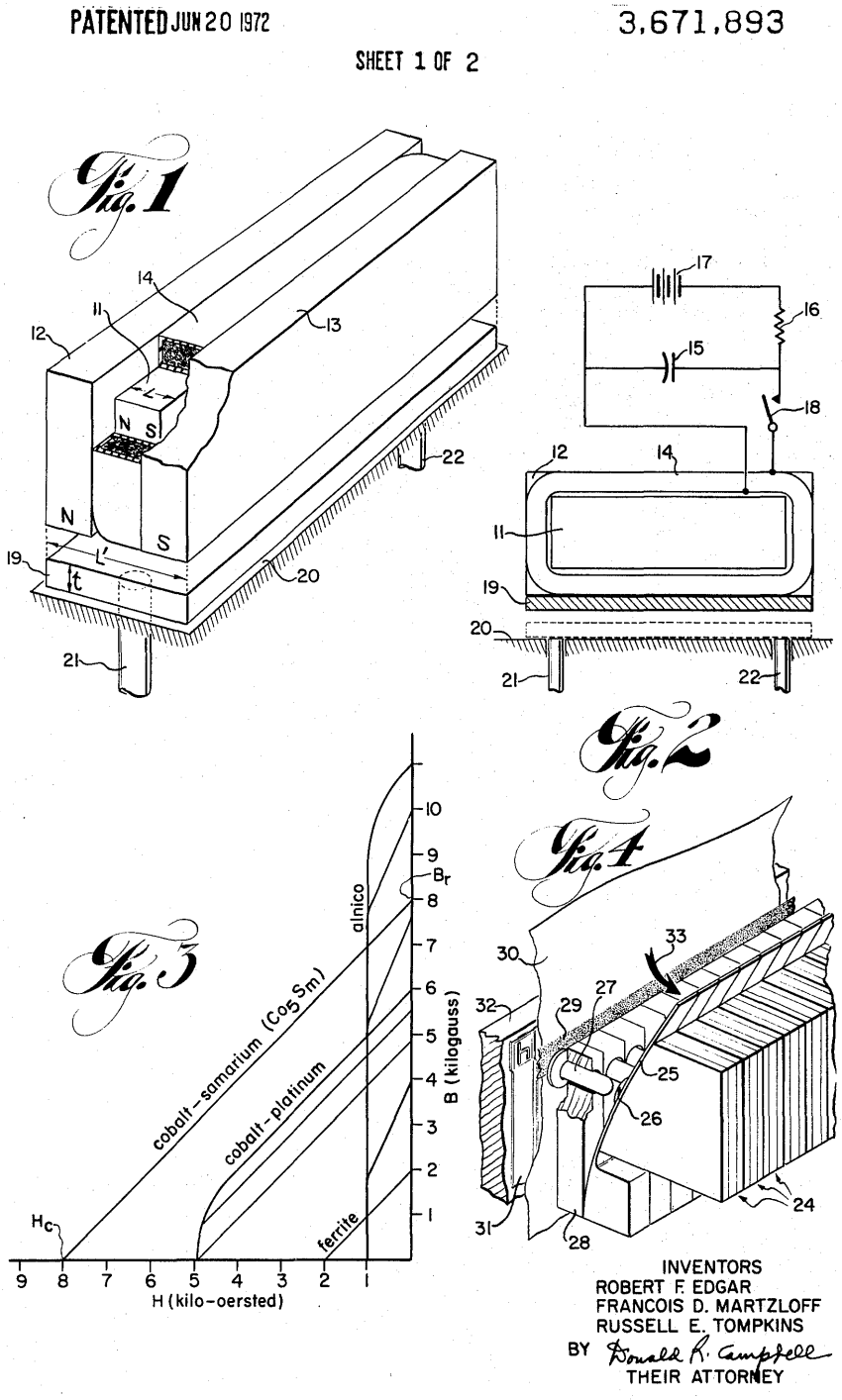


Figure 2-25: Monostable electropermanent magnet based on the flux-cancellation principle. (Edgar [21])

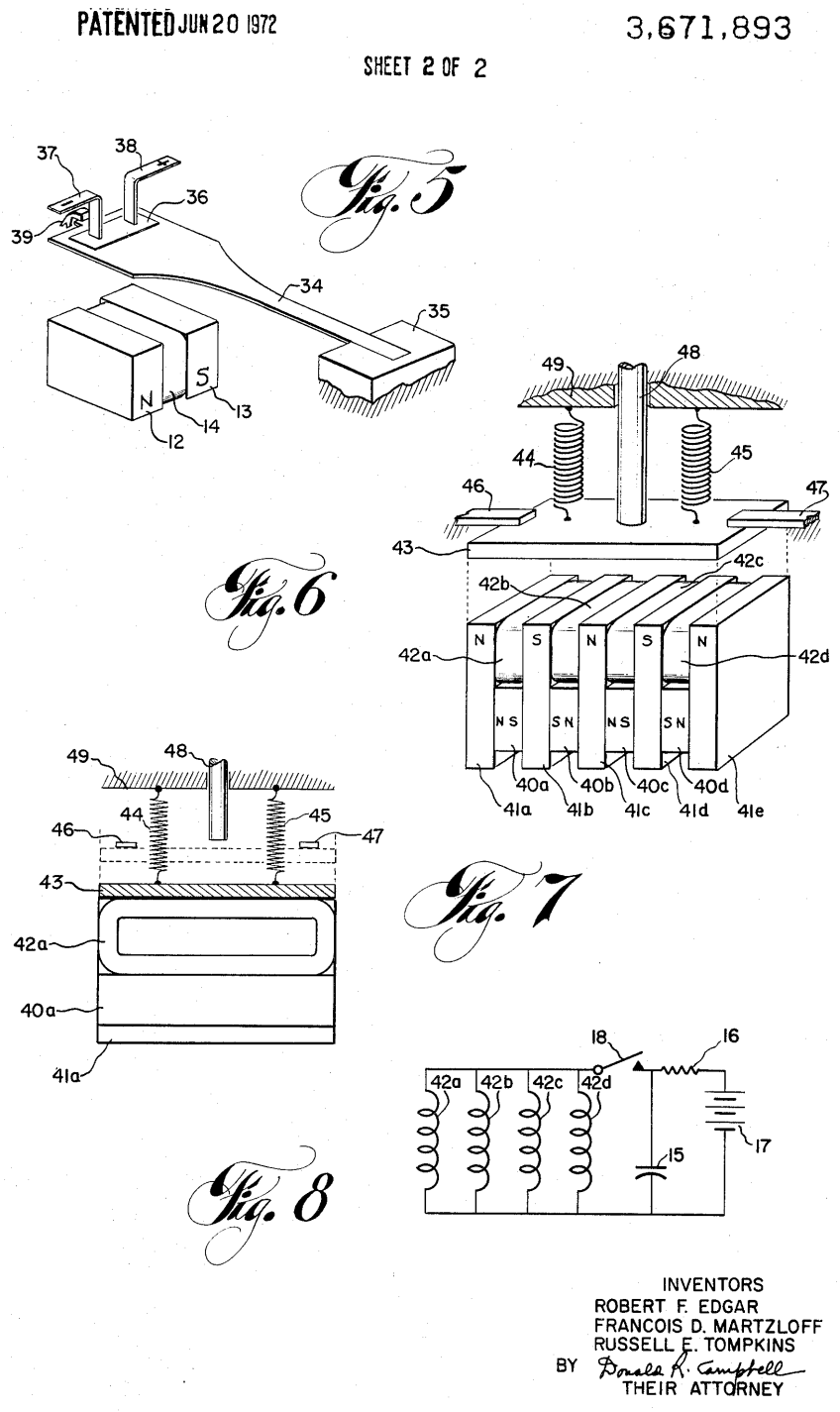


Figure 2-26: Monostable electropermanent magnet based on the flux-switching principle. (Edgar [21])

Inside the device is a row of permanent magnets, alternately made from a high-coercivity material and a lower-coercivity material. Initially, all the magnets are magnetized together and their flux passes through the bottom member. (Figure 2-27-2) Coils surround the low-coercivity magnets. Passing a momentary pulse of current through the coils reverses their magnetization. Now, the net field across the bottom member is zero so no flux flows through it. Rather, the flux from each magnet exits the plate separately through the top, holding down the workpiece. (Figure 2-27-3)

**Parallel Electropermanent Magnet**

In 2001, Dominic Pignataro of the Walker Magnetics Group patented the "Electrically Switchable Magnet System," shown in Figure 2-28. This device contains two types of permanent magnet materials, one with high coercivity (e.g. NIB) and one with a lower coercivity (e.g. Alnico) but both with approximately the same remanence. The two materials are placed in parallel and surrounded by a coil. Passing a pulse of current through the coil in one direction magnetizes the materials in the same direction. In this state, flux exits the device and exerts a holding force. Passing a pulse of current through the device in the opposite direction reverses the magnetization of the lower coercivity magnet, but leaves the higher coercivity magnet unchanged. In this state, the two magnets are oppositely magnetized, and so the magnetic flux only circulates inside the device, and there is no holding force.

The materials set and magnetic circuit described in this work, along with Feiner's work from 1960 on the Ferreed switch [24], provided the inspiration for the devices constructed, characterized, and modeled in this thesis. Parallel electropermanent magnets are used commercially in steel mills to lift loads weighing many tons, and switch with current pulses on a time-scale of seconds. In this thesis, we examine a different size regime for the parallel electropermanent magnet, lifting loads weighing just a few grams and with switching pulses on a microsecond time scale. One conclusion of this thesis is that the electropermanent magnet is a useful and efficient device at both of these extremes.

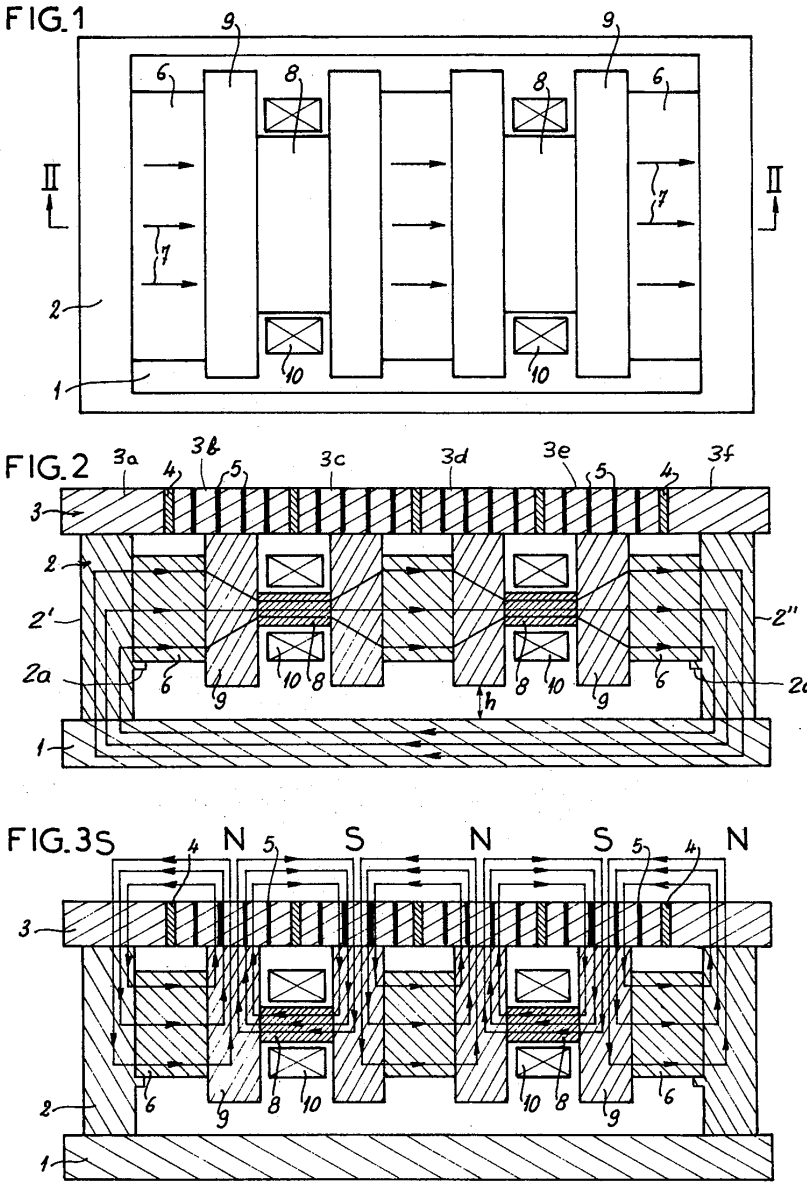


Figure 2-27: Series electropermanent magnet for magnetic workholding. With all the magnets magnetized in the same direction, flux travels through the bottom plate. (Fig. 2) With every second magnet oppositely magnetized, flux circulates locally, holding down the workpiece. (Fig. 3) (Braillon [8])

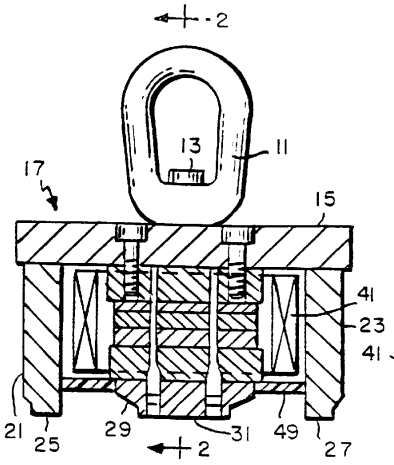


FIG. 1

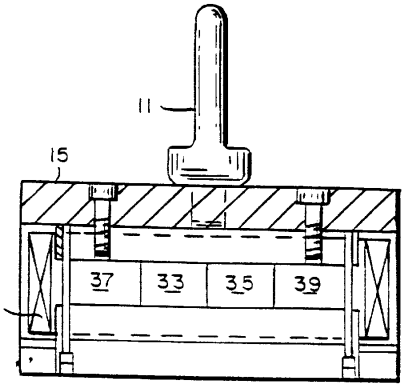


FIG. 2

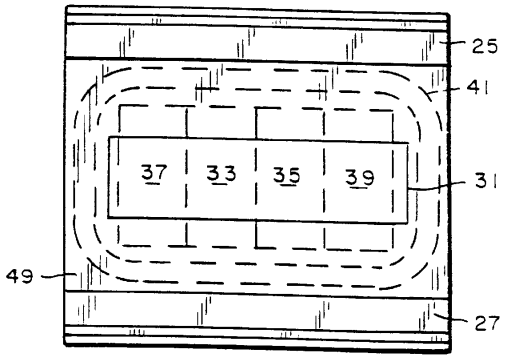


FIG. 3

Figure 2-28: Parallel electropermanent magnet, made from a series combination of materials with similar remanence but differing coercivity. A pulse of current through the coil 41 switches the magnetization of one material (37 and 35) but not the other (33 and 39), switching the device between holding and non-holding states. (Pignataro [75])

# Chapter 3

# The Electropermanent Magnet

## 3.1 Introduction

At the macroscale, the electromagnetic force is overwhelmingly the most common physical mechanism for electromechanical energy conversion. [1] At the microscale, the dominant commercial mechanism is electrostatic [23] [79] and a variety of physical principles are under active research, including electrostatic, magnetic, piezoelectric, and electrothermal, to name just a few. [7] Traditionally, use of the electromagnetic force has three disadvantages at small scales: the need for specialized materials, the need for high-density coiled geometries, and low ratios of force to static power consumption due to the unfavorable scaling of coil resistance in small devices. [61]

For our work constructing programmable matter [36] [98] and soft robotic systems [90] we are interested in millimeter-scale and smaller devices that allow electronically-controlled holding between surfaces. For the Robot Pebbles, [33] described in Chapter 4, we found electrostatic holding to be too weak and require impractically large voltages, electromagnets to be too power-hungry, and mechanically switched permanent magnets [88] [60] tend to be too bulky and expensive.

We will show that that the electropermanent magnet is a more desirable device for small-scale systems than electromagnets, so long as the time between switching events is not too short. The reason is that the energy to switch an electropermanent magnet is proportional to its volume, while it can exert force proportional to its area.

| | Coercivity | Residual Induction |
|---|---|---|
| Grade N40 NIB | 1000 kA/m | 1.28 T |
| Sintered Alnico 5 | 48 kA/m | 1.26 T |

Table 3.1: Magnetic properties of NIB and Alnico. From [72], [77]

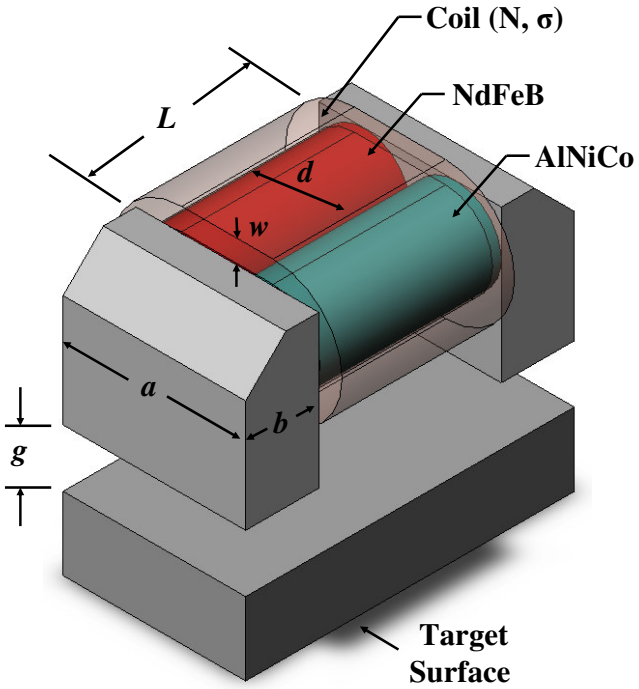


Figure 3-1: Switchable electropermanent magnet construction.

Also, electropermanent magnets do not require coils with as high a density as electromagnets, so long as the average time between switching events is long enough. After presenting these theoretical results, we will describe our device fabrication process and present experimental data characterizing the performance of these devices.

## 3.2 Theory

### 3.2.1 Qualitative

Figure 3-1 shows a schematic view of an electropermanent magnet with a keeper bar, and Figure 3-7 shows a photo of an actual device. The electropermanent magnets described in this paper are made from the parallel combination of Neodymium-Iron-

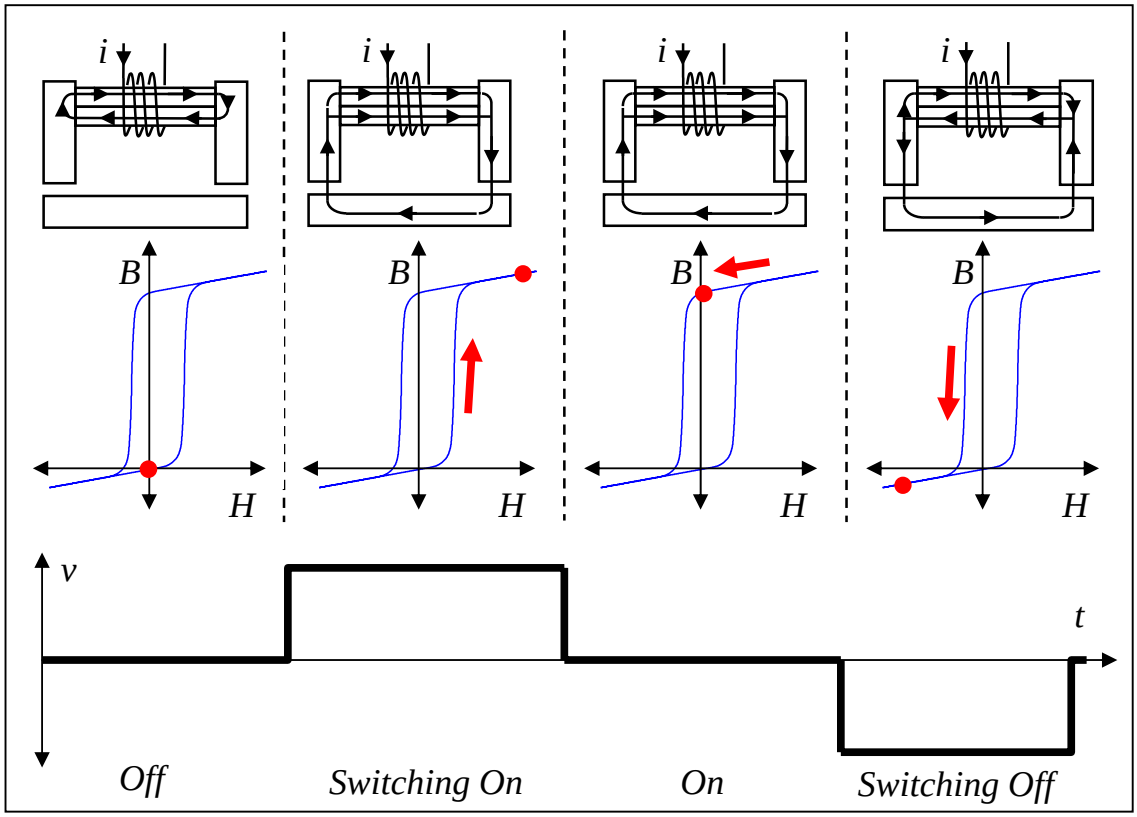


Figure 3-2: Switchable Electropermanent Magnet Operation. In the off state, the two magnetic materials are oppositely polarized, so magnetic flux circulates inside the device, and there is no force on the target. In the on state, the two magnetic materials are polarized in the same direction, so magnetic flux travels outside the device and through the target, attracting it to the magnet. A current pulse in the coil of proper magnitude and sufficient duration switches the device between the on and off states, by switching the magnetization of only the Alnico magnet, which has a lower coercivity than the NIB magnet.

Boron (NIB), which has a very high coercivity, and Aluminum-Nickel-Cobalt (Alnico), which has a relatively lower coercivity. Both have about the same residual induction. (See Table 3.1)

Because the NIB magnet has a very high coercivity, under our experimental conditions the flux through it is always in the same direction. When the device is in the off-state, the NIB and Alnico magnets are oppositely magnetized, so the flux circulates inside the device and does not cross the air gaps to the keeper. (See Figure 3-2) When the magnet is on, the NIB and Alnico magnets are magnetized in the same direction, so the flux from both crosses through the keeper, and force is required to pull the two halves apart.

Figure 3-2 shows the operation of the device through a full cycle. A positive current pulse through the coil results in a clockwise flux through the magnet and keeper, magnetizing the Alnico magnet rightward, turning the device on. A negative current pulse imposes a counterclockwise flux through the magnet and keeper, magnetizing the Alnico magnet leftward, turning the device off.

To understand the origin of the bistability of the device, it is helpful to consider Figure 3-2. The NIB magnets and the Alnico magnets are in parallel and are the same length, so they see the same magnetic field H, and their magnetic flux adds. On the scale of the Alnico B/H curve, the NIB B/H curve appears as a horizontal line, because of its much higher coercivity. (See Table 3.1) So, the polarized NIB magnet biases up the symmetrical B/H curve of the Alnico magnet, such that the two taken together have a residual induction near zero on the lower part of the hysteresis loop, but a positive residual induction on the upper part of the hysteresis loop. A current pulse through the coil imposes a magnetic field H across the device, cycling it around the biased-up hysteresis loop shown in the figure.

### 3.2.2 Quantitative

#### Force Computation

In this section we compute the force vs. air gap for the device shown in Figure 3-1, using a magnetic circuit approach. We denote the axial magnetic field intensity within any of the magnets $H_m$, and the magnetic field intensity in the air gap $H_g$. The coil has N turns and carries a current I. Starting with Ampere's law, using a loop passing through either of the magnets, through both air gaps, and through the keeper bar, we can write:

$$H_m L + 2H_g g = NI \tag{3.1}$$

We denote the axial magnetic flux density in the magnets of the two materials $B_{Alnico}$ and $B_{NIB}$, the magnetic flux density in the air gap $B_g$, and the pole-to-pole leakage flux $\Phi_{leak}$. Using Gauss's law for magnetic fields and a magnetic circuit approach, we can write the flux conservation expression:

$$\frac{\pi}{8} d^2 N_{rods} (B_{alnico} + B_{NIB}) = B_g ab + \Phi_{leak} \tag{3.2}$$

For the NIB magnet, we use a straight-line demagnetization curve. [1]

$$B_{NIB} = B_r + \mu_0 H_m \tag{3.3}$$

The air-gap field and flux are linearly related.

$$B_g = \mu_0 H_g \tag{3.4}$$

We can approximate the pole-to-pole leakage flux $\Phi_{leak}$ as being due to a constant leakage permeance $\mathcal{P}_{leak}$.

$$\Phi_{leak} = (NI - H_m L)\, \mathcal{P}_{leak} \tag{3.5}$$

The Alnico magnet has a nonlinear B/H relationship, $B_{alnico}(H_m(t), t)$, which

is dependent on $H_m(t)$ and on the progression of time t, because of the hysteresis. Combining the above equations, we can write an implicit expression for $H_m(t)$ in terms of this function and geometric parameters. This equation can be solved numerically for $H_m(t)$ in terms of the current I(t) and the device parameters.

$$\begin{aligned}\frac{\pi}{8}d^2 N_{rods}\left(B_{alnico}(H_m(t),t)+B_r+\mu_0 H_m(t)\right)= \\ \left(\frac{\mu_0 ab}{2g}+\mathcal{P}_{leak}\right)\left(NI(t)-H_m(t)L\right)\end{aligned} \tag{3.6}$$

Since the field is perpendicular to the iron at the surface of the gap, neglecting fringing fields, the force per area is given by the $T_{zz}$ component of the Maxwell stress tensor.

$$\frac{F}{2ab}=T_{zz}=\frac{B_g^2}{2\mu_0} \tag{3.7}$$

Given $H_m(t)$ from a numerical solution of Equation 3.6, we can write the expression for the force by combining Equations 3.1 and 3.4.

$$F=\mu_0\frac{ab}{4}\left(\frac{NI(t)-H_m(t)L}{g}\right)^2 \tag{3.8}$$

**Holding Force**

When both the Alnico and NIB magnets are fully magnetized in the same direction, as $g \to 0$, $B_{alnico}=B_{NIB}=B_r$. Also in this case, $\Phi_{leak} \to 0$ since $g \to 0$. In this case, we can write a simple expression for the air gap flux using Equation 3.2.

$$B_g=B_r\frac{\pi d^2 N_{rods}}{4ab} \tag{3.9}$$

Combining this with Equation 3.7, we can write an expression for the holding force.

$$F=\frac{1}{\mu_0 ab}\left(\frac{\pi B_r d^2 N_{rods}}{4}\right)^2 \tag{3.10}$$

With all other terms held constant, as we reduce the pole area ab the force increases. This is because the force per area goes as the square of the flux density. With constant flux, as we make the area smaller the force increases.

For maximum force, we should then set the pole area so that the air gap flux density is just below the saturation flux density of the iron from which the pole pieces are constructed, which we denote $B_{sat}$. Given this, we can write an expression for the optimal value of the dimension b.

$$b = \frac{B_r}{B_{sat}} \frac{\pi d^2 N_{rods}}{4a} \tag{3.11}$$

If this value is used, the poles are near saturation when the magnet is on, so the the holding force is simply:

$$F = \frac{B_{sat}^2 ab}{\mu_0} \tag{3.12}$$

**Electrical Characteristics**

Energy and power are very limited in autonomous microsystems. If we are to integrate these devices, their electrical terminal characteristics, switching energy, and temperature rise upon switching are of paramount importance.

**Current to Magnetize** To switch on the magnet, we will apply a pulse of voltage V to the coil for a time T, until the coil current rises to $I_{max}$. (See Figure 3-2) We denote the magnetic field intensity for the Alnico to reach saturation $H_m = H_{mag}$, and the associated magnetic flux density $B_{alnico} = B_{mag}$. Substituting these values into Equation 3.6 and solving for I, we obtain an expression for the current.

$$I_{max} = \frac{H_{mag} L}{N} + \frac{\pi d^2 N_{rods} \left(B_{mag} + B_r + \mu_0 H_{mag}\right)}{8N \left(\frac{\mu_0 ab}{2g} + \mathcal{P}_{leak}\right)} \tag{3.13}$$

From this expression, we can see that there is a linear dependence of $I_{max}$ on length scale. As all of the dimensions in the problem, including L, d, a, b, and g, are scaled down linearly, we expect the required current $I_{max}$ to decrease linearly as well.

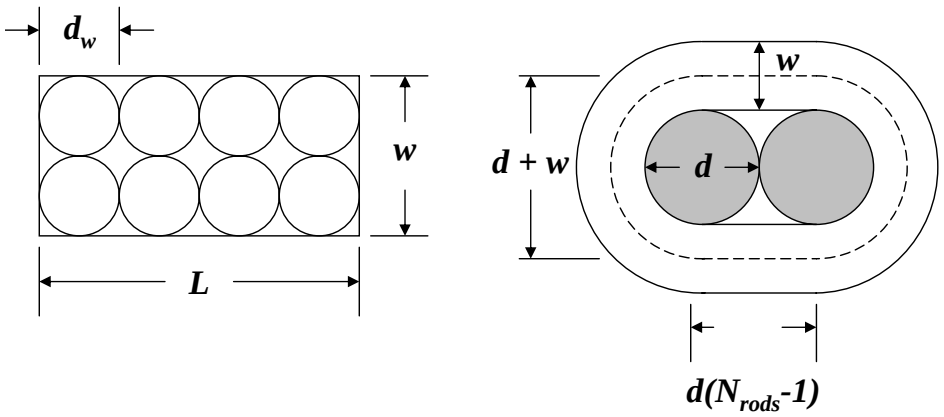


Figure 3-3: Left: Cross-section view of coil. Assuming square wire packing, the sum of the area of the bounding boxes around each wire equals the total cross-sectional area of the coil, so $Nd_w^2 = Lw$. Right: Side view of the coil. The dotted line shows the middle turn, distance w/2 from the core. This is an average-length turn; the total length of the wire is N times the length of this turn. By adding the lengths of the straight segments and circular caps, we can find the length of the wire, $l = N(2d(N_{rods} - 1) + \pi(d + w))$.

As $g \to 0$, $I_{max}$ reduces to $H_{mag}L/N$.

**Coil Resistance** To proceed further to obtain the magnetizing voltage and switching energy, we will need the DC series resistance of the coil. The resistance of the coil is equal to the resistance of the unrolled wire.

$$R = \rho \frac{l_{wire}}{A_{wire}} \tag{3.14}$$

The length of the unrolled wire is N times the length of an average-length turn. (See Figure 3-3)

$$l_{wire} = N\left[2d\left(N_{rods} - 1\right) + \pi\left(d + w\right)\right] \tag{3.15}$$

The wire area, in terms of the wire diameter $d_w$, is simply

$$A_{wire} = \frac{\pi}{4} d_w^2 \tag{3.16}$$

Assuming square wire packing, we can relate the cross-sectional area of the coil to the wire diameter and the number of turns. (See Figure 3-3)

$$wL = Nd_w^2 \tag{3.17}$$

Combining Equations 3.14, 3.15, 3.16, and 3.17, we can write the resistance of the coil in terms of the device parameters.

$$R = \frac{4\rho N^2}{L}\left[1 + \frac{d}{w}\left(1 + \frac{2N_{rods} - 2}{\pi}\right)\right] \tag{3.18}$$

We see that as $w \to 0$, the resistance goes to infinity, but that R cannot be made arbitrarily small as $w \to \infty$, so that there are diminishing returns when increasing the coil thickness w much above d in an attempt to reduce the resistance.

**Switching Voltage** The voltage drop across the coil is the sum of the induced voltage, from Faraday's law, and the voltage across the series resistance, from Ohm's law.

$$V(t) = N\left(\frac{dB_{alnico}}{dt} + \frac{dB_{NIB}}{dt}\right)\frac{\pi d^2 N_{rods}}{8} + I(t)R \tag{3.19}$$

This equation can be solved numerically with Equations 3.6 and 3.18 to model the nonlinear electrical response of the device. However, we can determine a number of useful electrical characteristics without resorting to numerical techniques.

From the above equation, we can see that higher voltage results in faster switching. We can also see that there is a minimum voltage, $V_{min}$, below which the magnet cannot reach the switching field $H_{mag}$ after any amount of time T. We can find this minimum voltage by setting the $d/dt$ terms to zero, which gives the steady-state limiting value after a transient of arbitrarily long duration. This allows us to find the voltage $V_{min}$ below which a current $I_{max}$ will not flow after the transient.

$$V_{min} = I_{max}R \tag{3.20}$$

Combining Equations 3.20, 3.18, 3.13, we can write the minimum voltage in terms of device parameters.

$$V_{min} = \left[4H_{mag} + \frac{\pi d^2 N_{rods}\left(B_{mag} + B_r + \mu_0 H_{mag}\right)}{2L\left(\frac{\mu_0 ab}{2g} + \mathcal{P}_{leak}\right)}\right]\left[1 + \frac{d}{w}\left(1 + \frac{2N_{rods} - 2}{\pi}\right)\right]\rho N \tag{3.21}$$

Examining this equation, we can see that $V_{min}$ is independent of length scale and proportional to the number of turns N. For $g \to 0$, it simplifies to the expression below.

$$V_{min}(g = 0) = 4H_{mag}\rho N\left[1 + \frac{d}{w}\left(1 + \frac{2N_{rods} - 2}{\pi}\right)\right] \tag{3.22}$$

**Inductance** Although the device has a nonlinear inductance, we can approximate its behavior with an average constant inductance $L = \Delta\lambda/\Delta I$, in order to estimate the switching time T.

$$L = \frac{\Delta\lambda}{\Delta I} = \frac{N(B_{mag} + B_r + \mu_0 H_{mag})\frac{\pi}{8}d^2 N_{rods}}{\Delta I} \tag{3.23}$$

We can combine this expression with Equation 3.13 to eliminate the dependence on I, since $\Delta I = I_{max}$. After some algebraic rearrangement, we see that the effective inductance while magnetizing is the parallel combination of two inductances, one for the magnetization of the material and one for the inductance due to the air gap.

$$L = N^2\left[\left(\frac{\mu_0 ab}{2g} + \mathcal{P}_{leak}\right)^{-1} + \left[\frac{\pi d^2 N_{rods}(B_{mag} + B_r + \mu_0 H_{mag})}{8H_{mag}L}\right]^{-1}\right]^{-1} \tag{3.24}$$

**Pulse Length** Under the linear inductance model, the device is a series LR circuit, and applying a voltage pulse results in a first-order rise in the current.

$$I(t) = \frac{V}{R}(1 - e^{-\frac{tR}{L}}) \tag{3.25}$$

We denote the switching pulse length T. Equation 3.25 is monotonically increasing, so $I(T) = I_{max}$. Combining with Equation 3.25 and 3.20, we can solve for the pulse length.

$$T = \frac{L}{R} ln \left( \frac{V}{V - V_{min}} \right) \tag{3.26}$$

Solving for the time constant, $\tau = L/R$, by combining Equations 3.26, 3.18, and 3.24, we arrive at an expression for the pulse length in terms of $V$ and $V_{min}$. Tallying up the scale dependences, the time constant and pulse length decrease quadratically with length scale.

**Switching Energy** We can compute the energy E required to switch the magnet by integrating the power $VI(t)$ over the pulse.

$$E = \int_0^T VI(t)\, dt \tag{3.27}$$

Performing this integral, using Equations 3.26 and 3.25, we obtain an expression for E in terms of the previously computed inductance L, resistance R, and minimum voltage $V_{min}$.

$$E = \frac{V^2 L}{R^2} \left[ ln \left( \frac{V}{V - V_{min}} \right) - \frac{V_{min}}{V} \right] \tag{3.28}$$

Again tallying up the scale dependencies, if we set the driving voltage V independently of length scale, then the switching energy E is proportional to the cube of length scale.

Electropermanent magnets require a uniform energy per volume to magnetize—which makes them compatible with use in a scalable integrated robotic device. This is for two reasons: availability of power and dissipation of heat.

Energy sources (e.g. batteries) typically have a constant volumetric energy density, so a battery powering an electropermanent magnet will last for the same number of switching events as the whole system is scaled down. Because materials have a constant volumetric thermal capacity and the rate of heat dissipation from an object

| Symbol | Parameter | Length Scaling | Turns Scaling | Eqn. |
|---|---|---|---|---|
| $F$ | Force | $L^2$ | Const. | 3.8 |
| $I_{max}$ | Current | $L$ | $L^-1$ | 3.13 |
| $R$ | Resistance | $L^-1$ | $N^2$ | 3.18 |
| $V_{min}$ | Voltage | Const. | $N$ | 3.21 |
| $L$ | Inductance | $L$ | $N^2$ | 3.24 |
| $\tau$ | Time Constant | $L^2$ | Const. | 3.25 |
| $T$ | Pulse Length | $L^2$ | Const. | 3.26 |
| $E$ | Pulse Energy | $L^3$ | Const. | 3.28 |

Table 3.2: Scaling properties of electropermanent magnets, assuming constant pulse voltage and scaled air gap.

is roughly proportional to area, using electropermanent magnets we can expect a scale-independent temperature rise and a cooling time that gets proportionally shorter with decreasing length scale.

## 3.3 Comparison with Other Approaches

In this section, we compare programmable holding by electropermanent magnet with two other solid-state approaches: holding by electromagnets and holding by electrostatic force between capacitor plates. As will be shown, the electropermanent magnet allows for larger forces than air-breakdown-limited electrostatics and for lower energy consumption than electromagnets, so long as the switching events are spaced sufficiently far apart in time.

### 3.3.1 Electrostatics

Electrostatic motors and actuators [23] are commonly used in microfabricated systems. [79]

Consider two side-by-side capacitor plates, with the same area footprint of the electropermanent magnet described in this paper. The capacitor plates are coated with a thin layer of insulation, to prevent conduction should they come into direct contact.

If the two capacitor plates on separate bodies are brought into face-to-face contact,

and a voltage is applied to the plates, a force will be required to separate the plates. Very low static power (only leakage) is required to maintain the holding force; thus the capacitor plates are also a zero-power holding device.

In practice, the limitation on such a system is the high voltage required to obtain reasonable forces. The high voltages present several problems; one is switching and the other is the dielectric breakdown of air.

### Switching High Voltages

Up to 5V, standard CMOS logic devices can be used. From 5V - 18V, one can use legacy metal-gate CMOS IC's to drive electrostatic devices. [58] From 15V through 300V, a variety of special-purpose high voltage IC's [85] and processes [2] designed for display, printer, and medical applications are available. Discrete transistor switches are commercially available with $V_{ds}$ up to about 1000V. To switch higher voltages, multiple discrete transistors, coupled by transformers, can be used.

### Breakdown Voltage of Air

The dielectric strength of air is not a constant electric field intensity, but is dependent on the distance between the electrodes. [16] A commonly quoted figure for the dielectric strength of air is $3 \times 10^6$ V/m, [89] but this figure applies only for gaps of millimeter size and above.

The Paschen curve describes the dielectric strength of air due to the phenomenon of avalanche breakdown. (See Figure 3-4) At atmospheric pressure, the Paschen curve is valid down to its minimum, which occurs at $7\mu m$ and 365 volts. [30] Between $7\mu m$ and $3\mu m$, while the Paschen curve predicts a rise in breakdown voltage with decreasing distance, avalanche breakdown is still possible along longer fringing paths, so the maximum permissible voltage for practical applications is a constant 365V. The curve for the vapor-arc breakdown voltage of vacuum intersects the 365V line at $4\mu m$. The mean free path of an air molecule at STP is about 3.4 microns, so vacuum phenomena are possible at this scale, and the vacuum curve limits the permissible plate voltage below $4\mu m$. [14] [92]

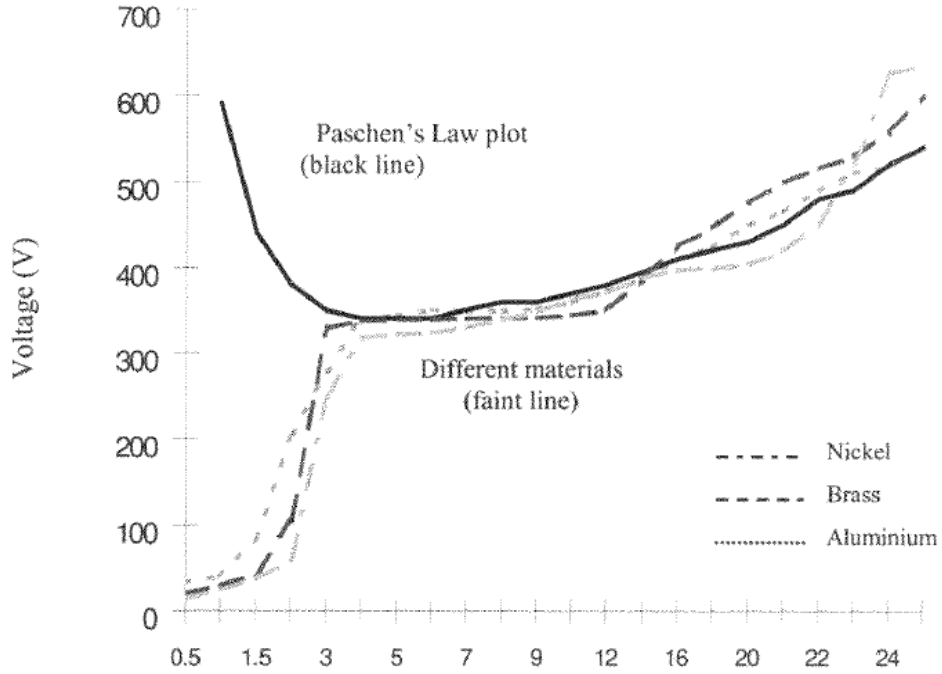


Figure 3-4: Breakdown voltage of air vs. gap. (Torres [30])

**Force between capacitor plates**

The force per area between two parallel conductive plates with normal electric field E at the surface, and area A, neglecting fringing, is given by the Maxwell Stress Tensor term Tzz.

$$F = \epsilon_0 E^2 A \tag{3.29}$$

Substituting A for the footprint area of the electropermanent magnet with which we are making this comparison, $a(L + 2b)$, and in terms of the voltage V and air gap g:

$$F = \epsilon_0 \left(\frac{V}{g}\right)^2 a\,(L + 2b) \tag{3.30}$$

By solving for V, we can get the voltage on the plates needed to equal the strength of an electropermanent magnet exerting force F.

$$V = \frac{Fg^2}{\epsilon_0 a\,(L + 2b)} \tag{3.31}$$

Figure 3-5 shows the plate voltage required to achieve the same force as the electropermanent magnet for the same design air-gap, plotted on the same axes as the Paschen curve. The voltage required is higher than Paschen curve limit at all scales, meaning that the electropermanent magnet is capable of applying larger forces than breakdown-limited electrostatic plates, even when both devices are scaled to microscopic dimensions.

The conclusion is that electropermanent magnets can produce larger forces than capacitor plates in air, even at microscopic dimensions. However, capacitor plates have a lower profile, are simpler to fabricate, and have lower switching energy, which is more important for many applications.

### 3.3.2 Electromagnets

An electromagnet working through an air gap requires continuous power dissipation to maintain holding force, in contrast to an electropermanent magnet, which changes state in response to a discrete energy pulse.

#### Force Computation

Consider an electromagnet with the geometry shown in Figure 3-1, but with the hard magnetic materials replaced with a soft magnetic material, $\mu \to \infty$, to form a horseshoe-type electromagnet. The Ampere's law loop expression is:

$$2Hg = NI \tag{3.32}$$

H is the magnetic field in the gap, g is the gap thickness, N is the number of turns, and I is the current. Following the approach of the electropermanent magnet force computation, the force is:

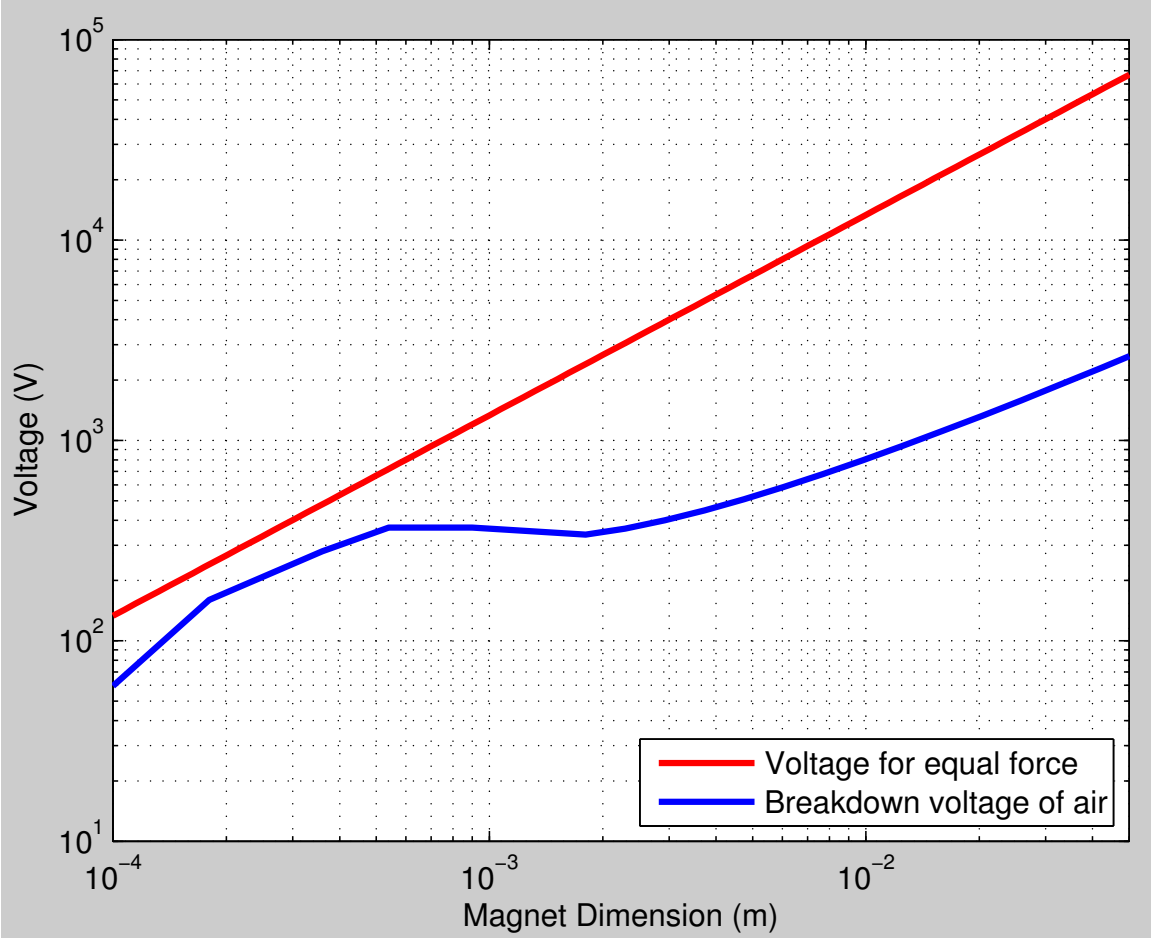


Figure 3-5: Electrostatic plate voltage required to equal the holding force of the electropermanent magnet, using the same area footprint and air gap. The red curve is the voltage required, the blue curve shows the voltage at which air will break down for the design air gap. Since the required voltage would be higher than the breakdown voltage, electropermanent magnets are capable of applying larger forces than capacitor plates across the same size air gap. The design used for this analysis is a scaled version of the device shown in the Experimental section. The air gap length is also scaled.

$$F = \mu_0 \frac{(NI)^2 ab}{4g^2} \tag{3.33}$$

Rearranging this expression, the steady-state current required to maintain a particular holding force is

$$I = \frac{2g}{N}\sqrt{\frac{F}{\mu_0 ab}} \tag{3.34}$$

In the steady-state, the power dissipation of the electromagnet is the $I^2R$ resistive power dissipation in the windings. Using the expression for coil resistance, Equation 3.18, the power dissipation of the magnet is

$$P = \frac{16Fg^2\rho}{\mu_0 abL}\left[1 + \frac{d}{w}\left(1 + \frac{2N_{rods} - 2}{\pi}\right)\right] \tag{3.35}$$

Switching on an electromagnet also takes a finite time and energy, due to the magnetizing inductance introduced by the air gap. The energy required to reach a given current is $\frac{1}{2}LI^2$. The inductance of this structure is

$$L = \mu_0 \frac{N^2 ab}{2g} \tag{3.36}$$

The energy to switch the equivalent electromagnet is then:

$$E = \frac{1}{2}LI^2 = Fg \tag{3.37}$$

The $L/R$ time constant to switch after a step to voltage V is:

$$\tau = \frac{\mu_0 Lab}{8\rho g\left[1 + \frac{d}{w}\left(1 + \frac{2N_{rods}-2}{\pi}\right)\right]} \tag{3.38}$$

### Time to Break-Even

Keeping the same dimensions, with a soft magnetic core substituted for the permanent magnet materials, the switching time and switching energy are always lower for the electromagnet. However, the electromagnet dissipates finite power in the steady-state,

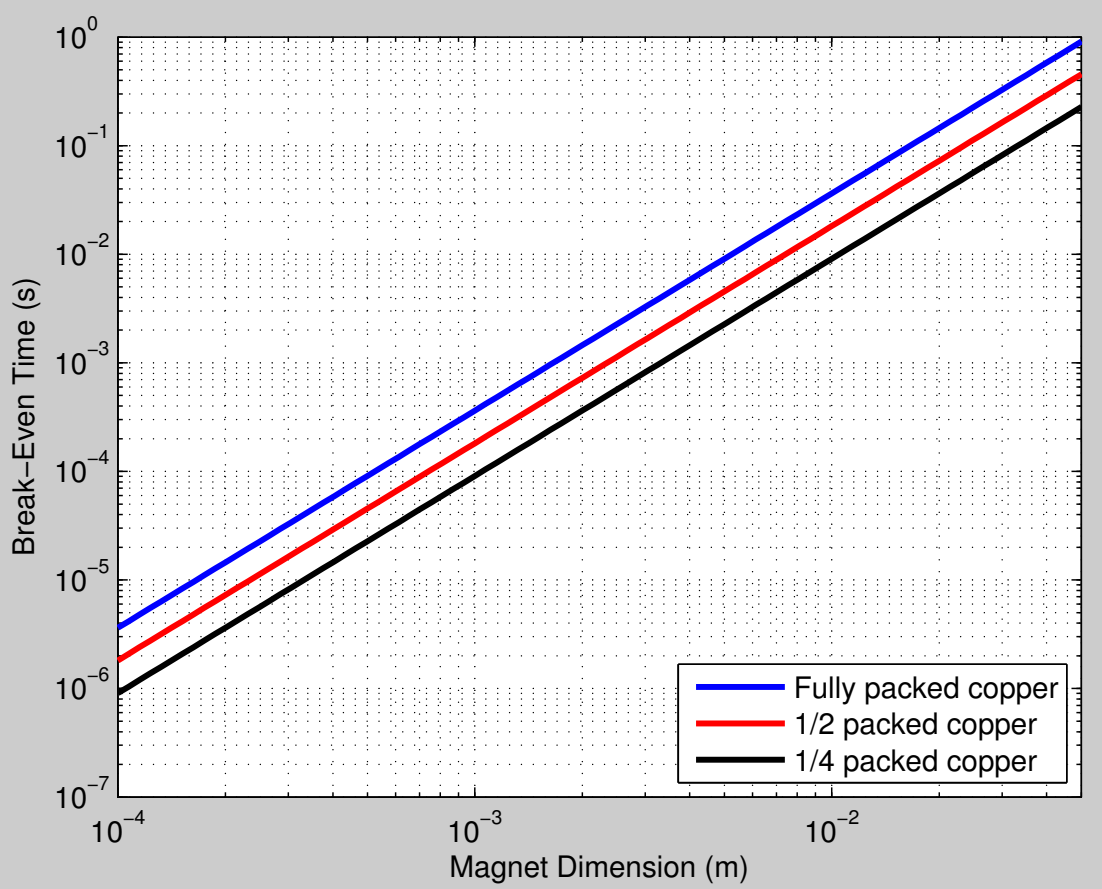


Figure 3-6: Time to break-even energy consumption for electromagnets vs. electropermanent magnets, for a scaled version of the device described in this paper. At centimeter scale, the break-even time is about 10 ms, and at millimeter scale, 100$\mu s$. The break-even time gets lower with reduced wire packing density.

while the electropermanent magnet does not. Therefore, there is a break-even time $T_b$ at which the energy consumption of the electromagnet and the electropermanent magnet are equal. If holding is required for times longer than $T_b$, the electropermanent magnet uses less energy.

We can formalize the definition of $T_b$ above as

$$T_b = \frac{2E_{electropermanent} - E_{electromagnet}}{P_{electromagnet}} \tag{3.39}$$

$E_{electropermanent}$ is multiplied by two because the electropermanent magnet must be switched twice for each holding period: once to switch on, and again to switch off.

Figure 3-6 shows a plot of $T_b$ versus the length scale of the magnet, computed using the equations dervived above. The plot shown is for L/g = 100; the breakeven time is shorter for longer air gaps. $T_b$ is milliseconds at centimeter scales, and tens of microseconds at millimeter scales. Electropermanent magnets use less energy than electromagnets in applications where the expected holding time is longer than $T_b$.

For magnetic programmable matter, where we want millimeter-scale modules able to hold for human-perceptible time scales, and want to permit large air gaps to reduce the cost of fabrication and increase the resistance to dust and contamination, electropermanent magnets are clearly preferable to electromagnets.

### Sensitivity to Wire Conductivity and Winding Fill Fraction

Microfabricated inductors typically have a lower Q than discrete inductors, [59] and one important reason is the lower conductivity of the available wiring materials (e.g. polysilicon instead of copper) and the lower fill fraction of the windings of coils produced by lithographic methods over winding methods. Figure 3-6 shows the break even time at multiple winding fill fractions. (Which is also equivalent to varying the conductivity of the wire.)

The break-even time $T_b$ is lower for lower conductivity or lower winding fill-fractions. High-resistance, compact coils increase the energy consumption of electropermanent magnets less than that of electromagnets. The intuitive explanation for this difference is as follows: With an electropermanent magnet, a significant fraction of the electrical input energy is transferred to the magnetic material and only some of it goes to resistive heating. In an electromagnet, once the air-gap field is set up, the current remains on and essentially all of the energy input is dissipated in resistive heating. This makes the energy consumption of the electromagnet more sensitive to the coil resistance than the energy consumption of the electropermanent magnet.

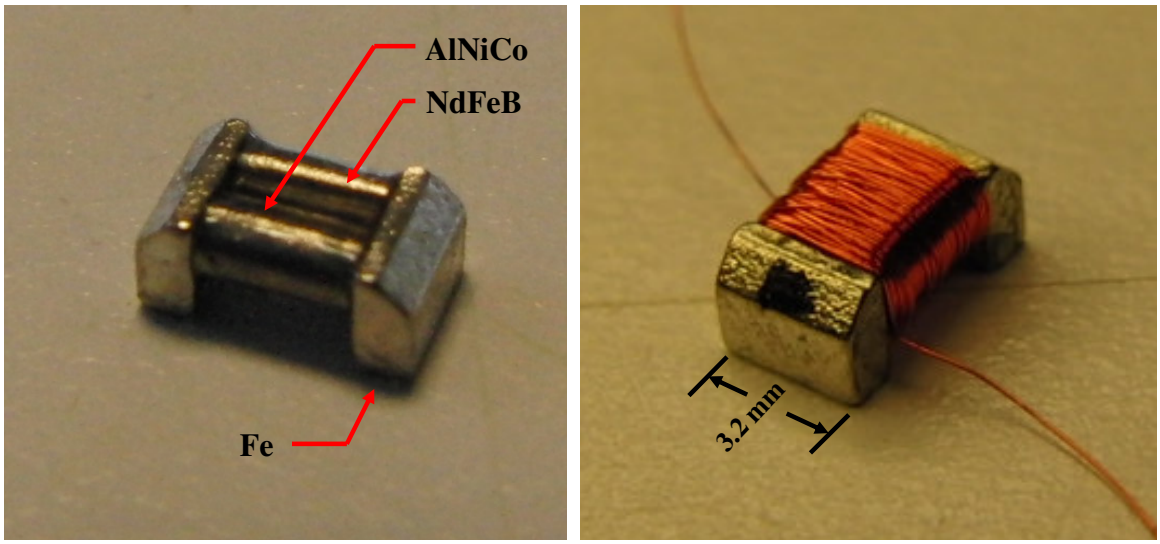


Figure 3-7: Miniature electropermanent magnet. This magnet is made from cylindrical rods of the magnetic materials, 1.6 mm in diameter, and iron pole pieces The magnetic rods were machined by cylindrical grinding, the pole pieces by wire EDM. The pieces were then assembled with tweezers under a microscope.

## 3.4 Experimental

### 3.4.1 Materials and Methods

We constructed several prototype electropermanent magnets. Each device has an NIB magnet, an Alnico magnet, iron pole pieces, and a copper wire coil.

Prototype pole pieces were made from a sheet of No. 5 relay steel, obtained from Carpenter Steel Corporation. (Reading, PA) We cut the pole pieces from the sheet on an abrasive waterjet cutter. We left the pole pieces secured to the sheet with tabs, to keep them from falling into the machine due to their small size. After cutting, we broke the tabs with a cold chisel and filed them away. We then honed the faces of the pole pieces flat with a steel file. In greater quantities, we purchased wire-EDM-cut, chromate-coated pole pieces, made from grade ASTM-A848 magnetic iron, from BJA Magnetics, Inc.

For the prototypes, we purchased NIB magnets from Amazing Magnets, Inc and Alnico 5 magnets from Magnet Kingdom, Inc. As purchased, the Alnico magnets were longer than the needed length. We cut them to length by striking with a cold

chisel, then grinding to final length using an abrasive file. In greater quantities, we purchased custom-length Grade N40SH NIB and Grade 5 Alnico magnets from BJA Magnetics, Inc.

We assembled the magnets using a microscope and tweezers. After cutting and handling, particles of ferromagnetic contamination tended to accumulate on the magnets. We tried several methods to remove contamination from the ends of the magnets, and eventually found that the best method was to wrap a large permanent magnet with clear packing tape, adhesive out, and to rub the magnets and pole pieces against the adhesive of the packing tape to remove the contamination. [1]

We secured the magnets to the pole pieces using Loctite Hysol E60-HP epoxy adhesive. We placed glue on the surface between the magnets and pole pieces, but also formed fillets of adhesive in the gap between the magnets.

We waited 24 hours for the glue to cure, then honed the target-contact face of the device flat using a abrasive file. We then wound the devices with N=80 turns of 40AWG solder-strippable magnet wire, purchased from MWS Wire Industries.

### 3.4.2 Experimental Setup

To measure the force vs. distance and force vs. pulse length of the device, we used a custom-built experimental setup, shown in Figure 3-8. A personal computer controls all of the hardware to allow for automated experiments and data collection.

The device under test mounts into a flexure clamp sample holder , shown in Figure 3-9. The device is positioned by a stepper-motor-driven ballscrew linear motion stage, purchased from Dahner Motion Systems. The motor is driven by a Geckodrive Model G203V stepper motor drive. The magnet pulls against an iron target plate, 72 mm square and 6.4 mm thick. The motion of the target is constrained in five axes by a Nelson Air Model RAB1S linear air bearing, so that it it can move only coaxially with the magnet. The force on the target is measured using a Futek Model LSB200 tension/compression load cell with a 4.4 N range. The signal from the load cell is

[1] Thanks to Paul Lituri of BJA Magnetics (Rutland, MA) for his suggestion to use packing tape for cleaning magnets.

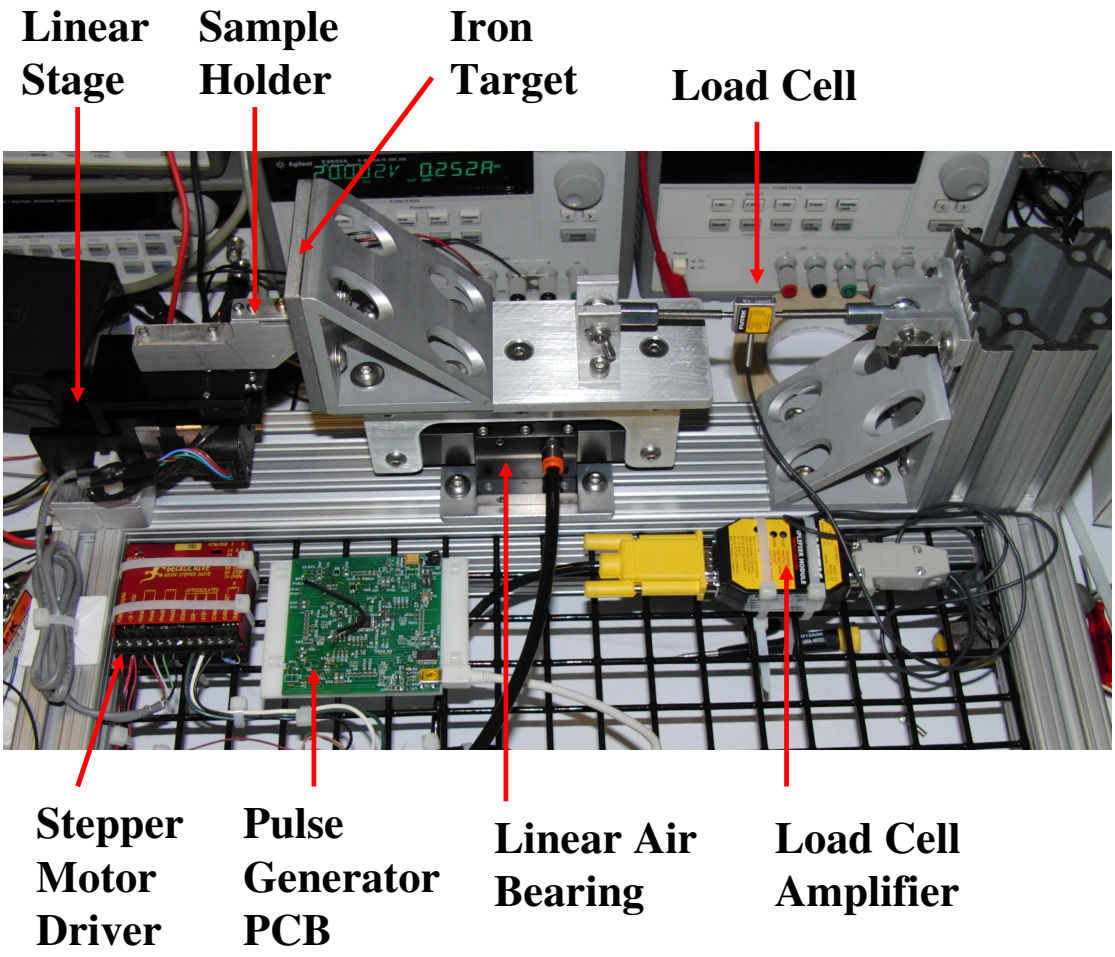


Figure 3-8: Experimental setup used to measure the force vs. displacement relationships.

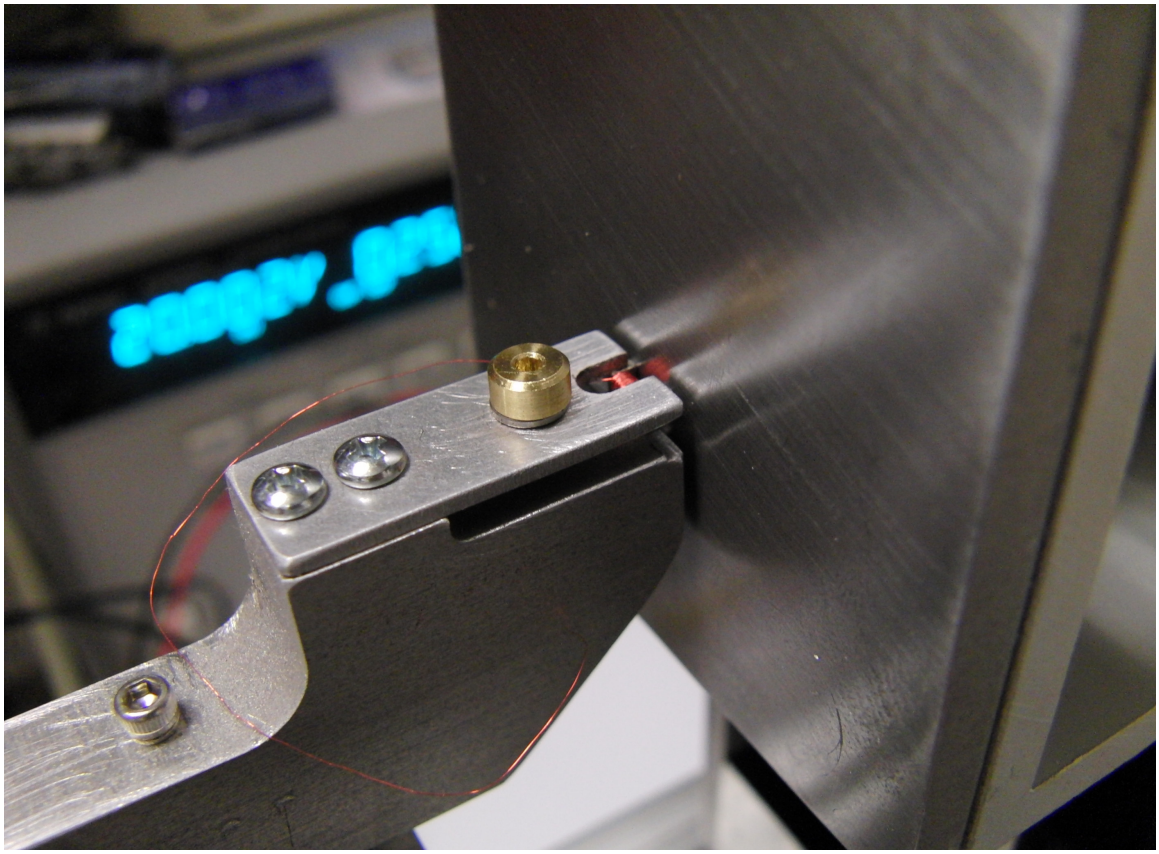

Figure 3-9: Flexure clamp used to hold the magnet square as it is pulled away from the iron target plate.

amplified using a Futek Model CSG110 load cell amplifier, and then sampled by a National Instruments Model USB-6211 data acquisition unit.

A custom-designed pulse-generator PCB switches the state of the magnet using MOSFET transistor switches controlled by an Atmel AVR microcontroller. The PC can switch the magnet on or off with any desired pulse length in $1\mu s$ increments via serial port command. A Hewlett Packard E3631A DC supply powers the magnet, and allows the PC to vary the pulse voltage. The current through the magnet is measured by sensing the voltage drop across a $0.01\Omega$ series resistor. The pulse voltage and current signals are amplified by a pair of Texas Instruments OPA445 operational amplifiers, and sampled by a Tektronix TDS3054 digital oscilloscope, also connected to the PC.

## 3.5 Results

### 3.5.1 Qualitative

The devices reliably switch between holding and non-holding states upon application of momentary, opposite polarity current pulses. Discharging a $100\mu F$ capacitor charged to 20V across the device is sufficient to switch it between states. The mass of the device is about 200 mg. Upon switching, the magnets can lift themselves vertically onto an overhead iron bar from a starting distance of about 3 mm. When the device is switched off, it falls down under its weight only. Figure 3-10 shows the device holding up a 250 g test mass. The devices can switch states in free air, without a keeper bar present, although the eventual holding force is lower.

### 3.5.2 Quantitative

#### Holding Force

Figure 3-11 shows the plot of force versus air gap for the device as it is pulled away from the iron plate. The blue dots are experimental data from the load cell, the red line is data from a finite-element simulation, and the black line is the prediction of

Figure 3-10: Electropermanent magnet, switched on, holding up a 250g test mass.

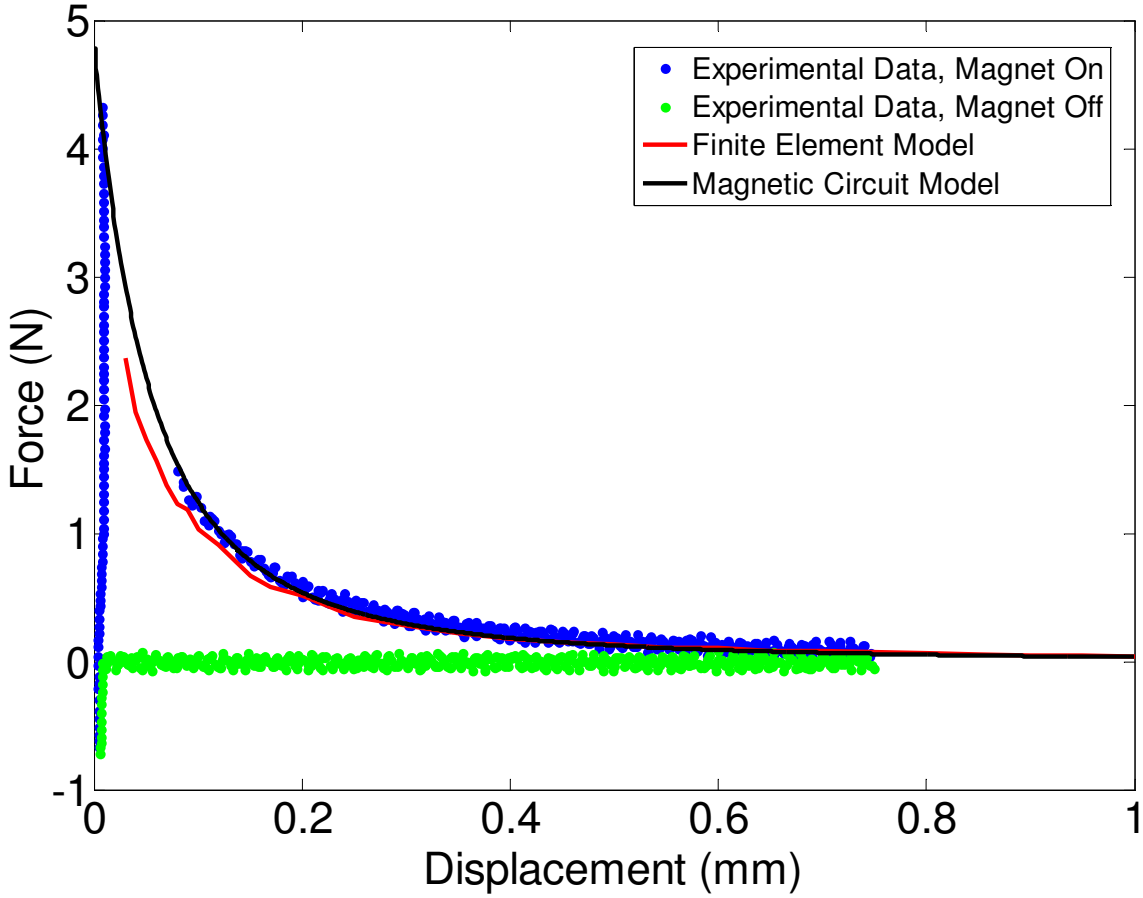


Figure 3-11: Comparison of experimental data and model predictions for force vs. air gap, showing close agreement over the range of validity for each type of data. (The experimental data is missing points in the non-equilibrium region of the magnet/spring system, and the finite element analysis is missing points at close spacing where the resulting mesh required too many elements.

| Symbol | Parameter | Value |
|---|---|---|
| $L$ | Magnet Length | 3.2 mm |
| $d$ | Magnet Diameter | 1.6 mm |
| $a$ | Pole Width | 1.6 mm |
| $b$ | Pole Thickness | 1.3 mm |
| $N$ | Turns | 80 |
| $B_r$ | NIB Remnant Flux Density | 1.28 T |
| $B_{sat}$ | Iron Saturation Flux Density | 1.5 T |
| $\mathcal{P}_{leak}$ | Leakage Permeance | 23 nH |

Table 3.3: Device parameters.

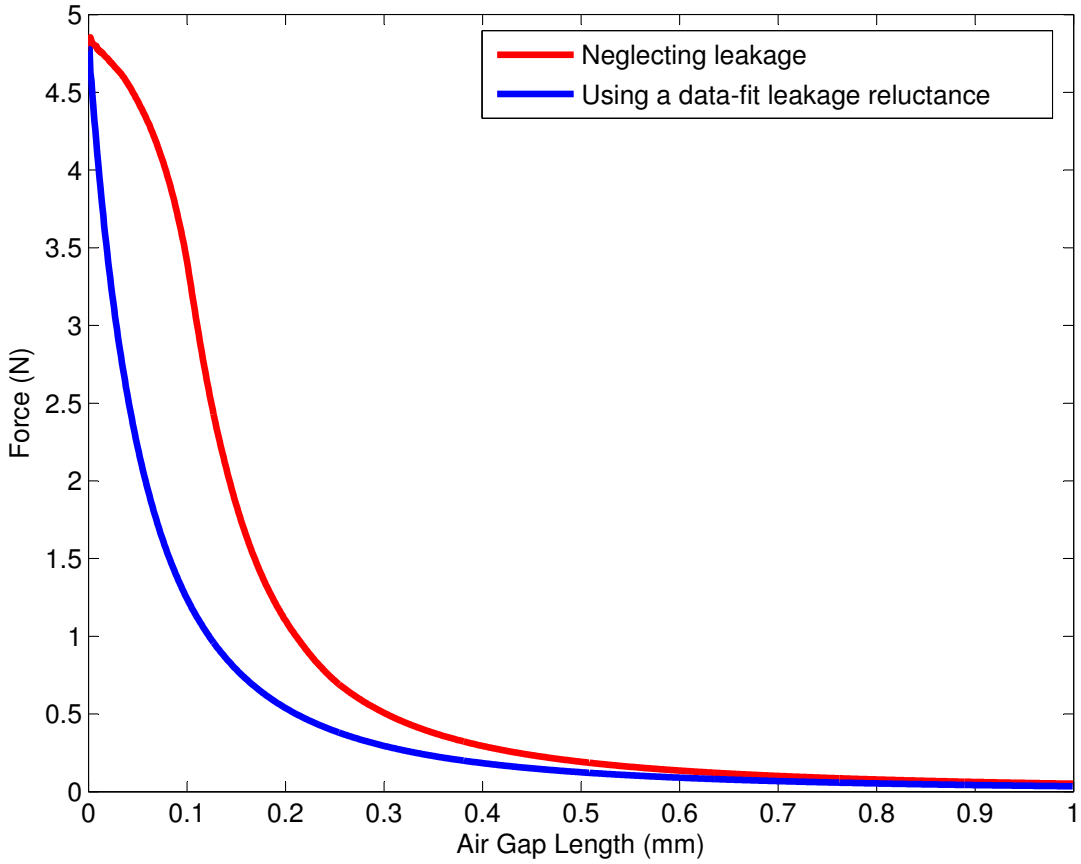


Figure 3-12: Force vs. air gap, computed using the magnetic circuit model, with and without leakage. The top curve neglects leakage, while the bottom curve uses a leakage permeance fit to match the finite element analysis result.

the magnetic circuit model. The three curves show close agreement over their valid ranges. The green dots are experimental data from the load cell with the magnet switched off.

Figure 3-12 shows the prediction of the magnetic circuit model in two cases; with the leakage permeance set to zero (red curve) and with the leakage permeance fit to match the finite-element analysis result. (See Table 3.3) From the plot, we can see that pole-to-pole leakage does not change the holding force at zero air gap, but significantly changes the slope of the force vs. distance curve around zero air gap. This makes it an important effect to take into account during the design of electropermanent magnet systems, even those operating over relatively small air gaps.

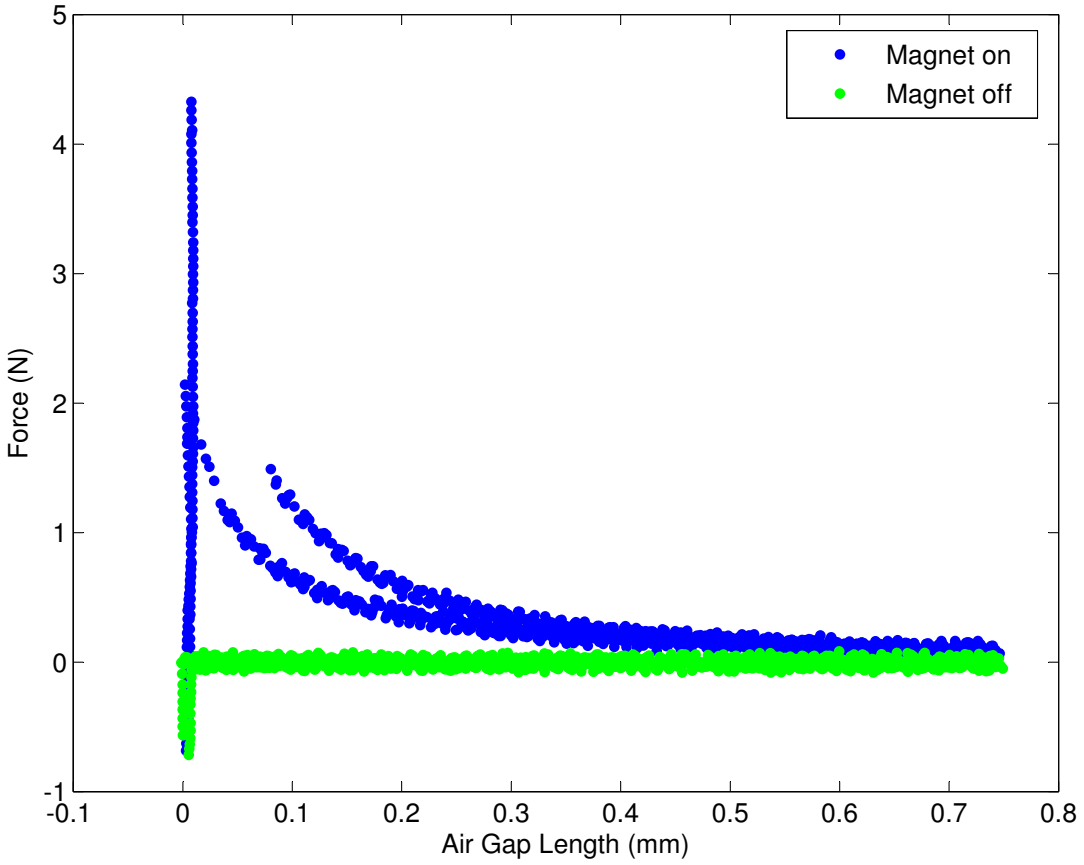


Figure 3-13: Force vs. air gap length. The device was switched on while in contact with the plate, pulled away to a distance of 0.75 mm, returned to the plate, switched off, and pulled away again. While still in contact with the plate, the peak force reached 4.4 N. When the linear stage drove the device further from the target, the device broke away from the plate dynamically, reaching a new static equilibrium (between the magnetic force and load cell stiffness) at a distance of 0.07 mm, which is why there are no data points on the upper curve between 0 and 0.07mm. The middle curve shows the magnet returning to the plate; the force is lower because the device has been partially self-demagnetized. The lower (green) curve shows that, with the magnet switched off, the force is near zero.

Figure 3-13 shows the effect of self-demagnetization. The device is pulled away from the plate to a distance of 0.75 mm, following the upper blue curve, then returned to the plate, following the lower blue curve. This excursion decreases the final holding force to about half its initial value.

Figure 3-14 shows data on the holding force vs. switching pulse length at zero air gap. The holding force increases linearly from zero with increasing pulse length, then saturates at 4.4 N force at about $100\mu s$ pulse length. This shows that it is possible to set the holding force to any value within a range by controlling the switching pulse length.

Figure 3-15 shows the current transient to turn on the magnet. The time constant is about $20\mu s$. Substituting the device parameters into Equation 3.24, using air gap g=0, we get $L = 76\mu H$. Since V=20V and $I_{final} = 5.3A$, $R = V/I = (20V)/(5.3A) = 3.8\Omega$. Following the assumptions of our model, the predicted $L/R$ time constant is $21\mu s$, versus the measured time constant of $20\mu s$.

## 3.6 Conclusion

Electropermanent magnets can have their holding force switched on and off by the application of a momentary electrical pulse. Electropermanent magnets have low power consumption and temperature rise compared to electromagnets, especially at small length scale. Electropermanent magnets require energy proportional to their volume and hold with force proportional to their area, so fundamental scaling favors their low-energy operation at small dimensions.

At centimeter scale, electropermanent magnets can hold hundreds of times their own weight, can exert force comparable to their weight from a distance comparable to their length, and switch is a fraction of a millisecond. At millimeter scale, scaling laws predict each of these metrics should improve.

Electropermanent magnets use higher instantaneous power but lower overall energy than electromagnets, with break-even times in the milliseconds at centimeter scale in the microseconds at millimeter scale according to our analysis. Electroper-

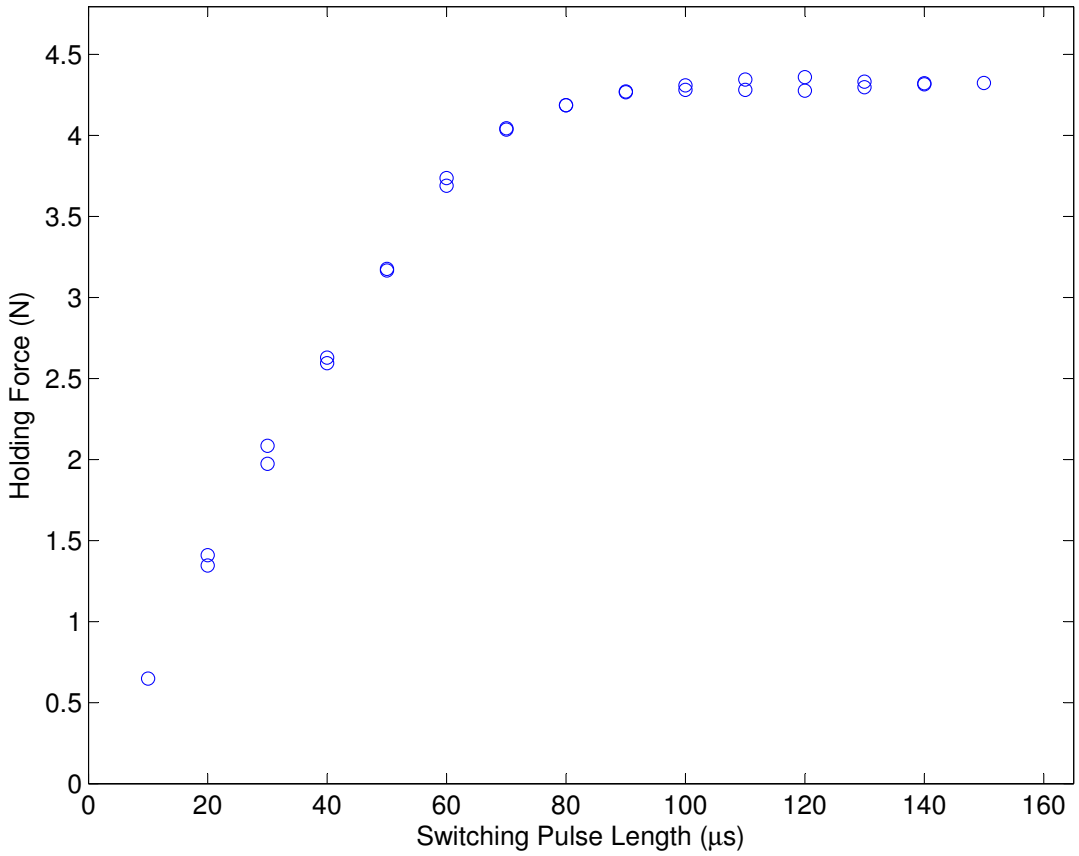


Figure 3-14: Holding force vs. switching pulse length. While in contact with the plate, the device was AC pulse demagnetized, switched ten times using pulses of the indicated length, then pulled away from the plate. The holding force is the force measured just before separation. The holding force increases linearly with increasing pulse length and then saturates, so that above 100 $\mu s$, no increase in holding force with increasing pulse length is observed.

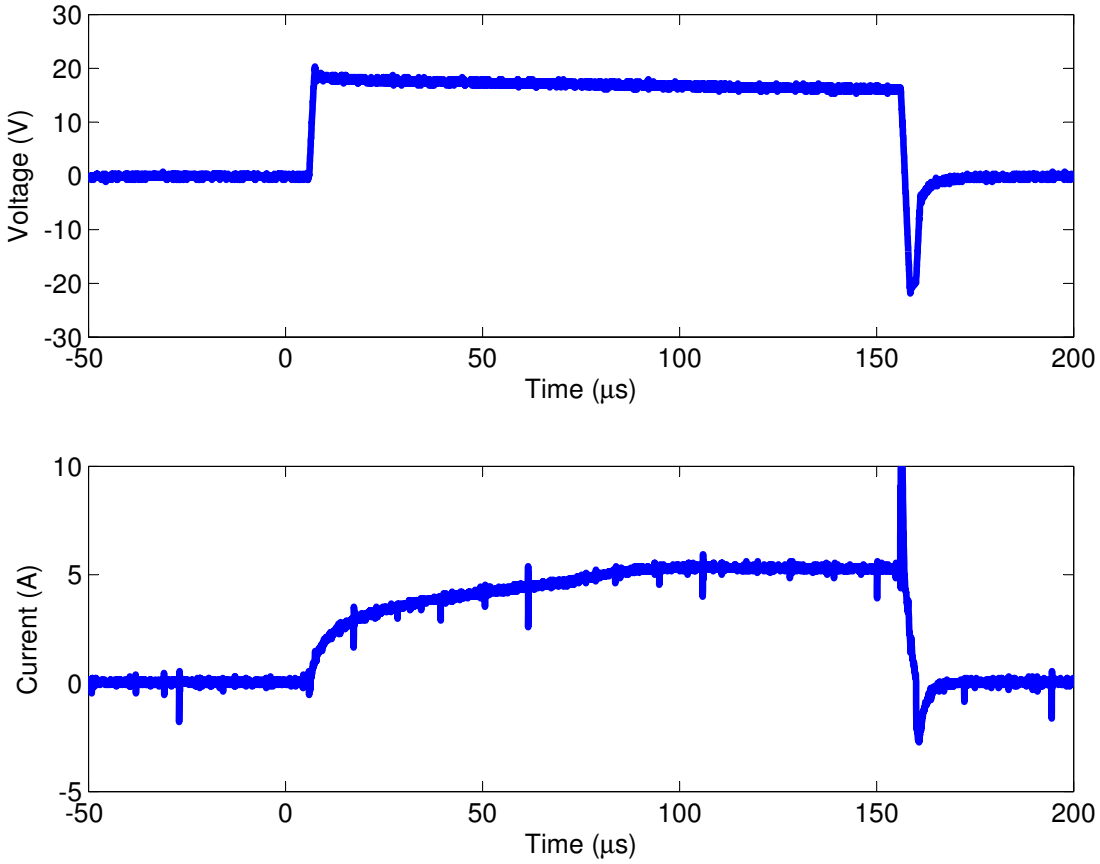


Figure 3-15: Measured voltage and current for the 150 $\mu s$ pulses. The peak current of 5.3 A is reached after about 100 $\mu s$, the same pulse length at which the holding force saturates.

manent magnets are less sensitive than electromagnets to lower winding fill fractions and lower conductivity wire, making them more amenable to microfabricated coils.

Electropermanent magnets are stronger than breakdown-limited electrostatic plates in air, operate at much lower, more practically switched voltages, and allow larger air gaps for higher resistance to dust and contamination. On the other hand, they have a higher profile and use more energy to switch.

All of the above conclusions make electropermanent magnets a promising building block for actuators in the next generation of batch-fabricated, millimeter-scale robotic systems.

# Chapter 4

# The Robot Pebbles

## 4.1 Introduction

This chapter describes the first of the two new modular robotics platforms constructed as part of this work, which my collaborator Kyle Gilpin and I call the "Robot Pebbles." [1] [33]

The Pebbles are a two dimensional, lattice-type system. The modules are cubes and pack a square grid. Each cube has four mating faces, each with a custom-designed electropermanent magnet connector to allow it to draw in a nearby module, mechanically bond to it, communicate, and transfer power. The electropermanent magnet connectors, which we cover in detail in Chapter 3, only require power to switch between holding states, and otherwise dissipate zero power. Figure 4-1 shows a pile of Pebbles, plus the unfolded printed circuit and internal components.

The Pebbles can self-reconfigure in one of two ways. In self-assembly mode, the nodes are placed on a shaker-table and vibrated. One node, called the seed node, is externally powered and programmed with the desired shape. When a node is agitated into magnet range of the seed node on a face where the structure needs to grow, the seed node can pull in the node and make it part of the structure. The new node powers up, learns the plan, and assists in the construction. The shape grows over

[1] During its initial development, this system was called "Smart Sand." However, it turns out that geologists do not call something "sand" unless its particles are below 2 mm in diameter, so we decided to save that name for a future system and call this system the "Pebbles" instead.

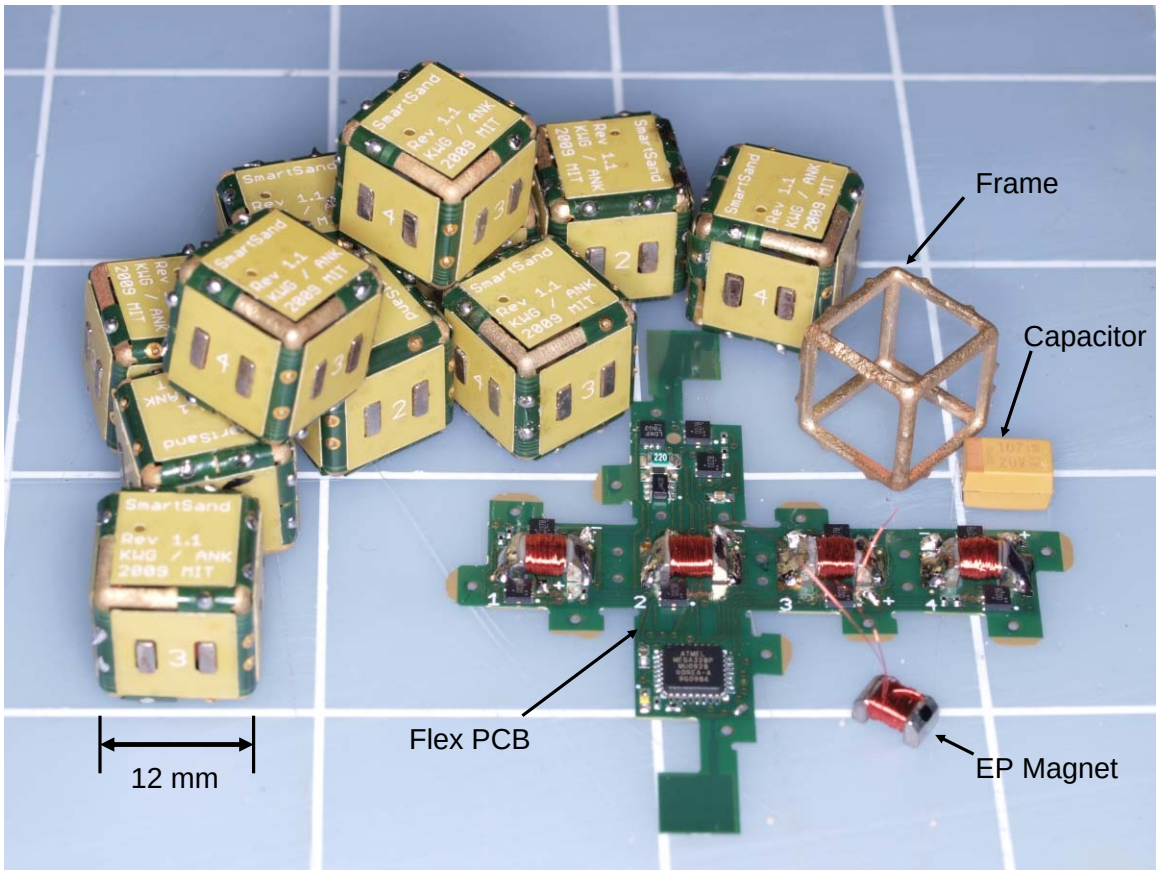


Figure 4-1: The Robot Pebbles are fully printed-circuit integrated, solid-state programmable matter. All of the components, including the four electropermanent magnet connectors, are soldered to a flexible printed circuit board. The printed circuit is then wrapped around and soldered to the frame.

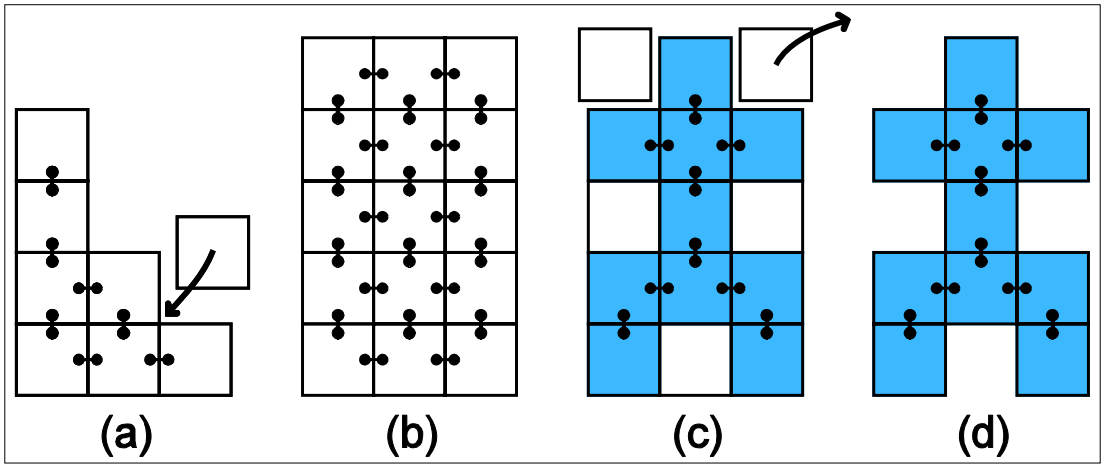


Figure 4-2: Reconfiguration algorithm used by the Pebbles. On a shaker table, the Pebbles draw in nodes from the environment (a) to form a rectangular block (b). The system then releases the extra nodes (c) revealing the final structure. (d)

time until finished, and can then be removed from the shaker table.

In self-disassembly mode, the nodes start out in a square block. (The square block could be formed earlier by self-assembly.) The user inputs the desired shape. The system turns off the magnetic bonds between nodes that are not part of the desired structure. These nodes then fall away, by gravity or user agitation, leaving the desired shape.

The Robot Pebbles are a solid-state, all-electronic system, meaning that there are no moving parts. They are also a fully printed-circuit integrated system, made only of surface-mount electronic components, a flexible printed circuit board in the net of a cube, and a skeleton frame, which the board is wrapped around and affixed to by soldering.

Because we did not use any off-the-shelf mechanical components (e.g. motors, gears, bearings, standard connectors) or any batteries, the size of the node was limited only by the size of the smallest available off-the-shelf electronic components. To our knowledge, these 12 mm modules are the smallest of any modular robot in the published literature.

In the following sections, I will describe the design of the nodes and the connectors,

show the results of some unit tests on the modules, and finally show the results of some full-system self-reconfiguration experiments.

## 4.2 Module Design

### 4.2.1 Connector Design

The key enabling component for the Robot Pebbles is the electropermanent magnetic connector.

The electropermanent magnet connector is shown schematically in Figure 3-1, and in Figures 4-1, 4-4, and 4-6. Looking at Figure 4-6, it consists of two iron pole pieces (a) and (b), an Alnico magnet (c) and an NIB magnet (d). The rods are 1.6 mm in diameter and 3.2 mm long. The assembly is secured together with epoxy adhesive (f), and wrapped with a coil of 80 turns of 40 AWG copper wire (e).

The Alnico magnet and NIB magnet have the same remanence but greatly differing coercivity. A pulse of current through the coil will switch the magnetization of the Alnico magnet but leave the magnetization of the NIB magnet unchanged. A positive pulse magnetizes both magnets in the same direction, causing the flux to exit the device and turning the magnet "on." A negative pulse results in opposite magnetization, causing the flux to circulate inside the device, and turning the magnet "off." For a detailed magnetic circuit model of the electropermanent magnet, including design formulas, as well as materials and methods for constructing and testing these millimeter-scale electropermanent magnets, see Chapter 3.

The power supply bus voltage is 20 V. At this voltage, a $100\mu s$ square pulse, resulting in a peak current of 5 A, is sufficient to switch the magnet on or off. In the Pebbles, the required 5 mJ of energy for a pulse is supplied by a $100\mu F$ tantalum capacitor, also visible in the figures.

The connectors are arranged on the faces of the module as shown in Figure 4-3. The north and south poles align on each face, causing the modules to attract and hold to one another while the magnet is enabled. The arrangement is four-way rotation

symmetric, so a module can approach with any orientation.

When the connectors are mated, the magnetic force is primarily in a direction normal to the mating face. The connectors are also able to resist shear loads, although lesser in magnitude, due to static friction.

When mated, the connectors also serve as two-terminal electrical connectors to transfer power from module to module. Power is transmitted through simple ohmic conduction, using the iron poles of the magnet as contacts. Electrical connectors typically require a spring in order to achieve intimate contact; in this case, the spring is the compliance of the flex circuit on which the connector is mounted, and the magnetic force provides the preload. Because the permanent magnet materials are conductive, to ensure electrical isolation of the poles, we coated the two rods of permanent magnet material with $7\mu m$ of insulating Parylene before assembling the connectors.

In each module, the four north poles and the four south poles of the connectors are each bussed together. (See Figure 4-3) Between modules, north connects to south. This means that, if the north poles are electrically positive on one module, they will be electrically negative on its neighbor. The resulting power distribution grid looks like a checkerboard, with north positive on red squares, and south positive on black squares. Power to ground shorts are not possible because on the grid any closed path back to the same module involves an even number of polarity reversals. A full-wave bridge-rectifier inside each module converts the incoming power, which has unknown polarity, to a known polarity to power the module's electronics.

Communication between modules is by magnetic induction. The same electronics used to produce the drive pulses apply a sequence of $1\mu s$ pulses for communication. Through magnetic induction, these pulses result in a corresponding pulse in the neighboring node, which is detected using the microcontroller's built-in comparator. The system transmits data at 9600 baud, using on/off keying.

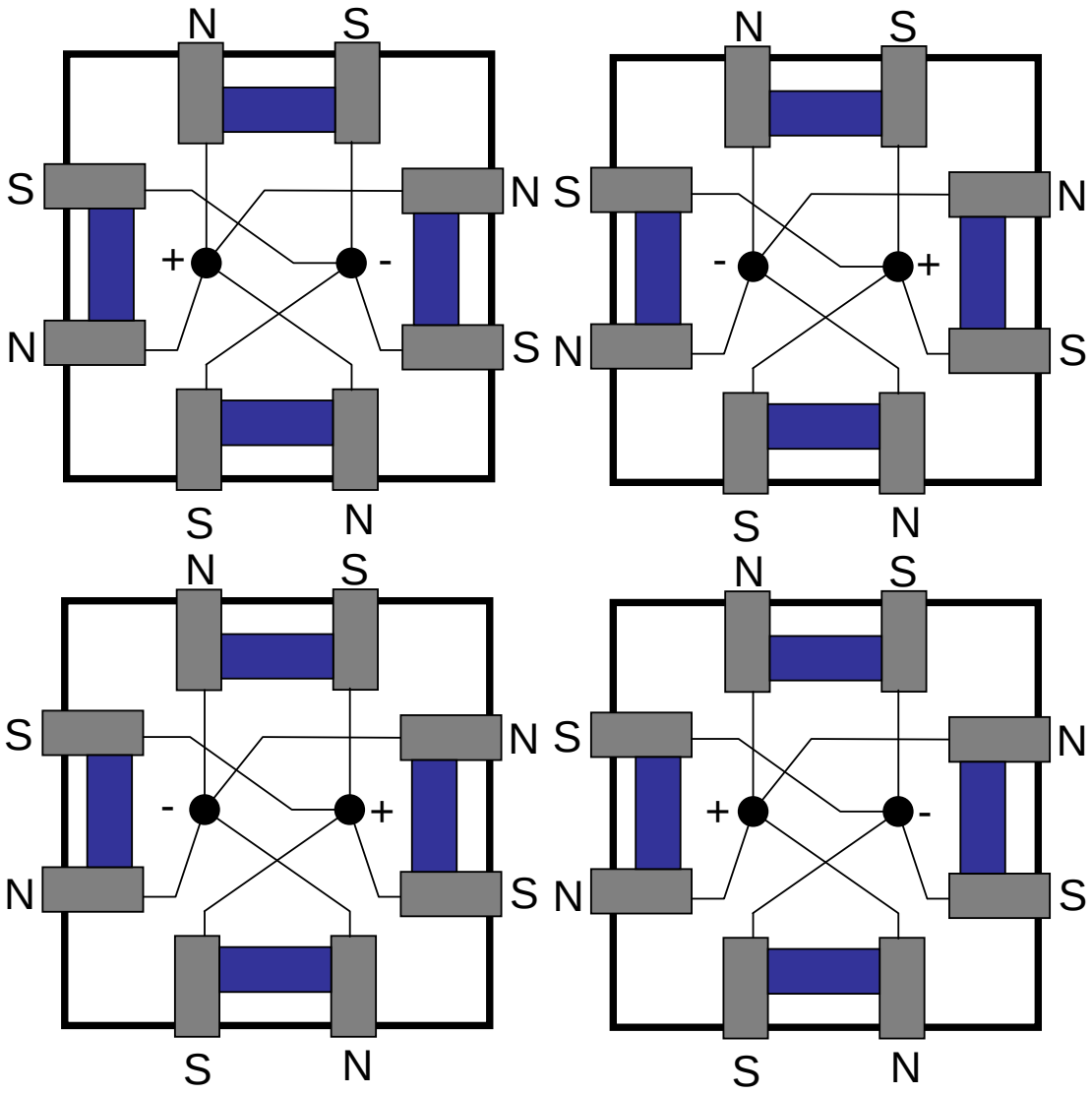


Figure 4-3: Arrangement of the connectors on the faces of the module. The north and south poles align on each face, so that the magnets attract. The arrangement is four-way rotation symmetric, so a module can mate from any of four possible orientations.

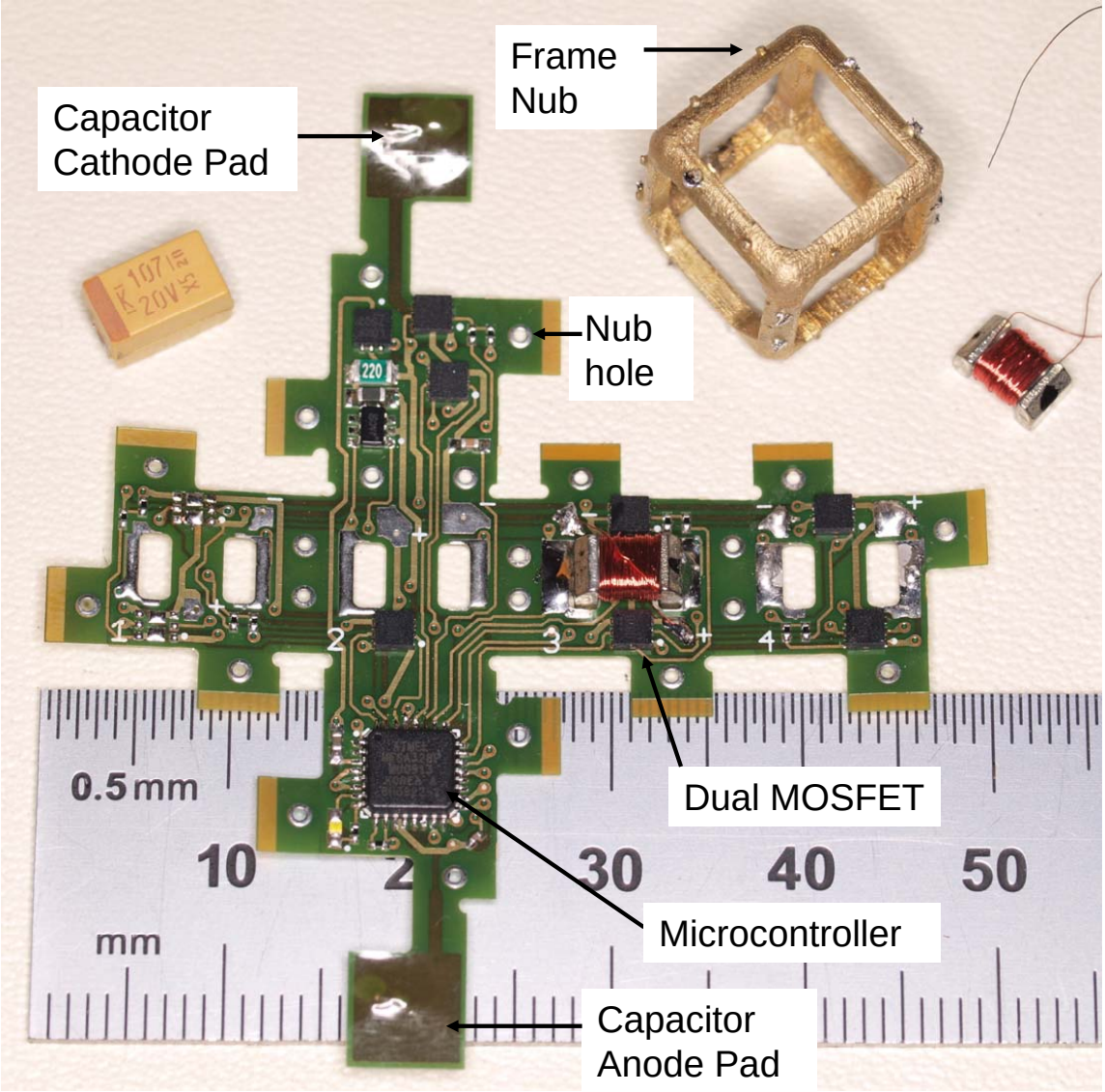


Figure 4-4: Pebble printed circuit. The electropermanent magnets are soldered to the flex PCB like the other components. The microcontroller is packaged in a 7 mm square TQFP, and the MOSFETS are packaged in 2 mm square DFN packages. The nubs on the frame are soldered to the holes on the PCB to complete the assembly.

### 4.2.2 Electronic Design

Figure 4-4 shows the pebble printed circuit. All of the logic and timing for reconfiguration, communication, and magnet drive is performed by an ATMEGA328 microcontroller. This is an 8-bit machine with 32K of program memory and 2K of data memory.

Power for the system is bussed through the electropermanent magnetic connector poles, as described in the previous section. This power is of uncertain polarity, depending on the node location, so it is first passed through a full-wave bridge rectifier (SDA006, Diodes, Inc.) and a 22 ohm current-limiting series resistor, which feeds the nodes +20V internal power rail. A linear regulator (LT3009, Linear Technology) steps down this voltage to provide +5V for the microcontroller.

A $100\mu F$, low ESR capacitor (B45197A, Kemet) is connected between the +20V rail and ground. It provides the 5 A peak current needed to switch the electropermanent magnets.

The drive and sense circuitry for the electropermanent magnetic connectors is shown schematically in Figure 4-5. The four electropermanent magnet coils require bidirectional drive, but only one needs to be switched on at any one time, so we are able to avoid building an H-bridge for each. One terminal from each electropermanent magnet is tied together onto a common bus. This bus can be driven with +20V or GND, or left floating, by one MOSFET half-bridge circuit. The other terminal of each electropermanent magnet is tied to its own half-bridge, so that it can be individually addressed.

The half-bridges are made from a push-pull pair of N-channel (FDMA2002, Fairchild) and P-channel (FDMA1027, Fairchild) power MOSFET transistors. The gate of the N-channel transistor is controlled by an I/O line from the microcontroller. The P-channel transistor gate needs to be switched between +20V (off) and +15V (on). The circuit shown, which uses a third N-channel MOSFET with a center-tapped resistive load provides this gate drive.

In order to receive messages from neighboring modules, the microcontroller needs

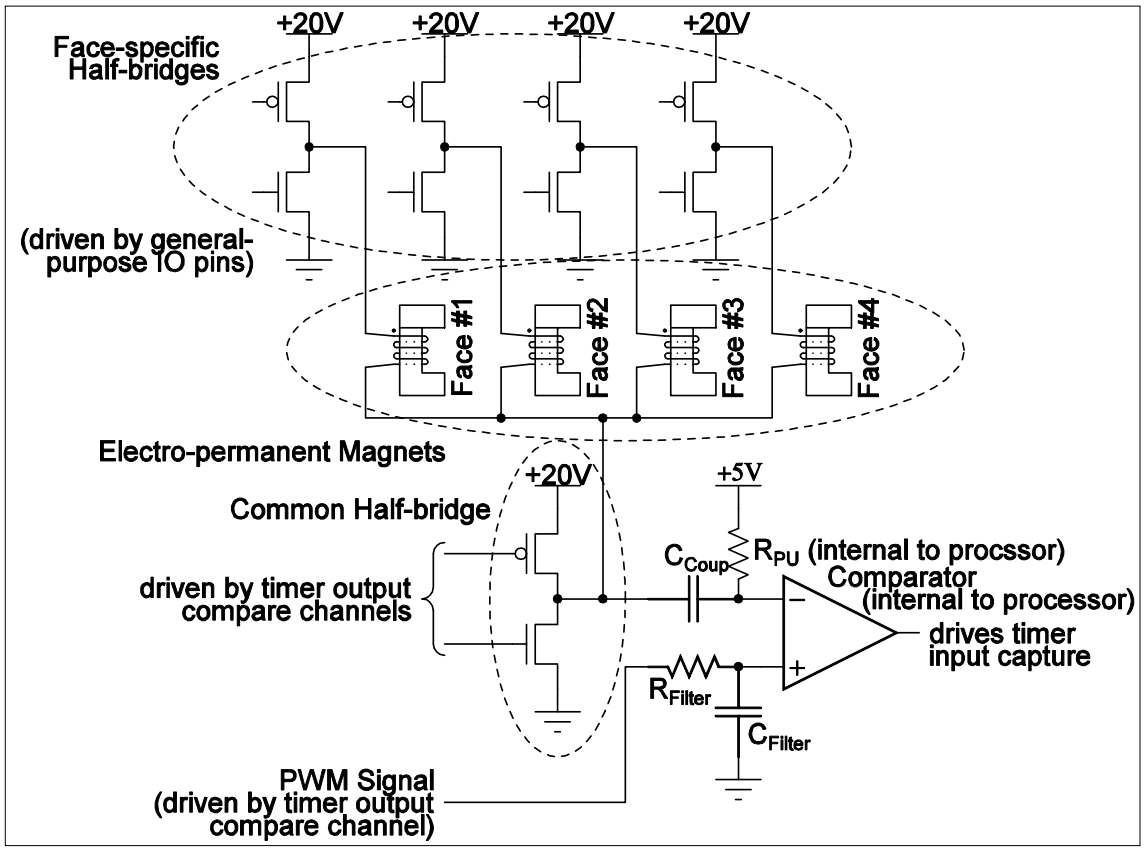


Figure 4-5: The circuit on each pebble, not including the microcontroller, power regulator, bridge rectifier, and energy storage capacitor.

to be able to detect pulses of induced voltage on the electropermanent magnet coils. To allow this, the common bus is connected to one terminal of the microcontroller's analog comparator through a high-pass RC filter. The other terminal serves as a DC voltage reference; it is connected to the output of a low-pass RC filter, which is driven by the microcontroller with a variable duty-cycle square wave to set the voltage threshold for communication pulse detection.

The module contains a white LED, driven by a microcontroller power pin, for user status updates.

### 4.2.3 Mechanical Design

The module printed circuits (Figure 4-4) are a two-layer Copper-on-Kapton flex circuits, with Kapton stiffeners on the cube faces. We populated them with components using automated pick-and-place assembly. In principle, it would be possible to design the electropermanent magnets for automated assembly, but for these prototypes, we soldered them in place by hand. We used a temporary spacer to make the ends of the magnet poles protrude from the frame by about 0.1 mm, to ensure good contact during mating.

Figure 4-6 shows a nearly assembled module, although missing one of its magnets for clarity. The skeleton frame (i) is fabricated from yellow brass by investment casting from 3D inkjet-printed positives. The frame has hemispherical nubs (j) on its edges; these mate with holes in the flex circuit to align the circuit with the frame. The nubs are hand-soldered to the pads on the flex circuit, so that the flex circuit can be removed by desoldering for repair or debugging. The energy storage capacitor (g) is the largest electronic component of the system, and does not fit on the board. Instead, it is mounted at center of the cube, between two flex-circuit tabs that protrude into the interior.

In the initial prototype, the tabs containing the frame mating holes would protrude at an angle. We solved this problem by adding a non-soldermask-coated, thin section ($25\mu m$) at the end of each tab; we then tuck this section under the adjacent face during assembly to secure the tab in place before soldering.

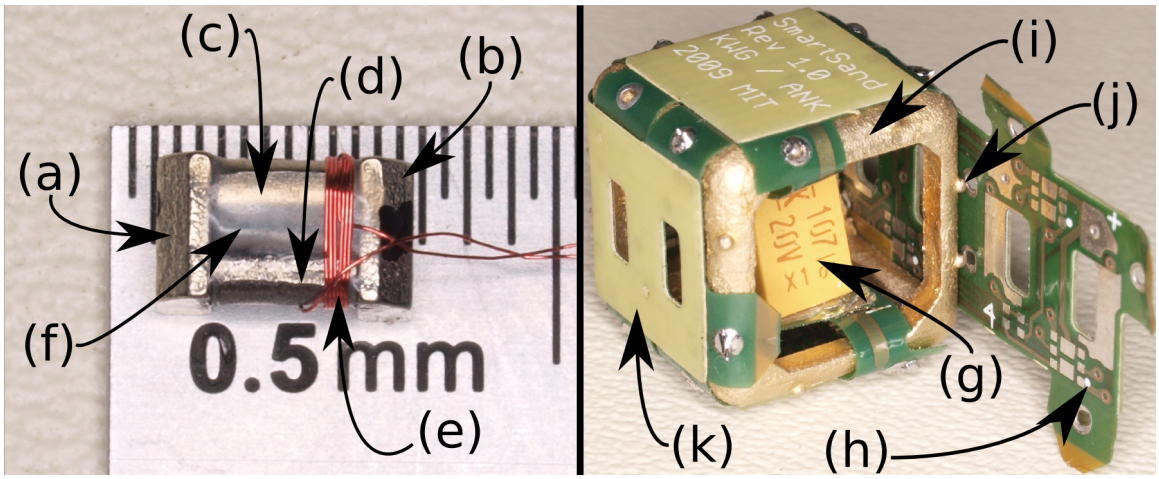


Figure 4-6: Partially disassembled view of a pebble. (Left) The electropermanent magnet connector, with most of the coil removed to show the permanent magnet rods. (Right) A pebble opened to show the mounting of the capacitor in the center of the cube, and the mating of the frame nubs with the flex circuit holes.

## 4.3 Results

### 4.3.1 Module Pair Latching Force

To compare the efficacy of different drive waveforms, we performed pull tests using two cubes. One cube was mounted on a linear motion stage, the other on an air bearing, with a load cell measuring the force along the allowed direction of motion. (For details about this experimental setup, see Section 3.4.2.) For each of the pull tests, the module attached to the motion stage is connected to an external power source through an attached magnetic connector. The linear stage is used to bring the modules together. When they come into contact, the second cube powers up, and the two exchange a synchronization message.

A representative sampling of the normal force after three different latching waveforms in shown in Figure 4-7. The average peak force, (over nine tests), for two asynchronous pulses, (one from each magnet), was 2.16N. When both magnets were pulsed synchronously, the resulting force was 2.06N (averaged over 15 tests). When both magnets were pulsed synchronously twice, the average peak force was 3.18N (averaged over 4 tests). In addition to the normal force required to separate two

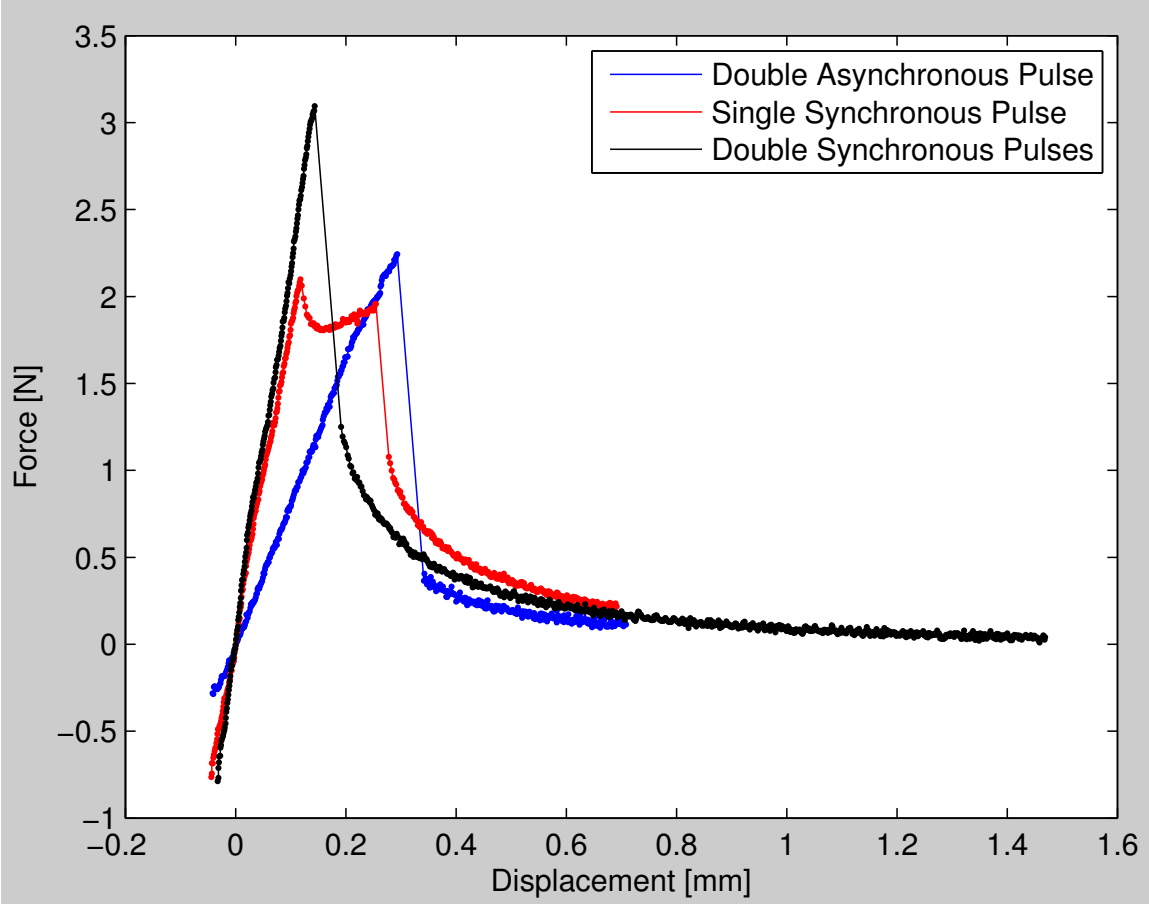


Figure 4-7: Force vs. displacement when two latched modules are pulled apart, using one of three switching waveforms. The modules have a mass of 4.0 g. The peak magnetic latching force, 3.2 N, could in principle support the weight of 82 modules. The modules stretch 1-3% before detaching when pulled. The weight of a single module can be supported from a distance of 1.4 mm, 12% of the module size.

cubes, we measured the shear force between two cubes using the same fixture. Five shear tests yielded forces of 0.22 to 0.83N with an average of 0.69N.

We also measured the normal force between the magnets after they had been switched off and it was zero to within the precision of apparatus. Holding the cubes in our hands and pushing them together, we can observe no tendency for the modules to hold together when the magnets are off. Any remnant force is certainly much less than the weight of a module.

All three traces show an initial linear rise in force with displacement, corresponding to the elastic deformation of the cubes in the fixture as they are pulled apart before the magnetic connectors separate. A peak is reached, and then the LED in the load-cell-side cube extinguishes, corresponding to separation of at least one pole of the connectors, and the force decreases as the air gap distance between the magnets increases. The distance over which the connectors remain in contact as the stage displacement increases, the distance from zero displacement until the peak force, provides a way to measure the tolerance to misalignment of the system. A large network of cubes is mechanically overconstrained, so one might be concerned about the ability to get reliable power transmission between modules, which requires continuous contact. From the data, one can see that a displacement between 0.14 to 0.30mm (1% to 3% of the total module size) is possible before separation, allowing a large network of cubes to achieve precision connector alignment through elastic averaging.[84]

In the single synchronized pulse experiments, (red line in Figure 4-7), we observed a plateau in force following the peak, before the rapid decrease. Observation was difficult, but it appeared that the plateau corresponds to a case where one pole of the connectors is still in contact while the other is separated.

After separation, there is a non-continuous jump in the data, which we have interpolated with a thin line. We suspect this is because, after the connectors are pulled apart, and the contact force stiffness has been removed from the system, the magnet pulls away and a new static equilibrium between the magnetic force and load cell stiffness is reached at an air gap distance greater than zero.

Figure 4-8 shows the coil current and voltage during a single synchronized pulse.

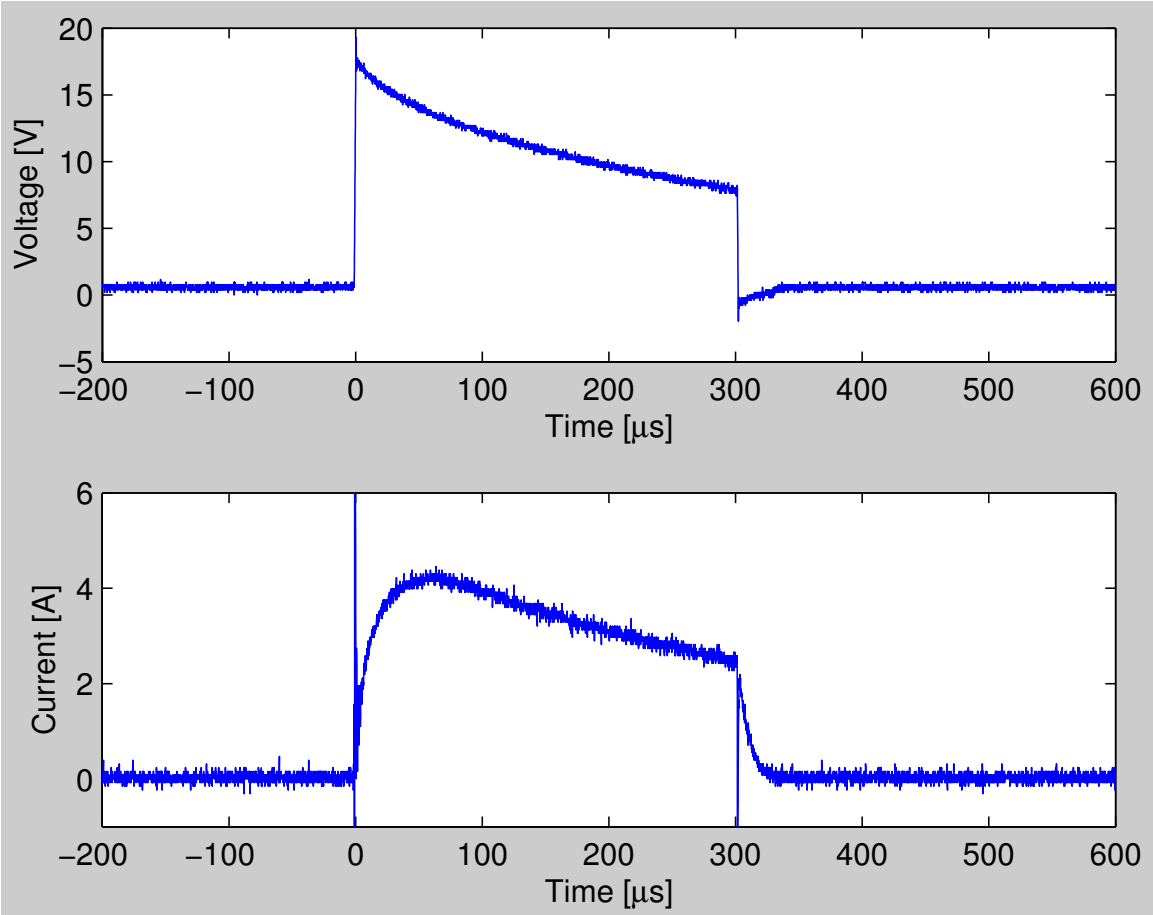


Figure 4-8: Voltage and current vs. time through the electropermanent magnet coil, driven with a $300\mu s$ pulse from the $100\mu F$ module energy storage capacitor. The peak magnetizing current of 4.2 A is reached after $60\mu s$.

The current reaches a momentary peak and then decreases during the pulse, indicating that the magnetic material is not saturating during the pulse, but that the peak current is instead limited by the discharge of the capacitor. This was the inspiration for the double synchronous pulse, which energizes the coils a second time after waiting for the capacitor to recharge, and as Figure 4-7 shows, does result in a larger force. The force measured for the double synchronous pulse is 73% of the 4.4 N peak force measured in the experiment shown in Figure 3-13, where a single electropermanent magnet was pulled away from an iron plate, a stiff power supply was used, and full saturation of the magnetic material was achieved.

### 4.3.2 Power Transfer

The magnets were strong enough to achieve intimate contact between the two poles of the electrical connector, and the connectors reliably transferred power between modules. The connectors tolerated misalignments of about 1 mm and continued to operate. Sometimes we observed visually that, in a lattice of modules, at least one of the connectors was not in physical contact. However, this did not matter operationally, because the node would still received power from a connector on another face.

We assembled a 3 x 4 block of Pebbles and measured the electrical resistance between each neighboring pair of modules using an ohmmeter. The results are shown in Figure 4-9. The average resistance was 0.3$\Omega$. The Pebbles draw about 11 mA from the 20 V supply. Based on this, the power dissipation through each connection, for each Pebble served by that connection, is 27 $\mu$W. This is about 10,000 times less than the power used by the Pebble to power its microcontroller and LED, 220 mW.

There is a 22 $\Omega$ current-limiting resistor in series with the power input of each Pebble. After the magnet switching pulse, the capacitor is discharged to 8 V, and needs to recharge to 20V, resulting in a (calculated) peak current of 540 mA. At this current, 87 mW is dissipated in each connection through which the power flows, and the 11 W delivered to the Pebble.

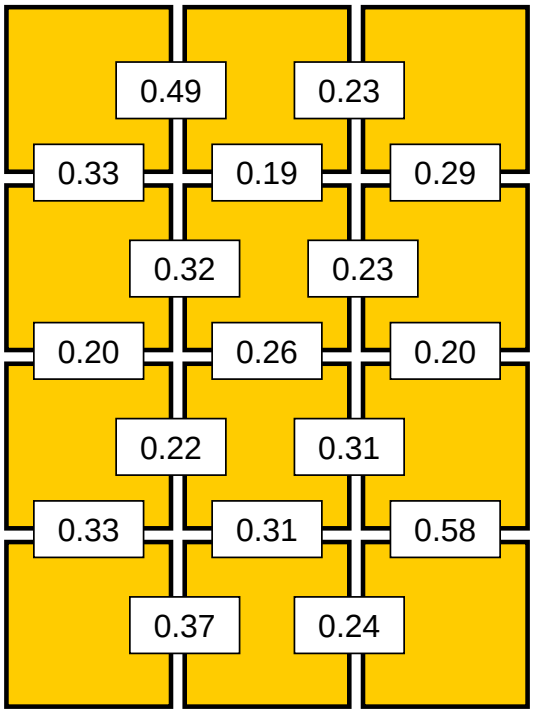


Figure 4-9: Electrical resistance of power connections in a block of Pebbles, in ohms, measured with an ohmmeter on a block of Pebbles. The mean resistance is 0.3Ω. For each connection though which the power for a Pebble travels, the $I^2R$ dissipation at 11mA is 27 $\mu$W. This is about 10,000 times less than the power used by the Pebble to power its microcontroller and LED, 220 mW.

### 4.3.3 Self-Disassembly Experiments

We manually constructed a 3x5 block of Pebbles then commanded the system to self-disassemble into a several shapes by selecting the Pebbles to remain in the structure using a graphical user interface. When we issued the disassemble command, the unselected Pebbles turned off their electropermanent magnets, disconnecting themselves from the structure. See Figure 4-10. In trials, the system formed the desired humanoid shape 23/25 times. The other times, it appeared that communication messages did not get through correctly. We tried several methods for removing the disconnected Pebbles, including placing the structure on a vibration table and tapping the side table; neither was sufficient to remove the Pebbles separating the arms and legs of the humanoid, which are surrounded on three sides. One method that did work was to simply pick up the structure and shake it manually; the disconnected Pebbles would then fall away.

### 4.3.4 Self-Assembly Experiments

We placed several Pebbles onto an inclined vibration table. The Pebbles slide down toward a powered root Pebble. Once a Pebble comes within magnet range, about 2mm, the magnets assist in drawing it in and aligning it. Once a Pebble makes contact, it receives power and switches on its own magnets. Through a combination of falling into a cluster and magnetic attraction, the Pebbles self-assemble into a square lattice. The self-assembled block of Pebbles can then be used as a block of raw material for shape formation by self-disassembly. Assembly of the 8 Pebbles took 5 seconds. The shaker table was inclined at $7^\circ$ to the horizontal in X and Y. See Figure 4-12.

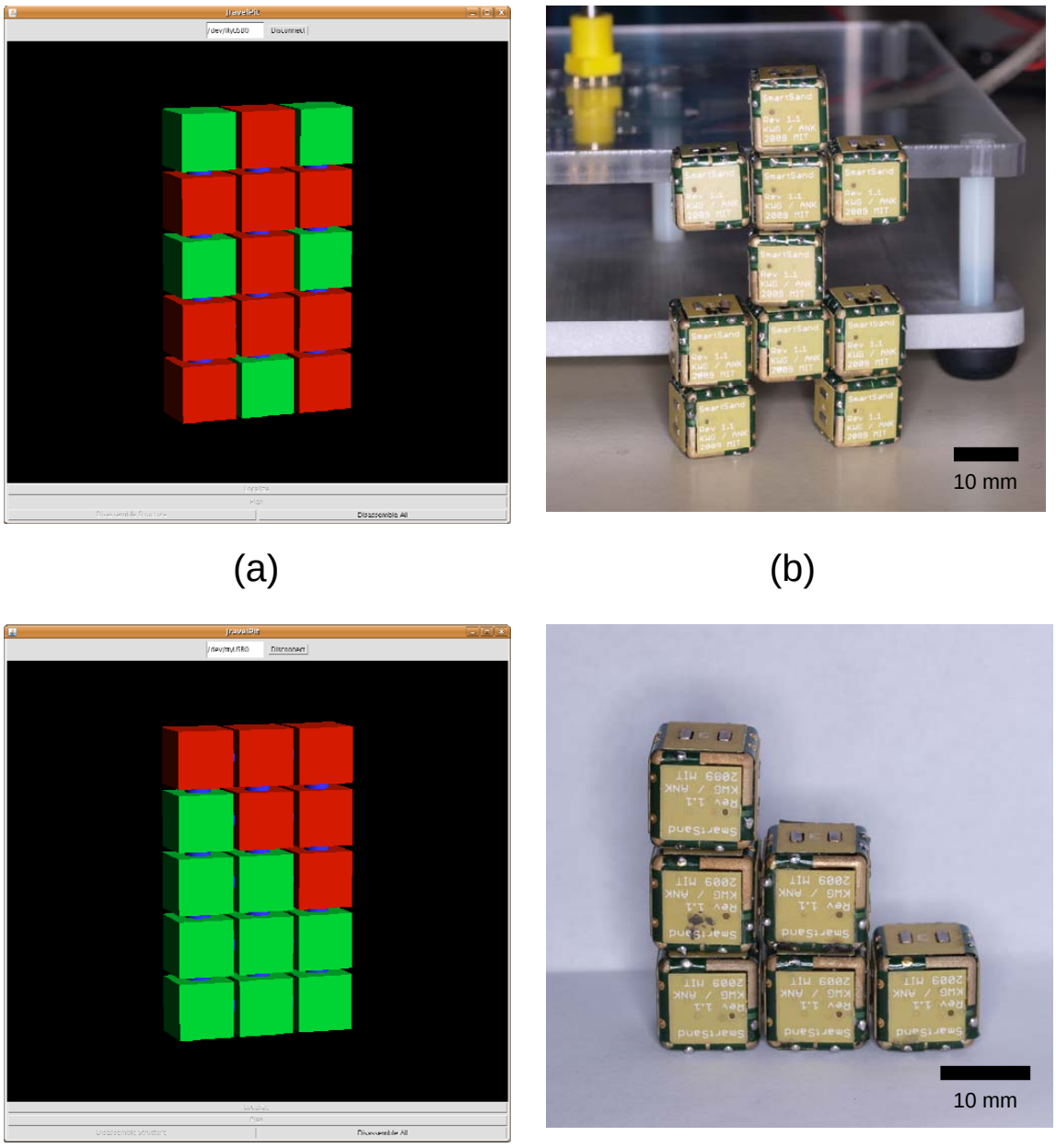


Figure 4-10: Self-disassembly experiments. (a) A humanoid drawn on-screen. (b) The resulting humanoid. (c) A triangle drawn on-screen. (d) The resulting triangle.


Figure 4-11: Experimental apparatus showing a humanoid after a completed disassembly trial. The clamp holds the root module in place onto a bed of pogo pins, which provide the root with power and a data connection to the PC.

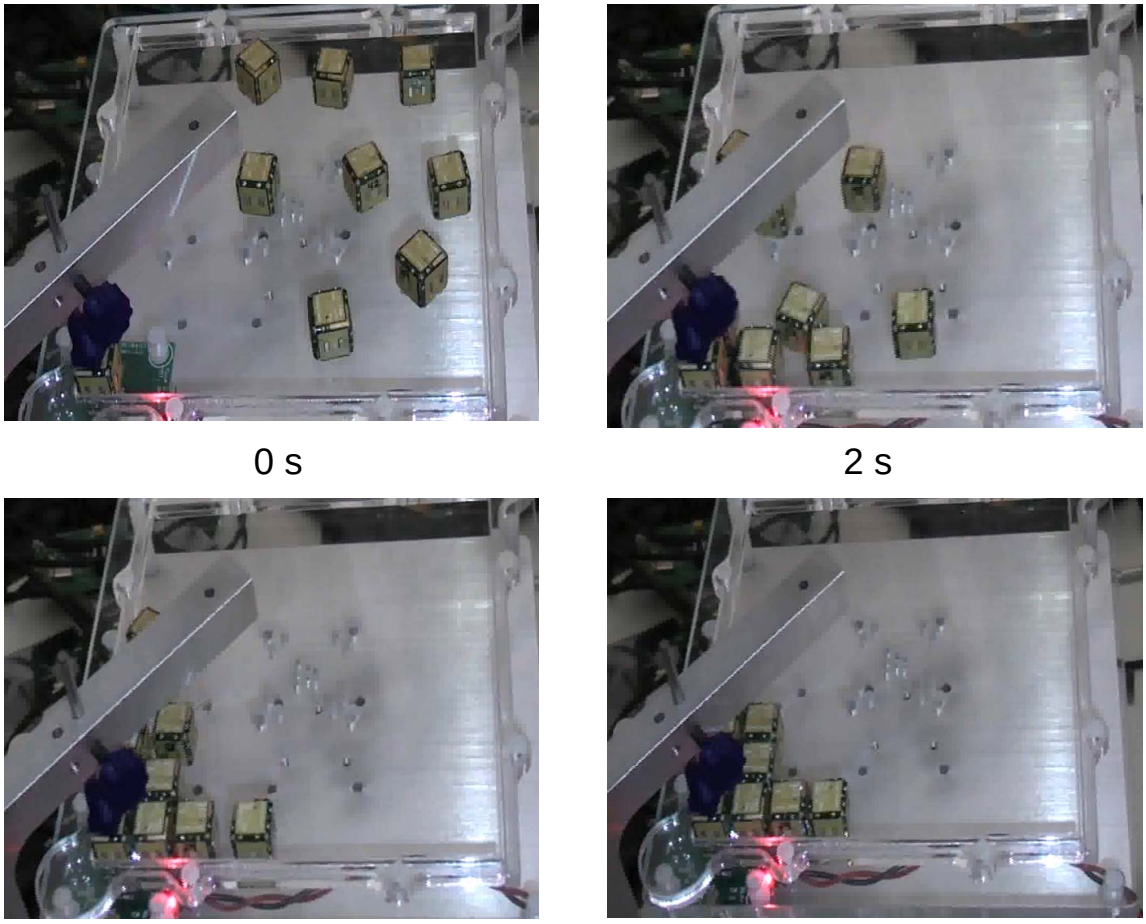


Figure 4-12: Self-assembly experiment. The Pebbles start out at random positions on an inclined vibration table, falling down toward a powered root node. Through a combination of falling into a cluster and magnetic attraction, the Pebbles self-assemble into a square lattice.

# Chapter 5

# Electropermanent Actuators

## 5.1 Introduction

Electropermanent magnets can do mechanical work. The switching pulse stores magnetic energy in the device and this energy is released as the magnet pulls on the load, until the system reaches mechanical equilibrium. The time for the release of the mechanical energy can be arbitrarily long and no electrical energy input is required during this period. The $I^2R$ losses are proportional to the work done. This remarkable characteristic leads to some major advantages for our new electropermanent motors over other magnetic motors: larger continuous torque, efficiency at low speeds, ability to operate without gearing in many applications, the ability to do work at high torque on an arbitrarily low source of electrical power, and zero-power holding. For the designer of a low-power, low-cost system, these are exciting capabilities.

Ordinary permanent-magnet motors exert torque proportional to the current; the constant of proportionality is the well-known torque constant. Electrical power input, lost as heat due to the DC resistance of the windings, is required to maintain this current and torque. At low enough speeds, the mechanical power output becomes insignificant compared to this $I^2R$ loss; so ordinary permanent-magnet motors require some minimum input of electrical power to maintain a given torque. In contrast, electropermanent motors have $I^2R$ losses only during the switching pulses, which become farther apart in time as the speed is reduced. Their $I^2R$ losses are instead

proportional to the work done, which means that electropermanent motors maintain efficiency at arbitrarily low speed, and thus can do work on a load, perhaps slowly, on an arbitrarily low source of electrical power.

The continuous torque rating of an ordinary magnetic motor is limited by heating due to the $I^2R$ losses to produce torque. In contrast, the continuous torque rating of an electropermanent motor is limited only by the saturation flux density of its magnetic materials; its self-heating at stall is zero. The continuous torque of electropermanent motors can be many times higher than an ordinary electromagnetic motor—and they run cold at this torque, whereas an ordinary motor runs at its heat dissipation limit. Because of their higher continuous torque and efficiency at low speed, electropermanent motors can be run without gearing for many applications.

Electropermanent motors are not for every application. Because they continuously cycle a magnetic material around its hysteresis loop, they are intrinsically dissipative devices. Later in the chapter, we prove that their efficiency is limited to 20%. This is better than other inherently dissipative actuators, such as shape memory alloys, which typically have efficiency below 1%. But it is not as good as a magnetic or piezoelectric motor run at its optimal operating speed, or than an electrostatic motor.

Electrostatic motors require high drive voltages, and have lower peak torque than magnetic motors, due to electrical breakdown limits. Magnetic motors 1-10 mm in size run most efficiently at speeds in range of 100,000 RPM. Effective utilization of their power in robotic systems requires a large gear ratio which is difficult to achieve in small systems. Piezoelectric motors are the closest competition to electropermanent motors and can achieve higher torque density. However, piezoelectric motors are also inherently dissipative devices, due to kinetic friction between the rotor and stator and due to hysteresis losses from rapid cycling of their ferroelectric materials. When operated away from their optimal, resonant speed, piezoelectric motors also incur losses that push their efficiency to zero in the low-speed limit.

In this chapter we will introduce a model to describe the flow of energy through electropermanent actuators and motors. We will give formulas for design, introduce the electropermanent stepper motor, and give experimental data on its performance.

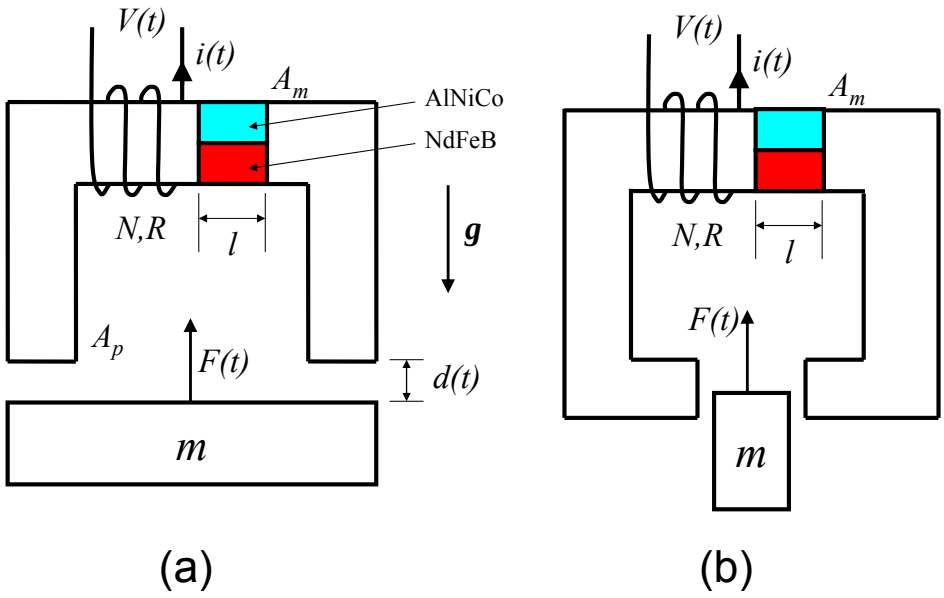


Figure 5-1: Electropermanent magnetic actuators: (a) gap-closing and (b) side-drive. An electrical pulse in the coil transfers energy to the permanent magnets and air gap, which then do mechanical work to accelerate and lift the bar.

## 5.2 The Electropermanent Power Cycle

Figure 5-1 shows two basic configurations of electropermanent actuator. Both are variable-reluctance actuators; the one on the left is a gap-closing actuator, the one on the right is a side-drive actuator. Unlike a standard magnetic actuator, a parallel electropermanent magnet has been placed in series with the flux path.

Like a heat engine, a electropermanent actuator is a cyclic energy conversion device, whose operation consists of a series of processes, repeated in sequence to do useful work. Probably the most famous thermodynamic power cycle is the Otto Cycle, which describes the operation of an internal combustion engine as a series of four processes: intake, compression, combustion, and exhaust. The power cycle for a heat engine is plotted on a PV (pressure-volume) diagram, the conjugate variables of its primary means of energy storage.

In Figure 5-2, we have plotted the power cycle of an electropermanent actuator on a BH (flux-field) diagram. The field H is the magnetic field intensity inside the permanent magnets, while the flux density B is the magnetic flux density in the air

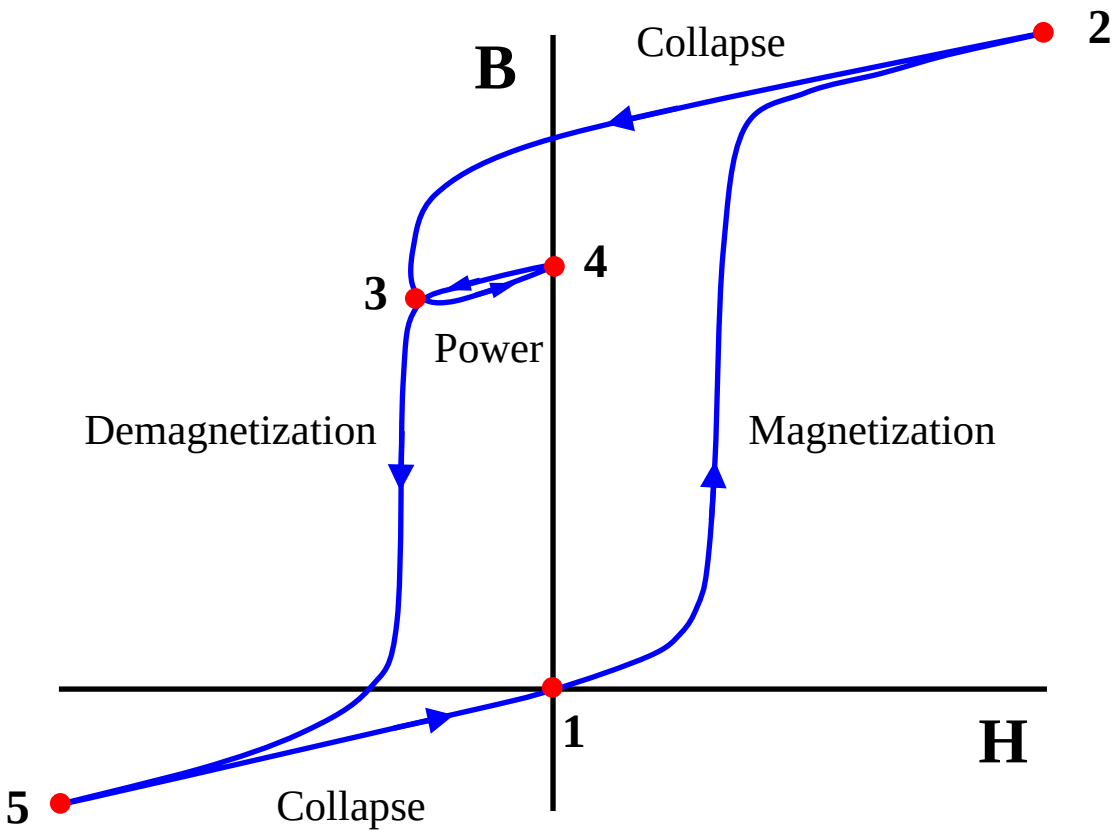


Figure 5-2: Electropermanent actuator thermodynamic power cycle.

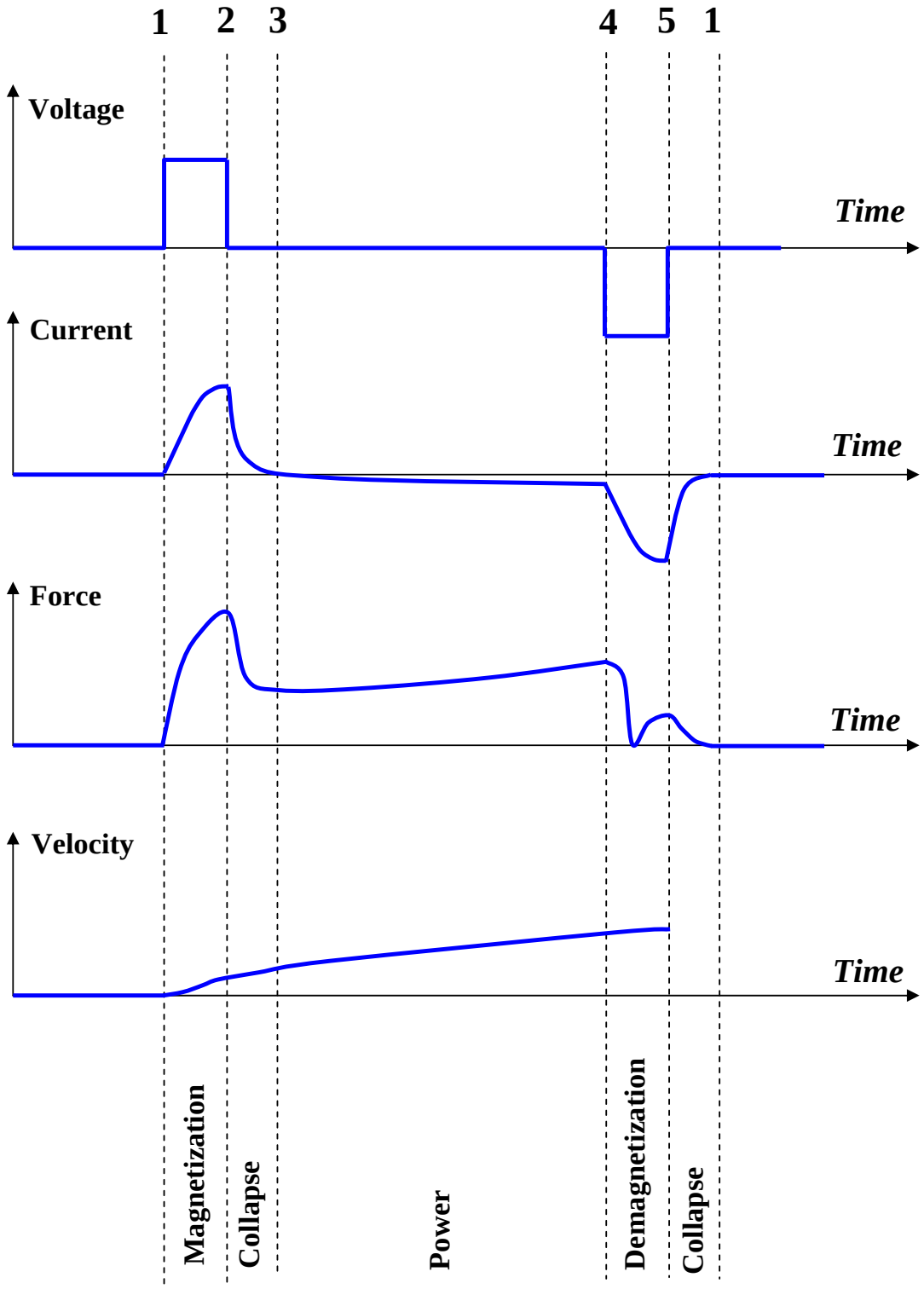


Figure 5-3: Electropermanent actuator power variables versus time.

gap. The conjugate variables of the electrical power input (voltage and current) and the mechanical power output (force and velocity) are plotted versus time in Figure 5-3.

The cycle starts at point 1, with the NIB magnet and the Alnico magnet oppositely magnetized, so that both the magnet field and air gap flux are zero. To begin the magnetization process, the drive circuit connects a voltage source to the coil, resulting in an increasing current and field. By the end of the magnetization pulse, the cycle has reached point 2.

At point 2, the magnetization pulse ends, and the system enters the collapse process. During the collapse process, the field in the permanent magnets undergoes a direction reversal, and the magnetic flux density decreases, until a new equilibrium between the permanent magnets and the air gap is reached. Once the system has reached point 3, the coil current is zero and the permanent magnets are supplying the field needed to overcome the reluctance of the air gap. The collapse process induces a voltage in the coil; if the coil is shorted, the collapse energy will be dissipated as heat.

At point 3, the power stroke begins. The magnetic flux exerts a force at the air gap, pulling it closed for a gap-closing actuator, or increasing its area for a side drive actuator; in either case reducing its reluctance and reducing the magnitude of the field. The state of the magnetic material proceeds along a recoil line from the magnetization curve toward point 4. Although mechanical work is done during every part of the cycle, the power stroke is typically much longer in duration than the other processes, so it is where the great majority of the work is done.

At point 4, once enough work has been extracted from the power stroke, the controller turns on the demagnetization pulse, which increases the magnitude of the field in the negative direction, driving the device toward point 5. This results in a direction reversal of the flux and field in the air gap, but still a positive force of attraction.

At point 5, the controller turns off the demagnetizing pulse, and the air gap flux and magnet field collapse back to zero. This sets the force to zero, allowing the power

stroke of another electropermanent actuator to return the air gap to its original size so the cycle can repeat from point 1.

This section has illustrated that an electropermanent actuator is a cyclic energy storage device, allowing the input of electrical energy on a short time scale, to allow for decreased $I^2R$ losses, and the output of mechanical energy on a longer time scale. In the next section, we describe the dynamics of power flow and energy storage in the device.

## 5.3 Electropermanent Actuator Dynamics

To examine the dynamics of energy flow through electropermanent actuators, we built a computer model of a gap-closing electropermanent actuator. The model is of the actuator shown in Figure 5-1 (a). The model uses a magnetic circuit approach, with a parallel-plate assumption for the air gap flux. It models the effects of coil resistance and $I^2R$ loss, the four-quadrant hysteresis behavior of the Alnico magnet, and the weight and inertia of the bar as it is lifted.

In this section, we first describe the model set-up, then show data from a run of the model. The model results illuminate the mechanism for power flow through the device, show which loss mechanisms are important during different parts of the cycle, and show the separation of time scales. It is remarkable to the author that, for the mm-scale devices constructed, electrical power is input at hundreds of watts for tens of microseconds, while mechanical power is output at hundreds of milliwatts for tens of milliseconds—a power and time transformation ratio of 1000:1. This ratio enables the high-force, low-power characteristic of electropermanent actuators, as compared to other electromagnetic actuators.

### 5.3.1 Model Set-Up

The model is a set of three ordinary differential equations. We solve the equations as an initial value problem in MATLAB using ODE45, which performs numerical integration using a Runge-Kutta method.

| Symbol | Parameter | Value | Unit. |
|---|---|---|---|
| $A_p$ | Air gap pole area | 4.8 | $mm^2$ |
| $A_m$ | Permanent magnet area | 2.4 | $mm^2$ |
| $N$ | Coil turns | 80 | |
| $R$ | Coil resistance | 3 | $\Omega$ |
| $l$ | Magnet length | 3.3 | mm |
| $m$ | Load mass | 300 | g |
| $g$ | Acceleration of gravity | 9.8 | N/kg |
| $B_r$ | NIB remnant flux density | 1.28 | T |
| $\mu_r$ | Alnico recoil permeability | 2.6 | |
| $V_0$ | Pulse voltage | 30 | V |
| $T$ | Pulse length | 60 | $\mu s$ |

Table 5.1: Input parameters of the model.

| Symbol | Variable | Initial Value | Unit. |
|---|---|---|---|
| $B_p$ | Air gap flux density | 0 | T |
| $d$ | Air gap length | 125 | $\mu m$ |
| $v$ | Air gap velocity | 0 | mm/s |

Table 5.2: State variable outputs of the model.

The state variables of the model, shown in Table 5.2, are the pole magnetic flux density $B_p$, the air gap length $d$, and the air gap closing velocity $v$. The input parameters and derived output variables of the model are shown in Tables 5.1 and 5.3.

The magnetic dynamics are described by Faraday's law of induction, combined with Ohm's law to model the effect of coil resistance.

$$\frac{d}{dt}B_p = \frac{V - IR}{A_p N} \tag{5.1}$$

The mechanical dynamics are described by Newton's law; the forces modeled are the magnetic force and the weight of the bar.

$$\frac{d}{dt}v = g - \frac{F_m}{m} \tag{5.2}$$

The final differential equation is simply the definition of velocity.

$$\frac{d}{dt}d = v \tag{5.3}$$

| Symbol | Variable | Unit. |
|---|---|---|
| $i$ | Coil current | A |
| $F_m$ | Magnetic force | N |
| $B_a$ | Alnico flux density | T |
| $B_n$ | NIB flux density | T |
| $H_a$ | Alnico field intensity | kA/m |
| $H_n$ | NIB field intensity | kA/m |
| $P_i$ | Electrical power input | W |
| $P_o$ | Mechanical power output | W |
| $P_l$ | $I^2R$ loss in coil | W |
| $P_m$ | Power flow into permanent magnets | W |
| $P_g$ | Power flow into air gap | W |

Table 5.3: Derived outputs of the model.

The magnetic force is computed using the Maxwell stress tensor expression for the air gap.

$$F_m = \frac{B_p^2 A_p}{\mu_0} \tag{5.4}$$

The current in the coil is computed using Ampere's law, with a path of integration through the Alnico magnet and the air gap.

$$I = \frac{H_a l}{N} + \frac{2dB_p}{\mu_0 N} \tag{5.5}$$

The Alnico and NIB magnets are in parallel and the same length, so they see the same magnetic field H, and their flux adds.

$$A_p B_p = A_m B_a(H_a, t) + A_m \left(B_r + \mu_0 H_a\right) \tag{5.6}$$

In the above equation we have written the Alnico magnetic flux as a function of the Alnico field and time. To compute the flux in the alnico magnet, we used experimental data from Campbell and Al-Murshid's paper "A model of anisotropic Alnico magnets for field computation." [11] We fit a 20th order polynomial to the up-switching and down-switching hysteresis curves, and used a linear model for excursions into the interior along recoil lines. The model function keeps track of the field direction-switching to select which curve to use. To compute the flux in NIB magnet, we used

the straight-line demagnetization curve from Fitzgerald. [1]

A major objective of the modeling is to visualize the flow of power through the device. The expressions for the electrical power input and $I^2R$ loss are particularly simple.

$$P_i = VI \tag{5.7}$$

$$P_l = I^2R \tag{5.8}$$

Because we want to accurately model hysteresis losses in the Alnico material, it is important to select an appropriate energy relationship. Since the material is dissipative, it is not correct to say that its magnetic energy density is $\boldsymbol{B} \cdot \boldsymbol{H}$. However, Haus and Melcher [40] show that the following relationship for magnetoquasistatic power flow into a fixed control volume follows from only Poynting's Theorem and Maxwell's Equations, with no assumption of linearity or energy conservation.

$$P_m = \int_V H \frac{dB}{dt} dV \tag{5.9}$$

Performing the integral and simplifying, we get

$$P_m = \frac{dB_p}{dt} A_p l H_a \tag{5.10}$$

The magnetic potential energy U stored in an air gap of volume V is

$$U = \int_V \frac{B^2}{2\mu_0} dV \tag{5.11}$$

So the power flow into the moving-boundary air gap control volume is

$$P_a = \frac{vA_pB_p^2 + 2dA_pB_p\frac{dB_p}{dt}}{\mu_0} \tag{5.12}$$

Finally, the mechanical power output, which goes into both accelerating and lifting the load, is

$$P_o = mv\frac{dv}{dt} - mgv \tag{5.13}$$

### 5.3.2 Model Results

Figures 5-4 through 5-8 show the results of the simulation, for the parameters in Table 5.1. These parameters were chosen to approximate those of our electropermanent stepper motor described in Section 5.7.

During the magnetization pulse, which lasts for 50 $\mu$s, power flows into the device as electrical current. A portion of this power is lost immediately to $I^2R$ heating, and the remainder flows into the permanent magnets and the air gap. Some of the power that flows into the permanent magnets is lost to hysteresis loss, and the remainder is stored. [1]

After the pulse ends, the collapse phase occurs over the next 10 $\mu$s. The magnetic field reverses direction, and some of the energy stored in the air gap and permanent magnets is lost to additional $I^2R$ heating. (A more advanced drive circuit might attempt to recover some of this energy.)

The power stroke lasts for roughly 15 ms. Note that this time is determined by the load; a heavier load results in less acceleration and so a longer power stroke. During the power stroke, power flows from the air gap to the load. A small amount of power flows from the permanent magnets and there is a small amount of $I^2R$ heating due to the changing magnetic flux linking the coil, but neither is significant. The induced voltage during the power stroke may be a useful input for control, as it provides a way to determine the progress of the power stroke.

The simulation stops when the air gap length reaches zero. In a real system, if the magnet was left on all the way to zero air gap length, there would be a collision and elastic losses at this point.

[1] Over a full cycle, the hysteresis loss is proportional to the area of the loop. The model presented here is in terms of magnetic power flow and not stored magnetic energy, so it does account for the hysteresis loss, although it does not indicate exactly when in time the hysteresis loss heating actually occurs. From thermodynamic considerations, we know that most of the heating must occur during the most irreversible processes of the cycle, which are magnetization and demagnetization.

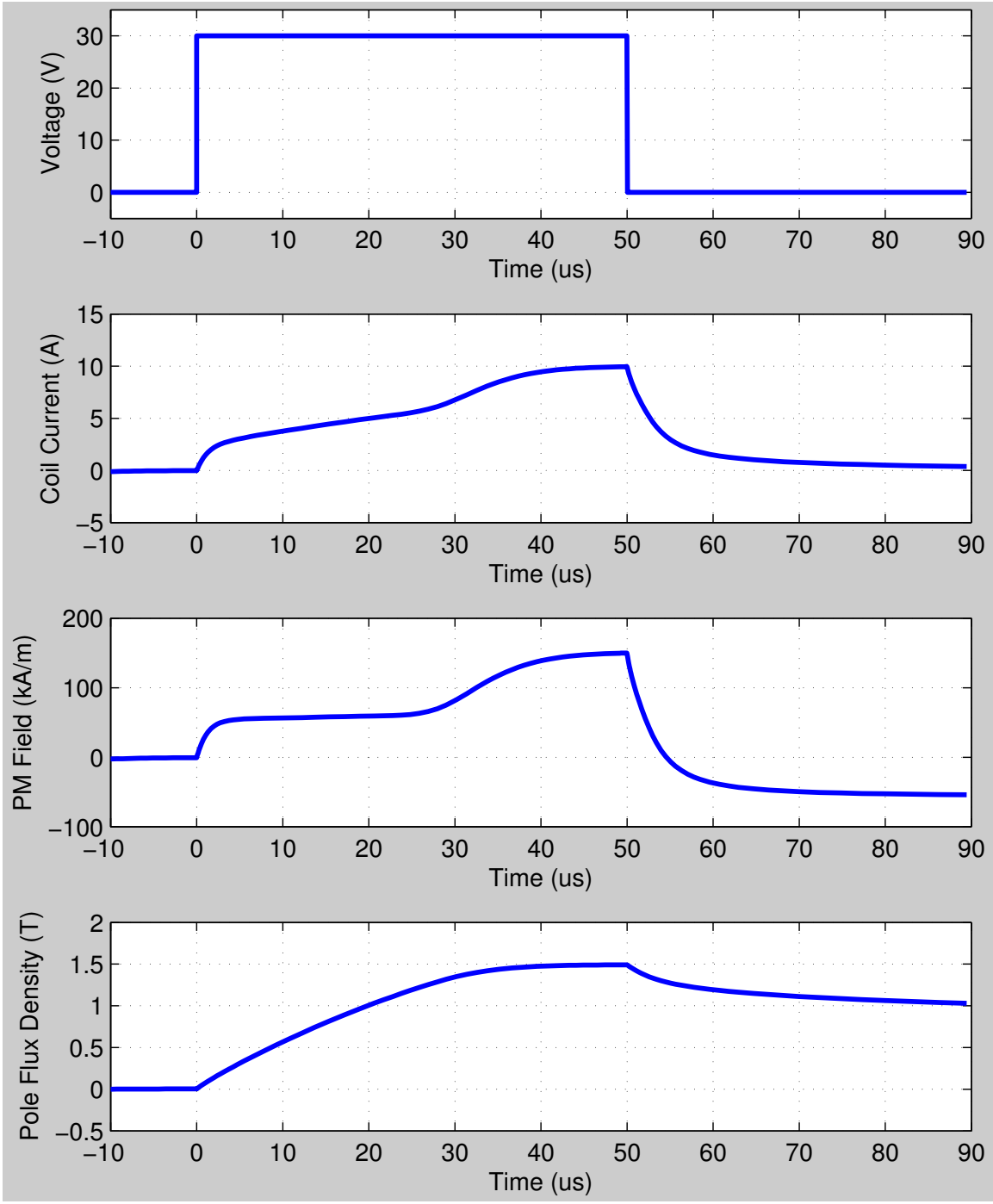


Figure 5-4: Actuator model results: electrical and magnetic power variables during the magnetization and collapse processes.

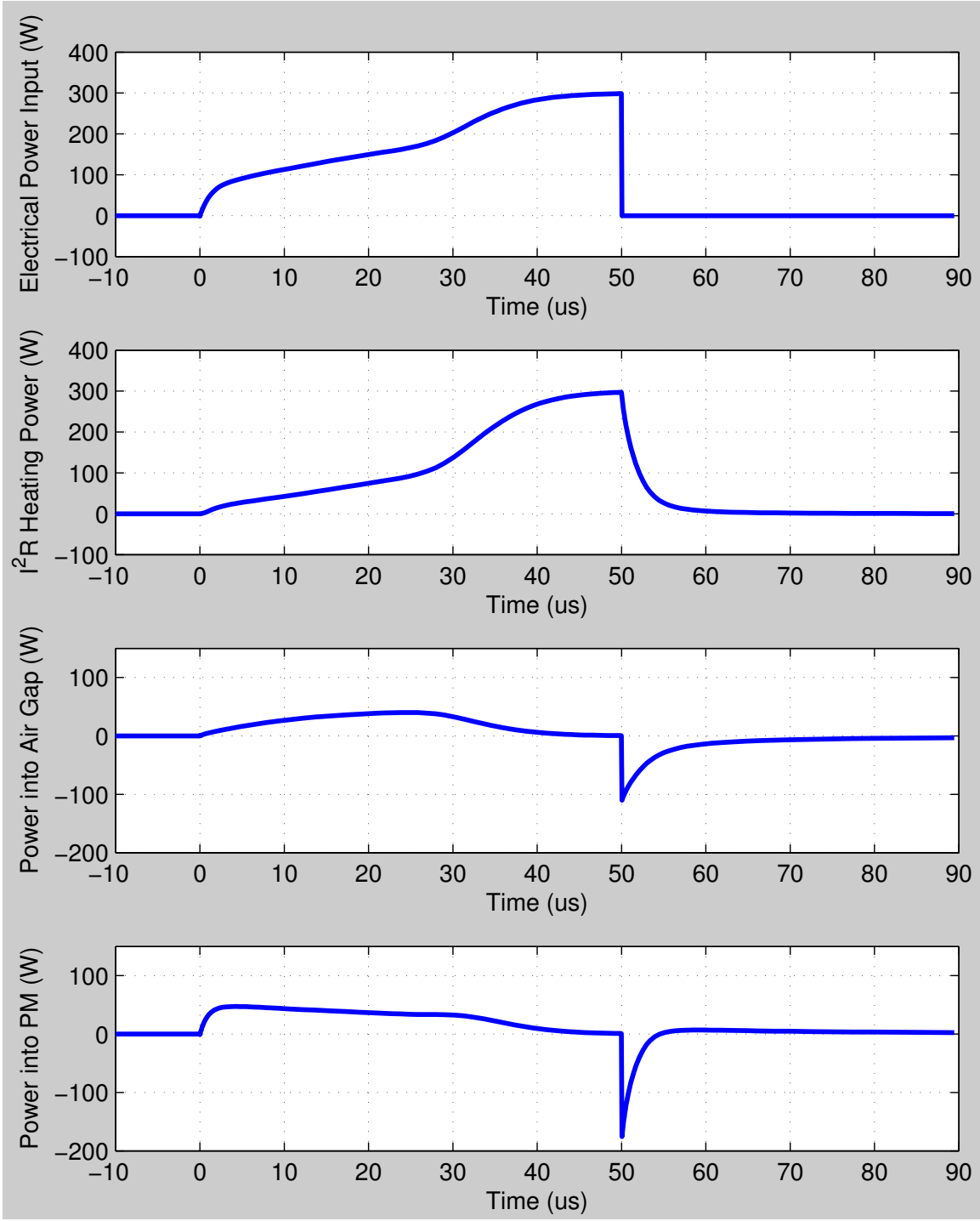


Figure 5-5: Actuator model results: power flow during magnetization and collapse.

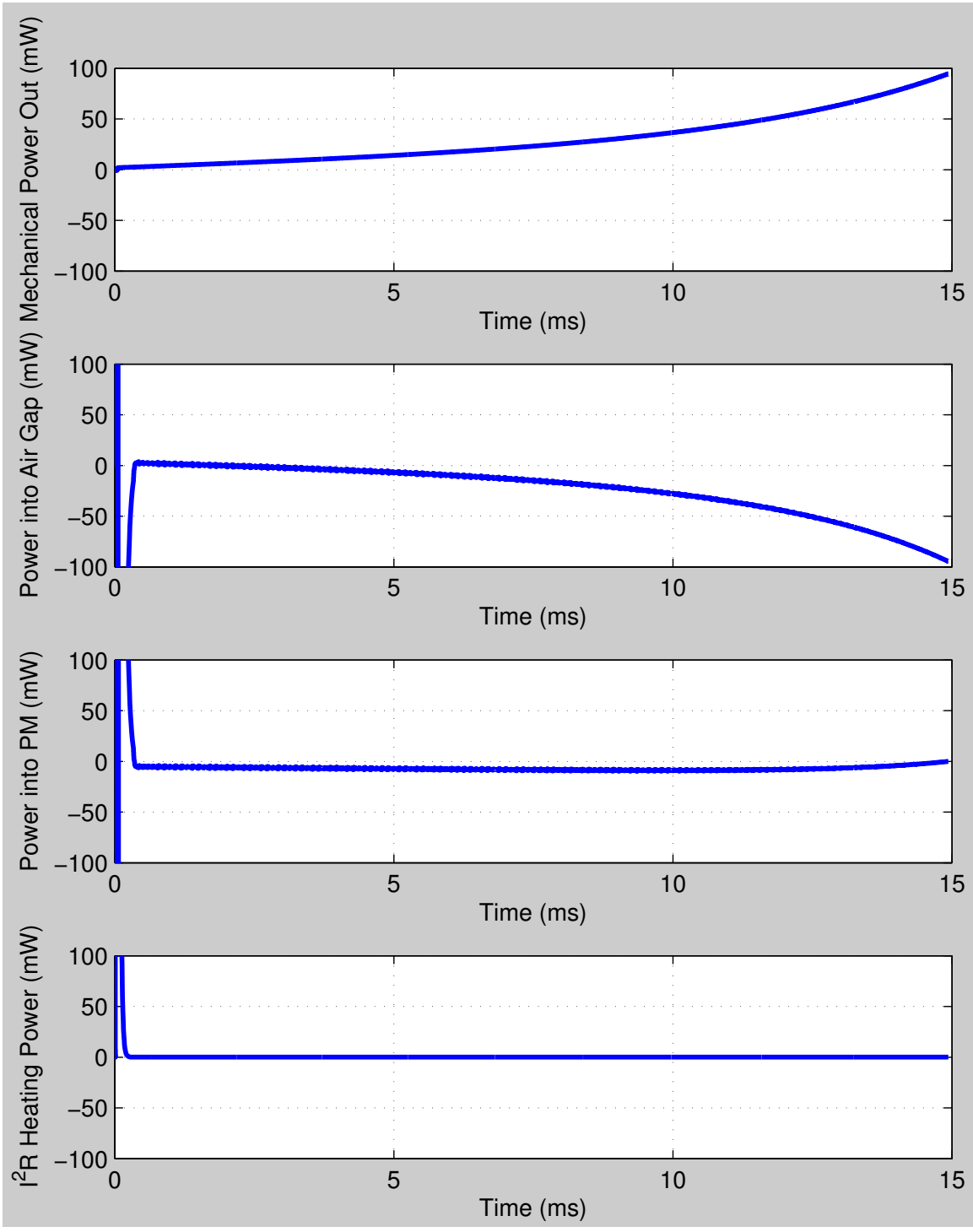


Figure 5-6: Actuator model results: power flow during the power stroke.

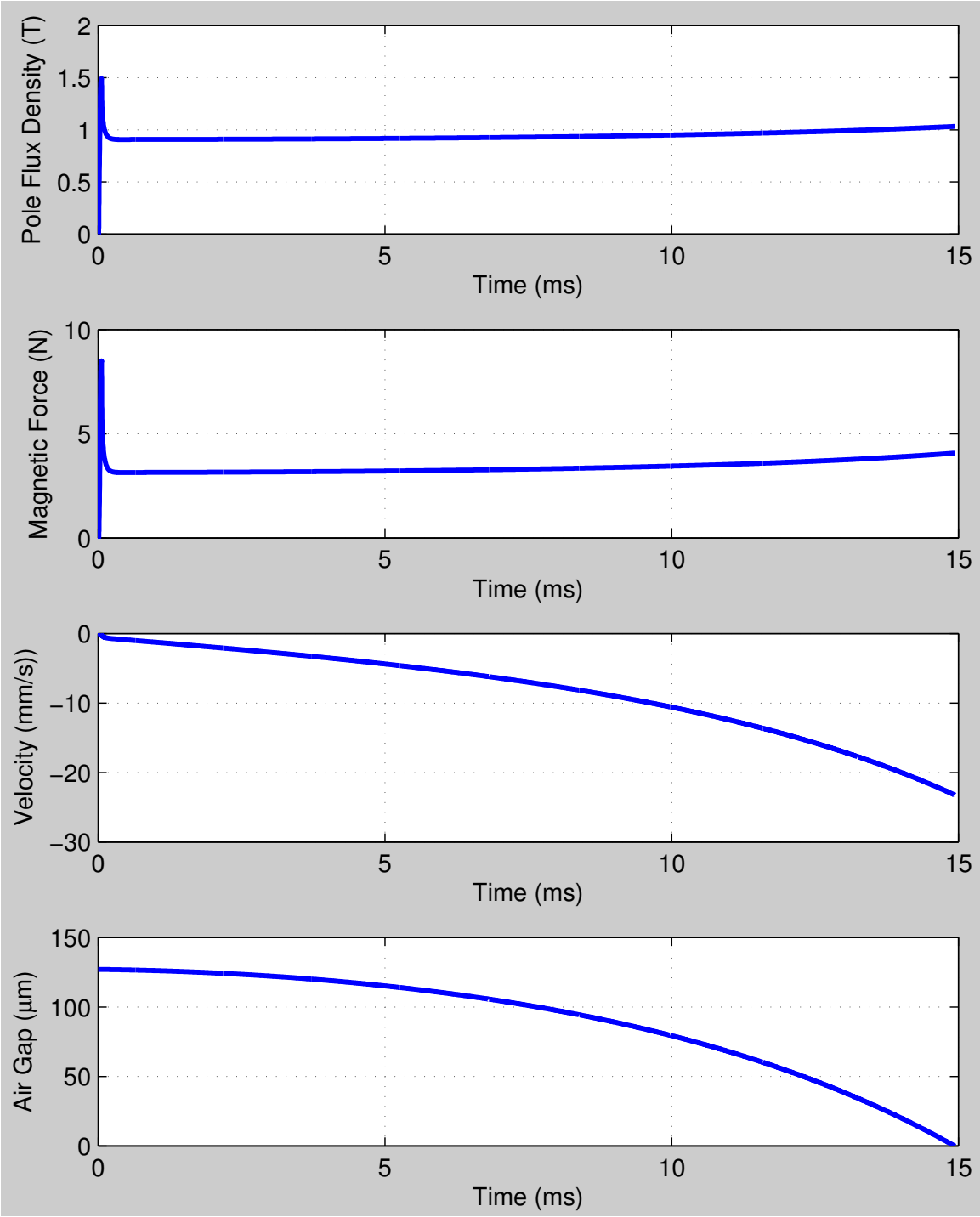


Figure 5-7: Actuator model results: mechanical variables.

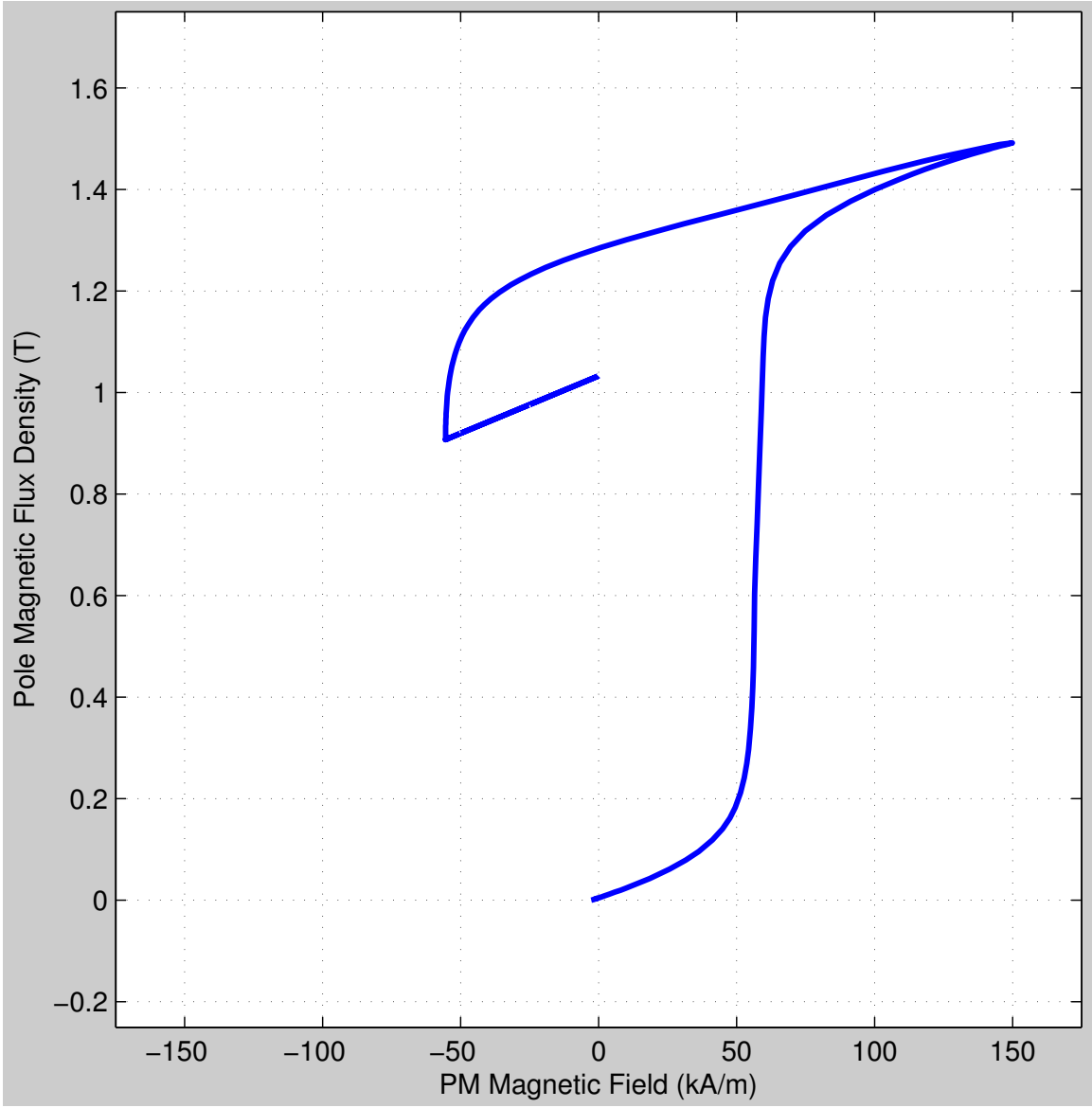


Figure 5-8: Actuator model results: BH diagram showing magnetization, collapse, and the power stroke.

## 5.4 Fundamental Limit on Efficiency

### 5.4.1 Loss Mechanisms in Electropermanent Actuators

The three major types of loss in an electropermanent actuator are $I^2R$ losses due to electrical resistance in the coil, hysteresis losses due to switching the magnetic field of the permanent magnet, and elastic losses due to collisions.

$I^2R$ losses can be reduced by decreasing the resistance of the coil by using larger wire. So then it is possible to trade reduced $I^2R$ losses for a reduced ratio of force to volume.

Elastic losses can be eliminated by using a motor topology that does not result in collisions, such as a side-drive motor with a bearing. Even in a gap-closing actuator, elastic losses can be reduced to zero by reducing the difference between the load force and actuator force.

Hysteresis losses in electropermanent actuators are fundamental to their operation and cannot be reduced beyond a certain limit. In this section, we present a proof, subject to certain assumptions and limitations, that hysteresis losses limit the efficiency of electropermanent actuators to 20%. This is not as bad as it might sound; many devices for direct-drive actuation, especially at small scale, have efficiency below 1%. It does mean that electropermanent actuators are likely to be useful for small-scale motion and control systems, rather than large-scale energy conversion application like automobiles or municipal water pumping.

### 5.4.2 Proof

Consider two electropermanent magnets from chapter 1, attached to a sliding shaft and configured back-to-back. By alternating turning the magnets on and off, the sliding shaft will execute a reciprocating motion. By using, for example, a slider-crank mechanism, useful work can be extracted from both directions of motion.

To compute the fundamental limit on electropermanent actuator efficiency, we can use idealized versions of the magnetic materials. For the semi-hard material we

use a rectangular-loop hysteresis model, with remanence $B_r$ and coercivity $H_c$. For the hard material we use a flat line at $B_r$, independent of magnetic field.

For a uniformly magnetized volume V of magnetic material, the energy lost to heat due to cycling around the hysteresis loop is proportional to the area of the hysteresis loop.

$$E_{loss} = V \oint \mathbf{HdB} \tag{5.14}$$

This relationship is attributed to Charles Proteus Steimetz. It is equal to the net energy flux into the material. Since the state of the material is the same at the beginning and end of the cycle, there can be no net change in the stored magnetic energy, so the net energy flux into the material over a cycle equals the heat loss. For a block of the idealized rectangular-loop semi-hard material, having area $A_{mag}$ and length $l_{mag}$, the hysteresis loss per cycle is

$$E_{hyst} = 4B_r H_c A_{mag} l_{mag} \tag{5.15}$$

The force on the reciprocating shaft during the power stroke, from the Maxwell Stress Tensor evaluated across the two air gaps, each with area $A_{gap}$, is

$$F = \frac{B_{gap}^2 A_{gap}}{\mu_0}; \tag{5.16}$$

From Gauss's law for magnetic fields, we have

$$B_{gap} A_{gap} = 2B_{mag} A_{mag} \tag{5.17}$$

where the factor of two is because the magnetic flux from the hard and semi-hard materials add. The maximum length of the gap $l_{gap}$ is limited by the length and coercivity of the semi-hard material. At the edges of the rectangular loop, where the magnetic material sees field $H_c$, from Ampere's law we see that

$$\frac{B_{gap}}{\mu_0} 2l_{gap} = H_c l_{mag} \tag{5.18}$$

The work done on the reciprocating shaft during each half-cycle of the shaft is

$$W = Fl_{gap} \tag{5.19}$$

Combining Equations 5.16, 5.17, and 5.18, all of the dependence on the geometry of the gap cancels out and we see that the work done has the same form as the hysteresis loss.

$$W = B_r H_c A_{mag} l_{mag} \tag{5.20}$$

Examining the expressions for $E_{loss}$ and W, we see that for every unit W of work, there are four units of dissipation; thus the energy efficiency of an electropermanent actuator with a rectangular-loop hysteresis material and no resistive loss is exactly 20%.

$$\eta = \frac{W}{W + E_{hyst}} = \frac{B_r H_c A_{mag} l_{mag}}{5 B_r H_c A_{mag} l_{mag}} = 20\% \tag{5.21}$$

To summarize the analysis up to this point, the work done is proportional to the area of the hysteresis loop in the second quadrant, while the hysteresis loss is proportional to the area of the whole hysteresis loop. Any real hysteresis loop will have a positive slope and will have additional area in the 1st and 3rd quadrant tails. So the 20% figure constitutes an upper limit on the achievable efficiency on an electropermanent actuator.

## 5.5 Characterization Data for an Electropermanent Actuator

Using the experimental set-up described in Section 3.4.2, we collected force versus displacement and voltage and current versus time data for an electropermanent magnet of the type described in Chapter 3 using Alnico 5 as the semi-hard material and Nd-Fe-B as the hard material. Figure 5-11 shows the energy efficiency, computed by dividing the work done by the energy input for two pulses.

To compute the work done, we numerically evaluated the integral

$$W = \int F dx \tag{5.22}$$

To compute the electrical energy input, we evaluated the integral

$$E_{in} = \int VIdt \tag{5.23}$$

To separate out the effects of hysteresis loss from $I^2R$ losses in the windings, we computed the electrical energy input not due to resistive loss, by subtracting out the resistive loss using the known winding resistance R.

$$E_{in-notR} = \int VI - I^2Rdt \tag{5.24}$$

Figure 5-9 below shows the measured electrical energy input for a single pulse and the portion of this due to $I^2R$ loss. Figure 5-10 shows the measured output mechanical energy.

For the case without resistive loss, we can see that the energy efficiency is roughly constant at 20%. The two data points for $10\mu s$ pulses are at 30.2% and 32%; the location of these points is very sensitive to the zero voltage, zero current, and zero force baseline location. We believe they are due to an offset error in the instruments.

For the case including resistive loss, the efficiency is about 14% for $20\mu s$ pulses, and decreases roughly linearly. When the material saturates with $100\mu s$ pulses, the efficiency is 6%.

## 5.6 Permanent-Magnet Motors at the Low-Speed Limit

Any motor that requires steady electrical power input to produce torque has zero efficiency at zero speed, because it requires electrical power input but produces no work. In the case of magnetic motors, in the stalled condition, 100% of the input

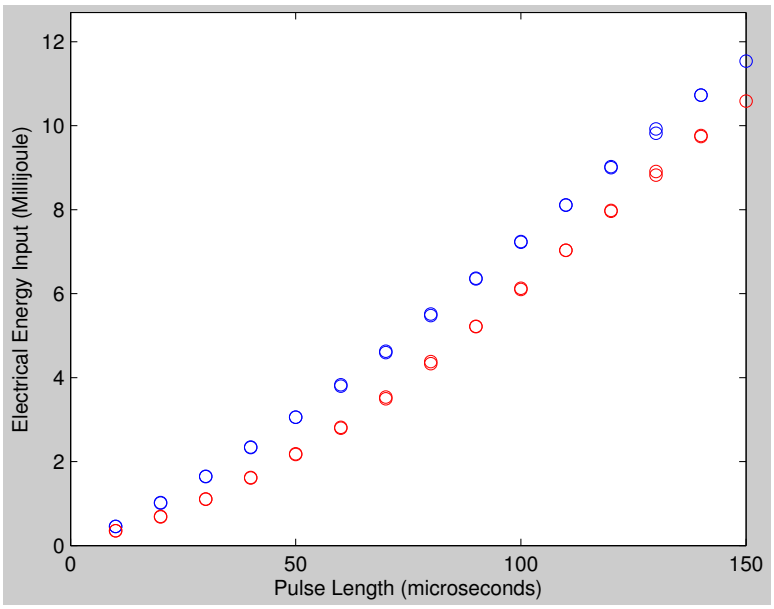


Figure 5-9: Electropermanent actuator electrical pulse energy vs. pulse length. Blue dots are the measured electrical pulse energy, $\int VIdt$ over the pulse. Red dots are the $I^2R$ dissipation, $\int I^2Rdt$, using a value of R measured using an ohmmeter.

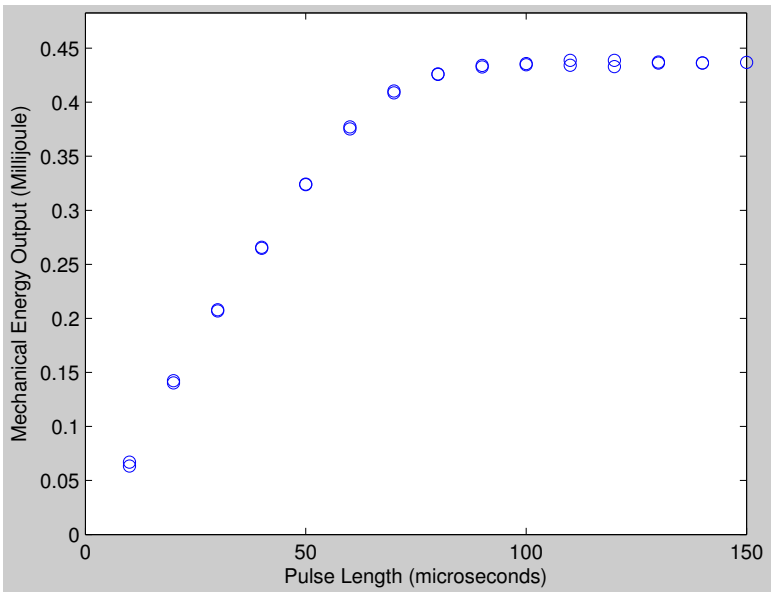


Figure 5-10: Electropermanent actuator efficiency vs. pulse length. The mechanical work is numerically integrated from the measured force and displacement data, $\int Fdx$. These plots are for a magnet slowly pulled away from an iron plate.

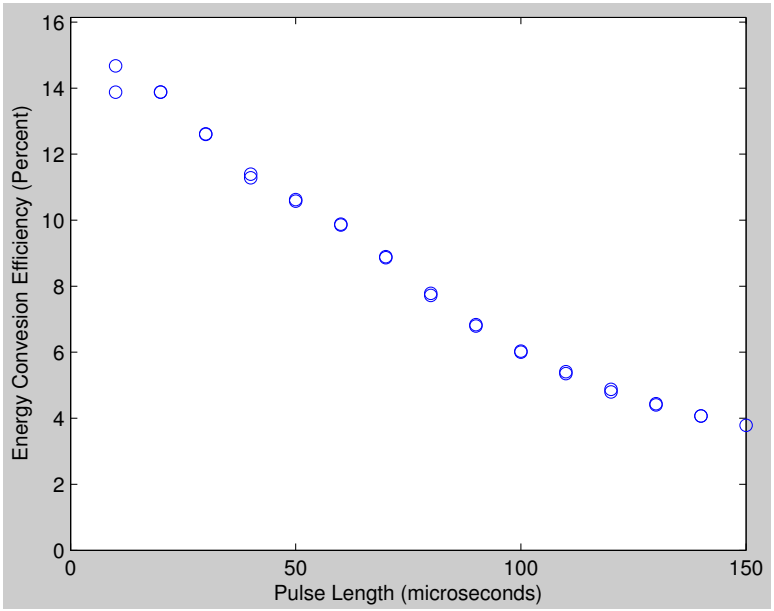


Figure 5-11: Electropermanent actuator efficiency vs. pulse length. The efficiency is the total mechanical work divided by the electrical energy in two switching pulses.

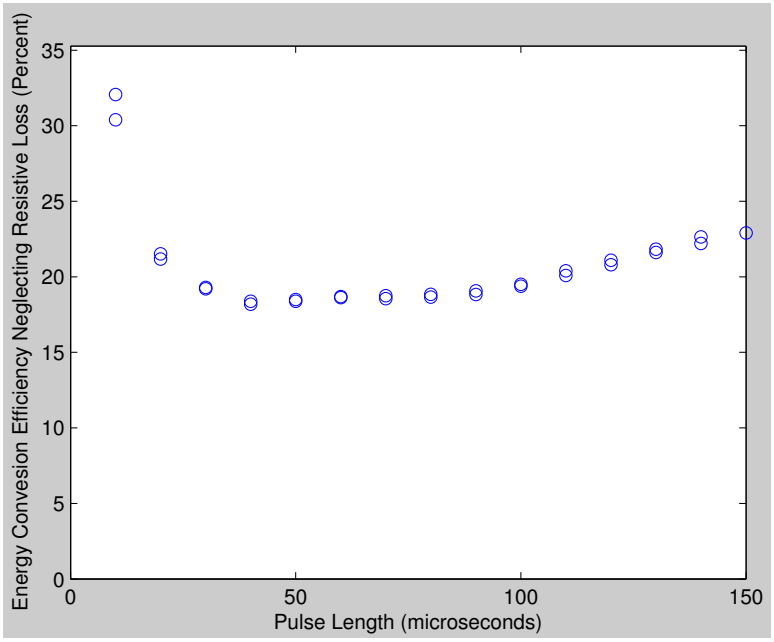


Figure 5-12: Electropermanent actuator efficiency after subtracting $I^2R$ loss. The efficiency is the total mechanical work divided by the electrical energy in two switching pulses after subtracting $I^2R$ losses using the measured values of I(t) and R.

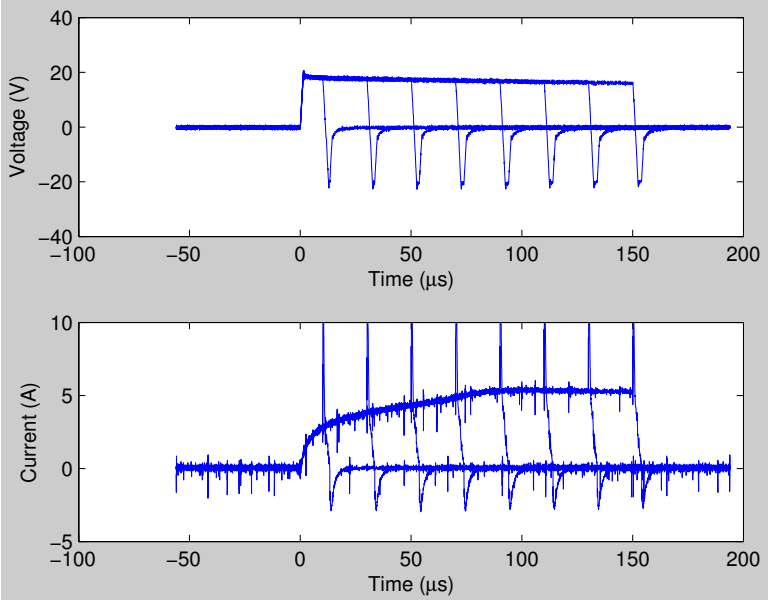


Figure 5-13: Electropermanent actuator pulse voltage and current vs. time. In the figures above, we have overlaid the plots for eight linearly-spaced pulse lengths from 10 $\mu$s - 150 $\mu$s. Demonstrating the causality and repeatability of the system, the pulses follow identical trajectories until the voltage is turned off, when a negative-voltage spike corresponding to the partial collapse of the magnetic field is observed.

energy goes to resistive losses in the windings.

As the running speed is increased from zero, the efficiency increases from zero as mechanical work is produced. Eventually, the efficiency reaches a maximum at some optimal running speed, above which other loss mechanisms, such as frictional losses and magnetic hysteresis losses dominate resistive losses.

Figure 5-14 shows a simple but illustrative permanent-magnet motor upon which the following analysis is based, although the analysis applies without loss of generality to any motor having torque proportional to current and having resistive losses in its windings.

The torque produced by the motor shown is given by the Lorentz force law. Here, $\tau$ is the torque, I is the current, B is the constant magnetic flux density, l is the total length of the windings, and r is the radius of the windings from the center point.

$$\tau = IlBr \tag{5.25}$$

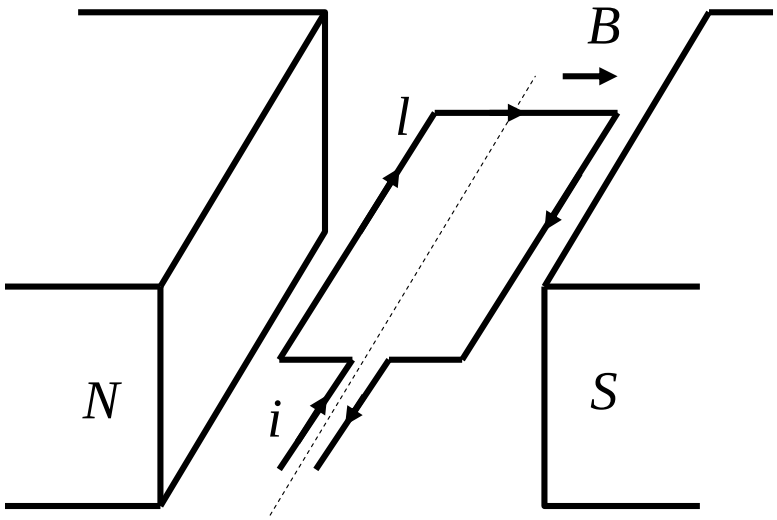


Figure 5-14: A sketch of the basic operating principle of a standard permanent-magnet DC motor. A current-carrying loop is placed in a uniform magnetic field. The Lorentz force on the wire results in a torque about the axis shown, causing the loop to rotate.

Neglecting mechanical and magnetic losses which become important at high speeds, the heat output of this motor $Q_{out}$ is equal to the $I^2R$ resistive loss. Taking $\rho$ as the resistivity of the wire, and $A_{wire}$ as the area, we can write the heat output.

$$Q_{out} = \frac{I^2 \rho l}{A_{wire}} \tag{5.26}$$

The first law of thermodynamics for the motor control volume is written below.

$$P_{in(elec)} = Q_{out} + P_{out(shaft)} \tag{5.27}$$

$\eta$ is the efficiency of the motor.

$$\eta = \frac{P_{out(shaft)}}{P_{in(elec)}} \tag{5.28}$$

Combining Equations 5.27 and 5.28,

$$\eta = \frac{P_{out(shaft)}}{P_{out(shaft)} + I^2 R} \tag{5.29}$$

After some algebra, taking into account that $P_{out(shaft)} = T\omega$, we arrive at an expression for the efficiency of the motor in terms of the speed $\omega$ and the design parameters.

$$\eta = \frac{(B\omega r)^2}{\frac{\tau\rho}{lA_{wire}} + (B\omega r)^2} \tag{5.30}$$

As $\omega$ approaches zero, the efficiency of the motor approaches zero. At the low speed limit, which we define to be where $\omega$ is small compared to $Br\sqrt{\tau\rho/lA}$, the efficiency is approximated by the following expression.

$$\eta \approx \frac{B^2}{\rho}\frac{\omega^2}{\tau}r^2 lA_{wire} \tag{5.31}$$

We take B and $\rho$ to be constant, since in a practical design, B is limited by the saturation flux density of available magnetic materials, and $\rho$ is a material property, the resistivity of the wire. We recognize $lA_{wire}$ as the volume of copper wire in the coil.

In an application where the motor's primary task is to push against a viscous damping force, the force scales with the square of length scale (frontal area), and the length of the lever arm scales with length, so the torque scales with the cube of length. In this case, if we designed a working system at macroscale using permanent magnet motors and then scaled down all the components equally, the efficiency of a permanent-magnet motor would decrease with the square of length scale.

## 5.7 The Electropermanent Stepper Motor

In this section we introduce a new motor topology, the electropermanent stepper, that is particularly suited to applications in micro-robotics and programmable matter. Using the principle of electropermanent actuation developed in the preceding sections, it maintains efficiency in the low-speed limit, allowing it to do work on high-torque loads with low power consumption.

The motor is a wobble motor. Wobble motors are a mechanically simple motor

topology where a gap-closing electrostatic or electromagnetic force is converted to an eccentric (wobbling) rotary motion. Wobble motors work by static friction, with the rotor rolling around a stator of a smaller diameter. Wobble motors are attractive for microfabrication due to their simple geometry and reduced relative precision requirements on fabrication. [44]

Wobble motors have proven their utility in microrobotic applications. Dario [19] and his colleagues won a 1998 IEEE microbot maze competition with a mobile robot using two electromagnetic wobble motors for drive wheels. The robot fit inside a cubic centimeter; the wobble motors were slightly larger that those presented here, 10 mm in diameter and 2.5 mm thick. They had a maximum torque of 0.16 N-mm and no load speed of 200 RPM. Heat dissipation limited the coil current to 140 mA, for an $I^2R$ power dissipation of 82 mW.

Our electropermanent wobble motors, which are 25% smaller than Dario's electromagnetic wobble motors, have a maximum torque of 1.1 N-mm, which is seven times higher. Operating at 0.16 N-mm and 10 RPM, they consume 16 mW, five times less power. This demonstrates the improvement to a motor's torque and low-speed efficiency that is possible using the electropermanent magnet principle—although it should be noted that it comes at the expense of reduced efficiency at high speeds.

### 5.7.1 Principle of Operation

Figure 5-16 shows the construction of the electropermanent stepper motor. The stator is cross-shaped, with an outer circular profile. The rotor has a slightly larger inner diameter, and rolls around the stator in an eccentric pattern combining oscillating translation and continuous rotation.

The rotor, stator core, and stator tips are made from soft magnetic iron. Alnico and NIB permanent magnets are placed in parallel at the center of each arm of the stator. An insulated copper wire coil is wrapped around each arm, which is used to switch the magnetization of its Alnico magnet. The NIB magnet in each arm has a high coercivity, so is magnetization is not substantially changed by current through the coils. Thus, each arm of the stator is an electropermanent magnet.

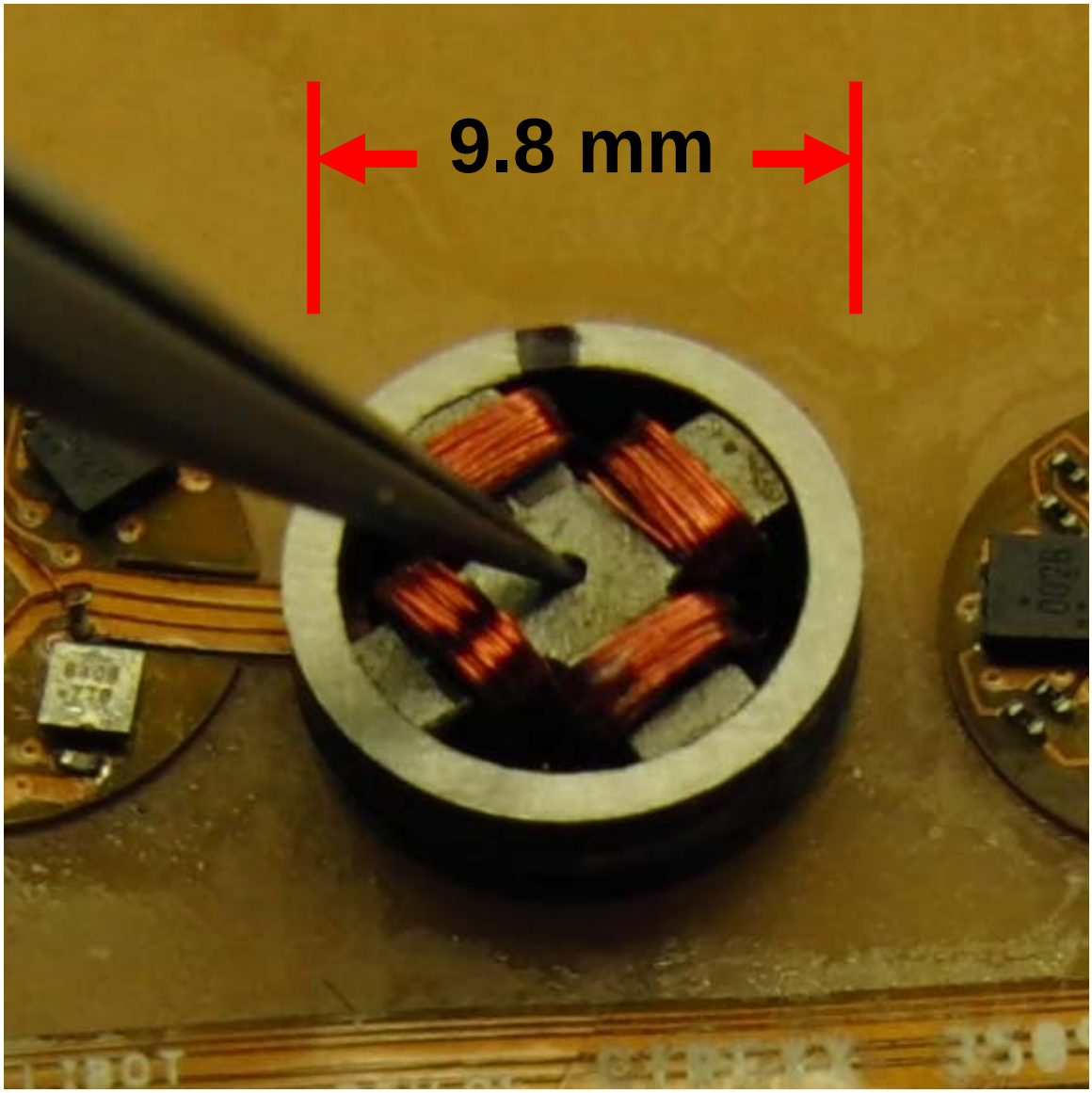


Figure 5-15: Electropermanent stepper motor, being driven by the Millibot electronics. The stator is fixed by a pair of tweezers, and the outer ring rotates. A pair of Alnico and NIB permanent magnets are located under each coil, making each arm of the stator an electropermanent magnet.

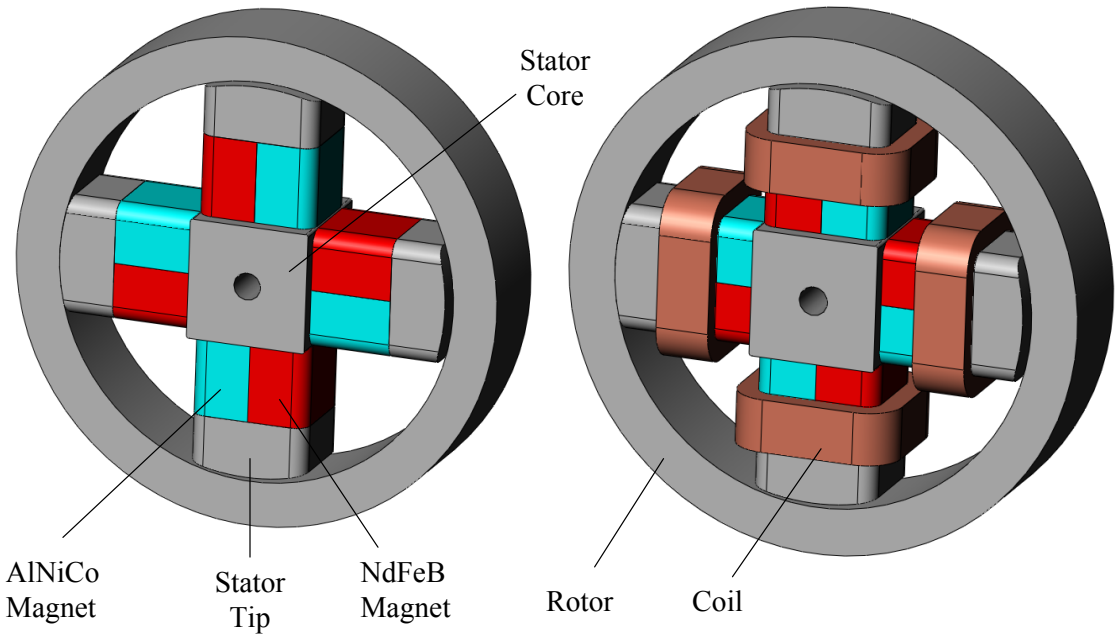


Figure 5-16: Electropermanent stepper motor construction.

Figure 5-17 shows how the motor takes a step. In the initial condition, two adjacent magnets are switched on, causing the rotor to adhere to their ends by friction. A pulse simultaneously turns off one magnet and turns on the opposing magnet. The rotor rolls along the perpendicular magnet, which stays on continuously, moving away from the magnet that switched off and toward the magnet that switched on. Repetition of this sequence results in continuous rotation with superimposed vibration.

The NIB permanent magnets are placed with alternating magnetization direction around the stator, so that when adjacent arms are switched on, there can be a loop of flux through the two arms and the rotor. The magnetic flux paths during operation are shown in Figure 5-17. Because the coils on opposite arms are always used together, they are continuously wound, so that the device has two electrical phases. Because the two phases do not need to be driven at the same time, one terminal of each can be connected to a common, making the electropermanent stepper a three-terminal device. The drive sequence is shown in Figure 5-18. Reversing this sequence in time makes the motor turn backwards.

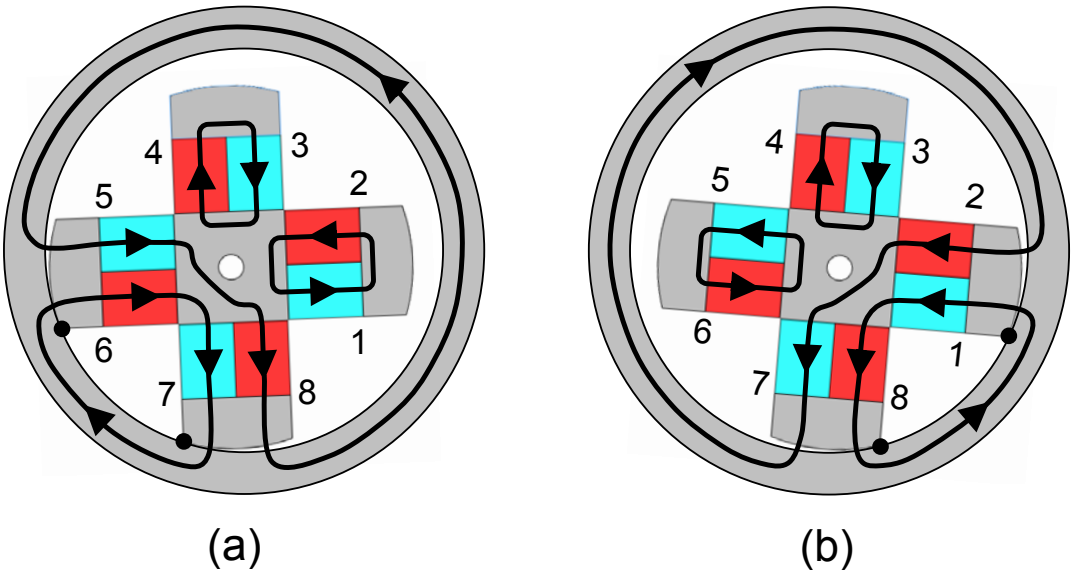


Figure 5-17: Electropermanent stepper motor principle of operation. The red magnets are NIB, always polarized in the direction shown. The magnetization of the blue Alnico magnets switches as the motor operates. The motor starts in position (a), with magnets 5-6 and 7-8 on, and magnets 1-2 and 3-4 off. Flux flows through the rotor and stator as shown. Applying a current pulse to the horizontal winding around magnets 5-6 and 2-1 switches the magnetization of magnets 5 and 1, turning magnet 5-6 off and magnet 2-1 on, resulting in the new flux paths shown at right. The rotor pivots counterclockwise about magnet 7-8, taking one step to arrive at the new position shown in (b). Repeated steps drives the rotor abound the stator with a continuous rotary motion and oscillating translational motion.

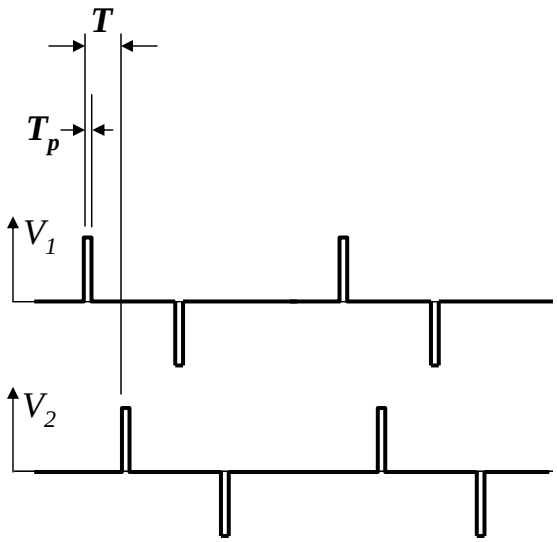


Figure 5-18: Drive waveform for the electropermanent stepper motor. The pulses switch the magnetization of the permanent magnets, which then apply torque for the rest of the cycle. The pulse width $T_p$ is $10 - 60\mu s$, depending on the torque, and the pulse period T is 4 ms or longer, depending on the speed.

### 5.7.2 Design

#### Calculation of No-Load Speed

The rotor, with inner radius $r_o$, rolls around the stator, with radius $r_o$ and $N_a$ arms. Figure 5-19 shows a diagram of the rolling geometry. After one step, the contact point moves from A to C; the rotor has rolled a distance AC along the stator. After a full cycle of $N_a$ steps, the rotor has rolled a distance $N_aAC$, slightly less than the rotor circumference, $2\pi r_o$, resulting in the circumferential displacement of the point A by $2\pi r_o - N_aAC$ after $N_a$ steps. So the rotor rotates through $2\pi - N_aAC/r_o$ radians every $N_aT$ seconds, resulting in an angular rate $\omega$ of

$$\omega = \frac{2\pi - N_aAC}{r_oN_aT}$$

Because the shape of the rotor is an interrupted disc rather than a disc, the curve ABC is made up of two circular arcs, AB with radius $r_i$ and BC with radius $r_o$. If we approximate the curve as a single arc with radius $r_i$, then AC is $2\pi r_i/N_a$ and the

expression for angular rate becomes

$$\omega = \frac{2\pi}{N_a T}\left(\frac{r_o - r_i}{r_o}\right)$$

For an exact expression, we can find the length of arc AB by calculating the half-angle $\alpha$ that it subtends, then multiplying by the radius to get the arc length. To do this, we need to introduce w, the width of a stator arm.

$$AB = 2r_i sin^{-1}\left(\frac{w}{2r_i}\right)$$

We can find the length of the chord connecting B and C by drawing triangles on the stator, and then use this chord length, 2s, to get find the subtended rotor angle and finally the arc length BC.

$$BC = 2r_o sin^{-1}\left(\frac{s}{r_o}\right)$$

The exact expression for the no-load speed is then

$$\omega = \frac{2}{T}\left[\frac{\pi}{N_a} - \frac{r_i}{r_o} sin^{-}1\left(\frac{w}{2r_i}\right) - sin^{-1}\left[\frac{sin(\pi/N_a)}{r_o}\left(\sqrt{r_i^2 - \frac{w^2}{4}} - \frac{w}{2}\right)\right]\right]$$

For our motor, which had $r_o$ = 4.076 mm, $r_i$ = 4.000 mm, $w$ = 2.4 mm, and $N_a$ = 4, for T = 40 ms, the approximate formula predicts $\omega$ = 0.73 rad/sec , and the exact formula predicts $\omega$ = 0.77 rad/sec, a difference of about 5%. For comparison, the experimentally measured no-load speed under these conditions was 0.5 rad/sec, implying that the rotor may be slipping somewhat even at no load.

### Calculation of Torque

The (instantaneous) torque $\tau$ on the rotor of the wobble motor about its pivoting arm, in terms of the force from the moving arm $F$, is

$\boldsymbol{\tau} = \mathbf{r} \times \mathbf{F}$

Figure 5-20 shows the motor executing a step. For motors with a small gap, where

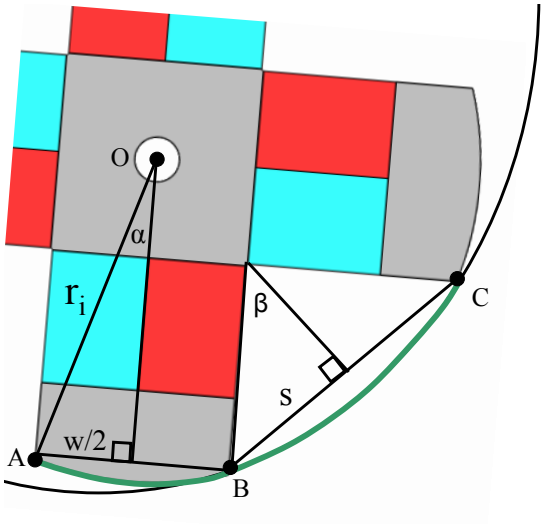


Figure 5-19: Figure for calculation of no-load speed. The inner surface of the rotor rolls along the path from point A to point C as the motor takes one step.

the diameter of the inner and outer ring are very close, the gap-closing force is very nearly radial. The length of the vector **r** above is the length of the chord of the circle between the two arms:

$|\boldsymbol{r}| = 2r_i sin(\frac{\theta}{2})$

where $\theta$ is the angle between the arms, equal to $2\pi/N_a$. From the figure, the angle $\phi$ between the (radial) force and the chord is $\pi/2 + \theta/2$. So then

$|\boldsymbol{\tau}| = |\boldsymbol{r}||\boldsymbol{F}|sin(\phi) = d_i sin(\frac{\theta}{2})sin(\frac{\pi}{2} + \frac{\theta}{2})$

Writing in terms of $N_a$, removing the vector notation, and simplifying, we can write

$\tau = 2r_i F sin(\frac{\pi}{N_a})cos(\frac{\pi}{N_a})$

For $N_a = 4$, this expression reduces to $\tau = r_i F$.

### Selection of the Diameter Difference

The torque, speed, and relative efficiency of the motor are all strongly influenced by the diameter difference between the rotor and stator, which determines the air gap length at the start of a step. A larger diameter difference results in higher speed but lower magnetic flux and so lower torque.

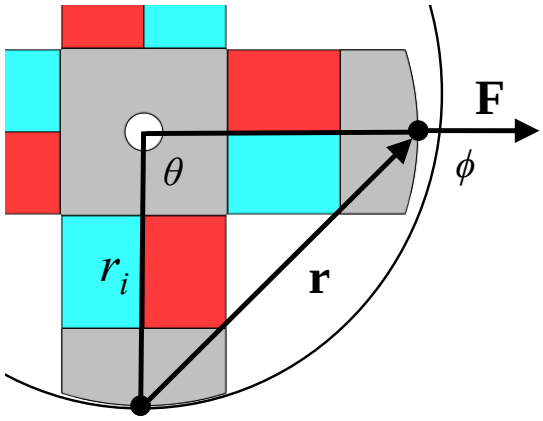


Figure 5-20: Figure for calculation of low-speed torque. The rotor pivots about the instantaneous axis at the end of the bottom arm, resulting in a torque $\boldsymbol{\tau}$.

The magnetic flux density at the start of the power stroke can be determined from a load line analysis. In Figure 5-21 we plot the hysteresis curve in the second quadrant for parallel Alnico 5 and NIB magnets with equal area. The operating point of the system at the start of the power stroke will be the intersection of this curve with the load line of the gap.

For a total magnet length on the flux path $l_m$ (length of two magnets), air gap length $l_g$, magnet area $A_m$, and pole area $A_p$, the slope of the load line is

$$\mu_r = \frac{B}{\mu_0 H} = \frac{l_m A_g}{l_g A_m}$$

For our electropermanent stepper motor, at the start of the power stroke the flux loop passes through two magnets and a gap approximately equal to the diameter difference of the rotor and stator. The area of the pole is approximately equal to the area of the magnets. So we can write a simplified expression for $\mu_r$ in terms of the problem parameters.

$$\mu_r = \frac{l_m}{d_o - d_i}$$

Figure 5-22 plots the force density at the poles against $\mu_r$. Figure 5-23 plots the relative power efficiency, which we define as the ratio of mechanical work done to

hysteresis loss in the Alnico. With $\mu_r = 17$, efficiency is maximized and the force density is at about 75% of its maximum value, making this an attractive design point. It corresponds to the intersection of the load line with the maximum power point on the hysteresis plot.

The motors we constructed have $d_o - d_i = 0.15$ mm and $l_m = 3.3$ mm, for $\mu_r = 22$. Reading the chart in Figure 5-22, we would then expect their magnetic force density to be about 540 kPa. Since they have 4.8 $mm^2$ pole area, we would expect F = 2.6 N, so from the previous section, $\tau = 10$ N-mm. In static torque tests hanging weights on a string from the rotor, it was able to support an 80 gram weight. Depending on the position of the pivot, this could correspond to a static torque around the pivot of up to 7 N-mm, in moderate agreement with this calculation. However the dynamic torque capability was about four times lower. We suspect that the vibrational dynamics of the motor, which are not modeled here, have a significant impact on its dynamic torque capacity.

**Experimental: Materials and Methods**

Figure 5-15 shows a photo of an electropermanent stepper motor that we fabricated in the lab.

The iron portions of the rotor and stator were made from Carpenter Electrical Iron, grade ASTM-A848, purchased from Scientific Alloys, Inc (Westerly, RI) We annealed the iron in a hydrogen atmosphere, heating to 850 C, holding for two hours, then cooling at 100 C / hour to 540 C. We purchased Grade N40 NIB from Amazing Magnets, Inc. (Irvine, CA), and Alnico 5 from Magnet Kingdom. (Medford, NY)

All of the parts were cut by wire EDM. To assemble the stators, we used a needle to coat the mating faces of the magnets and iron pieces with a layer of Loctite Hysol E-60HP epoxy, then we assembled the parts under magnification with non-magnetic titanium tweezers. After assembly, we cleaned away excess wet glue with isopropanol. We used a custom-machined fixture plate to assist in final alignment of the parts. After the glue dried, we secured the stators to a plate using paraffin wax, then we machined the circular outer profile using a 1/4 inch diameter end mill.

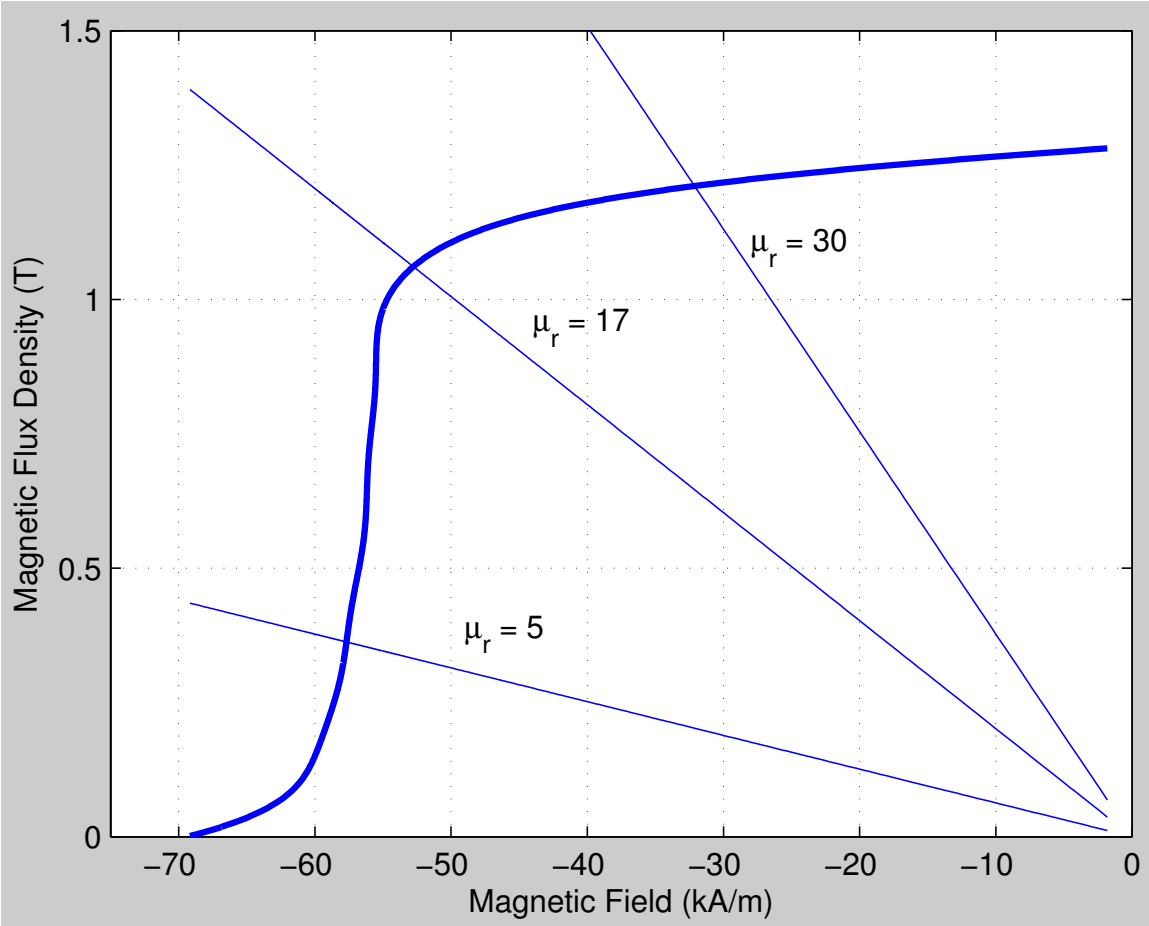


Figure 5-21: Load line analysis. The second-quadrant hysteresis curve for Alnico 5 in parallel with NIB is plotted with three gap load lines. The magnet/gap size ratio $\mu_r$ is defined in the text; for a design with equal permanent magnet and pole area, it is equal to the ratio of the total magnet length on the flux path to the length of the air gap. The system will start the power stroke at the intersection of the load line and the hysteresis curve.

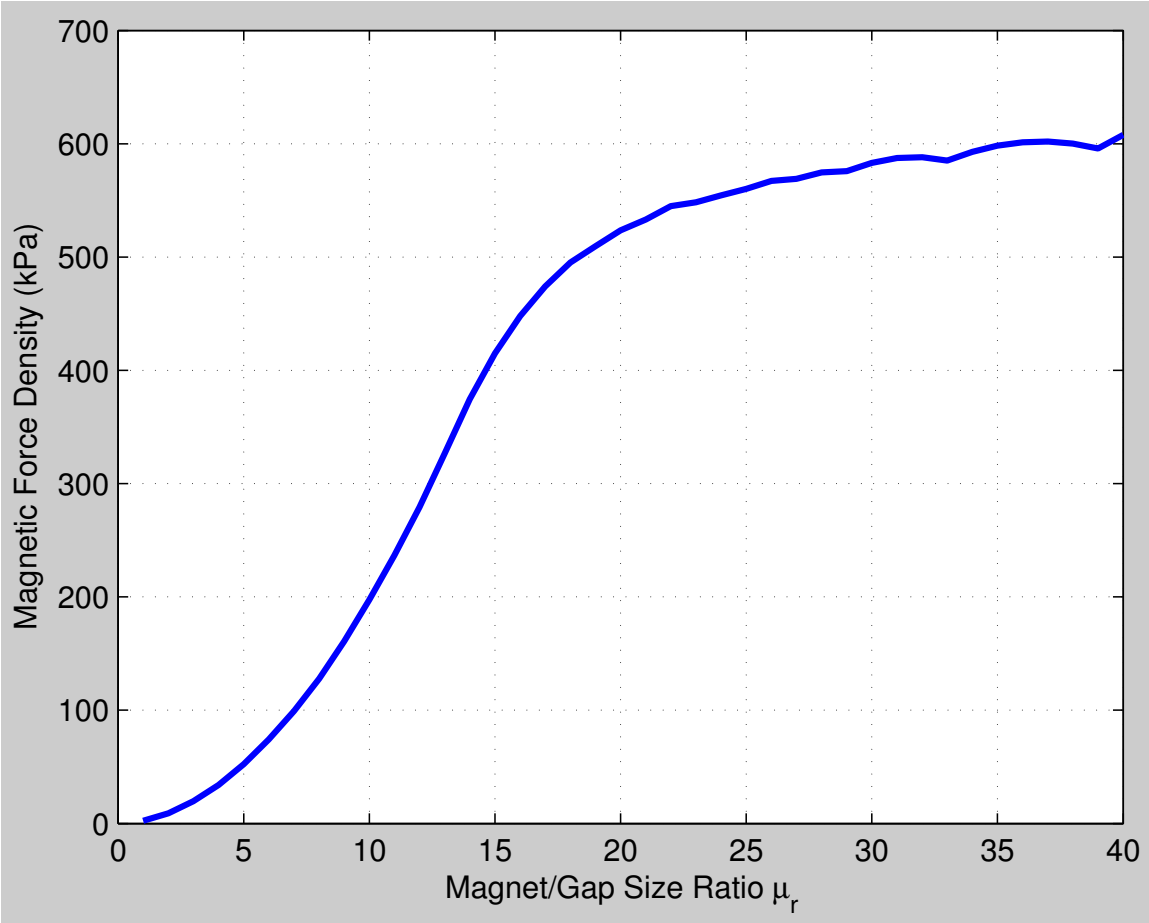


Figure 5-22: Magnetic force density vs magnet/gap size ratio. The magnet/gap size ratio $\mu_r$ is defined in the text; for a design with equal permanent magnet and pole area, it is equal to the ratio of the total magnet length on the flux path to the length of the air gap.

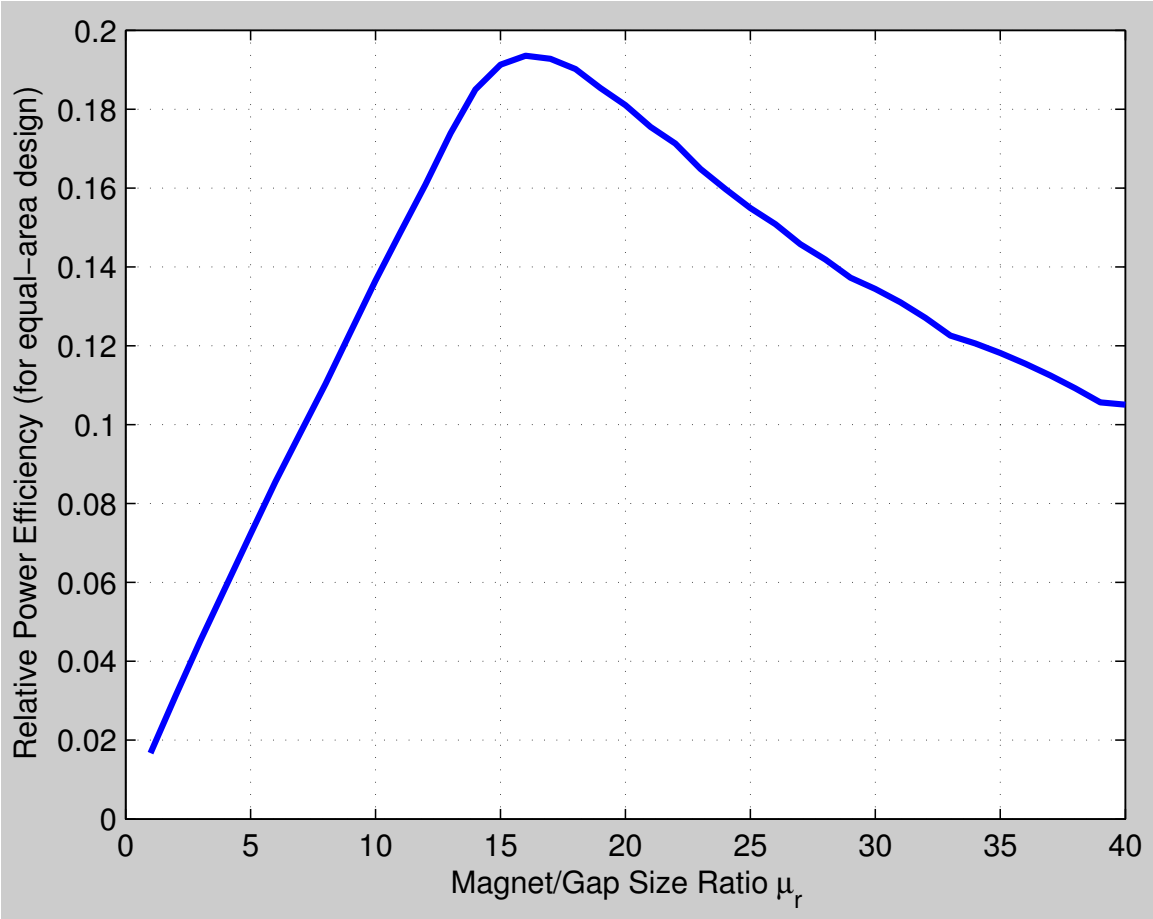


Figure 5-23: Relative power efficiency vs size ratio. The relative power efficiency is the ratio of the mechanical work done by the gap closing to the hysteresis loss of the Alnico magnet. The magnet/gap size ratio $\mu_r$ is defined in the text. This plot is valid only for a design with equal magnet and pole area; in that case, the magnet/gap size ratio is the ratio of the total magnet length on the flux path to the length of the air gap.

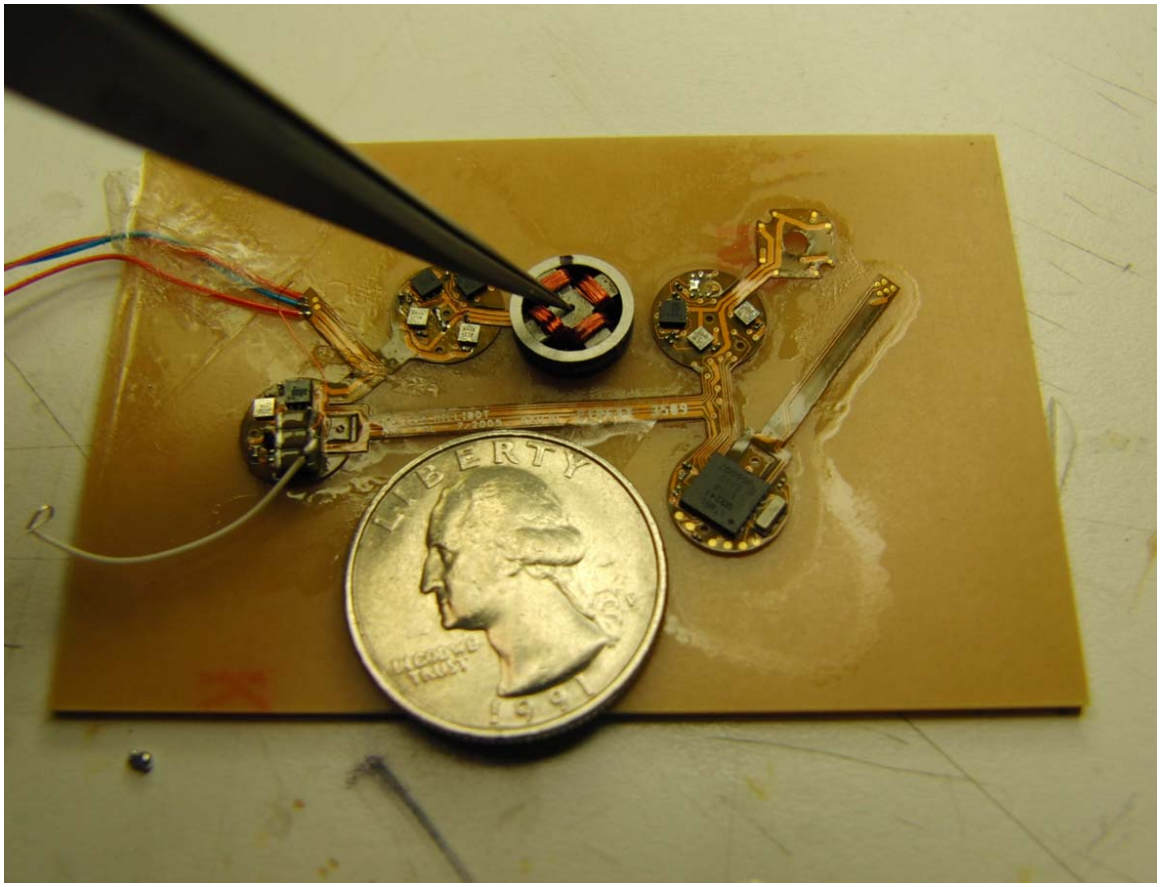


Figure 5-24: Complete friction-drive electropermanent stepper, shown with an early version of the Millibot flex circuit, which provides the drive pulses.

The coils are wound from 40 AWG bondable magnet wire with solderable polyurethane-nylon insulation, purchased from MWS Wire Industries (Westlake Village, CA). Before winding the coils, we used a diamond file and hobby knife to remove excess glue and ensure a smooth winding surface. We wound the coils using a coil winding machine, mounting the stators onto the machine's chuck using a custom-designed aluminum flexure clamp. The clamp served as the left-hand spool side for winding the coil; we used a laser-cut, break-away balsa wood spacer for the right-hand spool side. We positioned a stereomicroscope over the coil winder and hand-wound the 40 turn coils. After winding, to reflow the bond coat and make the coils freestanding, we applied a drop of ethanol, waited 5 seconds, then dried away the remaining ethanol using a heat gun. We found it critical to us an ohmmeter to test for shorts between the coils and the stator core, and to re-wind coils showing any conductivity to the core before energizing the motor.

To drive the motor, we used a Millibot circuit, described in the next chapter. The drive voltage was 30V. We applied drive pulses from 10-50 $\mu$s in length, spaced apart by 4-400 ms.

### 5.7.3 Experimental: Results

To measure the motor's torque, we mounted the motor vertically, fixed a piece of thin wire to the outside of the rotor, and hung weights from the wire. As the motor turned, it wrapped the wire around its outer diameter, lifting the weights. We timed the interval for a quarter-turn of the motor using a stopwatch to measure the speed.

We plotted the pulse voltage and current waveforms on an oscilloscope, and calculated the input power by multiplying voltage times current. To measure the current, we placed a 0.03 $\Omega$ series resistor in series with each phase, and measure the voltage drop across the resistor using a differential amplifier.

Figure 5-25 is a torque-speed curve for T=40 ms and T=4 ms. Note the dropping torque-speed curve, which is characteristic of wobble motors in the literature. We suspect that this curve is due to vibrational dynamics and partial backdriving during the wobble cycle, because the stall torque, shown in Figure 5-26 is much higher than

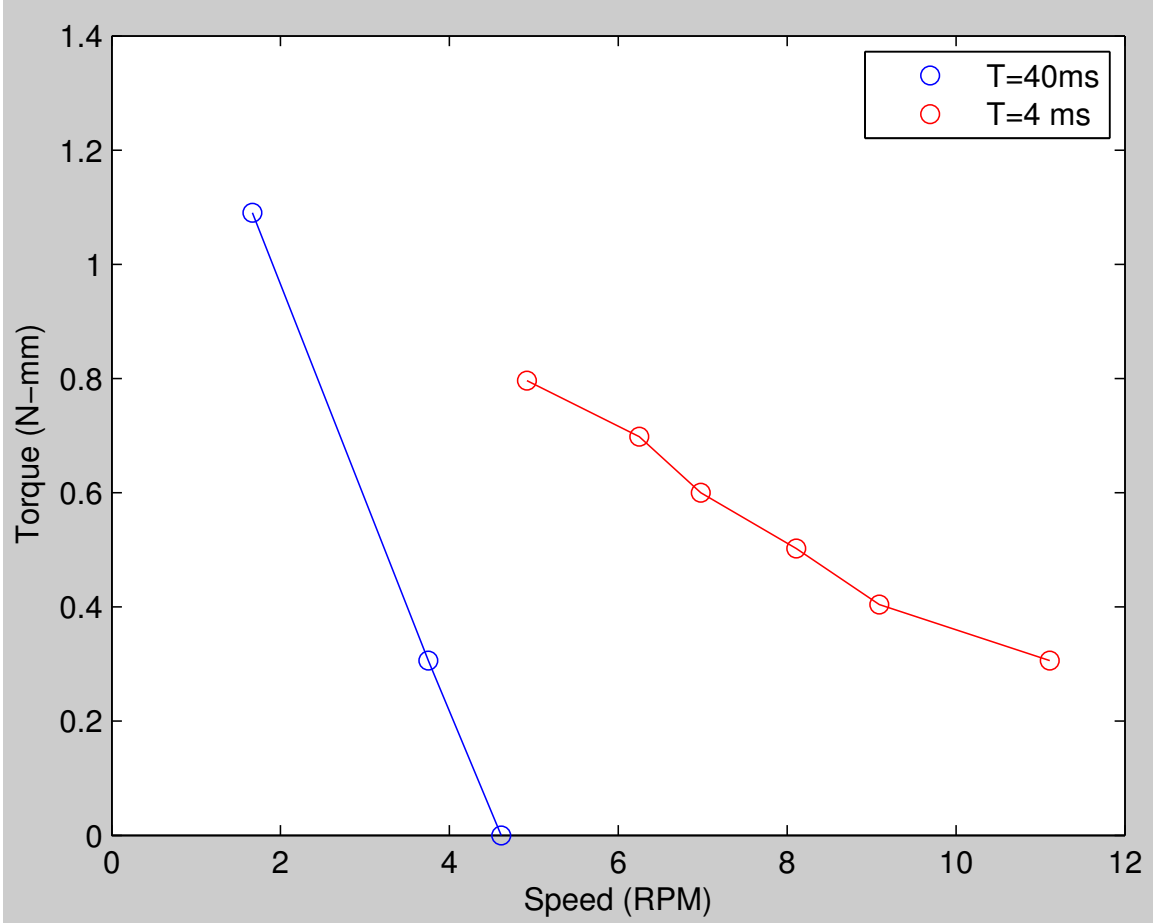


Figure 5-25: Electropermanent stepper torque vs. speed curves, measured by hanging weights on a string from the rotor, and measuring the time for one revolution with a stopwatch.

the low-speed dynamic torque.

For most efficient drive, it is necessary to reduce the driving pulse length until the motor can just lift the weight. For a 0.16 N-m torque, the efficiency was 1%, maintained over two orders of magnitude in speed, from T=4 ms to T=400 ms.

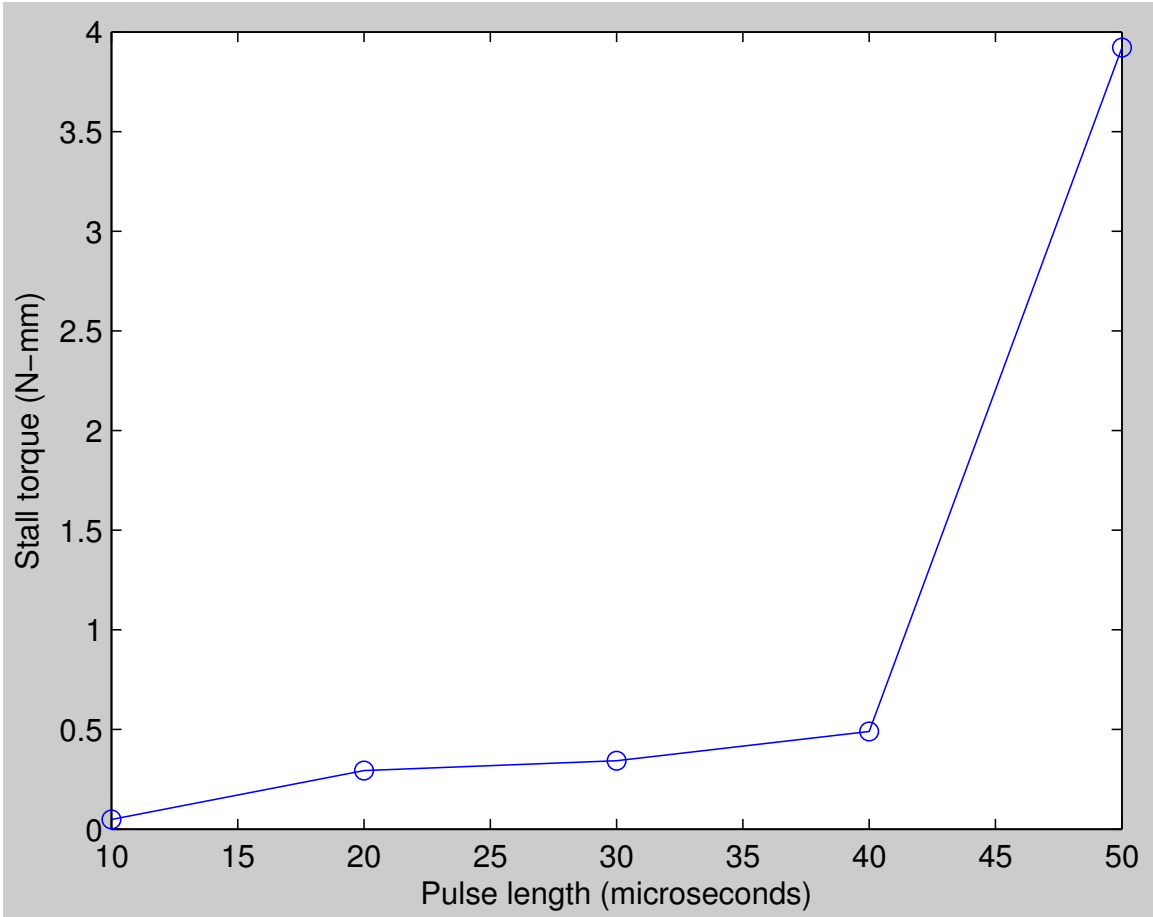


Figure 5-26: Electropermanent stepper torque vs. pulse length, measured by hanging weights on a string from the rotor until the backdriving occurred. This plot shows that the stall torque of the motor is considerably higher than its dynamic torque and that the torque can be controlled by the driving pulse length.

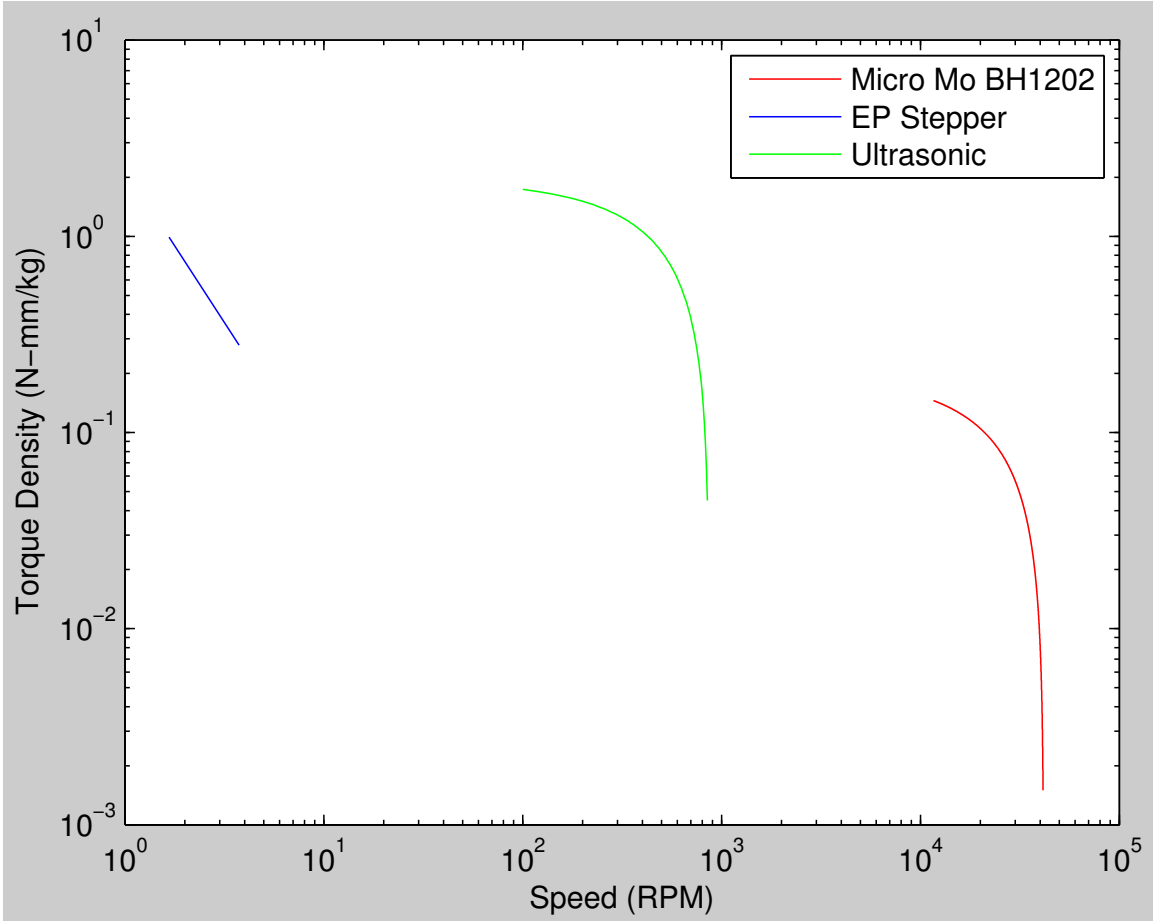


Figure 5-27: Torque density vs. speed comparison with two motors of similar size to the electropermanent stepper. The electropermanent stepper torque/speed curve at T=40 ms is plotted against the torque speed curve for a Micro-Mo BH1202 electromagnetic penny motor and Flynn's 8 mm diameter ultrasonic motors. [27] The electropermanent stepper has higher torque density than the electromagnetic motor, but lower torque density than the ultrasonic motor.

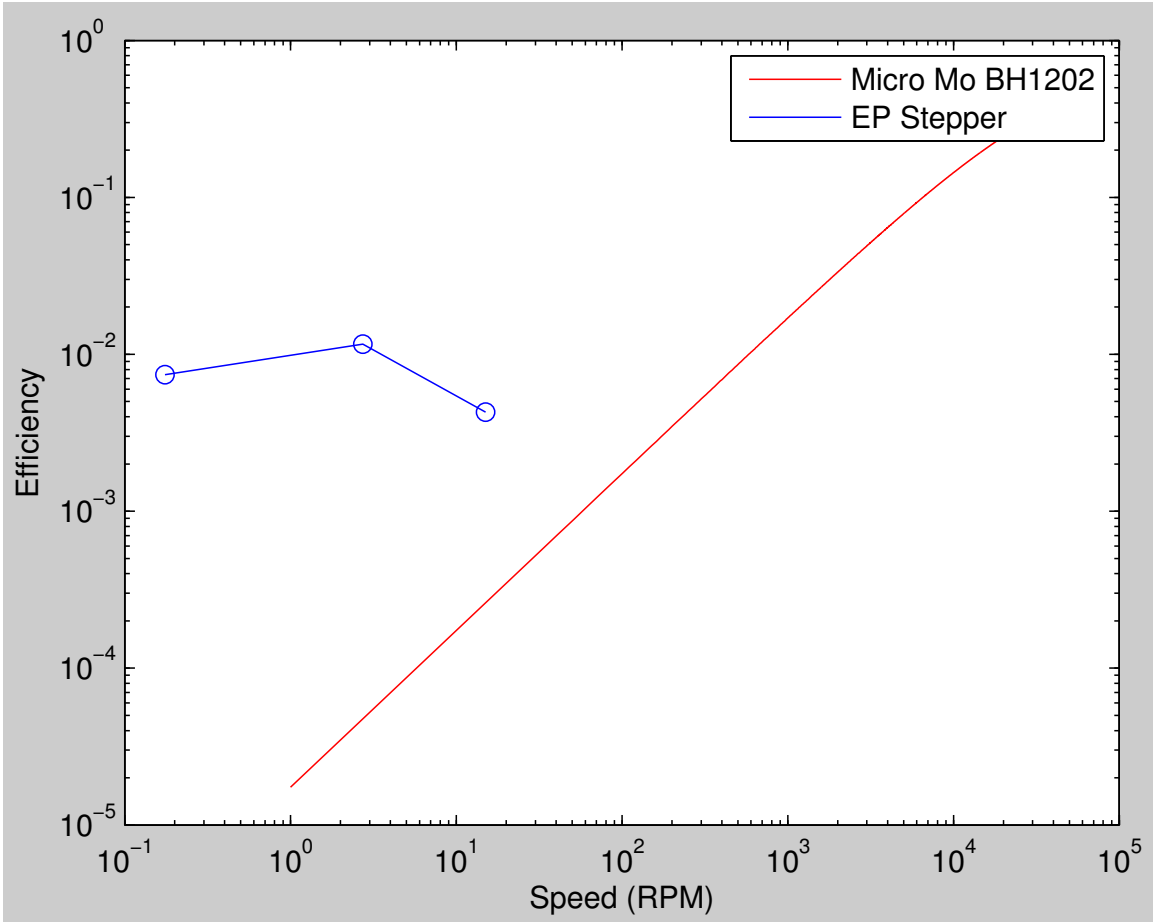


Figure 5-28: Efficiency vs. speed comparison with the Micro-Mo BH1202 electromagnetic motor. Lifting the maximum rated load of the BH1202, 0.16 N-mm, the electropermanent stepper has 1% efficiency, independent of speed. This is a higher efficiency that the Micro-Mo BH1202 at speeds below 1000 RPM. Note that this is a log-log plot.

# Chapter 6

# The Millibot

## 6.1 Introduction

Nature builds proteins by encoding their blueprint as a one-dimensional code (DNA), transcribing that code to a linearly connected chain of amino acids, then folding that chain. These proteins acting together produce all of the richness and variety of life. In our quest to produce a "universal object" which can transform itself into some approximation of any object, it seems sensible to consider borrowing from nature's approach. In his PhD thesis, entitled "Growing Machines," Griffith [38] describes mechanical and electromechanical systems built to emulate the protein-folding machinery of biology.

## 6.2 The Millibot

The Millibot is a continuous flexible printed circuit with electropermanent stepper motors placed at a 12 mm pitch. It is designed to move along the ground like an inchworm, then fold itself into a user-defined shape.

The Millibot is a testbed for the idea of roll-to-roll robotics; that robotic modules with no internal moving parts, only field interactions between neighbors, can be inexpensively manufactured as a continuous strip. As such, when designing the Millibot we had the following goals:

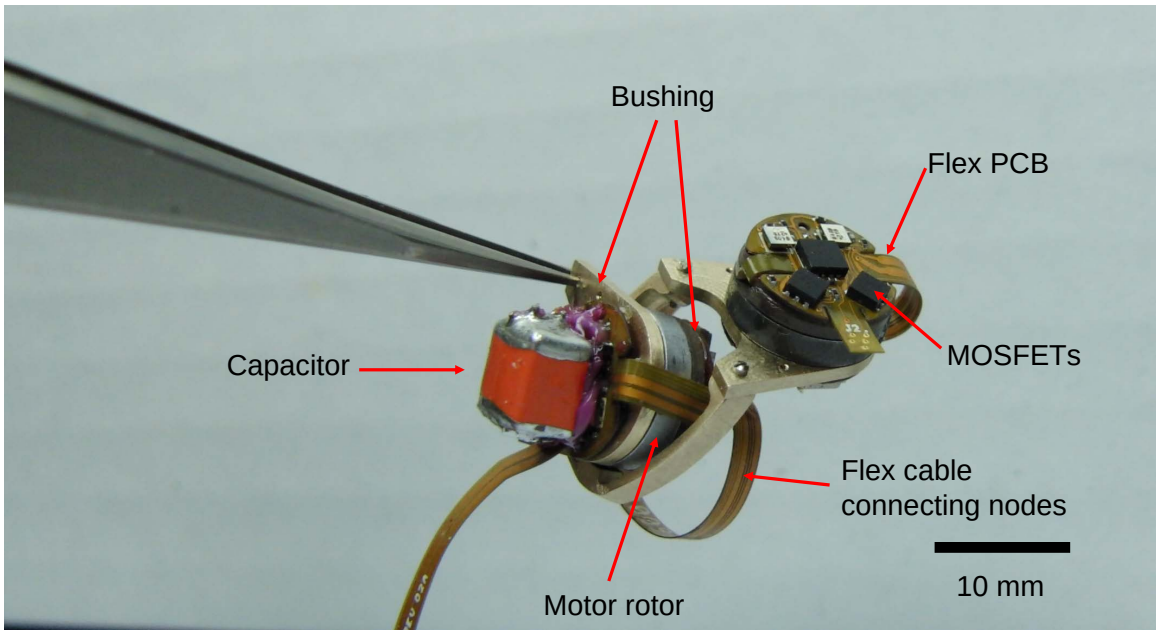


Figure 6-1: A two-module Millibot, showing the major components.

- Smallest axis-to-axis pitch possible, while still using off-the-shelf electronic components for control.

- Minimum number of moving parts: For a chain with N joints, the minimum number of moving parts is N+1. This ruled out, for example, gear reduction as a means to achieve large torques.

- Scalable physics: The basic design, actuation devices, and computational capacity per node should be feasible to shrink to sub-millimeter axis-to-axis dimensions, without encountering any surface-area-to-volume-ratio type limitations.

- Planar Fabrication: As much as possible, the parts should be manufacturable via two-dimensional, layered techniques, such as photolithography, laser cutting, and wire EDM.

- Connected geometry: We wanted to build a permanently-connected chain of nodes, because chains are strong in tension, and allow passing power and communication messages down the chain.

## 6.3 The Arm-Wrestling Number

A limitation on the motion paths of any chain-style modular robot is that a given joint must be capable of providing enough torque to lift its neighbors. To quantify a system's capability to lift itself in a scale-independent way, we have defined a non-dimensional number which we call the "arm-wrestling number," equal to the number of nodes that a single node can lift, with the chain configured as a straight horizontal line. Note that this is the worst-case condition: if there were already any bends in the part of the chain being lifted, the effective moment arm would be shorter, because of the triangle inequality, and so the required torque would be lower.

For a system with nodes with mass $m$, axis-to-axis distance $l$, motor torque $\tau$, and taking the acceleration of gravity as g, the arm-wrestling number $N$ is

$$N = \sqrt{\frac{2\tau}{mgl}} \tag{6.1}$$

Both the torque of the motors and the mass of a node are expected to scale with the cube of length, so the arm-wrestling number is expected to scale as the inverse square root of length—to increase as the size scale is decreased. This is good news. Using the experimentally measured torque of the Millibot motors, 1.1 N-mm, mass of a Millibot node, 4.0 g, and axis-to-axis distance, 12 mm, one Millibot joint should be able to lift three modules. If the whole system were scaled down by a factor of 10, we would expect one joint to be able to lift nine modules. Of course, as the size scale decreases other types of resisting forces may become more significant than weight.

## 6.4 Folding Geometry

Cheung, Demaine, and Griffith have proven that folding is universal—that a voxelized version of any shape can be folded without self-interference using a space-filling curve. [15]

For the Millibot we have selected the hexagonally-bisected cube folding geometry, used in V. Zykov's Molecubes. [103] This geometry turns out to reduce to a chain of

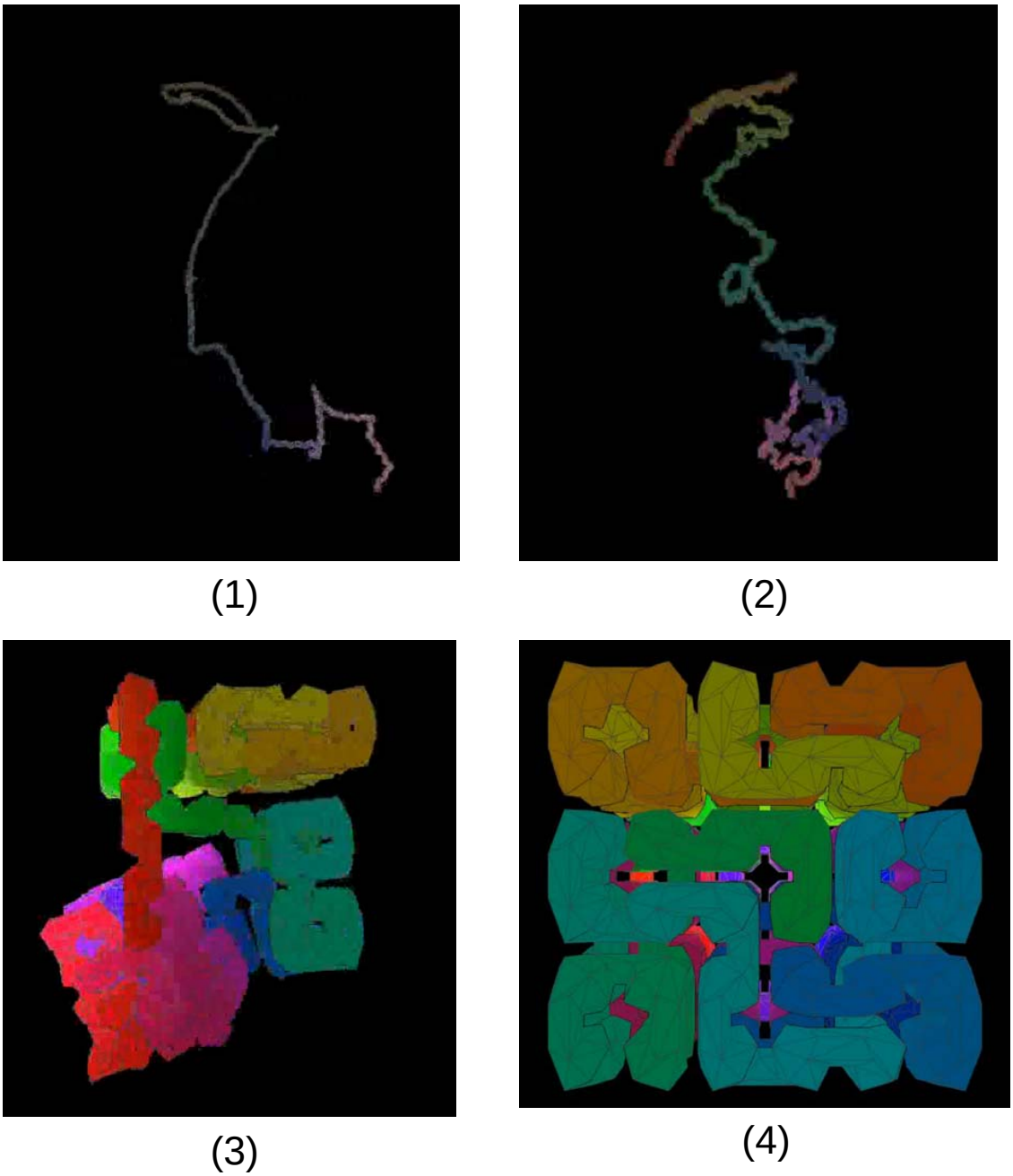


Figure 6-2: Results of a dynamic simulation by J. Bachrach, showing a 216-segment Millibot folding into a cube.

rotary joints, rigidly linked to each other at a 109.57° angle. Each joint needs to be able to turn through 240°. Figure 6-2 shows the results of a dynamic simulation by J. Bachrach, showing a 216-segment Millibot folding into a cube in a neutral buoyancy tank.

## 6.5 Mechanical Design

Figure 6-5 is a drawing of an assembled Millibot chain. Figure 6-4 is a drawing of the repeated unit, and Figure 6-3 is an exploded view diagram of the repeated unit.

Millibot modules are rotary joints. An electropermanent stepper motor at the center of the module provides the rotation. The rotor includes a tapered dovetail key for attachment to the rotor joiner. The rotor is made of iron, as it is a component in the motor's magnetic circuit, and is manufactured by wire EDM.

The rotor joiner is a structural piece that mechanically connects a module to its neighbor. Its shape results in the required 109.57° angle between modules. It is made of bronze for strength and machinability, and manufactured by 5-axis machining.

The motor bushings act as thrust bearings for the motor rotors and provide mounting points for the flex circuit. The motor driver side bushing is made of bearing-grade Torlon polyamide-imide plastic, to avoid causing motor connection short circuits. The processor (and power electronics) bushing is made of 932 Bearing-grade bronze, for strength and lubricity.

## 6.6 Electrical Design

We attempted an electrical design with a single processor per motor, but were unable to find a small enough microcontroller to fit. So we used a design with one processor for every two motors, greatly relaxing the PCB layout requirements.

The Millibot flex circuit is a repeated series of three boards: the power board, the processor board, and the motor driver board.

The processor board contains an Atmel ATMEGA324P 8-bit microcontroller. It

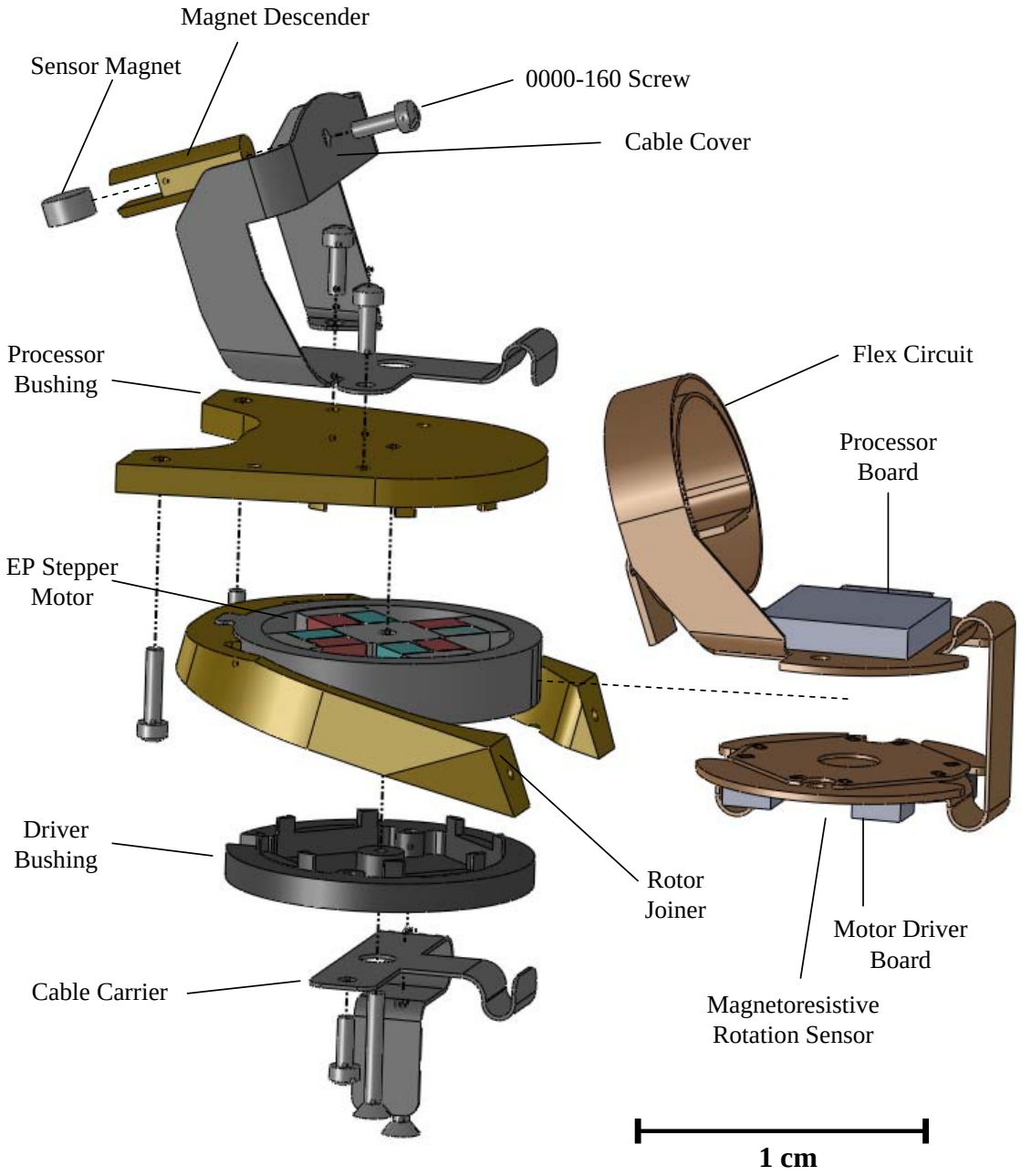


Figure 6-3: Millibot module exploded view. This assembly is repeated for each joint. One segment of the continuous flex circuit is shown in its folded configuration. The electropermanent stepper motor rotates the rotor joiner relative to the rest of the assembly. The rotor joiner connects to the processor bushing of its neighbor using two screws. See Figure 6-4 for an assembled view.

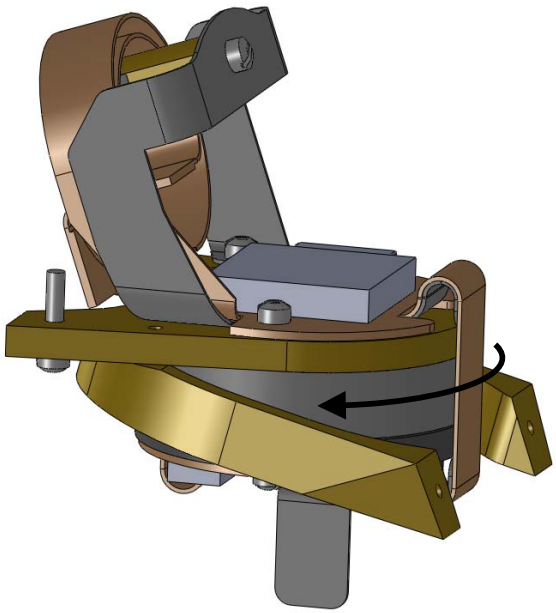

Figure 6-4: Millibot module. This assembly is repeated for each joint. The electropermanent stepper motor rotates the rotor joiner relative to the rest of the assembly, as shown. The rotor joiner connects to the processor bushing of its neighbor using two screws. See Figure 6-4 for an exploded view.

uses its two UART's to communicate serially with its two neighboring microcontrollers on the chain. The microcontroller's general purpose I/O pins control one LED, and the two adjacent motor driver boards. Normally, the microcontroller is programmed using a serial chain bootloader, but for initial programming, pads on the processor board allow in-system programming through a pogo pin fixture.

The motor driver board contains two MOSFET half-bridges, for driving the two electrical phases of an electropermanent stepper motor. The common terminal of the motor is connected to a half-bridge on the power board, which is shared between two motors. The half-bridges are capable of supplying the motor with 30V, 10A switching pulses for up to 60 $\mu s$. They use the same circuit topology as the Robot Pebble magnet drive circuit. (See Section 4.2.2) The motor driver board also contains a two-axis magnetoresistive rotation sensor, the Measurement Specialties KMT36H. The rotation sensor measures the orientation of a permanent magnet attached to the adjacent module; see Figure 6-3. Analog signals from the rotation sensor connect to

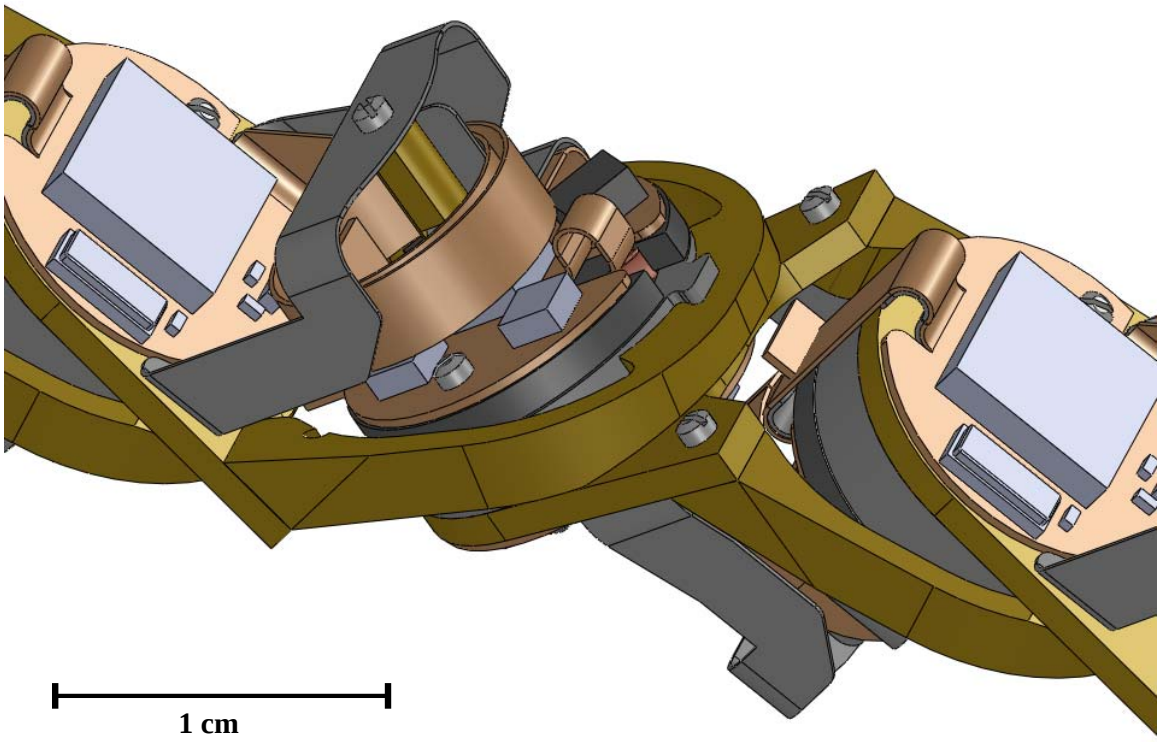


Figure 6-5: Millibot chain, assembled by building a Millibot module around each section of the continuous flex circuit. This view shows how the rotor joiner of each module attaches to the processor bushing of its neighbor. When the chain is assembled, the sensor magnet is positioned above the magnetoresistive rotation sensor of the next module. Power and data are transferred between modules over the coiled section of the continuous flex circuit.

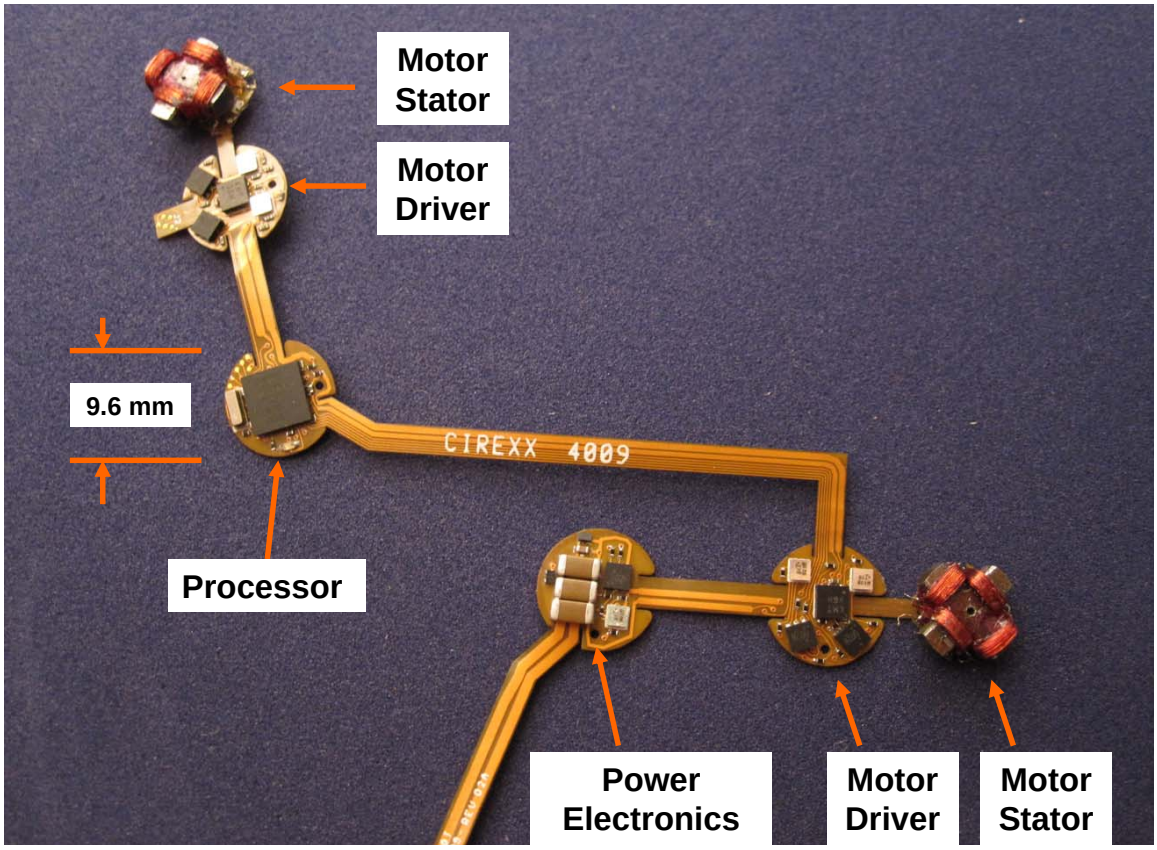


Figure 6-6: Millibot flex circuit. The circuits link together in a continuous reflow-soldered chain. Shown is the electronics to drive two joints: one microcontroller, one power electronics board, two motor driver boards, and the stators of two motors.

the A/D inputs of the microcontroller.

The power board contains the 150 $\mu$F tantalum capacitor used to supply the pulse current for the electropermanent stepper motor. It also contains the common half-bridge, shared by the two motors controlled by the microcontroller.

Power is bussed at 30V for the motor and 5V for the electronics along a 2 mm wide flexible circuit tether connecting the boards.

## 6.7 Assembly Process

The Millibot chain is made from a continuous flexible printed circuit. In the current prototype, the flex circuit segments are two modules long and attached to each other

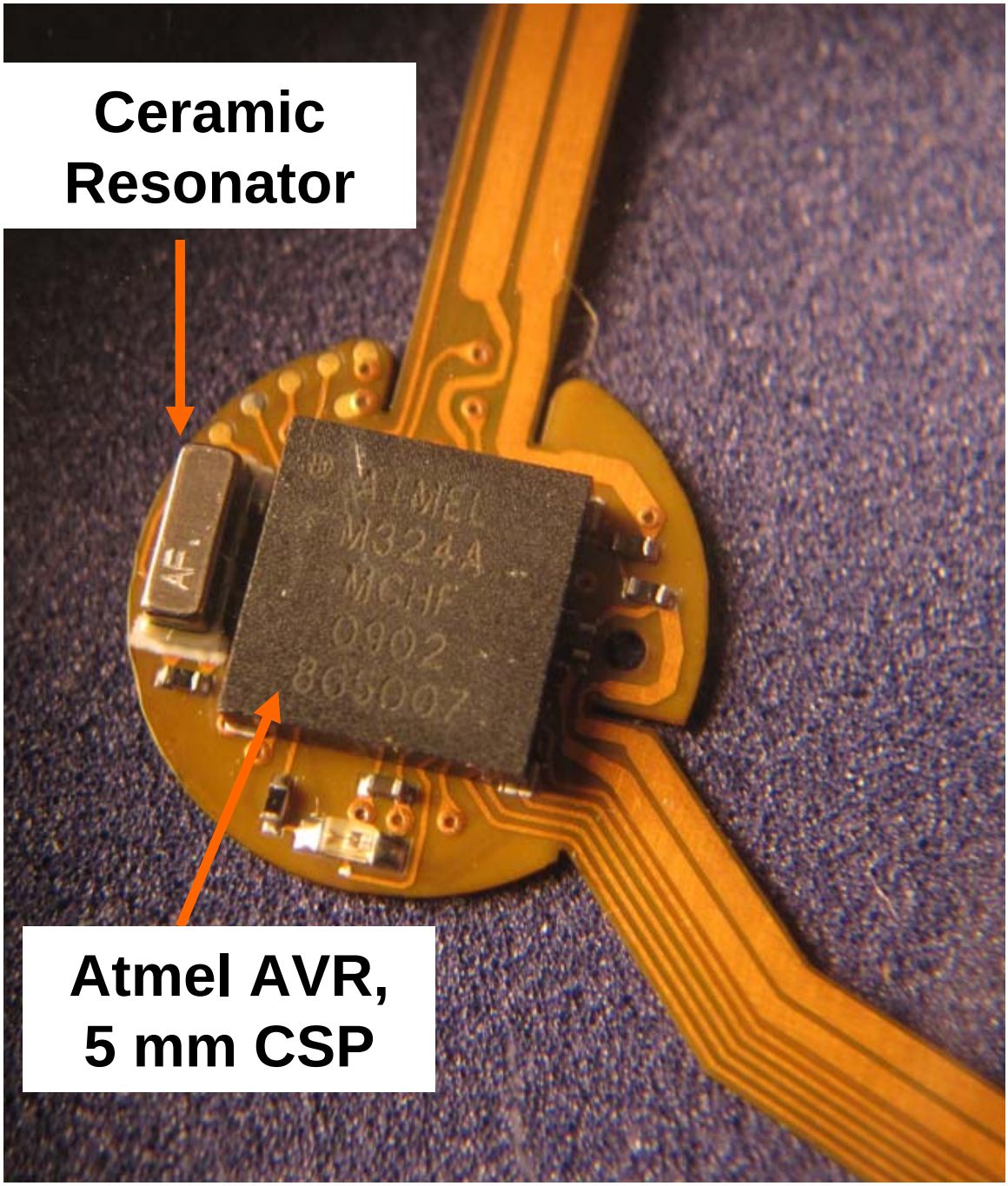


Figure 6-7: Millibot flex circuit: microcontroller board. Major components are the Atmel ATMEGA324P microcontroller, in a 5 mm square DFN package, a 16 MHz ceramic resonator, and a 0402 blue LED.

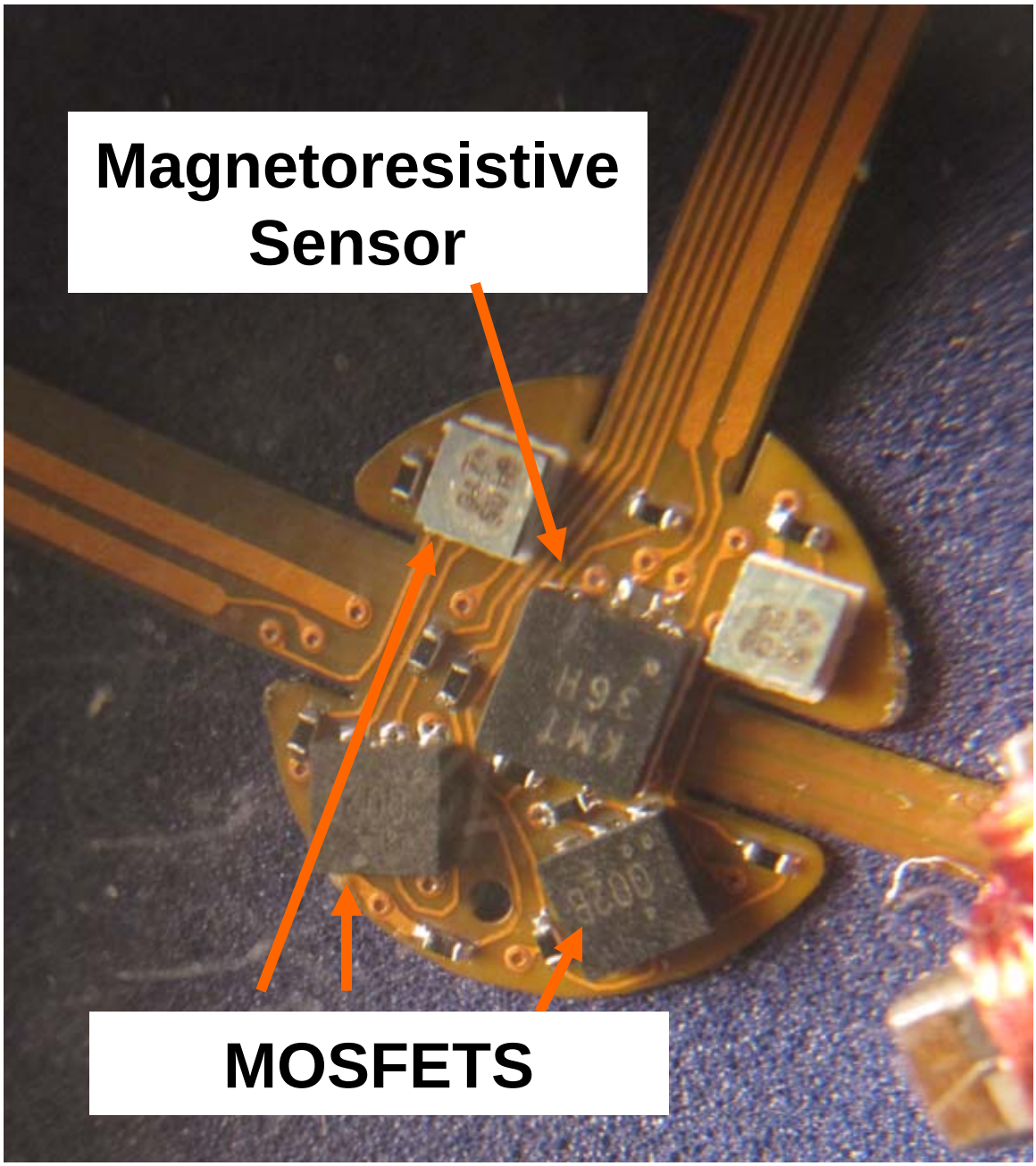


Figure 6-8: Millibot flex circuit: motor driver board. Major components are the dual-axis hall-effect position center (center) the dual N-channel MOSFETs (bottom) and the P-channel MOSFETS (top).

via hot-air reflow soldering.

Solder paste is stenciled onto the board and the electronic components are placed by an automated pick-and-place machine. The components are attached by hot-air reflow soldering in an oven.

The motor stators, which are assembled separately (see Section 5.7.2) are hand-soldered onto the flex circuit. The motor rotor, connecting yoke, and top/bottom bushings are then placed around the stator, and fixed in place with a single 0000-160 screw.

The flex circuit is then wrapped around the motors. On the motor side, the cable carrier is inserted under the board, and the board and cable carrier are secured in place with a single 0000-160 screw. The flex circuit cable is then fixed to the carrier with Kapton tape.

On the opposite side, the cable cover is inserted under the board, and the board and cover are secured to the bushing using a pair of 0000-160 screws.

At this point, the system consists of a set of motor units, connected by a common flex circuit spine. To assemble the nodes into the chain, the flex cable is coiled around the magnet descender, and the rotor joiner is attached to the next node's bushing with two screws to complete the assembly.

## 6.8 Results

We assembled a two-node Millibot, shown in Figure 6-1. The mass of each module is 4.0 g. After some iteration on the motor assembly procedure and power electronic design, we have achieved a working chain of two modules. The electropermanent stepper motor is strong enough to lift the weight of at least one module. We have fabricated parts for an eight-unit chain, and as of this writing are proceeding with assembly.

# Chapter 7

# Conclusion

## 7.1 Comparison to Related Work

Among switchable mechanical connectors, electropermanent magnets are strong for their size. Table 7.1 compares the tensile holding pressure of our electropermanent magnet, measured over its whole footprint, against other modular robot connectors. These include macroscale mechanically-latching modular robot connectors from Khoshnevis [52] and Nilsson [69], as well as a microscale connector based on van der Waals forces from Northern [69]. The electropermanent magnet presented here has the largest tensile holding pressure of all of these connectors, 231 kPa. This is surprising because the yield strength of metals is in the range of 200 - 1000 MPa, while the holding pressure of the magnetic field at 2 T is 3 MPa. But, mechanically latching connectors are typically based on pins and hooks with a relatively small area, and the failure mechanism is not tensile stress but bending and buckling. It is important to note that electropermanent magnets are much weaker in shear and twisting than in tension; we do not have precise data but it is very likely that the mechanically-latched connectors are stronger in these directions. Thus, when using magnetic connectors it makes sense to have a supplemental strengthening method for rotation and shear; for example, mechanical interlocking or van der Waals adhesion.

Electropermanent magnets are a suitable connector for millimeter scale modular robotics. Our Robot Pebbles have the smallest modules of any functional modular

| Connector | Operating Principle | Length | Mass | Holding Pressure | Force per Weight | Switching Energy |
|---|---|---|---|---|---|---|
| EP Magnet (this work) | Electropermanent Magnet | 6 mm | 0.2 g | 231 kPa | 2200 | 25 J/kg |
| CAST [52] | Magnetically actuated mechanical latch | 25 mm | 60 g | 160 kPa | 170 | 20 J/kg |
| Dragon [69] | SMA actuated mechanical latch | 75 mm | 170 g | 155 kPa | 410 | |
| Programmable Adhesion [70] | Magnetically switched van der Waals force | 1.7 mm | | 14 Pa | | |

Table 7.1: Connector comparison.

| System | Connectors | Length | Mass | Modules Supported |
|---|---|---|---|---|
| Robot Pebbles (this work) | Electropermanent magnet | 12 mm | 4 g | 81 |
| MICHE [35] | Gearmotor driven mechanically switched permanent magnet | 46 mm | 128 g | 15 |
| M-TRAN [57] | SMA retractable permanent magnet | 132 mm | 440 g | 6 |
| ATRON [71] | Gearmotor driven mechanical latch | 110mm | 850 g | 97 |

Table 7.2: Modular robot connection comparison.

robotic system in the published literature and this is enabled by their use of electropermanent magnets, which remove the need for off-the-shelf mechanical components.

Table 7.2 compares the number of modules that can be supported by the connectors of four modular robot systems: the Pebbles, MICHE, M-TRAN, and ATRON. ATRON uses a screw-driven mechanical connector, and can support 97 modules. The Pebbles come in second place with the solid-state electropermanent magnet, able to support 81 modules.

Because of the absence of torque-dependent $I^2R$ losses, electropermanent motors can have higher ratings for continuous torque than electromagnetic motors. Table 7.3 is a comparison of the torque and efficiency of four motors with similar dimensions to the electropermanent stepper. Even though its measured torque of 1.1 N-m is less than our modeling predicts, it is several times higher than the 0.16 N-mm maximum continuous torque of Dario's electromagnetic wobble motor and the MicroMo BH1202

| Motor | Operating Principle | Mass | Torque Density | Efficiency (Peak) | Efficiency (1 RPM) |
|---|---|---|---|---|---|
| EP Stepper (this work) | Elecropermanent wobble motor | 1 g | 1.1 N-m/kg | 1% | 1% |
| Dario [19] | Electromagnetic wobble motor | 1 g | 0.16 N-m/kg | 1.2% | 0.02% |
| MicroMo BH1202 | Electromagnetic brushless DC penny-motor | 1 g | 0.16 N-m/kg | 51% | 0.002% |
| Flynn[27] | Piezoelectric ultrasonic mini-motor | 0.5 g | 1.73 N-m/kg | | |

Table 7.3: Low-speed rotary motor comparison.

electromagnetic motor. In both these cases, the continuous torque and low-speed efficiency of these motors are limited by heat dissipation concerns, which are absent at low speed for the electropermanent stepper. The efficiency of the electropermanent stepper at 1 RPM is 1%, much better than the 0.02% and 0.002% efficiency of the electromagnetic motors at the same conditions. However, the MicroMo BH1202 has a peak efficiency of 51%, better than even the theoretical limit for electropermanent motors. For applications requiring a high absolute efficiency, such as energy conversion, or when high-speed, low-torque performance in needed, electromagnetic motors are more suitable.

Ultrasonic motors, which use piezoelectric vibration to move a load, are also known for their high-torque, low-speed characteristics. Indeed, Flynn's highest-torque "Green" mini-motor, 8 mm in diameter and 2 mm thick, had a torque density of 1.73 N-m/kg, somewhat higher than the 1.1 N-m/kg torque density of the electropermanent stepper. Flynn did not report data on the efficiency of her motors, and we have not been able to find power consumption and torque density data on other rotary ultrasonic motors of a similar size. However, we can compare the efficiency of electropermanent linear actuation to the commercial Squiggle motor, an ultrasonic linear motor that vibrates a piezoelectric nut around a lead screw. Table 7.4 shows data on peak force and efficiency for linear actuators of a similar size to the electropermanent magnet. The electropermanent actuator under these conditions has an efficiency of

| Motor | Operating Principle | Mass | Force Density | Stroke | Eff (1 mm/s) |
|---|---|---|---|---|---|
| EP Magnet (this work) | Electropermanent magnetic | 0.2 g | 22 kN/kg | 0.12 mm | 8% |
| Squiggle Motor (New Scale Tech.) | Piezoelectric ultrasonic | 0.16 g | 3 kN/kg | 6mm | 0.002% |
| Nitinol wire (New Scale Tech.) | SMA | any | 100 MPa | 3.5% | 0.07% |
| PZT (New Scale Tech.) | Piezoelectric | any | 100 MPa | 580 pm/V | 80% |

Table 7.4: Low-speed linear actuator comparison.

8%, compared to 0.002% for the Squiggle motor. While PZT has 80% efficiency under ideal conditions, switching it requires the input of enough energy to deform a crystal with a tensile modulus of 100 MPa. If this level of force is not needed, elastic losses and electronic switching losses can reduce the efficiency of the complete system well below the efficiency of raw PZT. These considerations point to the desirability of developing multi-pole linear electropermanent motors for use in miniaturized medical instruments and other applications of piezomotors not requiring their picometer positioning resolution.

Finally, we can conclude that miniaturized chain-style modular robots driven by electropermanent motors can have the same relative capabilities as their larger cousins, which are driven by geared electromagnetic motors. Table 7.5 compares the size, actuation mechanism, and arm-wrestling number of several chain-style modular robot systems. The arm-wrestling number, which we define in Section 6.3, is the number of modules that a single joint can lift as a cantilever. Based on the experimentally measured torque of the electropermanent stepper motor and the weight of the Millibot modules, we have estimated the arm-wrestling number of the Millibot at 3. This is larger than M-TRAN and ATRON's arm-wrestling number of 2, but smaller than Polybot's arm-wrestling number of 6. All three of these systems use geared electromagnetic motors. Like the Millibot, the magnetic Catoms use direct-drive electromagnetic actuation—but because of heat-dissipation limits with the electromagnets, the arm-wrestling number of the magnetic Catoms is 0.6. Note

| System | Actuation Principle | Length | Mass | Modules lifted as a cantilever |
|---|---|---|---|---|
| Millibot (est.) (this work) | Electropermanent wobble | 12 mm | 2 g | 3 |
| Magnetic Catoms [54] | Free-space electromagnetic | 45 mm | 105 g | 0.6 |
| M-TRAN [57] | Gearmotor | 132 mm | 440 g | 2 |
| ATRON [71] | Gearmotor | 110 mm | 850 g | 2 |
| Polybot [99] | Gearmotor | 50 mm | 416 g | 6 |

Table 7.5: Modular robot actuation comparison.

however, that the magnetic Catoms are a 2D system, and that lifting of other nodes is not required for their operation.

## 7.2 Summary

To summarize, electropermanent magnetic connectors and actuators can provide miniature robotic systems with the same capabilities of movement and connection current as macroscopic systems. At the millimeter scale, electropermanent magnets and actuators are suitable substitutes for gear-motors and mechanical latches, with similar performance relative to their size and weight. Fundamentally, this is because of the favorable surface-area-to-volume scaling of electropermanent magnets. Electropermanent connectors and actuators are simple to fabricate and have no moving parts, enabling all-electronic motion systems. They will enable millimeter-scale programmable matter.

# Chapter 8

# Lessons Learned

At some level, this whole document is about the lessons I have learned. But the rest of the document is about positive results. This section is devoted to negative results, ideas for future work, and anecdotal tips for working in the lab.

## 8.1 High-Level Lessons

### Test early and often

In the beginning of my graduate student career, I would work for weeks on some detailed computer model or intricate design project, only to go into the lab and quickly find out that whole concept was flawed due to some very basic, very unmodeled phenomenon. Without doing experiments, the issues one chooses to analyze are rarely the important ones. After learning this lesson a few times, I got better about ruthlessly subjecting my ideas to experiment, as early as possible, and then incrementally increasing the complexity toward the desired system.

### Also, analyze early and often

About a year before starting in on the main work of this thesis, I decided to try switching the magnetization of a permanent magnet, to use as a latch for programmable matter. I went down to the hardware store and bought an Alnico magnet, wrapped

a coil around it, and tried to switch its magnetization with the power supply on my desk. It didn't work because the current was too low, but the wire burned up because the pulse was too long. Convinced the idea was futile, I abandoned that idea to work on others. Later, while I was doing a theoretical comparison of actuation methods, I did some analysis of the physics of the problem and was surprised to see that the concept was actually very sound. I went back into the lab, built a much more carefully thought-out experimental setup, and got a great result. This was the first experiment that ultimately led to this thesis.

So the counterpoint to "Test early and often" is "Analyze early and often." Doing a too-quick experiment, without understanding the theory behind the problem well enough, might lead you to a false conclusion. It is a delicate art to strike the right balance between generating concepts, testing them with experiments, testing them with analysis, and reading the literature to see if someone else has tried it or if there is something better.

## 8.2 Connector Lessons

### The contact faces should be plated

The contact faces of the magnetic connectors become non-conductive after several weeks, probably because of oxidation. For our experiments, we solved this problem by periodically filing them down. For the next revision, they should be plated with gold or tin.

### The next system should be 3D

Stuck on the design of a 3D Robot Pebbles system, following the mantra of "test early and often," we built a 2D system instead. That was useful and we learned a lot; but the range of experiments that can be done with a 2D system is much smaller than with a 3D system. Also, the magnetic connectors are weak in rotation, and so a single layer object easily falls apart. 3D objects would be more robust. The next Pebbles-like system should really be 3D.

### Interlocking is important for strength

To build a strong structure from bricks, they should be interlocked. This gives the structure the strength of covalent bonding in at least some directions. There is a lesson to be learned here for the design of programmable matter.

## 8.3 Motor Lessons

### Wobble motor performance is not as predicted by the model

The power efficiency of the wobble motors, 1%, was about 10 times lower than the simple quasistatic electropermanent linear actuator. Also, the dynamic torque was about 10 times lower than expected, 1 N-mm rather than 10 N-mm, while the force of the linear actuator was exactly as predicted by the model. This points to improving motor mechanical dynamics to reduce elastic losses as a major opportunity to improve on the results presented here, perhaps by an order or magnitude. One approach would be to study the wobble motor dynamics in detail, with high-speed video and modeling of the elastic dynamics, and to attempt to correct the problem. Another approach would be to apply the electropermanent principle to a more conventional mechanical design for a motor, using a bearing to simplify the kinematics to rotation only.

### Side-drive motors could work

Early in the project, when I had less insight into the magnetic operation of these motors than I do now, I developed a bias against side-drive designs, preferring gap-closing designs because of concerns about iron saturation during the magnetizing pulse. This led to the selection of the gap-closing wobble motor as the preferred topology. However, I now believe that by with castellated teeth, Hyperco-50 soft magnetic material, or both, the iron saturation concern could be addressed, and excellent side-drive electropermanent motors could be constructed.

### The magnets should be thinner and the pulse rate higher

Our wobble motor prototypes were designed to have the longest magnets that could fit. One reason for this was to support the rotor/stator diameter difference needed for geared wheels. Another design direction that might result in higher efficiency and smoother rotation would be to use the thinnest rotor/stator gap possible, and proportionally thin magnets. The resulting motor would operate with shorter, lower-energy, more closely-spaced pulses. The $I^2R$ losses would be lower due to the relatively large size of the coils compared to the magnets, and the amplitude of the wobble would be lower, which might reduce the elastic losses.

### Our geared wobble motor prototypes were unreliable

We built several prototype geared wobble motors, [86] using N teeth on the stator and N+1 teeth on the rotor. Our aim was to increase torque, with the gear teeth acting to reduce slip between the rotor and stator and enforce the intended motion path. We tried arc-segment teeth and involute teeth, both cut into the magnetic components and on separate coaxial wheels. Our experience was that gear teeth made the motor harder to assemble and less reliable. The basic problem was the motor would run for a short time, but then wedge itself into an invalid position (e.g. gears tip-to-tip) and stop turning. More development of the gear tooth shape and bearings might lead to a solution to this problem; if this is done it should be informed by imaging of the actual vibrational dynamics of the motor so that the nature of the wedging problem can be better understood.

## 8.4 Practical Lessons from the Lab

### Permanent magnets like to clump into balls

When assembling tiny magnetic parts on your desk, don't let them get too close together. Also, don't drop them on the floor. But if you do, a large magnet is a useful tool for finding them.

### Goo is bad

It is tempting to say "Oh, we'll get everything positioned just right and then encapsulate the whole assembly in goo," such as hot glue, silicone sealant, P2 wondermask, or epoxy. The problem is that once you do this, the system becomes becomes unchangeable and unobservable. This might be a fine strategy for production, but not for prototyping and experimenting. The reversible soldered nubs that hold the Pebble circuits onto the frames represent the triumph of good design over bad goo.

### Long work-time epoxy is wonderful

For fixing parts together at this scale, glue works well. The key is that it has to have a long open time, so you have time to get everything lined up, and the excess glue has to be cleanable with solvents. A machined fixture makes it easy to line up the parts, and then the assembly can be lifted out of the fixture. Loctite E-60HP worked very well for bonding metals and magnets, and cleans up with isopropanol. Loctite 409, an instant-setting cyanoacrylate, was useful for tacking down wires, but disastrous when we attempted to use it to hold parts in precision alignment.

### Small magnet wire is floppy

The hardest part of building these motors is separating the "big hairy mess" of wires after winding, then soldering them down to the circuit board. Looking at a CAD model, it is easy to imagine the magnet wire as a stiff metal rod, easily formed into precise shapes and easily poked through holes. Actually, its mechanical properties are more like spaghetti; it is much easier to pull it through a hole then to push it. A good motor design should make terminating the magnet wires as simple as possible, something you would be happy to do wearing giant spacesuit gloves. Soldering the wires to oversized surface mount pads next to the coils seems to work fairly well.

### Thin magnet wire is fragile

On 40 AWG magnet wire, the insulation is only about 5 microns think. One hard pull against a sharp edge will cause the insulation to fail. We had a lot of problems with the magnet wire shorting out to its conductive magnetic mandrel. The solution was to start with a nice, rounded, smooth surface, to immobilize the coils after winding by setting the bond coat, and then to treat them with the utmost gingerness and care.

### Acquire and use the right tools

Titanium tweezers are not attracted to magnets. Sharp knives work much better than dull ones. Screwdrivers with exactly the right size tip don't slip out of the screw head. Paying attention to things like this makes the difference between getting a working system and getting a big sad mess of broken parts.

### Cleanliness is important

Dust and dirt particles are a problem at this scale. Ferromagnetic dust particles lead to oversize air gaps when gluing up magnets. To make precise assemblies, it is important to have a separate area for fabrication (e.g. filing, cutting) and assembly. The assembly area and all of the parts should be scrubbed down with packing tape before starting; this is the only way I have found to remove ferromagnetic dust from magnets; thanks to Paul Lituri of BJA Magnetics for this suggestion.

### Fabrication is more precise than assembly

The most ordinary macro-machining center has $2.5\mu m$ positional resolution. Designing complexity into the parts (e.g. snap fits) to simplify the assembly makes sense. Of course, the ultimate limit of this idea is microfabrication, where the whole device is fabricated in one shot an there is no assembly at all; that is ultimately the right way to build these systems in quantity.

NOTE: The design documents for the systems presented in this thesis are available online at `http://groups.csail.mit.edu/drl/ara`

# Bibliography


[1] Jr. A. E. Fitzgerald, C. Kingsley, and S. Umans. *Electric Machinery*. McGraw-Hill, New York, NY, 2002.

[2] Austria Microsystems AG. High voltage ASIC processes. Austria.

[3] C.H. Ahn, Y.J. Kim, and M.G. Allen. A planar variable reluctance magnetic micromotor with fully integrated stator and coils. *Microelectromechanical Systems, Journal of*, 2(4):165–173, December 1993.

[4] A. P. Alivisatos. Semiconductor Clusters, Nanocrystals, and Quantum Dots. *Science*, 271(5251):933–937, 1996.

[5] Byoung Kwon An. EM-cube: cube-shaped, self-reconfigurable robots sliding on structure surfaces. In *Robotics and Automation, 2008. ICRA 2008. IEEE International Conference on*, pages 3149–3155, 19-23 2008.

[6] Kellar Autumn, Yiching A. Liang, S. Tonia Hsieh, Wolfgang Zesch, Wai Pang Chan, Thomas W. Kenny, Ronald Fearing, and Robert J. Full. Adhesive force of a single gecko foot-hair. *Nature*, 405:681–685, 2000.

[7] D J Bell, T J Lu, N A Fleck, and S M Spearing. MEMS actuators and sensors: observations on their performance and selection for purpose. *Journal of Micromechanics and Microengineering*, 15(7):S153–S164, 2005.

[8] Philibert Maurice Braillon. Magnetic plate comprising permanent magnets and electropermanent magnets. US Patent 4,075,589.

[9] Thomas P. Burg, Michel Godin, Scott M. Knudsen, Wenjiang Shen, Greg Carlson, John S. Foster, Ken Babcock, and Scott R. Manalis. Weighing of biomolecules, single cells and single nanoparticles in fluid. *Nature*, 446(7139):1066–1069, 2007.

[10] W.J. Butera. *Programming a paintable computer*. PhD thesis, Massachusetts Institute of Technology, 2002. UMI Order Number: AAI0804036.

[11] P. Campbell and S. Al-Murshid. A model of anisotropic Alnico magnets for field computation. *Magnetics, IEEE Transactions on*, 18(3):898–904, May 1982.

[12] P.L. Cavallotti, M. Bestetti, and S. Franz. Microelectrodeposition of Co-Pt alloys for micromagnetic applications. *Electrochimica Acta*, 48(20-22):3013–3020, 2003. Electrochemistry in Molecular and Microscopic Dimensions.

[13] Robert J. Chapuis. *100 Years of Telephone Switching (1878-1978).: Manual and electromechanical switching (1878-1960's) Part 1 of 100 Years of Telephone Switching*. IOS Press, Fairfax, VA, 2003.

[14] Ching-Heng Chen, J Andrew Yeh, and Pei-Jen Wang. Electrical breakdown phenomena for devices with micron separations. *Journal of Micromechanics and Microengineering*, 16(7):1366–1373, 2006.

[15] Kenneth C. Cheung, Erik D. Demaine, and Saul Griffith. Programmable assembly with universally foldable strings. Under Review.

[16] J.D. Cobine. *Gaseous Conductors: theory and engineering applications*. Dover, New York, NY, 1958.

[17] Adam L. Cohen, Uri Frodis, Fan-Gang Tseng, Gang Zhang, Florian Mansfeld, and Peter M. Will. EFAB: low-cost automated electrochemical batch fabrication of arbitrary 3D microstructures. *Micromachining and Microfabrication Process Technology V*, 3874(1):236–247, 1999.

[18] John H. Comtois and Victor M. Bright. Surface micromachined polysilicon thermal actuator arrays and applications. In *Proceedings of the Solid-State Sensor and Actuator Workhop*, June 1996.

[19] P. Dario, M.C. Carrozza, C. Stefanini, and S. D'Attanasio. A mobile microrobot actuated by a new electromagnetic wobble micromotor. *Mechatronics, IEEE/ASME Transactions on*, 3(1):9–16, March 1998.

[20] K. Eric Drexler. *Engines of Creation: The Coming Era of Nanotechnology*. Anchor, Garden City, NJ, 1987.

[21] Robert F. Edgar, Francois D. Martzloff, and Russell E. Tompkins. Magnetic latch and switch using cobalt-rare earth permanent magnets. US Patent 3,671,893.

[22] J.A. Ewing and Helen G. Klaassen. Magnetic qualities of Iron. *Philosophical Transactions of the Royal Society of London*, 184:985–1039, 1893.

[23] Long-Sheng Fan, Yu-Chong Tai, and R.S. Muller. IC-processed electrostatic micro-motors. In *Electron Devices Meeting, 1988. IEDM '88. Technical Digest., International*, pages 666–669, 1988.

[24] A. Feiner, C.A. Lovell, T.N. Lowry, and P.G. Ridinger. The ferreed – a new switching device. *The Bell System Technical Journal*, 39(1), January 1960.

[25] Dan Ferber. Synthetic biology: Microbes made to order. *Science*, 303(5655):158–161, 2004.

[26] Richard P. Feynman. There's plenty of room at the bottom. *Engineering and Science*, February 1960.

[27] Anita M. Flynn. *Piezoelectric Ultrasonic Micromotors*. PhD thesis, Massachusetts Institute of Technology, 1997.

[28] L.G. Frechette, S.F. Nagle, R. Ghodssi, S.D. Umans, M.A. Schmidt, and J.H. Lang. An electrostatic induction micromotor supported on gas-lubricated bearings. In *Micro Electro Mechanical Systems, 2001. MEMS 2001. The 14th IEEE International Conference on*, pages 290–293, 2001.

[29] T. Fukuda and S. Nakagawa. Dynamically reconfigurable robotic system. In *Proceedings of the IEEE International Conference on Robotics and Automation*, pages 1581–1586. IEEE, 1988.

[30] S.B. Fuller, E.J. Wilhelm, and J.M. Jacobson. Ink-jet printed nanoparticle microelectromechanical systems. *IEEE Journal of Microelectromechanical Systems*, 11:54–60, 2002.

[31] N. A. Gershenfeld. *The Coming Revolution on Your Desktop — From Personal Computers to Personal Fabrication*. Basic Books, New York, NY, 2005.

[32] Neil A. Gershenfeld. *The Physics of Information Technology*. Cambridge University Press, Cambridge, UK, 2000.

[33] K. Gilpin, A. Knaian, and D. Rus. Robot pebbles: One centimeter modules for programmable matter through self-disassembly. In *Robotics and Automation, 2010. ICRA '10. IEEE International Conference on*, Anchorage, AK, 2010. IEEE.

[34] K. Gilpin, K. Kotay, and D. Rus. MICHE: Modular shape formation by self-dissasembly. *Robotics and Automation, 2007 IEEE International Conference on*, pages 2241–2247, 2007.

[35] Kyle Gilpin, Keith Kotay, Daniela Rus, and Iuliu Vasilescu. Miche: Modular Shape Formation by Self-Disassembly. *The International Journal of Robotics Research*, 27(3-4):345–372, 2008.

[36] S. Goldstein, J. Campell, and T. Mowry. Programmable matter. *Computer*, 38:99–101, 2005.

[37] Seth Copen Goldstein, Todd C. Mowry, Jason D. Campbell, Michael P. Ashley-Rollman, Michael De Rosa, Stanislav Funiak, James F. Hoburg, Mustafa Emre Karagozler, Brian Kirby, Peter Lee, Padmanabhan Pillai, J. Robert Reid, Daniel D. Stancil, and Michael Philetus Weller. Beyond audio and video: Using claytronics to enable pario. *AI Magazine*, 30(2), July 2009.

[38] S. Griffith. *Growing Machines*. PhD thesis, Massachusetts Institute of Technology, 2004.

[39] S. Griffith, D. Goldwater, and J. Jacobson. Self-replication from random parts. *Nature*, 437:636, 2005.

[40] Herman A. Haus and James R. Melcher. *Electromagnetic Fields and Energy*. Prentice Hall, Upper Saddle River, NJ, 1989.

[41] Peter-Konrad Hermann. Hysteresis motor. US Patent 3,610,978.

[42] Roger T. Howe and Charles G. Sodini. *Microelectronics: an Integrated Approach*. Prentice-Hall, Upper Saddle River, NJ, 1997.

[43] Arlo F. Israelton. Turn-off permanent magnet. US Patent 3,452,310.

[44] S.C. Jacobsen, R.H. Price, J.E. Wood, T.H. Rytting, and M. Rafaelof. The wobble motor: design, fabrication and testing of an eccentric-motion electrostatic microactuator. In *Robotics and Automation, 1989. Proceedings., 1989 IEEE International Conference on*, volume 3, pages 1536–1546, 14-19 1989.

[45] Stuart A. Jacobson and Alan H. Epstein. An informal survey of power MEMS. In *The International Symposium on Micro-Mechanical Engineering*, December 2003.

[46] Hartmut Janocha. *Actuators*. Springer-Verlag, Berlin, Germany, 2004.

[47] Chang-Hyeon Ji, Youngjoo Yee, Junghoon Choi, Seong-Hyok Kim, and Jong-Uk Bu. Electromagnetic $2 \times 2$ MEMS optical switch. *Selected Topics in Quantum Electronics, IEEE Journal of*, 10(3):545–550, May-June 2004.

[48] U. Kafader and J. Schulze. Similarity relations in electromagnetic motors – limitations and consequences for the design of small dc motors. In *Ninth International Conference on New Actuators*, pages 309–312, June 2004.

[49] M.E. Karagozler, J.D. Campbell, G.K. Fedder, S.C. Goldstein, M.P. Weller, and B.W. Yoon. Electrostatic latching for inter-module adhesion, power transfer, and communication in modular robots. In *Intelligent Robots and Systems, 2007. IROS 2007. IEEE/RSJ International Conference on*, pages 2779–2786, October 2007.

[50] Mustafa Emre Karagozler, Seth Copen Goldstein, and J. Robert Reid. Stress-driven MEMS assembly + electrostatic forces = 1mm diameter robot. In *Proceedings of the IEEE International Conference on Intelligent Robots and Systems (IROS '09)*, October 2009.

[51] R. Ketchledge. The No. 1 electronic switching system. *Communication Technology, IEEE Transactions on*, 13(1):38–41, March 1965.

[52] B. Khoshnevis, P. Will, and Wei-Min Shen. Highly compliant and self-tightening docking modules for precise and fast connection of self-reconfigurable robots. In *Robotics and Automation, 2003. Proceedings. ICRA '03. IEEE International Conference on*, volume 2, pages 2311–2316, 14-19 2003.

[53] Sangbae Kim, M. Spenko, S. Trujillo, B. Heyneman, D. Santos, and M.R. Cutkosky. Smooth vertical surface climbing with directional adhesion. *Robotics, IEEE Transactions on*, 24(1):65–74, February 2008.

[54] Brian T. Kirby, Burak Aksak, Jason D. Campbell, James F. Hoburg, Todd C. Mowry, Padmanabhan Pillai, and Seth Copen Goldstein. A modular robotic system using magnetic force effectors. *Intelligent Robots and Systems, 2007. IROS 2007. IEEE/RSJ International Conference on*, pages 2787–2793, October 29 2007-November 2 2007.

[55] A.N. Knaian. *Design of Programmable Matter*. PhD thesis, Massachusetts Institute of Technology, 2008.

[56] K. Kotay and D. Rus. Locomotion versatility through self-reconfiguration in robotics and autonomous systems, 1998.

[57] H. Kurokawa, A. Kamimura, E. Yoshida, K. Tomita, S. Murata, and S. Kokaji. Self-reconfigurable modular robot (M-TRAN) and its motion design. *Control, Automation, Robotics and Vision, 2002. ICARCV 2002. 7th International Conference on*, 1:51–56, 2-5 December 2002.

[58] D. Lancaster. *CMOS Cookbook*. Butterworth-Heinemann, Oxford, UK, 1997.

[59] T.H. Lee. *The Design of CMOS Radio-Frequency Integrated Circuits*. Cambridge University Press, Cambridge UK, 2003.

[60] MagSwitch Technology (Worldwide) Pty Ltd. Web site, www.magswitch.co.au. North Ryde, NSW, 2113, Australia.

[61] Marc J. Madou. *Fundamentals of microfabrication: the science of miniaturization*. CRC Pressl, Boca Raton, FL, 2002.

[62] Wil McCarthy. Programmable matter. *Nature*, 407(6804):569–569, 2000.

[63] G. Moore. No exponential is foreverbut we can delay forever. Presentation at the IEEE International Solid-State Circuits Conference, February 10, 2003.

[64] G. Moore. Cramming more components onto integrated circuits. *Electronics*, 38, 1965.

[65] Lester R. Moskowitz. *Permanent Magnet Design and Application Handbook*. Krieger Publishing Company, Malabar, FL, 1986.

[66] S. Murata, E. Yoshida, A. Kamimura, H. Kurokawa, K. Tomita, and S. Kokaji. M-TRAN: Self-reconfigurable modular robotic system. *IEEE/ASME Transactions of Mechatronics*, 7(4):431–441, December 2002.

[67] Michael P. Murphy, Burak Aksak, and Metin Sitti. Gecko-inspired directional and controllable adhesion. *Small*, 5(2):170–175, 2009.

[68] T. Niino, T. Higuchi, and S. Egawa. Dual excitation multiphase electrostatic drive. In *Industry Applications Conference, 1995. Thirtieth IAS Annual Meeting, IAS '95., Conference Record of the 1995 IEEE*, volume 2, pages 1318–1325, October 1995.

[69] M. Nilsson. Heavy-duty connectors for self-reconfiguring robots. In *Robotics and Automation, 2002. Proceedings. ICRA '02. IEEE International Conference on*, volume 4, pages 4071–4076, 2002.

[70] Michael T. Northen, Christian Greiner, Eduard Arzt, and Kimberly L. Turner. A gecko-inspired reversible adhesive. *Advanced Materials*, 20(20):3905–3909, 2008.

[71] Esben Hallundbk Østergaard, Kristian Kassow, Richard Beck, and Henrik Hautop Lund. Design of the ATRON lattice-based self-reconfigurable robot. *Autonomous Robots*, 21(2):165–183, 2006.

[72] Rollin J. Parker and Robert J. Studders. *Permanent Magnets and Their Application*. John Wiley and Sons, New York, NY, 1962.

[73] L.S. Penrose. Self-reproducing machines. *Scientific American*, 200:105–114, 1959.

[74] L.S. Penrose and R. Penrose. A self-reproducing analogue. *Nature*, 179:105–114, 1957.

[75] Dominic F. Pignataro. Electrically switchable magnet system. US Patent 6,229,422.

[76] Manu Prakash and Neil Gershenfeld. Microfluidic Bubble Logic. *Science*, 315(5813):832–835, 2007.

[77] Dexter Magnetic Products. Nd-Fe-B curves and properties table.

[78] Cecilia D Richards, Michael J Anderson, David F Bahr, and Robert F Richards. Efficiency of energy conversion for devices containing a piezoelectric component. *Journal of Micromechanics and Microengineering*, 14(5):717, 2004.

[79] J. Sampsell. Digital micromirror device and its application to projection displays. *Journal of Vacuum Science & Technology B: Microelectronics and Nanometer Structures*, 12:3242–3246, 1994.

[80] Toshiiku Sashida and Takashi Kenjo. *An Introduction to Ultrasonic Motors*. Oxford University Press, New York, NY, 1993.

[81] D. Schurig, J. J. Mock, B. J. Justice, S. A. Cummer, J. B. Pendry, A. F. Starr, and D. R. Smith. Metamaterial Electromagnetic Cloak at Microwave Frequencies. *Science*, 314(5801):977–980, 2006.

[82] Stephen D. Senturia. *Microsystem Design*. Kluwer Academic Publishers, Dordrecht, The Netherlands, 2001.

[83] A.H. Slocum. Precision machine design: macromachine design philosophy and its applicability to the design of micromachines. In *Micro Electro Mechanical Systems, 1992, MEMS '92, Proceedings. An Investigation of Micro Structures, Sensors, Actuators, Machines and Robot. IEEE*, pages 37–42, February 1992.

[84] Alexander H. Slocum. *Precision Machine Design*. Society of Manufacturing Engineers, 1992.

[85] Supertex, Inc. Product catalog. Sunnyvale, CA.

[86] K. Suzumori and K. Hori. Micro electrostatic wobble motor with toothed electrodes. In *Micro Electro Mechanical Systems, 1997. MEMS '97, Proceedings, IEEE., Tenth Annual International Workshop on*, pages 227–232, 26-30 1997.

[87] Massood Tabib-Azar. *Microactuators*. Kluwer Academic Publishers, Dordrecht, The Netherlands, 1998.

[88] Thorlabs. Catalog. Newtown, NJ.

[89] P.A. Tipler. *College Physics*. Worth, New York, NY, 1987.

[90] D. Trivedi, C. D. Rahn, W. M. Kierb, and I. D. Walkercy. Soft robotics: Biological inspiration, state of the art, and future research. *Applied Bionics and Biomechanics*, 5:99–117, 2008.

[91] S. Ueha and Y. Tomikawa. *Ultrasonic Motors*. Oxford University Press, New York, NY, 1993.

[92] Rochester University. Electrical breakdown limits for MEMS, ECE234/434 handout. `http://www.ece.rochester.edu/courses/ECE234/MEMS_ESD.pdf`.

[93] S.A. Vittoro. MicroElectroMechanical Systems (MEMS), Cambridge Science Abstract.

[94] B.A. Warneke, M.D. Scott, B.S. Leibowitz, Lixia Zhou, C.L. Bellew, J.A. Chediak, J.M. Kahn, B.E. Boser, and K.S.J. Pister. An autonomous 16 $mm^3$ solar-powered node for distributed wireless sensor networks. *Sensors, 2002. Proceedings of IEEE*, 2:1510–1515, 2002.

[95] P.J. White, K. Kopanski, and H. Lipson. Stochastic self-reconfigurable cellular robotics. *Robotics and Automation, 2004. Proceedings. ICRA '04. 2004 IEEE International Conference on*, 3:2888–2893, 2004.

[96] Herbert H. Woodson and James R. Melcher. Electromechanical dynamics, 2007. 3 vols. (Massachusetts Institute of Technology: MIT OpenCourseWare). http://ocw.mit.edu (accessed 04 26, 2010). License: Creative Commons Attribution-NonCommercial-Share Alike.

[97] Akio Yamamoto, Toshiki Niino, Takahisa Ban, and Toshiro Higuchi. A high-power electrostatic motor using skewed electrodes. *Electrical Engineering in Japan*, 125(3):50–58, 1998.

[98] M. Yim, W. Shen an B. Salemi, D. Rus, M. Moll, H. Lipson, E. Klavins, and G.S. Chirkjian. Modular self-reconfigurable robot systems. *IEEE Robotics and Automation Magazine*, 14:43–52, 2007.

[99] M. Yim, David G. Duff, and Kimon D. Roufas. Polybot: a modular reconfigurable robot. In *Proceedings of the IEEE International Conference on Robotics and Automation*, pages 514–520. IEEE, 2000.

[100] M. Yim, Y. Zhang, K. Roufas, D. Duff, and C. Eldershaw. Connecting and disconnecting for chain self-reconfiguration with Polybot. *IEEE/ASME Transactions on Mechatronics*, 7:442–451, 2002.

[101] Mark Yim. Polybot website. `http://www2.parc.com/spl/projects/modrobots/polybot/polybot.html`.

[102] Marc Zupan, Mike F. Ashby, and Normal A. Fleck. Actuator classification and selection–the development of a database. *Advanced Engineering Materials*, 4(12):933–939, 2002.

[103] V. Zykov, E. Mytilinaios, B. Adams, and H. Lipson. Self-reproducing machines. *Nature*, 435:163–164, 2005.

# Appendix A

# Electrical Design of Microfabricated Module

Because semiconductor device fabrication is complex and requires high temperature process steps, we feel it makes sense to fabricate the integrated circuit containing the module's control and drive electronics seperately. However, because the size of the module is below that of commercially-available packaged VLSI functions, a single, custom-designed integrated circuit will be required.

A candidate process for the logic IC is TSMC's CL018HV HV-CMOS process, with $0.18\mu m$ feature size and up to 32 V drain-to-source voltage. A 1 mm square IC on this process can have about 50,000 transistors; compare this to the the Intel 4004 microprocessor's 2,300 transistors.

To size the energy source and drive transistors, we can estimate the electrical characteristics of the electropermanent magnets using the scaling information in Table 3.2. For 10 V drive and 0.5 mm magnets, we expect the switching pulse length to be 700 ns, the switching current to be 800 mA, and the switching energy to be $2\mu J$.

For energy storage, we could use a $0.22\mu F$, 10V ceramic capacitor, which holds $11\mu J$, and is commercially available in the size "0201" package, which is 0.6 mm x 0.3 mm x 0.3mm.

To size the drive transistors, we can use the formula for the saturation drain current of a MOSFET from Howe and Sodini. [42]

$$I_D = \left(\frac{W}{2L}\right) \mu_n C_{ox} (V_{GS} - V_{Tn})^2$$

With $\mu_n C_{ox} = 50\mu A/V^2$, gate-to-source voltage $V_{GS} = 10V$, gate threshold voltage $V_{Tn} = 1V$, and gate length $L = 0.18\mu m$, the gate width W needs to be just $40\mu m$ to support the drain current of 800 mA required to pulse the electropermanent magnets. Drive transistors with sufficient saturation current density will fit on the 1 mm chip.